



**Laser texturisation of photovoltaic module
superstrates for enhanced light trapping
performance**

A thesis submitted in fulfilment of the requirement for the degree
of
Doctor of Philosophy

David John Moore
(*B.Eng*)

Supervisors:
Prof. Dermot Brabazon
Prof. Patrick J. McNally

School of Mechanical and Manufacturing Engineering
Dublin City University, Ireland.

September 2016

Declaration

I hereby certify that this material, which I now submit for assessment on the programme of study leading to the award of Ph.D., is entirely my own work, that I have exercised reasonable care to ensure that the work is original, and does not to the best of my knowledge breach any law of copyright, and has not been taken from the work of others save and to the extent that such work has been cited and acknowledged within the text of my work.

Signed: _____

ID No.: 54325869

Date: 7th September 2016

Dedication

To Enrika

For always being by my side

List of Publications

This thesis describes original work that has not previously been submitted for a degree in Dublin City University or at any other University. The investigations were carried out in the School of Mechanical & Manufacturing Engineering, Dublin City University under the supervision of Prof. Dermot Brabazon. This work has been disseminated through the following publications.

Journal Papers:

Vazquez, M., **Moore, D.**, He, X., Ben Azouz, A., Nesterenko, E., Nexterenko, P., Paull, B., Brabazon, D., Focussed ion beam serial sectioning and imaging of monolithic materials for 3D reconstruction and morphological parameter evaluation, *Analyst*, 139, 1, 2014, pp. 99-104

Moore, D., Rahman, M., Dowling, D., McNally, P.J., Brabazon, D., Laser machined macro and micro structures on glass for enhanced light trapping in solar cells, *Applied Physics A*, 110, 3, 2013, pp. 661-665

Moore, D., Krishnamurthy, S., Chao, Y., Wang, Q., Brabazon, D., and McNally, P.J., Characteristics of silicon nanocrystals for photovoltaic applications, *Physica Status Solidi A*, 1-4, 2010, Vo. 208, Issue 3, pp. 604-607; DOI 10.1002/pssa.201000381

Peer Reviewed Conference Paper:

Moore, D., Brabazon, D., McNally, P.J., Laser texturisation for increased light absorption in silicon solar cells, Part 2: Proceedings 3rd International Conference on Sustainable Energy and Environmental Protection, Dublin, Ireland, 12-15 August 2009, pp. 218-224. ISBN: 97809555781-2-0.

Article:

Moore, D., Huet, G., Cousinet, S., Brabazon, D., and McNally, P., Developing a low-cost, noncontact, 3D optical surface profilometer with surface visualisation and roughness analysis capabilities in laser-processed surface characterisation, Read-out, Journal of Instrumentation, Control and Automation, Vol. 11.01, 2011, ISSN 0791-4369, pp.2-3.

International Conferences, Seminars & Posters:

Moore, D., Rahman, M., Dowling, D., McNally, P.J., Brabazon, D., Laser machined macro and micro structures on glass for enhanced light trapping in solar cells, Poster Presentation, COLA Conference, Playa Del Carmen, Mexico, 15th November 2011.

Moore, D., Krishnamurthy, S., Chao, Y., Wang, Q., Brabazon, D., and McNally, P.J., Light trapping in alkyl-capped silicon nanocrystals deposited on laser textured glass superstrates, Oral Presentation, E-MRS 2011 Spring Meeting Symposium R, Nice, France, 11th May 2011.

Moore, D., Brabazon, D., McNally, P.J., The effects of laser induced glass texturing on the absorption of light for photovoltaic applications, Oral Presentation, 4th Int. Conf on Sustainable Energy and Environmental Protection, Politecnico di Bari, Italy 30th June 2010.

Moore, D., Brabazon, D., and McNally, P.J., Pulsed CO₂ Laser Induced Micro and Nanostructures on Quartz Glass, Oral Presentation, E-MRS 2010 Spring Meeting Symposium R, Strasbourg, France, 11th June 2010.

Moore, D., Krishnamurthy, S., Chao, Y., Wang, Q., Brabazon, D., and McNally, P.J., Characteristics of silicon nanocrystals for photovoltaic applications, Poster Presentation, E-MRS 2010 Spring Meeting Symposium I, Strasbourg, 10th June 2010.

Moore, D., Brabazon, D., McNally, P.J., The effects of laser induced glass texturing on the absorption of light for photovoltaic applications, Poster Presentation, Faculty Research Day 2010, Dublin City University, Ireland 12th May 2010.

Moore, D., Brabazon, D., McNally, P.J., Laser texturisation of glass superstrate for increased light absorption in thin-film silicon solar cells, Poster presentation, 'Innovation fuelling the Smart Society' IRCSET Symposium 2009, Dublin, Ireland, September 25th 2009.

Acknowledgements

Firstly, I would like to acknowledge my supervisors, Prof. Dermot Brabazon and Prof. Patrick McNally. They have demonstrated great encouragement, provided guidance, assistance, and flexibility, and have shown great patience, all which has allowed me to take this thesis to where it is today. I have been very fortunate to have the opportunity to pursue a Ph.D., and for that I am extremely grateful.

I would like to thank all of the technical staff who assisted me along the way through, namely Michael May, Alan Meehan, Eoin Tuohy, Jim Barry, Cian Merne, Liam Domican, and the late Martin Johnson.

I would like to extend further thanks to those who helped my learning, namely Alain Fave of INSA Lyon who was kind enough to host me in his lab at the beginning of these studies. It was a great experience, and certainly opened my eyes to the world of semiconductor processing. I would also like all the collaborators who I was lucky enough to work with during this study.

I would like to give special thanks to my colleagues and friends, Evans, Saba, Tony, Irina, Ahmed, Sylvain, Arsalan, and Owen, just to name a few. There is no-one else I would rather have shared this experience with.

I'd like to thank my family, especially my parents for being voices of encouragement when life gets hard. Your love, support, and hard-work has made me who I am today.

I am eternally grateful to my amazing wife Enrika, without whose support I might never have had the energy to complete this thesis. A very special thanks goes to my little man Henry, there is no one else in this world who gives me perspective in the way that you do. You have changed everything in how I see the world.

Finally, I need to thank the Irish Research Council for funding this research. Without this funding my Ph.D. study is not something I would have been able to experience.

Table of Contents

Declaration	I
Dedication	II
List of Publications	III
Acknowledgements	VI
List of Figures	XI
List of Tables.....	XVI
Nomenclature	XIX
Abstract	1
Chapter 1 Introduction	2
Chapter 2 Literature Review	7
2.1 Introduction to solar cells	7
2.2 The mechanics of the generation of photocurrent	7
2.3 Silicon as a photovoltaic material	11
2.4 The Air Mass (AM) standard	11
2.5 Types of wafer based silicon solar cells	13
2.6 Factors limiting the absorption of light in silicon solar cells	13
2.7 Possible device configurations for effective light trapping	14
2.8 Important factors in surface texturisation	16
2.9 Common front surface textures	16
2.9.1 Pyramidal texture	16
2.9.2 Random texture	18
2.9.3 Honeycomb texture	19
2.9.4 Grooving	20
2.10 Laser micromachining in solar cell design	22
2.10.1 Design of solar cells on texturised substrates	22
2.10.2 Micro-structuring and Nano-structuring of glass substrate with laser	23
2.11 Computer simulation for optimum texture type	24
2.12 Thin-film solar cell designs	24
2.13 Silicon quantum dot solar cells	25
2.14 Solar Cell superstrate material selection	27
2.14.1 Refractive indices	27
2.14.2 Laser absorption characteristics	27
2.14.3 Cost and availability	28
2.14.4 Thermal properties and stability	28

2.14.5	Transparency to AM1.5G spectrum.....	28
2.15	Literature Review Summary	29
Chapter 3	Materials & Methods.....	30
3.1	Design of a Depth-from-Focus based Optical Profilometer.....	30
3.1.1	System Specification.....	34
3.1.2	Design of the Optical System.....	35
3.1.3	Design of the Motion Control System	36
3.1.4	Image acquisition and processing	37
3.1.5	Image stitching (tiling).....	39
3.1.6	Surface roughness calculation and evaluation	39
3.2	Verification of the optical plane of the 3D Profilometer.....	42
3.3	Performance analysis of the linear stages of the 3D Optical Profilometer..	43
3.3.1	Selection of Target Positions for Positional Analysis.....	43
3.3.2	Recording of the stage positions using Dial Gauge Indicators	44
3.3.3	Potential sources of measurement uncertainty.....	47
3.4	Verification of 3D measurement performance	49
3.4.1	Testing procedure of the 3D measurement performance of the Optical Profilometer	55
3.4.2	Potential sources of measurement uncertainty in the 3D measurement... ..	60
3.5	CO ₂ Laser System hardware and specifications.....	61
3.6	Glass materials selection for solar cells superstrates.....	62
3.7	Design of Experiments	62
3.8	ANOVA Analysis.....	65
3.9	Etching of processed glass with Hydrofluoric Acid (HF).....	65
3.10	Integrating sphere setup for reflection / absorption / transmission measurements	66
3.11	Correcting absorption data to AM1.5G solar irradiance spectrum	67
3.12	SEM and EDXS Analysis.....	68
3.13	Channel Dimensional Analysis	69
3.14	Solar cell selection and preparation.....	70
3.15	Measurements of I-V vs angle of incidence.....	70
3.16	Optical characterisation of alkyl-capped silicon quantum dots.....	72
3.16.1	Preparation	72
3.16.2	Silicon quantum dots size evaluations	73
3.16.3	Deposition of silicon quantum dots onto textured glass superstrates ..	75
3.17	Focused Ion Beam Serial Sectioning.....	76
3.17.1	Chemicals.....	76

3.17.2	Preparation of carbon monolith.....	76
3.17.3	Image acquisition	77
3.17.4	Image processing.....	79
3.17.5	3D reconstruction and morphological analysis	81
Chapter 4	Verification of the 3D non-contact optical profilometer.....	82
4.1	Positional Analysis of the XYZ stage system	82
4.1.1	Large scale positional analysis.....	83
4.1.2	Small scale positional analysis.....	88
4.1.3	Verification of 3D measurement performance.....	94
4.1.4	Comparison of measurement results with a commercially available system	95
4.1.5	Demonstration of capability in the measurement of translucent materials	97
Chapter 5	Laser texturisation of glass superstrate for enhanced solar cell performance	98
5.1	Laser processing and parasitic light absorption losses	98
5.2	Design of Experiments and Response Surface Methodology (RSM)	99
5.3	ANOVA Analysis.....	101
5.4	SEM and EDXS Characterisation	102
5.5	Effect of HF etching on absorption of light.....	109
5.6	Efficiency vs angle of incidence.....	113
Chapter 6	Characterisation for Quantum Dot Solar Cells	115
6.1	Absorption characteristics of alkyl-capped silicon quantum dots.....	115
6.2	Absorption characteristics of alkyl-capped silicon quantum dots on laser textured superstrates	117
6.3	FIB serial sectioning for the 3D reconstruction of macroporous structures....	119
6.4	3D reconstruction and morphological analysis of the carbon monolith....	120
6.5	3D reconstruction and morphological analysis of the silica-based monolith..	122
Chapter 7	Conclusions	125
7.1	Future Work	130
References	133
Appendix A	: Positional Analysis	i
Appendix B	: RSM Procedure	xiv
Appendix C	: Dial Gauge Technical Specifications	xvi
Appendix D	: ISO 230-2	xviii
Appendix E	: Fused Quartz Datasheet.....	xxiii

Appendix F	Channel Dimension Analysis	xxiv
Appendix G	: 3D Analysis	xxvii

List of Figures

Figure 1: Flowchart and structure of the thesis.....	6
Figure 2 - The Electromagnetic spectrum (source: Wikimedia Commons)	8
Figure 3 - Representative circuit of a solar cell. R_S and R_{SH} represent the series and shunt resistances respectively.	8
Figure 4 - Typical solar cell configuration.....	9
Figure 5: Band diagram for a photovoltaic cell. (source: Wikimedia Commons).....	10
Figure 6 - Solar radiation spectra according to ASTM G-173-03 [14].....	12
Figure 7. Schematics of superstrates with light rays incident vertically from the top shown in red for situations (a) with active layer (blue) on the textured side opposite incident rays, (b) with the active layer on the untextured side; and substrates (c) with the active layer on the textured surface, and (d) with the active layer on the flat surface.	15
Figure 8. Pyramidal texture on c-Si created by etching with TMAH [18].	18
Figure 9. Perspective view of a honeycomb structure formed by chemical etching [8]. Spacing of hexagons is 14 μm	20
Figure 10. Five possible texture types (a) V-Grooves, (b) V-Grooves double sided, (c) Pyramids, (d) Pyramids double sided, and (e) Perpendicular grooves or ‘Patch’ texture	21
Figure 11: Example of a quantum dot sensitised solar cell architecture [70].	26
Figure 12. 3D non-contact optical surface profilometer.	32
Figure 13: Main Graphical User Interface (GUI VI Front Panel) for the 3D non-contact optical surface profilometer.	33
Figure 14. Flowchart indicating operation of the 3D non-contact optical surface profilometer control software.....	33
Figure 15. Images of the (a) high resolution optical system and vertical actuator, and (b) XY positioning stage with stepper motors.	36
Figure 16. Raw data processing procedure. Both a topographical height map and a high resolution fully focused image are created.	38
Figure 17. 3D surface display of laser processed grooves in transparent glass. The surface has been shaded blue to improve visibility. Measurement area is 310 μm by 232 μm	38

Figure 18: (a) A representation of the actual surface being measured. (b) The components of the surface profile according to ISO 4287.....	40
Figure 19. Roughness profile is obtained using the ISO 4288 standard for profile correction.....	41
Figure 20 - PYSER-SGI PS78 Stage micrometer used for calibrating the optical plane of the microscope system.....	42
Figure 21: Mitutoyo 513-405E Dial Gauge when performing point to point measurements on the X-axis of the 3D Optical Profilometer.	45
Figure 22: The measurement procedure was performed according to the following sequence.....	46
Figure 23: SEM image of a 0.75 mm milling tool utilised for manufacturing the measurement artefact.	50
Figure 24 - Wide field Backscatter Electron SEM image of machined brass sample	50
Figure 25 - Secondary Electron SEM image of end face of a pillar on the machined brass sample. Machining debris is visible at the end face of the measurement artefact.	51
Figure 26 - 3D surface measurement of the machined brass sample using a Wyko NT1100 white light interferometer	52
Figure 27 - Cross sectional Wyko NT1100 measurement data of machined brass sample. Step height is measured as 103µm.....	53
Figure 28 - 3D surface profile of the machined brass sample using a DEKTAK V200Si Stylus profilometer.....	54
Figure 29 - Cross sectional profile of machined brass samples acquired using DEKTAK V200Si Stylus profilometer	54
Figure 30: Mitutoyo Rectangular Gauge Block Set (Grade 1)	55
Figure 31: Step height of nominal 500µm Mitutoyo Rectangular Gauge Block. The WLI measurement verified the dimension of the block to be 512µm.	56
Figure 32: a) 3D view of measurement, b) Fully focused image from a step height measurement, c) the height map from this measurement, d) the areas of high un-repeatability and noise due to steep flanks.....	59
Figure 33. Graphic illustration of pulse period, duration and peak power within pulse width.....	61
Figure 34. Central Composite Design of Experiments	63
Figure 35. Integrating sphere setup for absorption measurements.	66

Figure 36. Cut-away view of the integrating sphere setup.....	67
Figure 37: Diagram showing the SEM measurement locations on a cross sectional view of laser micro-machined channel.	69
Figure 38: Diagram showing the SEM measurement locations for the measurement of the Width (top) parameter. Top surface is represented by red line, and measurement locations are shown in orange.	70
Figure 39. a) Angle of incidence of 90°, and b) angle of incidence of 10°.....	71
Figure 40. Mounting device constructed to hold textured superstrate and encapsulated solar cell in contact. The rotational stage allowed for measurements of varying angles of incidence to be performed.....	71
Figure 41: The AFM image was taken on the Si-QDs cast onto mica. From the profile along the line (a), one can find out the height of clusters was about 10 nm, which is equivalent to the height of two layers of Si-QDs, as shown in (b) [115].....	74
Figure 42: Sketch of the sample/FIB-SEM system set-up for serial sectioning and imaging.....	78
Figure 43 Image captured by SEM after FIB sectioning of the carbon monolith.....	79
Figure 44 Image captured by SEM after FIB sectioning of the silica monolith.	80
Figure 45 From L to R: Outline of the pores, filling of pores and binarisation applied to the image stack obtained for the carbon monolith.	81
Figure 46: Large scale positional analysis along X axis.	84
Figure 47: Large scale positional analysis along Y axis.	85
Figure 48: Large scale positional analysis along Z axis.	86
Figure 49: Small scale positional analysis along X axis.	89
Figure 50: Small scale positional analysis along Y axis.	90
Figure 51: Small scale positional analysis along Z axis.	91
Figure 52: Measurement recorded using a Keyence VHX-5000 series 3D microscope.	95
Figure 53: Fully focused true colour image of the machined brass sample.....	96
Figure 54: 3D representation of the surface profile of the machined brass sample...	97
Figure 55: 3D measurement profile of laser micro-machined grooves in fused quartz glass. Axis values are in nm.	97
Figure 56. (a) Effect of Traverse Speed with PRF=400Hz and Duty Cycle=6%. (b) Effect of Duty Cycle with PRF=400Hz and Traverse Speed=8.333mm/s.	99

Figure 57. Values predicted by the model equation against the actual values. Points located along the line indicate the model provides an acceptable fit.	100
Figure 58. RSM surface plot showing the correlation between the significant input parameters and the resulting parasitic absorption in the processed material (PRF=280Hz).	100
Figure 59. Top down view of laser micro-machined channels in Fused Quartz. (a) Sample 21 with low absorption properties (PRF=400Hz, Speed=8.3mm/s, Duty Cycle=2%). (b) Sample 9 with high absorption properties (PRF=400Hz, Speed=1.7mm/s, Duty Cycle = 6%).....	103
Figure 60. Cross sectional view of the groove texture.(a) Sample 16 with the maximum (duty cycle 6%, PRF 160Hz, speed 5mm/s) and (b) Sample 21 with the minimum texture depths achieved by laser ablation (duty cycle 2%, PRF 400Hz, speed 8.33mm/s).	103
Figure 61: Average channel depths.....	104
Figure 62: Average channel widths at the top surface.	105
Figure 63: Average channel width at 50% depth.	106
Figure 64: 3D surface profile of sample 21, 70-80 micrometres in depth, as captured by the 3D optical profilometer.	107
Figure 65. EDXS results for (a) Sample 21 with low absorption, (b) Sample 9 with high absorption, and (c) untextured Reference Sample	108
Figure 66. The effect of hydrofluoric acid (40%) etching on the absorption of light at the surface.	109
Figure 67. An electron microscope image of the surface of sample 21 before acid etching. It is possible to see a large amount of re-cast material. Visible feature sizes range from approximately 400 nm to several microns.....	110
Figure 68. (a) Surface of sample 21 after 5 minutes HF etching, and (b) Surface of sample 21 after 10 minutes etching.....	110
Figure 69. Top down view of the surface morphology of laser ablated channels (duty cycle 4%, PRF 400Hz, speed 1.67mm/s). unetched (a), after etching for 10 minutes (b) and after etching for 20 minutes (c).	111
Figure 70. Absorption of AM1.5G spectrum by sample 21 with respect to etching time (data fitted with 6 th order polynomial trend line for clarity). It can clearly be seen that etching causes a shift in absorption towards the red end of the spectrum. This can be	

directly correlated to the elongation of nanostructures on the surface due to acid etching.....	112
Figure 71. EDXS spectrum of sample 21 after etching with HF. Composition is close to that before HF etching (Figure 65(a)).....	112
Figure 72. I-V curves for solar cell at the acute angle of 10° incidence. untextured reference (solid), sample 20 (dotted), and sample 21 (dashed).....	113
Figure 73. Solar cell efficiency with different angles of incidence for the untextured reference (solid), sample 20 (dotted), and sample 21 (dashed).....	114
Figure 74: Optical microscope image of nanocrystalline silicon on substrate shortly after drop deposition. Bubbles indicate that the solvent is still present.	116
Figure 75: Light absorption characteristics of Si QDs after 1 deposition (green), 2 depositions (blue), 3 depositions (red). The absorption of the glass and the solvent have been subtracted from this data.	117
Figure 76: Light absorption characteristics of Si QDs on laser textured superstrates after drop casting. Untextured reference (blue), Sample 19 (red), Sample 20 (green), and Sample 21 (violet).The absorption of the glass and the solvent have been subtracted from this data.	118
Figure 77: Spectra for untextured reference (blue) and Sample 19 (red). The spectra have been reference matched from 520 nm to 1000 nm.	119
Figure 78: 3D reconstruction of the porous carbon monolith.....	121
Figure 79: Mercury porosimetry results showing pore size distribution in the carbon monolith [122].....	122
Figure 80: 3D reconstruction of the porous silica monolith (Monotrap).	122
Figure 81: Mercury porosimetry results showing pore size distribution in the silica-based monolith [122].....	123

List of Tables

Table 1: Outline of physical and atmospheric conditions as detailed in ASTM G-173-03 [12].	12
Table 2. Texture performance in reducing reflection from silicon solar cells	19
Table 3. Optical system specification	34
Table 4. Motion control system specification	35
Table 5: Selection of Filter parameters according to ISO 4288.	41
Table 6: Analysis of large scale movements using Mahr 810SW dial gauge	44
Table 7: Analysis of small scale movements using Mitutoyo 513-405E dial gauge	45
Table 8: Position variation from the nominal point-to-point interval.	46
Table 9: Target positions for Large Movement analysis. All positions in millimetres.	47
Table 10: Target positions for Small Movement analysis. All positions in millimetres.	47
Table 11: Measurement results of brass sample step height taken by the various instruments	53
Table 12: Design of Experiments with specified sampling intervals	58
Table 13. Laser parameters held constant during the experiments	62
Table 14. Laser process parameters used for DOE	63
Table 15: Laser micromachining parameters for each sample produced in the DOE.	64
Table 16. EDXS compositional analysis parameters	68
Table 17: Acquisition details for carbon monolith	78
Table 18: Acquisition details for silica monolith	78
Table 19: Results from large scale positional analysis along X axis	87
Table 20: Results from large scale positional analysis along Y axis	87
Table 21: Results from large scale positional analysis along Z axis	87
Table 22: Results from small scale positional analysis along X axis	92
Table 23: Results from small scale positional analysis along Y axis	92
Table 24: Results from small scale positional analysis along Z axis	92
Table 25: Accuracy results from the 6 sub-run measurements	94

Table 26. The values of the Regression Co-Efficients for the quadratic response surface model shown in Figure 58.	101
Table 27. Contribution of the most significant factors to the quadratic response surface model.....	101
Table 28: R-squared values for the RSM model.....	102
Table 29. Comparison of samples with highest and lowest light absorption properties.	108
Table 30 Comparison of surface composition before and after HF acid etching.....	113
Table 31. Parameters and results for I-V measurement with light incident at 10° to surface.	114
Table 32: Large scale positional analysis of X axis using Mahr 810SW dial gauge indicator (1-5).....	ii
Table 33: Large scale positional analysis of X axis using Mahr 810SW dial gauge indicator (6-10).....	iii
Table 34: Large scale positional analysis of Y axis using Mahr 810SW dial gauge indicator (1-5).....	iv
Table 35: Large scale positional analysis of Y axis using Mahr 810SW dial gauge indicator (6-10).....	v
Table 36: Large scale positional analysis of Z axis using Mahr 810SW dial gauge indicator (1-5).....	vi
Table 37: Large scale positional analysis of Z axis using Mahr 810SW dial gauge indicator (6-10).....	vii
Table 38: Small scale positional analysis of X axis using Mitutoyo MT513-405E dial gauge indicator (1-5).....	viii
Table 39: Small scale positional analysis of X axis using Mitutoyo MT513-405E dial gauge indicator (6-10).....	ix
Table 40: Small scale positional analysis of Y axis using Mitutoyo MT513-405E dial gauge indicator (1-5).....	x
Table 41: Small scale positional analysis of Y axis using Mitutoyo MT513-405E dial gauge indicator (6-10).....	xi
Table 42: Small scale positional analysis of Z axis using Mitutoyo MT513-405E dial gauge indicator (1-5).....	xii
Table 43: Small scale positional analysis of Z axis using Mitutoyo MT513-405E dial gauge indicator (6-10).....	xiii

Table 44: Results from channel depth analysis.....xxiv
Table 45: Results from channel width (top) analysis.....xxv
Table 46: Results from channel width (50%) analysisxxvi

Nomenclature

Term	Description
Duty Cycle (%)	The ratio of the pulse duration to the pulse period. A duty cycle of 100% would indicate that the output is continuous.
Pulse Duration (s)	The amount of time the laser beam is actually irradiating energy.
Pulse Period (s)	The amount of time from the start of one pulse to the start of the next pulse.
Pulse Repetition Frequency (PRF) (Hz)	The frequency of the laser pulses. The inverse of pulse period.
AM1.5G Spectrum	American Society for Testing and Materials (ASTM) Terrestrial Reference Spectra for Photovoltaic Performance Evaluation
Spectral Irradiance _{λ} %	The percentage of the total incident radiant energy per wavelength of the incident spectrum. e.g 420 nm represents 0.16% of the total radiant energy between 420nm and 1000 nm.
Si-QD	Silicon Quantum Dots, also known as silicon nanocrystals

Abstract

Laser texturisation of photovoltaic module superstrates for enhanced light trapping performance

David John Moore

In order to increase the efficiency of solar cell modules it is necessary to make the optimum use of light incident upon them. Much research has been conducted to improve light absorption through front surface texturing and light trapping schemes. Laser light is commonly used in industry for various applications including marking and texturing. By controlling laser parameters, it is possible to tailor macro and micro structures in most materials. A CO₂ laser operating at 10.6 μ m wavelength was used to produce grooved textures in fused quartz material with a view to its usage as a cover glass on top of the photovoltaic cell surface. With correct texturing it is postulated that increased energy absorption can be promoted due to trapping of light within the photovoltaic cell due to total internal reflection and enhanced optical path lengths. Analysis of the effects of the laser parameters on the texture geometry and surface morphology was performed through a combination of cross-sectioning and scanning electron microscopy. Transmission spectra through the textured glass samples were recorded, and transmission through the glass was improved for most samples after acid etching. It was found that for acute angles of incidence of wavelengths of natural sunlight upon the cells, greater coupling efficiencies were achieved compared to flat surfaces, due to the increased light trapping effect. The main contributions of this work include examination and quantification that indicate the laser textured solar superstrates can increase the light trapping effect within silicon solar cells and that an enhanced light trapping can be achieved when silicon quantum dots deposited directly on a textured superstrate. Another two important contributions are found in the development of characterisation methods and analyses of microstructures relevant to light trapping in current and emerging solar cell technologies. These include the design, fabrication, development, and verification of a newly designed and commissioned depth-from-focus based optical profilometer with which new results in the metrology of translucent surfaces with micro-scale roughness are presented. Software to analyse serial FIB-SEM sections of monolithic porous microstructures was also developed. The results gained from these characterisation methods have allowed, and it is postulated will in the future provide, a more detailed understanding of the light trapping process with various microstructures.

Chapter 1 Introduction

Solar cells operate on the principle of the photoelectric effect; the conversion of light energy to electrical energy. While there are many variations of solar cells, this energy conversion can be achieved by illuminating a semi-conducting material with light to generate an electron-hole pair, also called an exciton [1]. There are various materials that are used as light absorbers in order to achieve the photoelectric effect, the most commonly used today being silicon, mainly due to its widespread availability, the availability of existing mature processing and handling technology from the electronics industry, and also its band-gap suitability for absorption of the solar spectrum.

While the efficiency of solar cells has greatly increased in recent years, the cost per Watt peak is still too high for photovoltaics to be considered more widely as a cost effective means of energy production. In order to reduce of the cost per Watt peak of the solar cells, it is necessary to achieve one of the following - higher solar cell efficiencies or lower manufacturing costs. While current high performance silicon solar cells obtain efficiencies upwards of 20 percent, there are still significant opportunities for further improvements [2]. The Shockley-Queisser limit states that the theoretical maximum efficiency of a single junction silicon solar cell is 33% under AM1.5 Global radiation. In order to achieve this goal, the solar cells must make optimum use of the light incident upon them. While there has been much research into the improvement of semiconductor fabrication techniques, there still remains an opportunity to better improve the optical performance of the solar cells. The optical performance of silicon solar cells is limited in two ways - silicon is a relatively poor absorber of near-infrared light, and silicon also has a high refractive index meaning there are large losses due to Fresnel reflection at the front surface [3]. Improved light absorption characteristics have been observed in silicon solar cells through the use of anti-reflective coatings, among which silicon nitride (Si_3N_4) is among the most popular [4, 5]. However, these anti-reflective coatings operate optimally only in certain ranges of wavelengths of light and at certain angles of incidence of solar radiation. Other steps implemented to improve the optical performance include direct texturisation of the front silicon surface in the solar cell. This can be achieved through

various methods, the most common of which is chemical etching and is most effective on single crystal silicon (c-Si). While single crystal silicon can be used to make the cells with the highest efficiencies, due to the lack of internal lattice defects, it is also the most expensive form of silicon to produce due to the energy intensive nature of the manufacturing process [6]. Also, more recently thin-film solar cells and quantum dot based solar cells are coming to the forefront of research and markets, and the direct texturisation of these layers is difficult using existing manufacturing methods. While thin-film solar cells in particular offer an excellent opportunity to reduce the manufacturing costs of the cells, the associated optical losses limit the maximum performance obtainable with this architecture. In order to reduce the optical losses and to simultaneously reduce the manufacturing costs associated with the solar cell, it is necessary to develop a method of improving light absorption characteristics which is suitable for use with wafer based bulk solar cells and thin-film type solar cells. It is postulated that an optimised surface texture can increase the ability of the solar cell to absorb incident light more effectively, in a process known as light trapping. Quantum dot based solar cells show great promise in being able to overcome the Shockley-Queisser limit, and the band-gap of silicon quantum dots can be controlled by controlling the size of the dot [7]. While the architecture of quantum dot based solar cells is somewhat different to the traditional approach in wafer based and thin-film silicon solar cells, there are emerging architectures that utilise micro- and nano-structured materials for improved light trapping performance.

Objectives of this work

There are two main objectives for this research. Firstly, the aim is to investigate fundamentally the use of lasers to texturise on the micro scale the front cover glass superstrate as would be used in a conventional solar module. From previous simulations performed in literature, it is estimated that the amount of light trapped in a solar cell by trapping secondary and subsequent surface reflections can increase the optical thickness of the solar cell by up to 40 times [8]. This is especially important for thin-film architectures when considering that light with photon energies close to the band-gap of the semiconductor are weakly absorbed in thin layers. The use of lasers to create the textures offers excellent flexibility in terms of process parameters to achieve a range of surface textures for use with the solar cells. Lasers also offer a

non-contact process which is highly scalable in terms of production speed and throughput, thus offering the possibility to reduce the manufacturing costs and simultaneously increase the efficiencies of the solar cells.

In the real world use of solar cells, modules are often installed in fixed orientations, such as on the roofs of houses or facades of buildings. The quoted efficiencies of solar cells are those under ideal testing conditions of AM1.5G in a laboratory environment. However, in day-to-day operations the solar module will experience different conditions and different angles of incidence of sunlight. Thus the motivation behind this research is to also encompass an investigation into how the angles of incidence of light will affect the solar cell performance, and how different superstrate textures could be used to improve light coupling into the solar cell. As the angle of incidence of light decreases from normal to parallel, it is postulated that the texture on the surface will assist the coupling of more light to the surface of the cell within the solar module, as opposed to having a flat superstrate surface where a large amount of light is lost due to reflection.

The objective of carrying out this research using glass as the front cover superstrate lies in the properties of the material itself, and also in its suitability for the application. Glass is currently the preferred choice for silicon based solar module manufacturers due to its low cost and wide availability, and its beneficial mechanical and optical transmission properties.

The second objective of this work is to investigate the characterisation methods of microstructures used in solar cells. While there are several established methods for the characterisation of surface nanostructures, the measurement of microstructures (on the order of 1 micrometre to 200 micrometres) still presents some challenges. Microstructures with high aspect ratios in this size range are outside the measurement capability of stylus instruments such as Atomic Force Microscopes (AFM), while significant surface roughness can also present measurement challenges to optical instruments such as White Light Interferometers (WLI). Some types of solar cells, particularly those based on quantum dot architectures, depend on semi-conducting materials for operations. This work also investigates the use of an advanced Electron Microscopy technique called Focussed-Ion Beam Serial Sectioning and Imaging, in

order to assess the 3D structure of macroporous monolithic materials. It is believed that this work will contribute better to the understanding of the suitability of these techniques for solar cell material and microstructure analysis. An additional benefit of this work lies in the fact that these characterisation methods allow surfaces of the structures topologies to be exported by the user for use in optical simulations such as ray-tracing, which would greatly add to the realism of simulations within the field of photovoltaics.

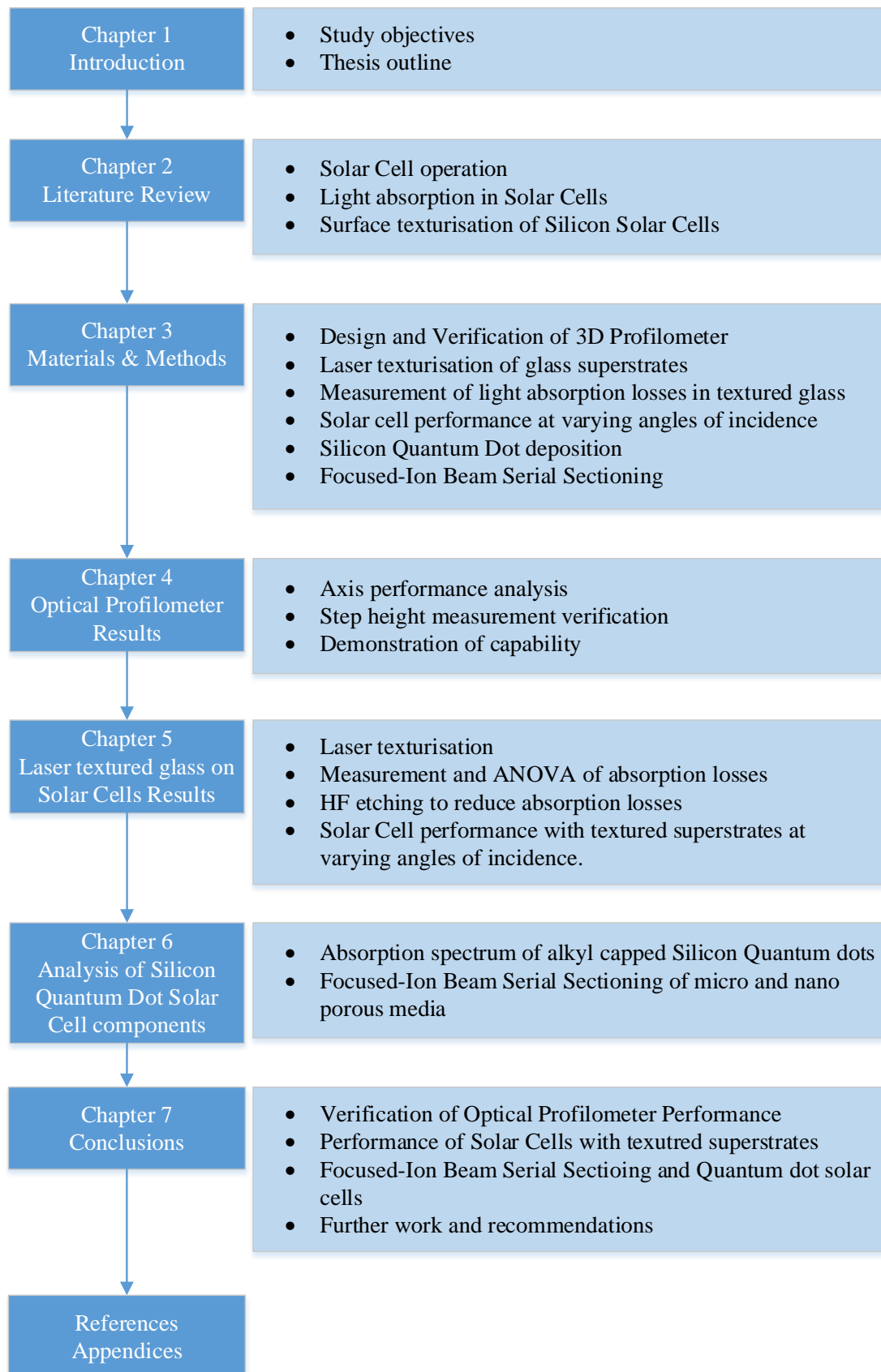


Figure 1: Flowchart and structure of the thesis

Chapter 2 Literature Review

2.1 Introduction to solar cells

What is a solar cell?

A solar cell, also called a photovoltaic cell, is a solid state device used for the conversion of light energy to electrical energy. The device makes use of the physical and chemical phenomenon known as the photovoltaic effect. Photovoltaic cells utilise the properties of semiconductors in certain configurations to effectively absorb photons of light incident upon the material and convert the energy of the incident photons into electrical current [9]. While there are various possible solar cell configurations, the most commonly used solar cells type is based on the use of silicon [5]. Silicon is a well understood widely used semiconductor material in the electronics industry, is widely available, and due to the accessibility to existing fabrication techniques lends itself well to creating a cost effective solution in the production of photovoltaic devices [6]. Importantly, silicon also absorbs electromagnetic radiation from the near-infrared end of the spectrum to the UV, which represents coverage of a significant band of electromagnetic solar energy incident upon Earth [1]. It is estimated that silicon based solar cells account for approximately 92% of the global solar cell market in 2014 [2]. Great improvements in silicon solar cell efficiency have been made in the last decade, through improved fabrication techniques, and better management of factors that can negatively influence solar cell performance.

2.2 The mechanics of the generation of photocurrent

The electromagnetic spectrum describes a range of wavelengths (or frequencies) of electromagnetic radiation, as displayed in Figure 2. From a solar cell perspective, one is typically concerned with electromagnetic radiation ranging from the near –infrared (NIR) to the ultraviolet (UV) [4, 5]. There are two main reasons for this. Firstly, the bulk of the solar radiation reaching sea level on Earth consists of wavelengths within this region of the electromagnetic spectrum. Secondly, the reason for this is due to the quantum mechanics of the photovoltaic effect. The photon energies of photons within the NIR to UV spectrum are well matched to the band-gap energies of common semiconductors, meaning that it becomes relatively efficient to generate photocurrent within this range. Photons of a particular wavelength also have a corresponding photon

energy which inversely proportional to the wavelength. For example, a photon with a wavelength of 500 nm has an equivalent photon energy of 2.48eV, while a photon with a wavelength of 700 nm has an equivalent photon energy of 1.77eV [10].

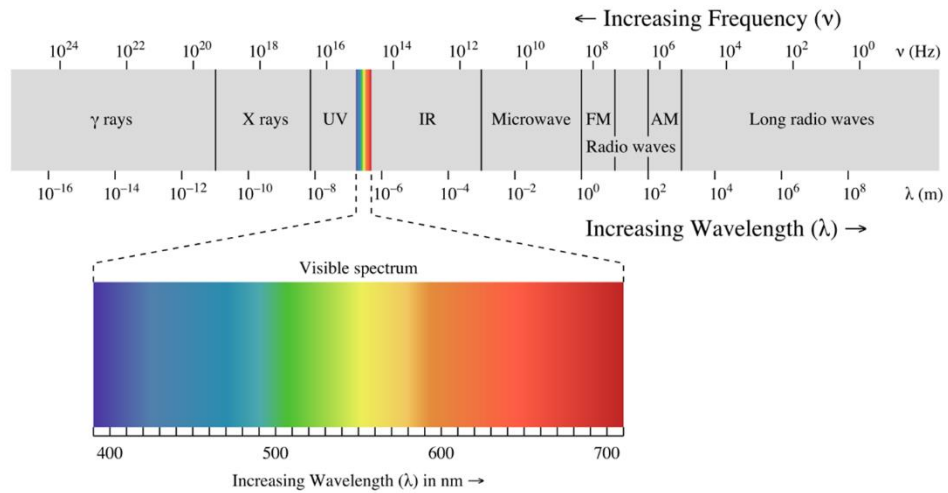


Figure 2 - The Electromagnetic spectrum (source: Wikimedia Commons)

The photovoltaic effect operates on the principle of utilising the properties of a P-N junction to achieve charge separation. From an electrical point of view, a solar cell can be represented as an ideal current source circuit with a series and shunt resistance, and behaviour identical to that of a traditional diode [1]. An example of the equivalent circuit can be seen in Figure 3.

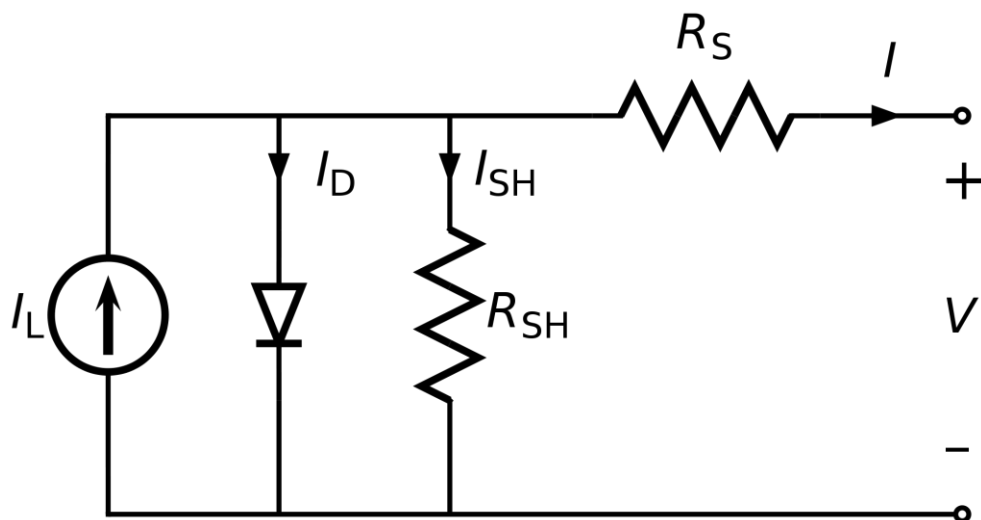


Figure 3 - Representative circuit of a solar cell. R_S and R_{SH} represent the series and shunt resistances respectively.

Traditional diodes are also comprised of a P-N junction [11]. This type of junction is formed by bringing into contact two differently doped semiconductors. Typically, in the case of silicon, the p-type semiconductor is doped with Boron, and the n-type semiconductor is doped with Phosphorous. There are several effects of doping in this manner. Firstly, the carrier concentrations of the intrinsic (pure) semiconductor are modified, meaning that the p-type semiconductor has excess holes, and the n-type has excess electrons. The amount of doping therefore modifies the conductivity of the semiconductor, which can be beneficial in reducing the series resistance of the solar cell to maximise cell efficiency. Secondly, the P-N junction formed has the property of only allowing current to flow in one direction. Finally, the P-N junction forms an internal electric field and a depletion region near the boundary of the junction, meaning it is possible to achieve charge separation, and hence to generate photocurrent by utilising the photovoltaic effect.

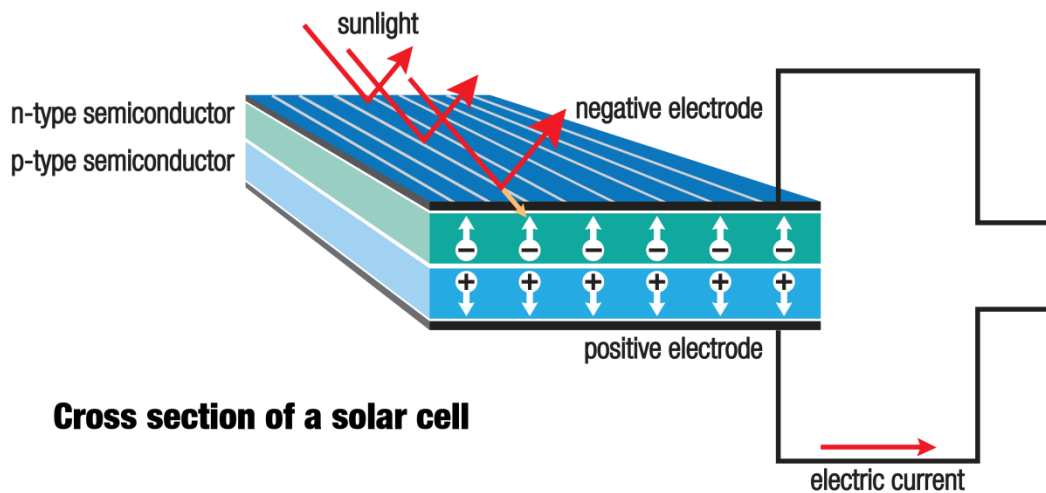


Figure 4 - Typical solar cell configuration.

In order to generate photocurrent in a solar cell, the incident photons of light must energise electrons within the absorber material. When a photon is absorbed by an atom, the energy of the photon is transferred to an electron. Typically, electrons are in a ground (valence) state, and then become excited to a higher state on the absorption of a photon as shown in Figure 5. However, there is a minimum amount of photon energy required to excite the electron sufficiently so that it can contribute to photocurrent. This minimum energy is known as the band-gap (eV), and is unique to

each semiconducting material [1, 3]. The band-gap has several important implications for the performance of a solar cell.

- Photons at energies below the semiconductor band-gap are not absorbed do not contribute to photocurrent.
- Photons exactly at the band-gap energy can generate photocurrent with high a spectral response, as the photons contain just enough energy to excite the electrons into the conduction band.
- Photons with energies higher than the semiconductor band-gap are absorbed and can contribute to photocurrent generation. However, the residual energy (photon energy minus band-gap energy) is lost in the form of thermalisation. This effect reduces the spectral response of the solar cell at shorter wavelengths, limiting the possible device efficiency.

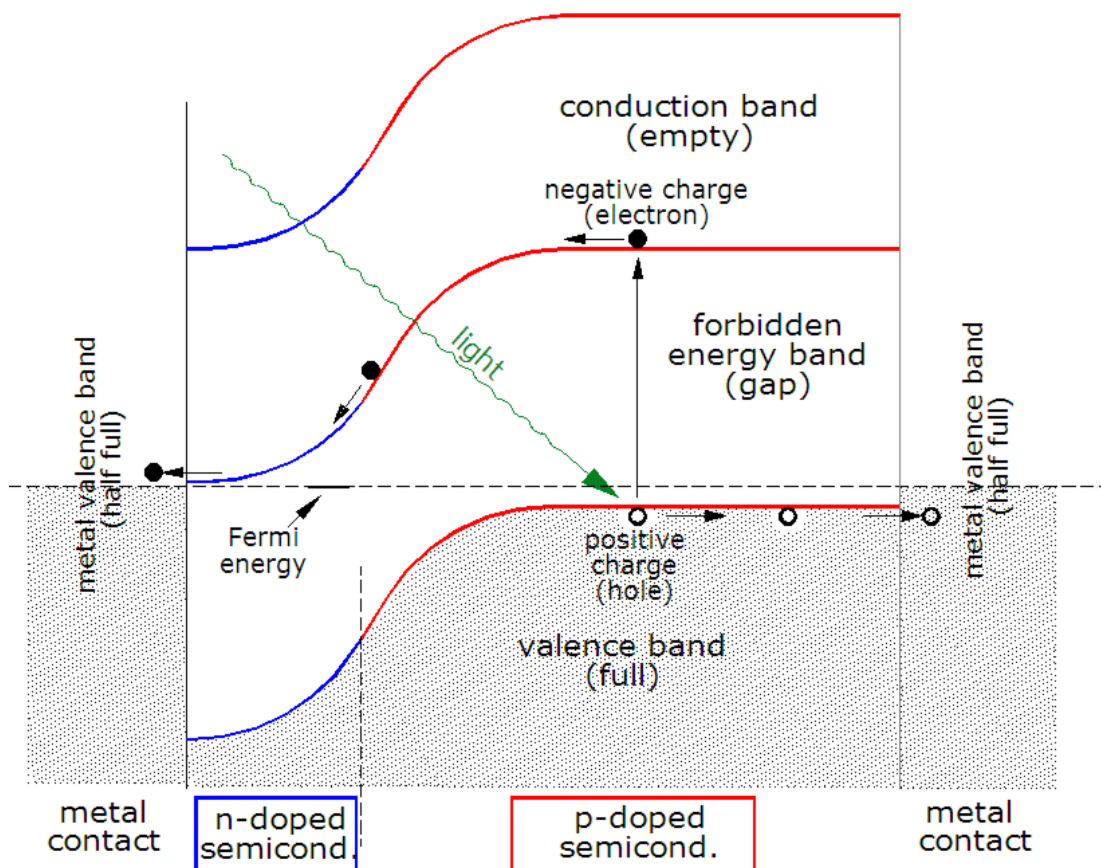


Figure 5: Band diagram for a photovoltaic cell. (source: Wikimedia Commons)

2.3 Silicon as a photovoltaic material

For silicon, the band-gap energy is approximately 1.1eV, which corresponds to an electromagnetic radiation wavelength of 1100nm. This means that silicon is very well suited as a photovoltaic material, as its band-gap energy is well matched with the solar radiation flux incident on the Earth [1]. As described in section 2.4, the majority of the solar radiation flux reaching Earth is at wavelengths shorter than 1100nm, and hence the band-gap of silicon offers a well suited balance between being low enough to allow for absorption for the majority of solar radiation and simultaneously offering reasonable quantum efficiency (QE) performance over the usable portion of the spectrum.

Crystalline silicon is an indirect band-gap material, which means that in order for an electron to move from the valence band into the conduction band a change in electron momentum (k-vector) must also occur in conjunction with transfer of energy from an incoming photon above the band-gap energy [3]. This change in momentum is normally provided by interaction with a phonon, or lattice vibration. What this means in physical terms is that the probability of an electron transitioning from the valence band to the conduction band is greatly reduced compared to the probability of the same transition in a direct band-gap semiconductor. The absorption co-efficient of crystalline silicon is dependent on the wavelength of light passing through it, as given by the Beer-Lambert Law [3]. Despite this, silicon is by far the most widely used semiconductor in photovoltaics. Combining the favourable band-gap characteristics of silicon with its wide availability and the availability of mature silicon processing technologies from the micro-electronics industry, it is clear why silicon solar cells have been so successful on an industrial production scale.

2.4 The Air Mass (AM) standard

The Air Mass standard provides information on the Spectral Irradiance of solar radiation; AM0 represents the extra-terrestrial spectrum, while AM1.5 Direct represents the irradiance of solar energy on the Earth's surface. The AM1.5 Global (AM1.5G) spectrum utilised in this work represents the combined direct and diffuse solar radiation reaching the Earth's surface at specific conditions. The AM1.5G standard is represented by ASTM G-173-03 and ISO 9845 [12, 13]. The Air Mass spectra are shown in Figure 6.

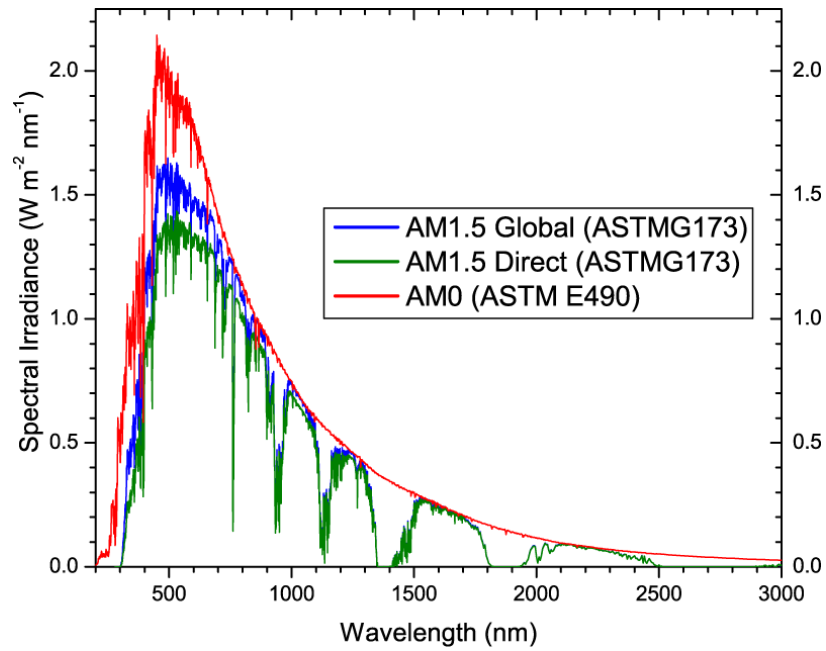


Figure 6 - Solar radiation spectra according to ASTM G-173-03 [14].

There are certain specifications involved in the calculation of the AM1.5G standard. Certain atmospheric and physical conditions are assumed. The main considerations are outlined in Table 1.

Table 1: Outline of physical and atmospheric conditions as detailed in ASTM G-173-03 [12].

Factor	Details
Receiving surface	Inclined plane at 37° tilt toward the equator, the surface normal points to the sun, at an elevation of 41.81° above the horizon
Atmosphere	The 1976 U.S. Standard Atmosphere with temperature, pressure, aerosol density (rural aerosol loading), air density, molecular species density specified in 33 layers
Atmosphere	An absolute air mass of 1.5 (solar zenith angle 48.19°s)
Atmosphere	Angstrom turbidity (base e) at 500 nm of 0.084
Atmosphere	Total column water vapour equivalent of 1.42 cm
Atmosphere	Total column ozone equivalent of 0.34 cm
Atmosphere	Surface spectral albedo (reflectivity) of Light Soil as documented in the Jet Propulsion Laboratory

2.5 Types of wafer based silicon solar cells

There are several manufacturing methods available for the production of Silicon solar cells. The most common method for producing high efficiency solar cells is through the use of single crystal silicon. Single crystal silicon (c-Si) is most commonly grown using the Czochralski process, and produces very high quality silicon [5, 6]. However this process is time and energy intensive, and hence this production method also attracts higher production costs. These solar cells are used in applications where energy density is critical such as in space applications, although improved manufacturing methods and economies of scale have also made this type of solar cell popular for terrestrial applications.

While single crystal based solar cells have the highest efficiencies in the Silicon PV market, multi-crystalline solar cells make up the majority of that market, with an estimated 56% of silicon solar cells produced in 2014 being based on multi-crystalline silicon technology [2]. The multi-crystalline form of silicon is significantly cheaper to produce, however, these cells have a drawback in that their maximum efficiency is significantly below that of cells manufactured from single crystal silicon. This is mainly due to the fact that the grain boundaries in the multi-crystalline material act as defects and are centres for electron-hole re-combination, essentially reducing the shunt resistance of the solar cell and the cell efficiency [3]. There are also several methods for manufacturing multi-crystalline solar cells. The most common manufacturing method is the casting of melted silicon, where the grain size can be somewhat controlled by controlling the cooling rate of the molten material. Another method, dubbed the Ribbon method, involves the continuous casting and cooling of a thin ribbon of silicon. This method has the potential to be the most cost effective way of making multi-crystalline solar cells, however the drawback of this approach is the difficulty in maintaining wafers without cracks or significant crystal defects [1].

2.6 Factors limiting the absorption of light in silicon solar cells

There are several significant factors that limit light absorption in traditional silicon solar cells. Firstly, silicon has a high refractive index meaning that at a silicon-air interface there is significant light loss due to Fresnel reflection [1]. In order to overcome this limitation certain anti-reflective coatings have been developed. Secondly, silicon is a relatively weak absorber of light in the near-infrared region of

the electromagnetic spectrum, near to the materials band-edge. The reason for this is that silicon is an indirect band-gap semiconductor, meaning that along with the absorption of a photon, an interaction with a lattice vibration (phonon) is required for an electron to transition between the valence band and the conduction band [3]. This means that crystalline silicon has a relatively low absorption probability for photon energies close to the band-gap. For crystalline silicon, this means the production of thicker solar cells, to enhance the absorption probability of lower energy photons. In thin film solar cell designs where material thickness is limited, amorphous silicon is often utilised as it behaves as a direct band-gap semiconductor which improves efficacy in thin layers, however silicon in this form also has a higher band-gap (closer to 1.75eV), which in turn has a knock on effect on the materials ability to absorb the solar spectrum [3].

2.7 Possible device configurations for effective light trapping

There are many possible device architectures and surface texturisation techniques that could be considered for enhanced photo-absorption. Regarding wafer based solar cells, most research work has been focused on the direct texturisation of the actual silicon wafer used in the solar cell. A relatively small amount of research work has investigated the effects of solar cell superstrate or substrate texturisation, which are utilised in front and behind the solar cell respectively. Figure 7 shows possible configurations of solar cell modules, including locations for the active medium positioning on textured superstrates and substrates. In thin-film and quantum dot solar cells, the active layer is usually less than 30 μm thick, meaning that this type of solar cell must be manufactured onto a supporting superstrate or substrate [1]. Therefore, in order to improve light trapping through texturisation it is necessary to texturise the supporting medium through etching, laser ablation, mechanical scribing or embossing. Possible configurations are shown in Figure 7.

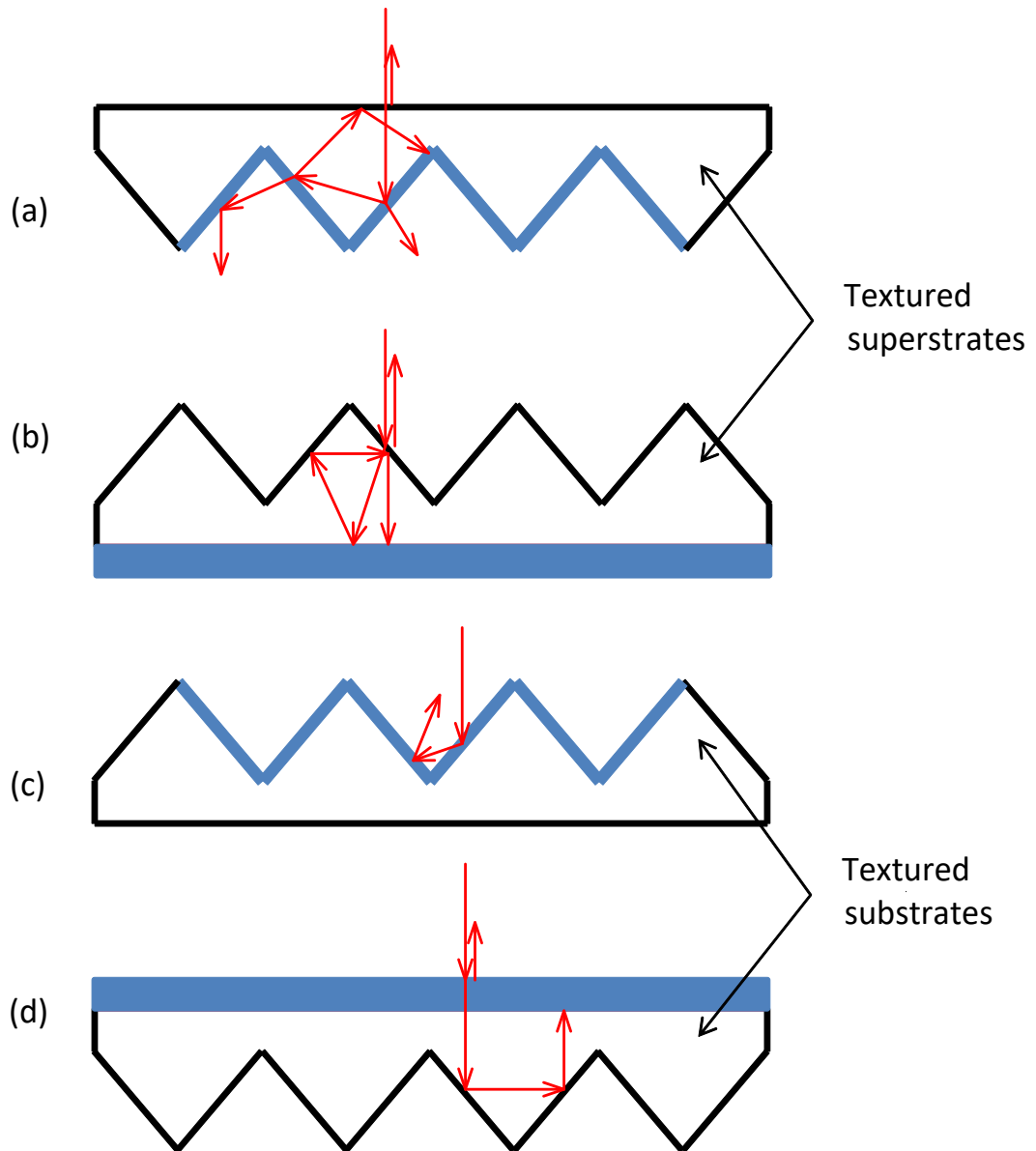


Figure 7. Schematics of superstrates with light rays incident vertically from the top shown in red for situations (a) with active layer (blue) on the textured side opposite incident rays, (b) with the active layer on the untextured side; and substrates (c) with the active layer on the textured surface, and (d) with the active layer on the flat surface.

2.8 Important factors in surface texturisation

As some light trapping approaches utilise direct texturisation of the active region of the solar cell, there are factors that must be taken into account when designing such a process. Not only it is necessary to ensure that the texture itself is effective in reducing the front surface reflection, but it is also important to consider the condition of the surface of the solar cell. One study looked into the relationship between front surface reflectance and minority carrier lifetime within a dry etching texturised solar cell [15]. It was concluded that there is an effective trade-off between surface damage and reflectivity. It is a common to perform a second wet-etching step after processes such as Reactive Ion Etching (RIE), laser machining, and mechanical grooving. Dobrzanski et al. investigated the effects of post-laser etching chemical treatment of multi-crystalline silicon, and it was found that there is a strong relationship between high surface damage and low cell efficiencies [16]. When surface damage was present, short-circuit current I_{SC} and open-circuit voltage V_{OC} were significantly reduced. The advantage of texturing the front surface was only observed after 20 minutes of wet etching in a 20% potassium hydroxide (KOH) solution. Li et al. investigated the effect of surface roughness of zinc oxide (ZnO) covered silver (Ag) layers on Corning glass on cell efficiency [17]. In their work, nano-crystalline Si was deposited on these substrates by hot-wire CVD, and after testing it was concluded that when a high substrate roughness is present, the small cavities on the substrate influence negatively the quality of the deposited silicon causing voids, thus leading to a lower V_{OC} and lower cell efficiencies.

2.9 Common front surface textures

2.9.1 Pyramidal texture

There are several types of textures that have been tested on solar cells for the purpose of increasing light trapping capabilities. One of the most common types is a pyramidal texture of the front surface, and can be achieved through a number of methods. This structure is more regularly used in the texturisation of mono-crystalline Si as it is desirable to have a crystal orientation of $\langle 100 \rangle$ to achieve a uniform pyramidal texture [18-20]. Frequently wet or chemical etching is used to create these pyramidal structures. This is possible by using chemical etchants such as KOH or tetramethyl ammonium hydroxide (TMAH). The etching is anisotropic along the $\langle 100 \rangle$ and

$\langle 111 \rangle$ crystallographic planes thus forming a pyramidal surface topography. In one study, TMAH and KOH were used to create a pyramidal texture [18]. It was found that while the TMAH etch was effective, the KOH etch still produced better anti-reflection characteristics. It was clear that the TMAH etched texture was non-uniform and a cause of less effective results. However in another study, TMAH and KOH were also used to etch the front surface over a period of 30 minutes at 80°C with concentrations of 2% and 1% respectively (with 8% isopropyl alcohol (IPA)) [19]. Using TMAH led to the creation of an optimum uniform surface network of pyramids, which when coated with a Si:N anti-reflective (AR) coating, reduced the weighted reflection to 2.7%. There are other methods that can be used in conjunction with mono-crystalline Si also. Reactive Ion etching (RIE) was used in one study to create hole and columnar structures on mono-crystalline Si by masking the surface in the desired pattern prior to etching [21]. This resulted in average reflectance values of 0.4% and 6.8% respectively. The main advantage of RIE lies in its ability to process with greater speed, and with the use of a mask, can also be used to texturise multi-crystalline Si. Furthermore, one study developed a novel combination of methods for the production of additionally textured pyramidal structures through the use of plasma texturing from a RIE source on a previously wet etched surface [22]. It was found that surface reflection was further reduced, particularly at the blue end of the spectrum. Xu et al. used plasma etching to form uniform conical surface structures which resulted in black silicon [23]. These conical surface structures were shown to be particularly effective at varying angles of incidence, considerably reducing surface reflections compared to polished silicon. Nevertheless, other studies have simulated that the optimum structure is a pyramidal structure with a period shorter than that of the wavelength of light incident on it due to the benefit of the elimination of diffraction order light reflection from such a sub-wavelength structured surface. Chen et al. used coupled-wave analyses to simulate sub-wavelength structures, and it is reported that a pyramidal texture on the Si surface with a period of 350nm almost completely eliminated reflection without the aid of an AR coating, as the sub-wavelength features eliminate almost all diffraction orders [24]. In their work, these structures were fabricated using a combination of optical lithography and RIE, and after testing were found to have a reflection value of approximately 2%.

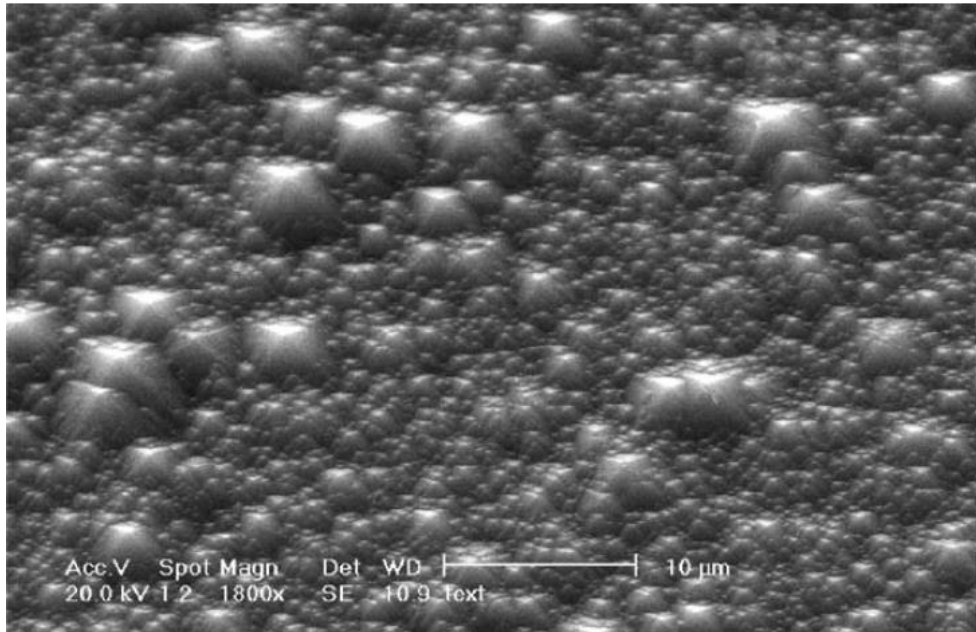


Figure 8. Pyramidal texture on c-Si created by etching with TMAH [18].

2.9.2 Random texture

Random texture structures are commonly created on multi- or poly-crystalline Si to reduce front surface reflection. The reason for the random appearance in comparison with that of mono-crystalline Si is that the preferred crystalline orientation is not in the $\langle 100 \rangle$ configuration, but is randomised, and thus it is not possible to wet etch in a uniform manner to form pyramids as is possible with mono-crystalline Si. In one study a method was developed to quickly texturise multi-crystalline Si with a randomised layout [25]. This method used negative potential dissolution in conjunction with KOH to etch small columns on the surface of the Si, and proved an effective way to reduce the surface reflection significantly with a process of only two minute duration. Schmiga et al. reported the development of 17.6% efficient tri-crystalline solar cells which were optimised by creating crater like structures in the front surface through sulphuric, nitric, and hydro-fluoric acid etching [26]. This resulted in a AM1.5G weighted front surface reflection of 8.8% with an AR coating. In another approach, Srivastava et al. utilised an Ag layer deposited onto the Silicon surface by electroless deposition to assist an etching process using HF and H₂O₂ [27]. This proved a beneficial approach, as the etching time for this process is reported to be 30 seconds, and when comparing this with a 4 minute etch time reported by Schmiga et al., a significant reducing in process time can be realised [26]. Interestingly, Parida et al. utilised a very similar approach as Srivastave et al., yet found that surface reflection

only reduced in the 300nm to 500nm region of the solar spectrum for an etching time of 30 seconds [28].

Table 2. Texture performance in reducing reflection from silicon solar cells

Texture Type	Method	Reflectivity % [Weighted AM1.5G]	Reference
Polished Si	N/A	34	[16]
Pyramid	Chemical Etch	<15	[18]
Pyramid	Chemical Etch	<13	[19]
Pyramid	Chemical Etch	<15	[20]
Pyramid	RIE	<6.8	[21]
Pyramid	RIE	<8	[22]
Pyramid	RIE	2	[24]
Random	Chemical Etch	<30	[25]
Random	Chemical Etch	8.8	[26]
Random	Chemical Etch	<3	[27]
Random	Chemical Etch	<30 (estimate)	[28]
Honeycomb	Chemical Etch	<20	[29]
Honeycomb	Chemical Etch	<5	[30]
Honeycomb	Laser Texturisation and Chemical Etch	<15	[31]
Honeycomb	Chemical Etch	<20	[8]
Groove	Laser Texturisation and Chemical Etch	8.3	[16]

2.9.3 Honeycomb texture

Hexagonal shaped pits etched into the surface of the Si have proven to be an effective method for reducing front surface reflection, and is comparable in terms of optical performance to an optimised pyramidal structure [8]. The honeycomb shape can be produced by masking the surface and etching using an appropriate technique such as Reactive Ion etching or wet chemical etching [21, 29, 30]. It is detailed that with this kind of texture, an efficiency of 19.8% was obtained for a multi-crystalline solar cell.

In a further investigation, Abbott and Cotter used a Q-switched neodymium-doped yttrium aluminium garnet (Nd:YAG) pulsed laser, with a wavelength of 1064 nm, to form pit shaped structures in multi-crystalline Si, similar in morphology to a honeycomb structure [31]. These pits were deep and at the front surface were about 20 μm in diameter. It was necessary to remove surface damage caused by the laser irradiation and ablation using a two stage wet etch; this was conducted with a 25% sodium hydroxide (NaOH) solution for 3 minutes at 40 $^{\circ}\text{C}$ followed by an isotropic etch with a 30:10:4 mixture of nitric, acetic, and hydrofluoric (HF) acids for a further 3 minutes. Several different combinations of texture were tested, including single sided and double sided laser textures. For incident light at wavelengths between 300 nm and 1000 nm, almost no difference in reflectance characteristics was observed, however, from 1000 nm to 1200 nm the double sided texture showed superior performance.

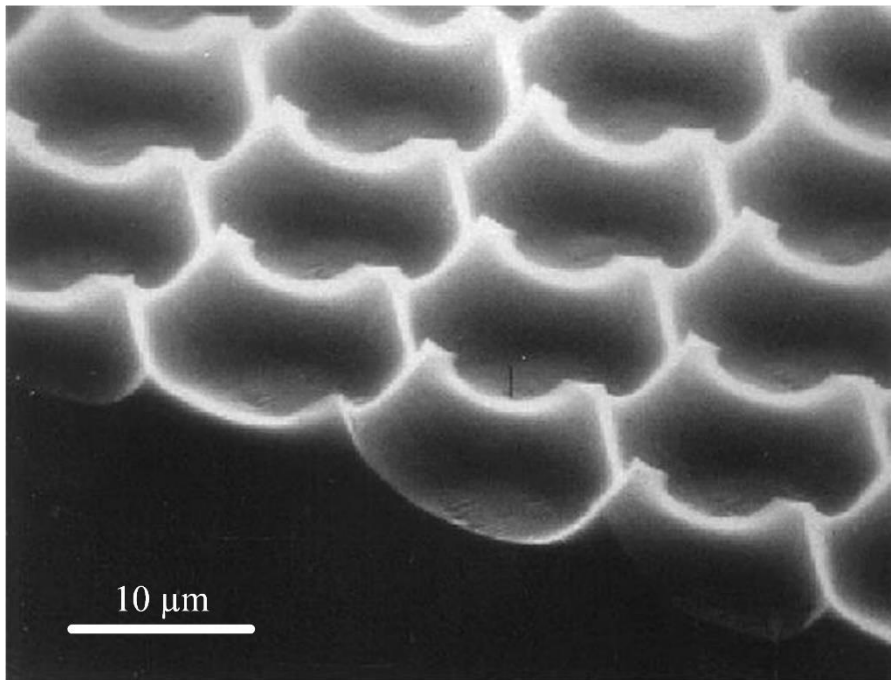


Figure 9. Perspective view of a honeycomb structure formed by chemical etching [8]. Spacing of hexagons is 14 μm .

2.9.4 Grooving

The term grooving is used to describe the technique of producing straight channels on the Si surface. This presents another possibility for the reducing surface reflection. Relative simple mechanical and laser methods can be used instead of etching

techniques to produce these structures. In one study, a 50 W fundamental frequency Nd:YAG laser was used to produce two different grooved surface structures on different sample surfaces; one was with parallel grooves and the other with a cross-hatched square grid pattern [16]. After a 20 minute post-process wet etch in KOH to remove laser induced surface damage, a reduction in reflection was observed from 34% for an untextured surface to just 8.3% for the cross hatched pattern, while cell efficiency was increased by 1.9%. This study demonstrated the effectiveness of using lasers in the texturisation of multi-crystalline Si.

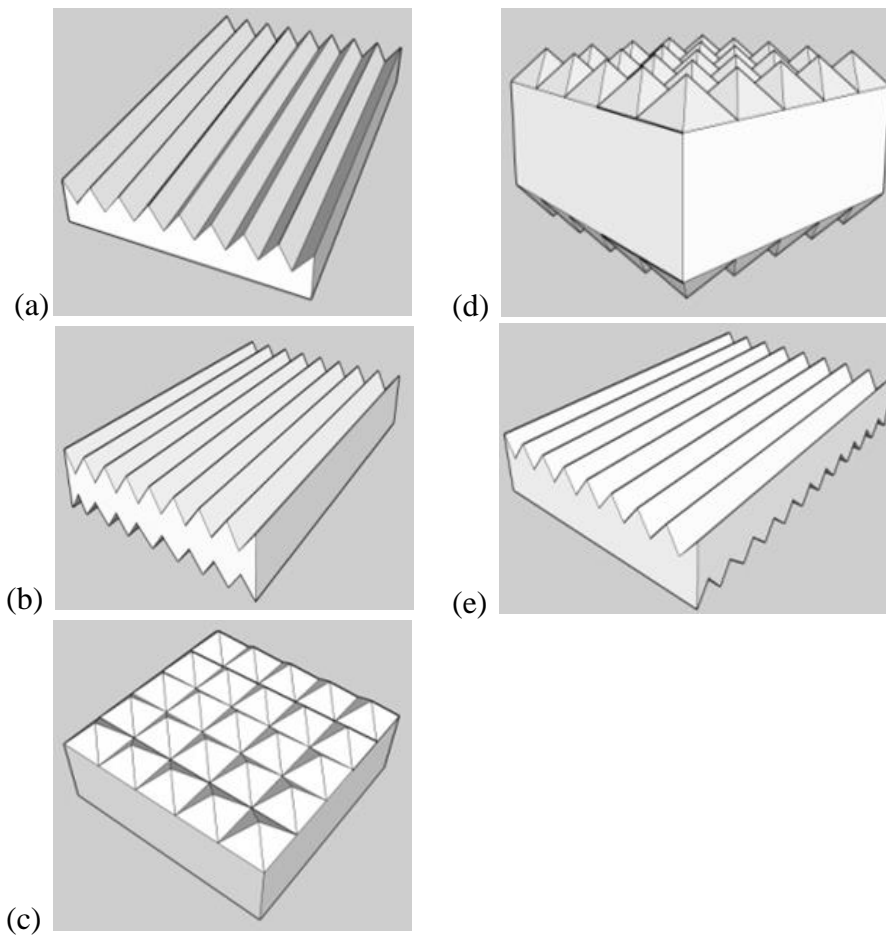


Figure 10. Five possible texture types (a) V-Grooves, (b) V-Grooves double sided, (c) Pyramids, (d) Pyramids double sided, and (e) Perpendicular grooves or ‘Patch’ texture

2.10 Laser micromachining in solar cell design

Lasers are frequently used tools in solar cell manufacturing [32, 33]. Edge isolation, scribing, selective ablation of layers (through the use of particular wavelength laser for specific materials), marking, and drilling. The most commonly used industrial lasers in solar cell manufacturing are Nd:YAG and Nd:YVO₄ lasers, as they are reliable and operate at high power which can increase process throughput [34]. Several studies have previously looked into the direct writing technique for the ablation and texturisation of Si solar cells with these types of lasers [16, 31]. Furthermore, other research has been carried out on the ablation of Si using short pulse lasers such as UV nanosecond and Ti:Sapphire femtosecond lasers [35, 36]. These investigations developed processes for efficiently structuring thin-film solar cells for the purpose of developing more efficient module solar modules and production methods of same.

2.10.1 Design of solar cells on texturised substrates

Rim et al. performed an interesting investigation into the fabrication of solar cells on V-shaped grooved substrates [37]. In their work, the thickness of the active layer of the solar cell was many times less than the profile of the texture. This meant that the active layer morphology was similar to that of the textured glass. The light trapping characteristics of this design were analysed for different types of active layers including amorphous and micro-crystalline Si, which were only 300nm and 1.6 μ m thick respectively. It was noted in their work that the V-shaped grooved surface was very effective on two counts; firstly the light trapping characteristics of the cell were improved and secondly, the texture significantly increased the surface area of the active layer on the substrate. Kang et al. also carried out an investigation in to the optimum textured superstrate design for inclusion in building integrated photovoltaics [38]. The study takes into account the average angle of the sun in order to optimise the light trapping effect. Asymmetric micro-textures were manufactured though the production of a metallic mould, from which PDMS casts were produced. These casts were subsequently attached to the cover glass of photovoltaic panels mounted vertically on a building façade. The study reported a significant increase in average cell efficiency under these conditions, with an average annual energy production enhancement of between 12.9% and 15% respectively.

2.10.2 Micro-structuring and Nano-structuring of glass substrate with laser

Laser ablation can be used for the production of micro and nano-scale structures on the surface of glass. For the ablation of glasses and ceramics in particular, CO₂ lasers have proven to be very effective as glasses absorb the corresponding wavelength of 10.6µm very strongly (i.e. they have a high quantum efficiency) [34, 39]. Much research has been carried out in the field of laser machining of polymers and glasses particularly for the purpose of micro-fluidics. Klank et al. studied microstructures produced by CO₂ laser micromachining of PMMA for the production of micro-fluidic channels [40, 41]. Another study completed an experimental investigation into the fabrication of micro-fluidic channels in a quartz glass block using a Nd:YAG laser [42]. In many applications it is desirable to use shorter pulse and shorter wavelength lasers as they offer tighter focussing and smaller heat affected zones (HAZ), meaning there is a higher degree of control over ablation [39]. Some studies have directly investigated the effect of pulse duration on the quality of the geometries fabricated via micromachining [35, 43]. It is indicated from these studies that it is possible to create smaller features with shorter pulse widths and low average powers. However, there is a trade-off between pulse width and quality. Markillie et al. discovered that pulse widths of 5µs created deeper craters in silica glass than 100µs pulse widths for the same fluence (J/cm²) settings. This was due to the higher peak power for the shorter laser pulse. However, it was noted that the shorter pulse also led to large amounts of debris from melt ejection. By selecting the correct type of laser with suitable pulse widths it is possible to have great control over the resulting micro and nano-structures. Issa et al. investigated the use of a 1.5kW CO₂ laser to perform micromachining in soda-lime glass [44]. It was shown experimentally that by controlling the parameters of the laser, it was possible to create an atlas for resulting channel widths, depths, and shape from a single pass with prescribed laser settings. Nikumb et al. also carried out an investigation into precision laser micromachining in glass using a frequency tripled Nd:YAG, a fundamental Ti:Sapphire, and a fundamental Nd: YVO₄ [45]. It was found that significantly better quality micromachining could be performed by using pulse of short duration. Both Kazansky et al. and Crawford et al. reported the creation of sub-micron structures, in bulk silica and Si respectively, using an infra-red femtosecond laser beam [46, 47]. These structures were detailed as having periodic structures as small as 140nm.

2.11 Computer simulation for optimum texture type

Much work has been carried out in the area of computer simulation of light trapping structures. Chung et al. carried out an investigation to find the optimum properties for light trapping using pyramidal structures [48]. For this analysis a simulation was performed to predict the absorption of photons in Si solar cells with respect to the incident angle and pyramidal texture. It was found that a high incident angle resulted in lower cell efficiencies. In a study by Campbell and Green, the light trapping properties of different surface structures are presented [49]. This investigation suggests that the optimum pyramidal structure for anti-reflection and light trapping characteristics should contain a slight randomisation. It was also proposed that the most efficient structure was a double sided structure (i.e. both sides of the support structure being textured) with a cross-hatched pattern. From simulation results of Campbell and Green, it was noted that the light trapping probability of such a double sided textured design is optimal for Si wafers above 100 μm thickness [50]. However, these simulations only concern Si wafer solar cells which are many times thicker than thin film devices (which are typically 5 μm or less). These thin films conform more closely to the surface profile of the support structure. Nevertheless, the same theory can be applied to thin film devices, with the exception that the support is texturised before deposition of the active Si layers, as performed by Li et al. [17]. Sanches-Illasca investigated the effect of pyramidal and cosine shaped structures on solar panel cover glass on the light trapping performance of the panel, and found that the textures can provide favourable transmission characteristics, particularly at oblique angles of incidence [51].

2.12 Thin-film solar cell designs

The function of glass in solar energy systems was presented in detail in 2008 [52]. For the fabrication of thin-film solar cells it is necessary to use a substrate or superstrate to provide mechanical support for the thin active layers. In order to reduce manufacturing costs, it is desirable to use a superstrate which will form an integral part of the finished solar cell. Therefore, glass makes the ideal candidate superstrate for thin-film solar cell production. Deubener et al. discuss various concepts in thin-film solar cell design, such as texturing the front surface of the glass and texturing the back side [52]. It is considered that texturisation of the front side would lead to dirt

accumulation under standard outdoor solar cell deployment conditions. Although it may be possible that, with careful texturisation, a hydrophobic surface could be produced to work in conjunction with the light trapping capabilities afforded by the texturisation [53]. Texturisation of the back and front sides of the glass however, could provide a promising solution as this would allow for a cell architecture and structure similar to those optimised through simulation by Campbell and Green [49]. An effective architecture, crystalline silicon on glass (CSG), is discussed in a study presented by Green et al. [54]. This cell architecture does not require a thin transparent conductive oxide (TCO) layer on a transparent glass ceramic superstrate, and is a cost effective and robust manufacturing process for thin-film cells. Other studies indicate that an effective operation to improve light trapping properties of the solar cell is to directly texture the TCO that has previously been deposited on the glass superstrate [52, 55, 56]. One possibility of texturing glass substrates is with the use of laser ablation mechanisms.

2.13 Silicon quantum dot solar cells

Much work has been done in recent research on quantum dot solar cells. There are many potential applications for quantum dots, from multi-junction tandem band-gap tuned architectures to photon energy down-converters [7, 57]. Silicon quantum dots in particular have been subject to much research due to their optical properties and biocompatibility [58]. It has been shown in literature that it is possible to change the optical properties of silicon quantum dots, not only by controlling their size, but also by controlling their surface chemistry [58-65]. The band-gap of the quantum dots can be controlled by controlling the diameter of the dot. As the size of the dot is reduced below the exciton Bohr radius in a semiconductor, the quantum confinement effect occurs, which causes significant changes to the optical properties compared to those found in the same bulk material [7]. By reducing the diameter of the quantum dot it is possible to increase the band-gap of the material, thus offering the possibility to optimally tune the band-gap of the material to suit the wavelength of light incident upon it.

There are several possible architectures in which quantum dot based solar cells can be realised. One such design, the quantum dot sensitised solar cell, shows particular promise [7, 66, 67]. This type of design is based on the sensitisation of a micro-to-

nano porous TiO_2 paste deposited on the surface of a transparent conducting substrate. It has been reported that the porosity, and pore size, and the pore connectivity are important issues for the efficient operation of this type of solar cell [66]. The benefits of solar cells based on TiO_2 are well known. Due to the simplicity of the cell design manufacturing costs can be reduced, and furthermore, there are optical benefits in the use of TiO_2 films as the micro and nano porous structures of these materials greatly enhance light scattering [68]. The benefits of this include less sensitivity to illumination directionality, and the possibility of enhanced light trapping effects. The high surface area of the nanostructured materials also enable the efficient absorption of light [69].

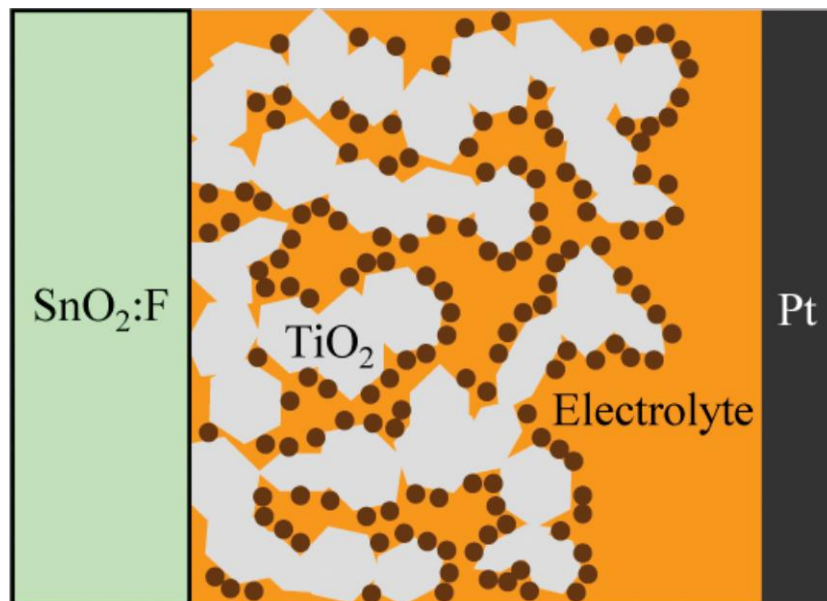


Figure 11: Example of a quantum dot sensitised solar cell architecture [70].

2.14 Solar Cell superstrate material selection

When choosing a superstrate material for this investigation there were several key factors that were taken into account, as follows.

- refractive indices
- laser absorption characteristics
- thermal and physical properties and stabilities
- cost and availability
- transparency to the AM1.5G spectrum

2.14.1 Refractive indices

In order to ascertain the feasibility of the laser texturing of the front cover superstrate of a solar module it is necessary to choose a superstrate material with similar optical properties to those used in conventional solar modules produced today. The majority of solar modules today use low-cost soda lime glasses, which tend to have refractive indices of between 1.50 and 1.55 [71]. However, it is possible that more expensive glasses such as fused silica may be used in cases where maximum power output is of highest importance. Refractive index is an influential parameter of this study also, as it will affect the amount of deflection the light rays will undergo during the geometrical light trapping effect induced by the textured surfaces.

2.14.2 Laser absorption characteristics

As most glasses are transparent across the visible electromagnetic spectrum, it is important to choose the materials carefully as how they absorb laser light is highly influential in determining the process quality and ability of the glass using a laser process. Unless the laser used is able to deliver pulses of light short enough with a high enough peak intensity to cause non-linear and two-photon absorption, such a picosecond or femtosecond laser, it is unlikely that a laser operating in the visible spectrum will be able to successfully obtain the required level of energy absorption for micro-machining [39, 72]. Far-infrared lasers are well suited to the machining of glasses as the laser light at this wavelength is absorbed well by SiO₂ structures [39, 73, 74].

2.14.3 Cost and availability

Soda-lime is the most commonly used glass, and is widely used in applications ranging from window glass to solar module cover glass due to its low cost and wide availability [71]. Other glasses such as borosilicate are higher in cost, and are used in instances where the physical properties of soda-lime glass are not sufficient. Borosilicate glass, widely known as Schott glass or Pyrex, is widely used in cookware for instance due to its excellent thermal characteristics [75]. Meanwhile, fused silica is a synthetically manufactured glass used only the highest quality base materials and is of high purity. This enables fused silica to exhibit its high transmission, high chemical resistance, and excellent thermal shock characteristics [72, 76]. While fused silica is significantly more expensive than its counterparts, its properties can be quite beneficial for certain applications, such as optics for high power lasers and windows in highly sensitive scientific equipment.

2.14.4 Thermal properties and stability

While most optical glasses are brittle, they exhibit a high level of hardness and excellent chemical resistance [1]. The thermal conductivities of glasses is normally quite poor. While poor thermal conductivity can mean that it is possible to laser machine locally with a very small heat affected zone (HAZ), it can also mean that the material is very sensitive to thermal shock and cracking [73]. Fused silica is known to be one of the glasses with the highest thermal-shock resistance of all common optical glasses, making it highly suitable for laser micromachining. Having this high thermal-shock resistance means it is possible to laser machine the material with a long-pulse infra-red laser, where thermal breakdown is the mechanism for laser ablation during micromachining.

2.14.5 Transparency to AM1.5G spectrum

According to the ASTM G173-03 Reference Spectra, the AM1.5G spectrum ranges in wavelength from the ultra-violet range at 280nm to the infrared at 4000nm [1]. However, as the electronic band-gap of silicon is 1.1eV, silicon will not absorb any light with a wavelength longer than approximately 1100nm [1, 77, 78]. Photon energies close to the band-gap of the silicon absorber also provide the highest spectral response of the solar cell, therefore it is most important that the superstrate material is

transparent in UV-VIS-IR region of the spectrum. Higher energy photons, with energies greater than 1.1eV, contribute the most significant energy flux of the spectrum and results in the majority of the carrier generation that occurs in the solar cell. Most commercially available glasses are highly transparent between 350nm and 1100nm [52].

2.15 Literature Review Summary

From this past research, it is clear that there remains a lot of interest and potential scope for solar cell superstrate topology optimisation. In this work fused quartz was chosen as the solar cell superstrate material to be investigated. This material provides favourable thermal shock characteristics and excellent optical transmission properties across the UV-VIS-IR spectrum. In particular, in this work a detailed design of experiments for the laser texturisation of this superstrate material was investigated for its effect on solar cell efficiency. Two characterisation methods were also developed and investigated to allow for more detailed characterisation of the solar cell structures. These included the design, commissioning, and verification of an optical profilometer based on the depth-from-focus principle for the metrology of textured superstrates. In this work an analysis of the FIB-SEM serial sectioning method was completed, which has applications in the evaluation of macro-porous solar cell materials.

Chapter 3 Materials & Methods

3.1 Design of a Depth-from-Focus based Optical Profilometer

The main investigation of this work was to assess the effect of laser texturised glass superstrates on the performance of solar cells. In order to thoroughly evaluate how solar radiation interacts with a textured surface and subsequently with the solar cell behind it, it is necessary to measure the surface shape and texture characteristics accurately. The laser processing parameters can then be correlated with the measured surface texture parameters. These surface characteristics of the solar cell can in turn be related to the cell performance under various conditions.

Optical profiling systems offer capabilities that are well aligned to this research, as they can measure with high-resolutions over larger surface profile depths compared to stylus type instrumentation. The non-contact nature of the measurement is also beneficial, as the optical profiling solutions can perform a measurement over a large surface area within a short measurement time. Examples of widely used optical profiling techniques for transparent and optical materials include White-Light Interferometry (WLI) and Laser Scanning Confocal Microscopy (LSCM). While these techniques are widely utilised in the measurement of optically smooth surfaces, they have limitations to their capabilities when measuring optically rough surfaces, especially due to effects from surfaces roughness with a high spatial frequency [79, 80]. While the term ‘optically rough’ is somewhat arbitrary and is highly dependent on the end application of the optical surface, in literature it has been referred to as surface roughness in the range of 10 nm to 100 μm R_a when considering WLI measurement applications [79]. The surface profiles created by laser processing glass can vary in depth and roughness, with some channels exhibiting steep flanks in excess of 70° [81]. These characteristics can be challenging to measure accurately using optical techniques, as the numerical aperture of the objective lens used in the measurements is directly correlated to the maximum surface angle that can be measured [79]. In WLI applications for example, these factors can result in data dropout, as the interference signal becomes too weak to provide any level of certainty at particular points of the measurement. This data then requires interpolation, which can introduce unknown amounts of measurement error.

In pursuit of the above research goals it was decided to perform an initial evaluation of a 3D non-contact optical profilometer based on the depth-from-focus principle, a method which requires varying the focal plane of a specially designed optical and imaging system with a low depth-of-field, from which it is then possible to extract surface contour information from the surface of the specimen [82]. Advantages of this method include sub-micrometre level resolution and the ability to measure and visualise surfaces in real colour. This measurement technique has shown good promise in the measurement of steep flanks and varying surface roughness conditions [80]. Little research has been performed on the suitability of an instrument with this operating principle for the measurement of optically rough transparent surfaces, although the measurement of translucent materials has been reported as a limitation of this technique [80]. As part of this work an optical profilometry system was designed and fabricated (see Figure 12), which facilitated the initial evaluation of the measurement technique with the aim of testing the feasibility of the depth-from-focus method for the measurement of optically rough transparent surfaces. Part of the device evaluation process included the manufacture of a brass measurement artefact by milling, which was evaluated using other measurement instruments (WLI and stylus) with two main aims: firstly, to provide a method of initial comparison of the designed profilometer with commercially available systems, and secondly, to provide an approximate dimensional verification of the designed system. While the traceable calibration and evaluation of such an artefact requires significant amount of work, testing, and statistical analysis with a certified metrology institution (such as NIST, NPL or PTB), the artefact manufactured in this work provides some initial information about the general accuracy of the device and also provides a method by which the measurement repeatability can be evaluated.

As the systems contains components of motion control, image processing, surface display, and signal analysis, NI LabVIEW was selected as the software development environment due to its ability to integrate with third party hardware and the availability of additional software libraries such as NI Vision.

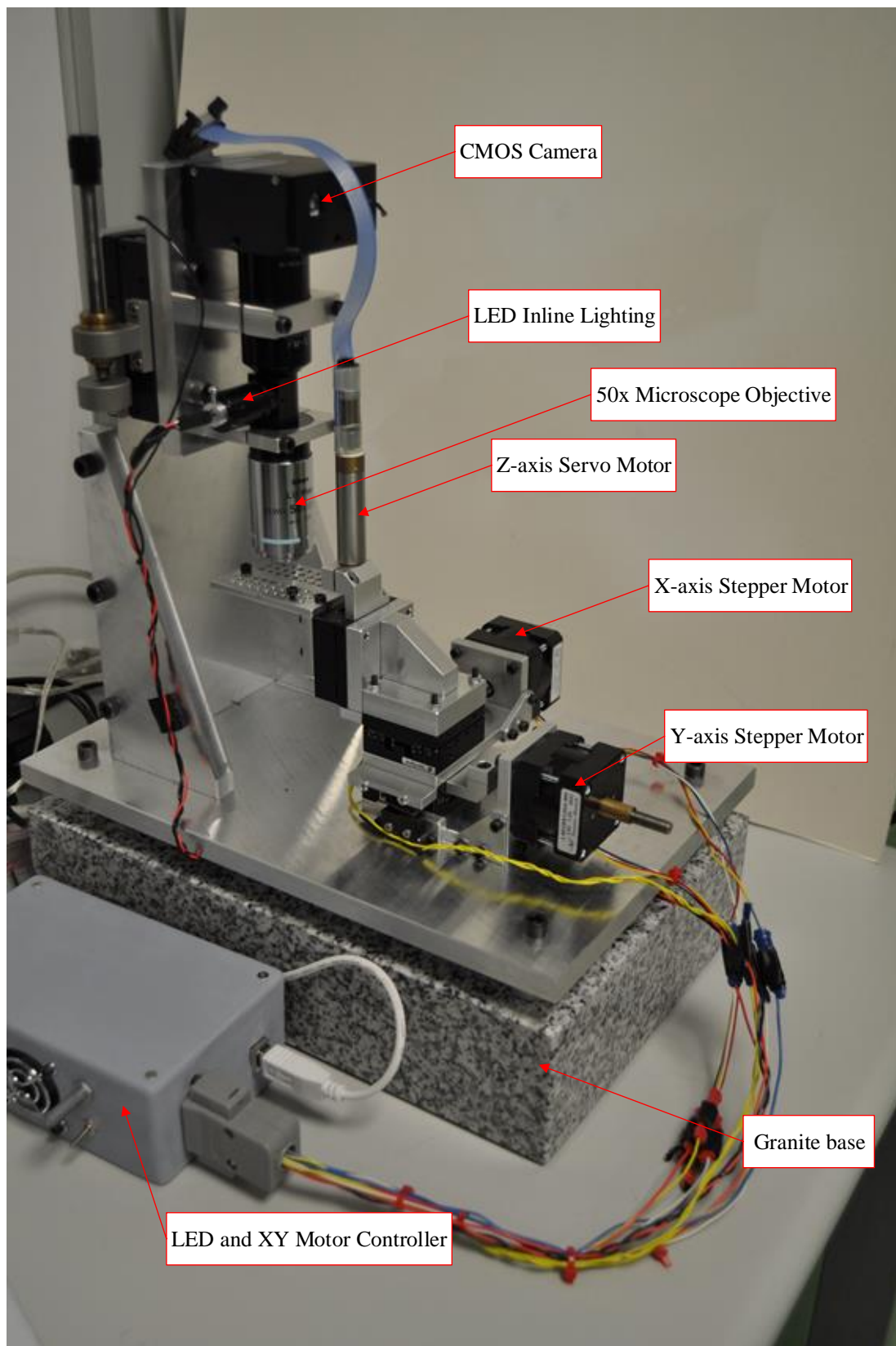


Figure 12. 3D non-contact optical surface profilometer.

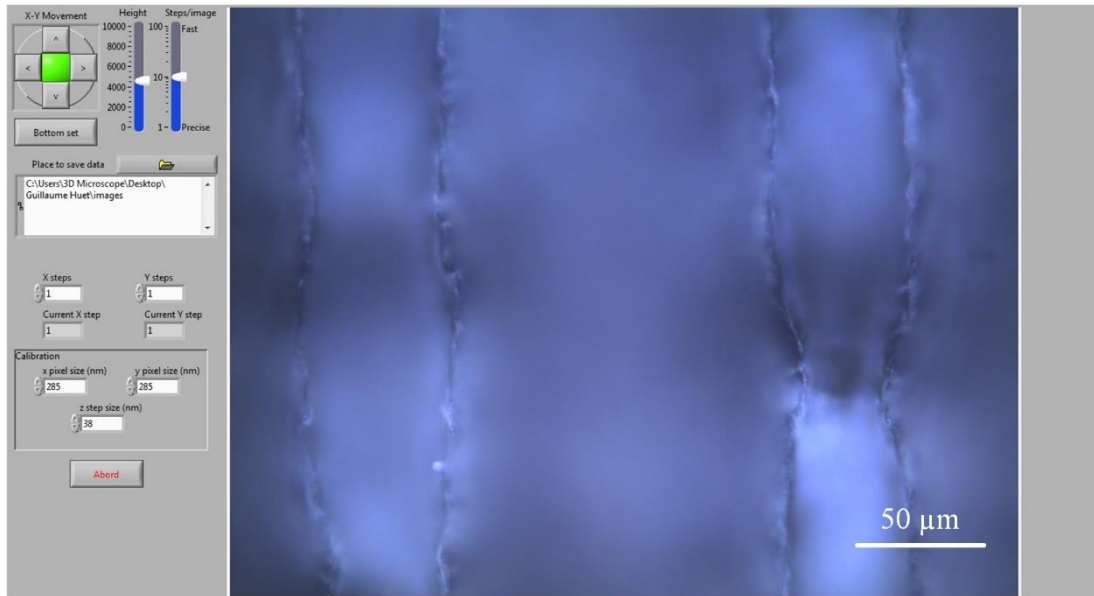


Figure 13: Main Graphical User Interface (GUI VI Front Panel) for the 3D non-contact optical surface profilometer.

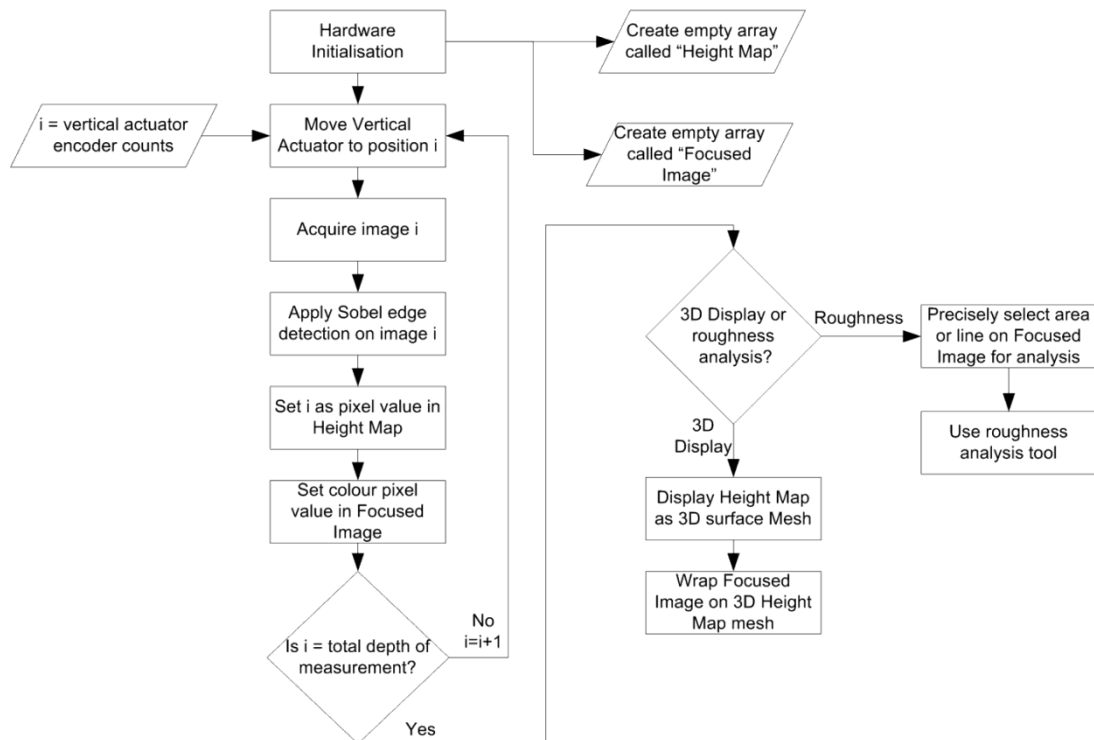


Figure 14. Flowchart indicating operation of the 3D non-contact optical surface profilometer control software.

3.1.1 System Specification

Table 3. Optical system specification

Objective lens model	Nikon CFI60 LU Plan Epi ELWD Infinity Corrected
Objective lens magnification	50x
Objective lens working distance	10.1 mm
Objective numerical aperture	0.55
Objective resolving power	0.5 μm
Objective depth-of-field	1.0 μm
Lens tube model	Infinitube FM-100
Lens tube focal length	100 mm (0.5x)
System magnification	25x
System field-of-view	310 μm x 232 μm
Camera model	Mightex Systems MCE-C030-U, USB2.0 CMOS camera, 3MP colour, Enclosed, w/ GPIOs, C-mount
Camera sensor	Aptina 1/2" Micron MT9T001, colour, Rolling Shutter
Camera pixel size	3.2 x 3.2 μm
Camera resolution	2048 x 1536 pixels (1024 x 768 with 1:2 decimation)
Image sampling distance	0.303 μm per pixel
Illumination	Single white LED, potentiometer adjustable output, co-axial illumination configuration

Table 4. Motion control system specification

Z-axis	
Actuator model	Thorlabs 612B
Motor type	12 V DC with 256:1 gearing
Encoder type	48 count encoder 12,288 counts/rev with gearing
Leadscrew pitch	0.5 mm
Travel range	12 mm
Resolution	40 nm
Speed	50 – 425 $\mu\text{m/s}$
Load capacity (axial)	4.5 kg
Controller model	Precision MicroControl Corp. DC2-PC 100 Series Motion Controller
X & Y axes	
Motor model	Nanotec L4018S1204-M6
Motor type	Bi-polar stepper, 3.5 V, 1.2 A
Steps/revolution	200
Leadscrew pitch	1 mm
Resolution	5 μm full step, 2.5 μm half-step
Speed	0.005 – 5 mm/s
Controller model	Byvac BV4113

3.1.2 Design of the Optical System

The high resolution optical system was implemented using a 50x magnification Nikon microscope objective lens. This objective lens was diffraction limited and has the power to resolve features in the order of 500 nm in size using white light illumination while providing a very shallow depth-of-field of 1 μm (as specified by the manufacturer), meaning only a fraction of the image is focused at any one time. The depth-from-focus measurement technique takes advantage of the limited depth-of-field to correlate various height points on a surface with a vertical scanning position. As the limited depth-of-field is the basis of the measurement method, using an objective with a larger depth-of-field (with a lower numerical aperture and

magnification) would reduce the vertical measurement resolution of the device. The objective lens was used in conjunction with a 100 mm focal length microscope tube lens and a 3MP colour USB CMOS camera as the imaging device. This configuration gave the optical system an overall effective magnification of 25x with a field of view of 310 μm by 232 μm , as determined in section 3.2 using a calibrated stage micrometer.

3.1.3 Design of the Motion Control System

There are two elements to the motion control system (Figure 15). The vertical positioning system was used to scan the sample along the vertical axis of the optical system, thus changing the position of the in-focus optical plane. A high-accuracy Thorlabs servo actuator (612B), with a stated minimum incremental movement capability of 200 nm, was used for the vertical positioning of the specimen and was controlled using a Precision Micro Control (DC2-PC) servo motor driver/amplifier. Third party hardware integration is possible as LabVIEW supports many third party hardware components. The vertical positioning system had a theoretical resolution of 40nm. The XY positioning system was controlled using two Nanotec stepper motors (L4018S1204-M6) using third party USB stepper drivers (Byvac BV4113), providing a theoretical resolution of 5 μm when full-stepping, allowing for the positioning of the specimen and for the implementation of mosaic acquisition with image stitching for large area measurement.

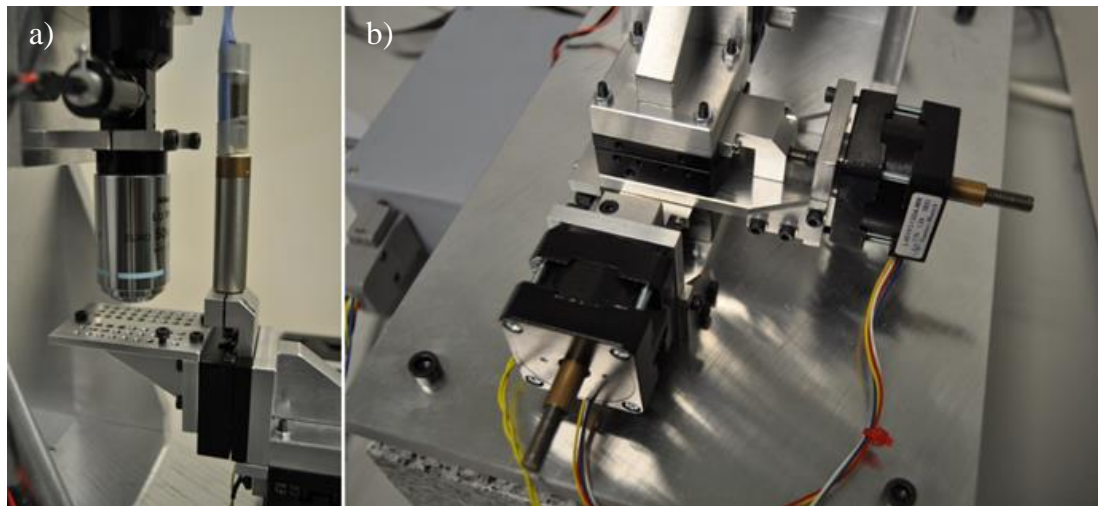


Figure 15. Images of the (a) high resolution optical system and vertical actuator, and (b) XY positioning stage with stepper motors.

3.1.4 Image acquisition and processing

The raw data acquired in the form of a stack of images is then processed to extract the focused regions from each image in the stack. As the vertical position of each image is known from the synchronisation of the motion control system during the image acquisition, it is possible to build a 3D surface mesh from the extracted focused regions. Significant work has been done in the area of image processing algorithms for the extraction of depth data [82-103]. There are a significant number of algorithms available which offer various advantages for various applications. In this implementation, it was decided to utilise a straightforward focus detection method through the use of a gradient magnitude algorithm. The feature extraction was performed through the use of the Sobel edge detection algorithm in this instance [104]. The Sobel algorithm is essentially an edge detection algorithm. By using a Sobel edge detector, an intensity value is assigned for the gradient of every pixel in the image being analysed. The stack of images was then parsed to find the highest gradient intensity in the image stack for each pixel along the vertical measurement plane. The highest intensity was the referenced to a height according to the vertical position that image was recorded at, which is stored in a 'Height Map'. This process is shown in Figure 16.

The 3D surface can then be visualised in full colour by placing the focused colour image data onto the height map. An inbuilt LabVIEW VI was used to process the height map of the surface, which is then able to display in a 3D Picture Control. Using a 3D Picture Control configuration VI it is possible to wrap the fully focused image (generated previously from the stack of images by extracting the focused regions) on the surface mesh, allowing the measured specimen to be displayed in full colour at sub-micron resolution as shown in Figure 17.

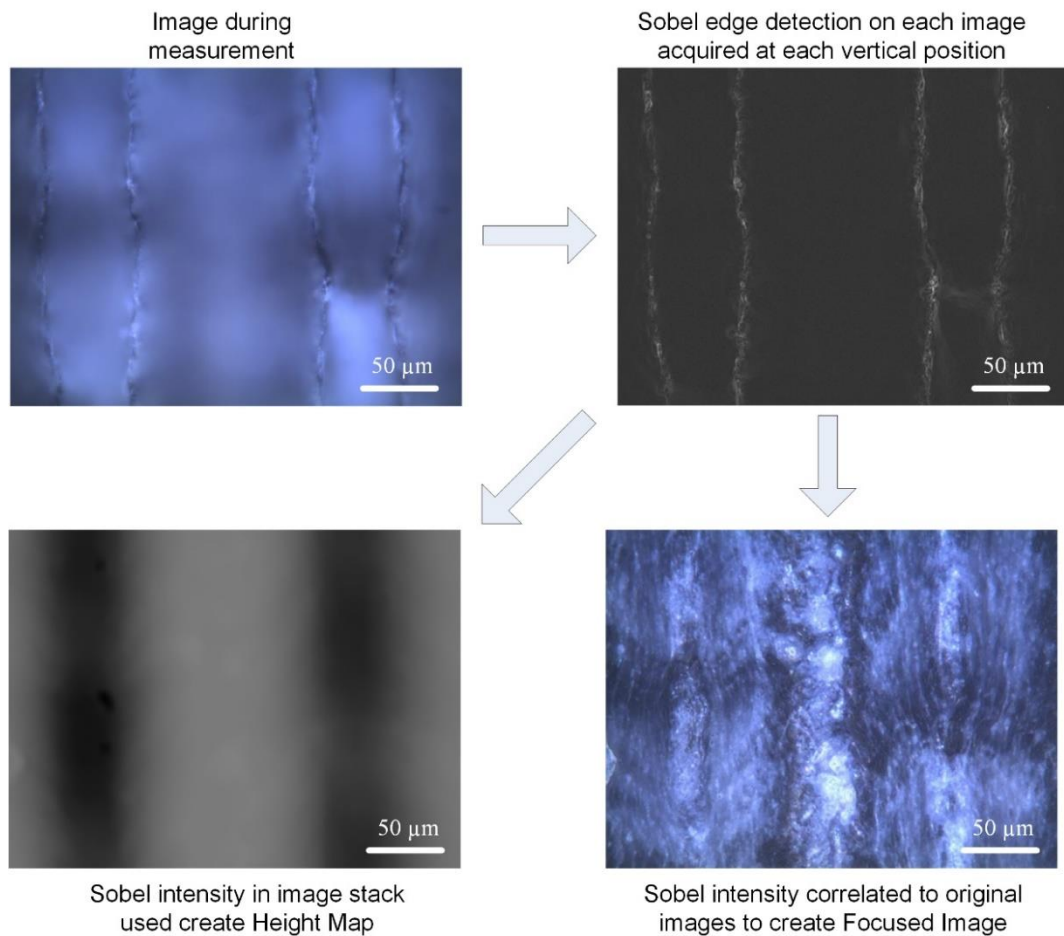


Figure 16. Raw data processing procedure. Both a topographical height map and a high resolution fully focused image are created.

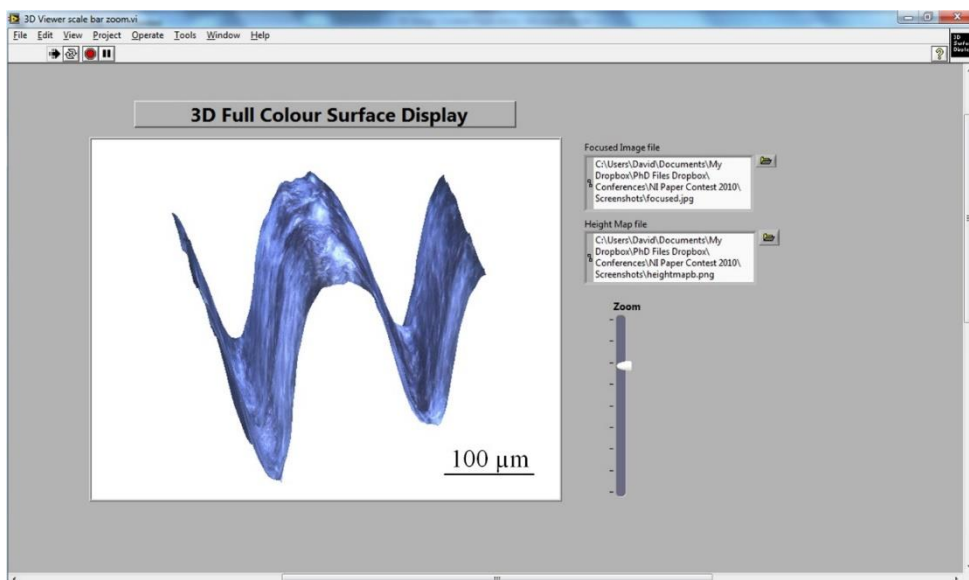


Figure 17. 3D surface display of laser processed grooves in transparent glass. The surface has been shaded blue to improve visibility.

Measurement area is 310 μm by 232 μm .

3.1.5 Image stitching (tiling)

When measuring large areas using a high-magnification optical configuration, it is often necessary to take measurements at various positions on the sample which are later combined together to create a larger image at high resolution. This process is frequently referred to as ‘tiling’, but is also known as image stitching. There are various approaches to this method, however typically this is achieved by overlapping the tiled areas of the acquisition. Overlapping the tiled sections allows for the registration of the measurement areas in all three axes of the co-ordinate system. A typical overlap amount is 10% which is generally seen as a reasonable compromise between data integrity and measurement speed [79]. In the implementation of image stitching in this work, no overlap or image registration algorithm was utilised in this initial investigation. Instead, tiled areas were placed beside one another in the correct order to form a larger high-resolution image.

3.1.6 Surface roughness calculation and evaluation

It is often necessary to measure the surface roughness of components in surface engineering, as the surface roughness can significantly affect the performance of a surface in a particular application. One example of this is in the manufacture of high tolerance mechanical parts, such as internal combustions engine components. However, with relevance to solar cells, surface roughness is a useful evaluation parameter as this can influence light scattering properties of a particular surface [105]. Different surface roughness parameters reveal different important characteristics of the material and the production processes. However, there are strict guidelines that must be met in order to make roughness analysis repeatable and accurate. Firstly, the data must be corrected for form error by linear regression. The following step involves using a Gaussian filter with a low cut-off frequency defined by ISO 4287, which removes the waviness component of the surface [106]. The waviness may appear as a repeating pattern in the data, whose wavelength is too large to be considered as roughness. A visual description of the components of surface roughness are given in Figure 18.

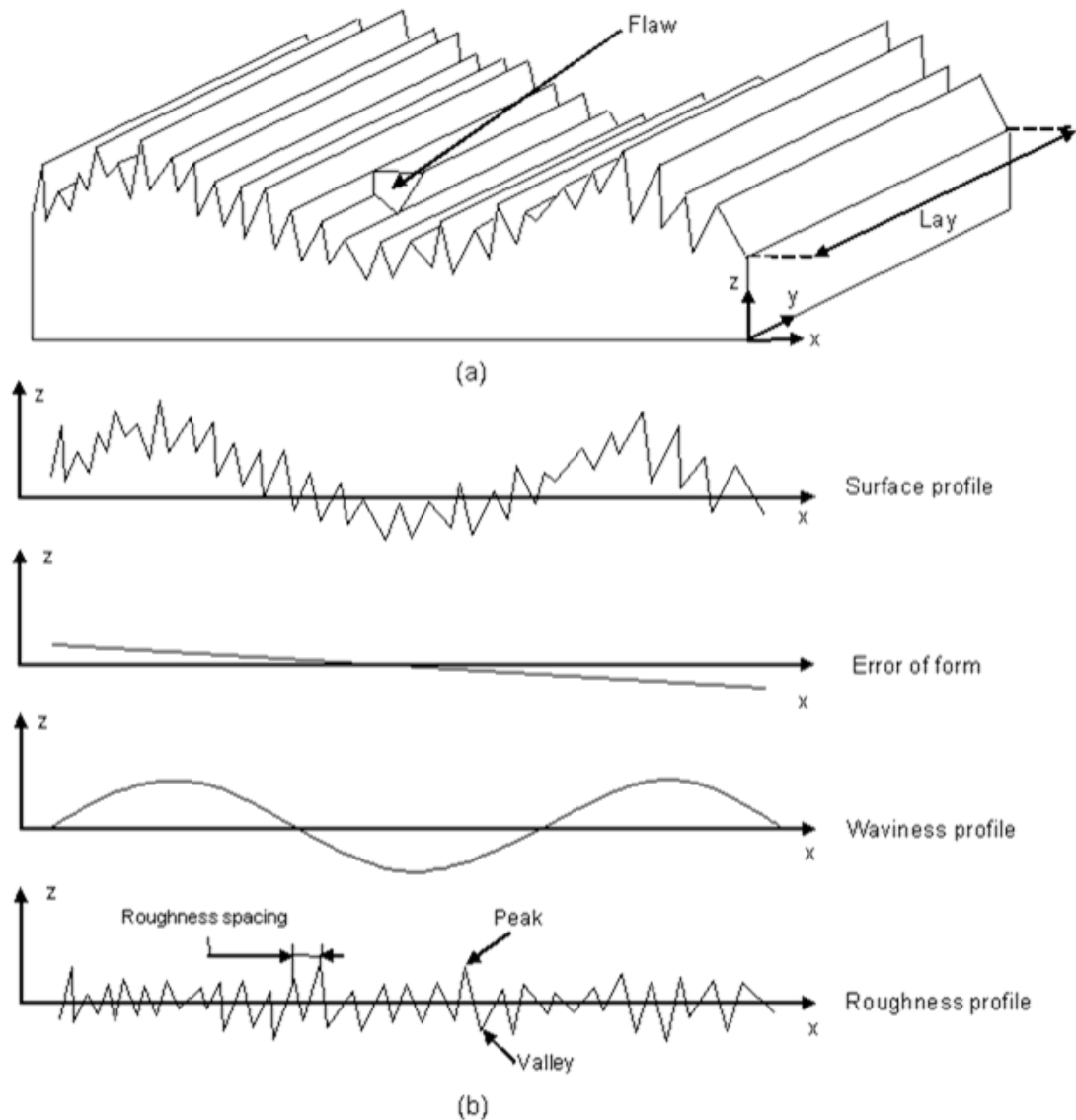


Figure 18: (a) A representation of the actual surface being measured. (b) The components of the surface profile according to ISO 4287.

In order to evaluate during the calculation exactly what surface form error and waviness constitute, it is necessary to consult ISO 4287 and ISO 4288 [106, 107]. This standard specifically defines the data filtering parameters that must be adhered with in order to achieve a compliant surface roughness measurement. These parameters are shown in Table 5.

Table 5: Selection of Filter parameters according to ISO 4288

Periodic profiles	Non-periodic profiles		Cut-off lengths	Sampling length	Evaluation length
Spacing distance (mm)	Rz (mm)	Ra (mm)	lc (mm)	l (mm)	L (mm)
> 0,01 to 0,04	to 0,1	to 0,02	0,08	0,08	0,4
> 0,04 to 0,13	> 0,1 to 0,5	> 0,02 to 0,1	0,25	0,25	1,25
> 0,13 to 0,4	> 0,5 to 10	> 0,1 to 2	0,8	0,8	4
> 0,4 to 1,3	> 10 to 50	> 2 to 10	2,5	2,5	12,5
> 1,3 to 4	> 50	> 10	8	8	40

The remaining filtered data is then used for the roughness analysis (Figure 19). Two types of analysis were programmed and performed using the developed software; line analysis and area analysis, where the area analysis provides similar information to that of the line analysis but in two directions instead of one.

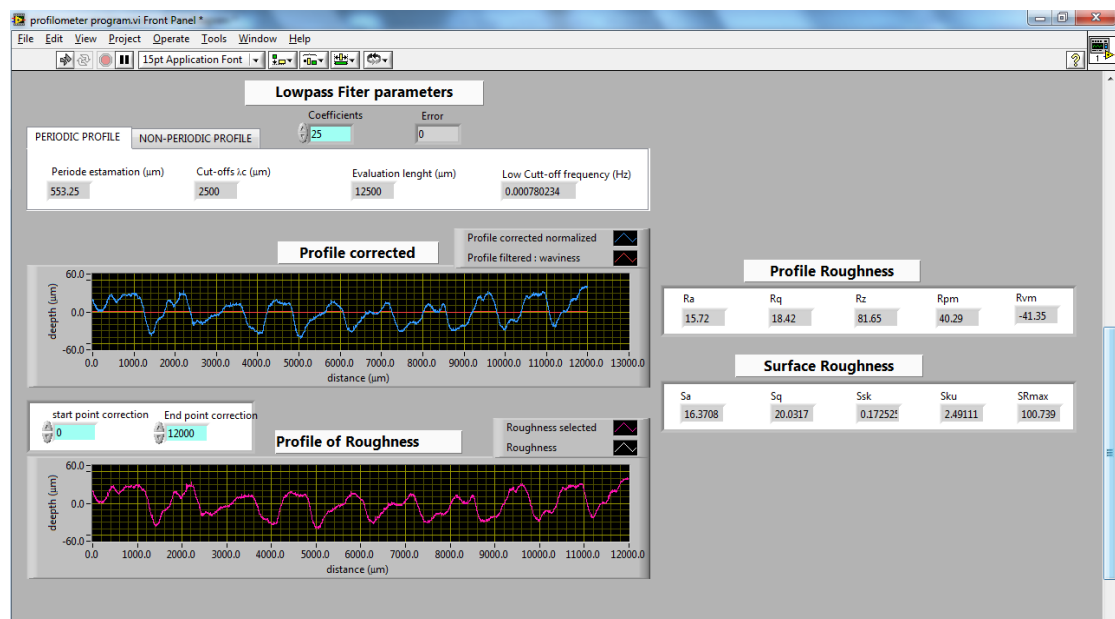


Figure 19. Roughness profile is obtained using the ISO 4288 standard for profile correction.

3.2 Verification of the optical plane of the 3D Profilometer

The optical XY plane was verified using an optical stage micrometer (PYSER-SGI PS78) which had been calibrated and certified by UKAS. The measurement uncertainty using this calibrated micrometre was ± 0.0005 mm, which allowed for accurate adjustment of the optical system. Figure 20 shows an image of the calibrated micrometre scale taken as a resolution of 2048 pixels by 1536 pixels with a 1:2 image decimation ratio, which meant the recorded image has an effective resolution of 1024 pixels by 768 pixels. By measuring the number of pixels in the image against the calibrated scale it was possible to calculate the camera calibration value to be 3.3 pixel/ μm , the reciprocal of which gives $0.303 \mu\text{m}/\text{pixel}$. Using this information, it is possible to calculate that the field-of-view of the optical imaging system at this resolution was $310 \mu\text{m}$ by $232 \mu\text{m}$. The adjustment of the system was achieved by storing the $0.303 \mu\text{m}/\text{pixel}$ value in the operating software of the system. This value was then taken into account when calculating the scale of the final data output.

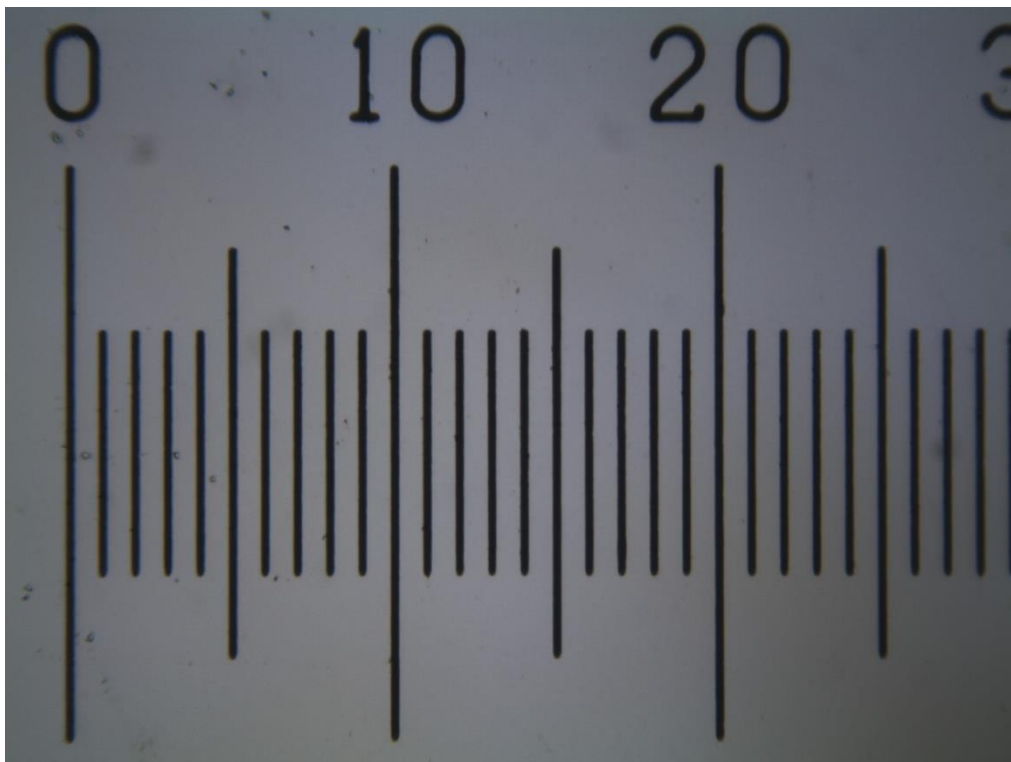


Figure 20 - PYSER-SGI PS78 Stage micrometer used for calibrating the optical plane of the microscope system.

3.3 Performance analysis of the linear stages of the 3D Optical Profilometer

In order to assess the performance of the linear stages, it was necessary to utilise measurement tools to evaluate the positional performance characteristics of the devices. The aim of the performance analysis was to determine the positioning accuracy and repeatability of the low-cost linear stage configurations for use in a 3D optical profilometry applications, data which can subsequently be used when evaluating the overall system measurement performance. To assess the accuracy and repeatability, it was necessary to follow a standard procedure to ensure that any values obtained for the stage performance was in line with international standards and that they could be compared readily with the performance of other devices.

The international standard ISO 230-2 standard is specifically designed for the analysis of stage performance [108]. The standard describes the methods which should be followed, and also details the selection of parameters used in testing. An extract from the standard of the parameters and formulae used in this analysis are included in Appendix D.

3.3.1 Selection of Target Positions for Positional Analysis

The analysis was performed by moving the linear stages point to point, from one target position to the next. The stages were allowed a settling time of a minimum of 5 seconds for every measurement taken, in order to ensure the axes had come to a complete stop, and that any residual vibrations did not affect the position measurement.

The X and Y stepper motor driver axes and the Z servo motor driven axis were driven point to point at a velocity of 1mm/s with a linear acceleration profile of 10mm/s². These low velocities and accelerations were chosen specifically in order to negate the effect of static friction and inertia on the accuracy and repeatability of the system.

The value of each target position can be selected without restrictions. However, it should take the general form presented in (1), in order ensure any period errors within the motion system are correctly sampled.

$$P_i = (i - 1) p + r \quad (1)$$

Where i is the number of the current target position; p is an interval based on a uniform spacing of target points over the measurement travel; and r is a random number within \pm the amplitude of possible periodic errors in the movement mechanism. It is recommended by the standard to use a changing value of this random number, for each target position, between $\pm 30\%$ of P , which allows for any periodic errors to be adequately sampled and evaluated.

3.3.2 Recording of the stage positions using Dial Gauge Indicators

In order to evaluate the positional accuracy and repeatability of the linear stages, dial gauge indicators were used to measure point to point movements. In this approach, a dual scale analysis was performed. The reason behind the dual scale approach is that some Dial Gauge indicators facilitate longer travels, which those that have shorter operating ranges typically offer improved accuracies. By performing the dual scale analysis, it allows the linear stage to be evaluated for accuracy and repeatability for both large and small scale movements. In this work, the two Dial Gauges utilised were the Mahr MarCator 810SW and the Mitutoyo 513-405E for the long and short range analyses respectively. Details of the analysis are outline in Table 6 and Table 7.

Table 6: Analysis of large scale movements using Mahr 810SW dial gauge

Axis	Analysis Nominal Range (mm)	Gauge Measurement Range (mm)	Measurement Point Spacing (mm) (p)
X-axis	5	10	0.5
Y-axis	5	10	0.5
Z-axis	0.5	10	0.05

Table 7: Analysis of small scale movements using Mitutoyo 513-405E dial gauge

Axis	Analysis Nominal Range (mm)	Gauge Measurement Range (mm)	Measurement Point Spacing (mm) (p)
X-axis	0.2	0.2	0.02
Y-axis	0.2	0.2	0.02
Z-axis	0.2	0.2	0.02

Measurement performed for with the Mahr Dial Gauge were recorded to the nearest 0.01mm, as this was the resolution of the dial. For measurements performed with the Mitutoyo Dial gauge, measurements were recorded to the nearest 0.001mm. Specification sheet for both devices are available in Appendix C. The measurement setup for the axes is shown in Figure 21. In both cases, the gauges were carefully aligned perpendicular to the stage motion using an engineer's square tool in order to minimise the influence of cosine error on the measurement.

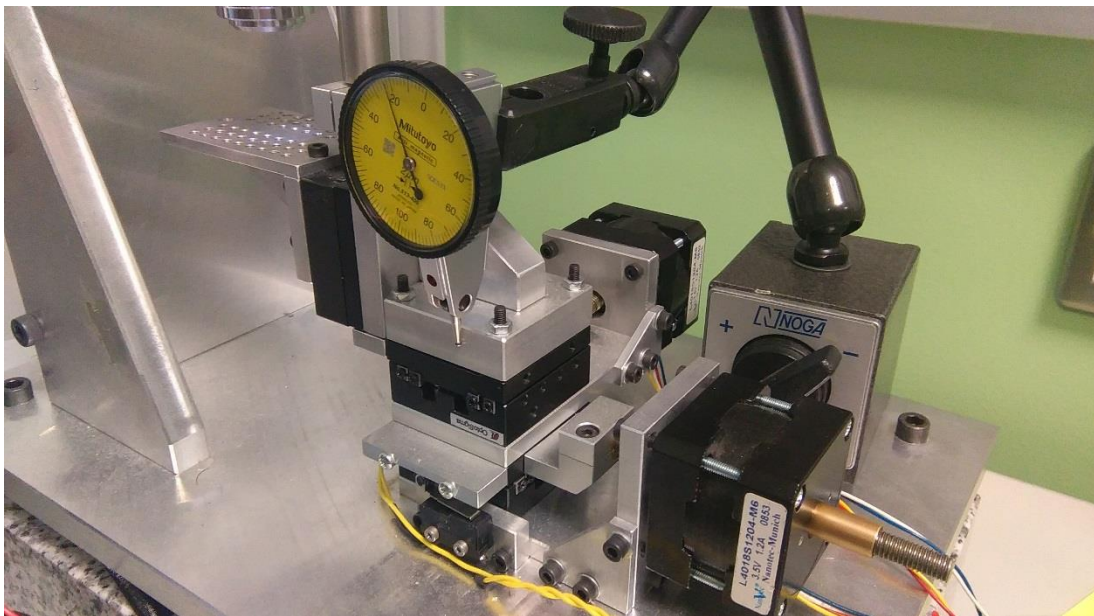


Figure 21: Mitutoyo 513-405E Dial Gauge when performing point to point measurements on the X-axis of the 3D Optical Profilometer.

In accordance with recommendations of ISO 230-2, the target positions for the point-to-point measurement evaluation were chosen according to (1), where p is the nominal

measurement interval, and r is the random variation from that position. The random position was listed as a percentage of the target position P with values as listed in Table 8. This ensured the proper sampling of any periodic errors in the system.

Table 8: Position variation from the nominal point-to-point interval.

Target Positions (i)	1	2	3	4	5	6	7	8	9	10
Random Position Variation % (r)	-5	9	2	-12	10	-4	-12	-7	10	2

In order to proceed with a repeatable experimental procedure, and to comply with ISO 230-2, the point-to-point sequence as shown in Figure 22 was followed. Starting at the top left of the figure, the stage movements move from the initial position to the first target position, P_1 . Subsequent movements are then made the remaining points in the cycle. It is important to note that while make the 3 individual cycles, the measurement setup is not reset to a zero position. This procedure then ensures that any cumulative errors are sampled across the three cycles.

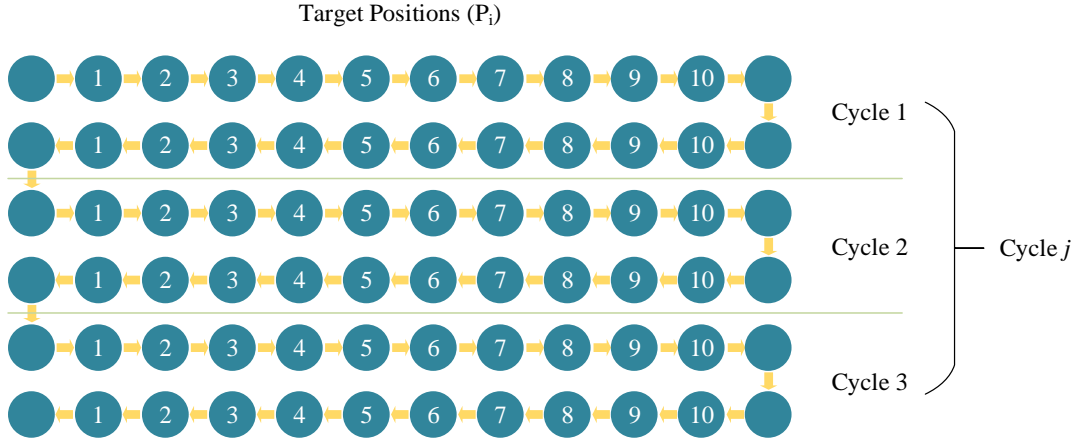


Figure 22: The measurement procedure was performed according to the following sequence.

The actual target positions used in the analysis for each axis are shown in Table 9 and Table 10 for the large movement and small movement analyses respectively. In Table 10 the values for the X and Y target positions have been rounded to the nearest 5 μm , and that is the theoretical minimum resolution of the stepper motor driven stages. The Z-axis has a smaller travel range than the X and Y axes, hence a smaller range of motion is investigated for the Large Movement analysis, as shown in Table 9.

Table 9: Target positions for Large Movement analysis. All positions in millimetres.

Axis		P ₁	P ₂	P ₃	P ₄	P ₅	P ₆	P ₇	P ₈	P ₉	P ₁₀	END
X	0	0.48	1.09	1.53	1.76	2.75	2.88	3.08	3.72	4.95	5.10	5.5
Y	0	0.48	1.09	1.53	1.76	2.75	2.88	3.08	3.72	4.95	5.10	5.5
Z	0	0.05	0.11	0.15	0.18	0.28	0.29	0.31	0.37	0.50	0.51	0.55

Table 10: Target positions for Small Movement analysis. All positions in millimetres.

Axis		P ₁	P ₂	P ₃	P ₄	P ₅	P ₆	P ₇	P ₈	P ₉	P ₁₀	END
X	0	0.020	0.045	0.060	0.070	0.110	0.115	0.125	0.150	0.200	0.205	0.25
Y	0	0.020	0.045	0.060	0.070	0.110	0.115	0.125	0.150	0.200	0.205	0.25
Z	0	0.019	0.044	0.061	0.070	0.110	0.115	0.123	0.149	0.198	0.204	0.22

3.3.3 Potential sources of measurement uncertainty

In evaluating the stage positioning the potential sources of measurement error must be considered. There are five main sources of error that must be considered in this work.

Gauge accuracy

The stage position measurements are limited by the resolution of the dial gauge. The limiting factor in term of accuracy is the accuracy of the gauge over its full length of travel. In the case of the Mitutoyo 513-405E, the measurement uncertainty is 3 μm over the range of travel, while the Mahr 810SW has an uncertainty of 17 μm over 10 mm of travel.

Cosine error

Cosine error occurs when the axis of a measurement instrument becomes misaligned with the axis of motion [109]. For an angular misalignment of 10° , a measurement compensation factor of 0.98 must be applied to the measurement result (as $\cos(10) = 0.98$). For example, over a 0.2 mm measurement, a 10° misalignment would mean the total measurement deviation due to cosine effects would be 4 μm . However, over a 5

mm range, the cosine error would be in excess of 0.1mm, which is significant. In this work the gauges were set up using an engineer's square tool to minimise the cosine effect.

Abbe error

Abbe error occurs when the measurement plane of a sample changes its angular attitude as it traverses an axis [109]. This type of error can be caused by inherent wobble in a motion stage, which is caused by the stage not being perfectly straight or flat. This in turn causes the stage to pitch and roll, an effect that can be greatly exaggerated if the sample being moved is far from the motion stage. To evaluate the type of error complex optical interferometry equipment is required. In order to minimise the influence of Abbe error in this work, the gauges were placed as close as practically possible to the normal position of an artefact during measurement.

Thermal effects

Thermal effects cause materials to expand and contract, which can affect not only the device being measured, but also the measurement gauge itself. The dial gauges are calibrated for use at 20°C according to the manufacturers specifications. No temperature controlled environment was available for use during this work, however the stage position measurements were recorded in quick succession (within 1 hour for each stage) in order to minimise any thermal effects. For example, the thermal expansion of an aluminium stage would be on the order of 25 $\mu\text{m}/\text{m.K}$, which for a stage 50 mm in length equates to a change in length of 1.25 μm per Kelvin.

Vibration effects

Vibration from external sources can cause measurement variations, and can cause particular issues when performing dynamic position measurements (i.e. where the stage is measured while in motion). In this work, the designed profilometer was rigidly mounted to a granite base to lower the centre-of-gravity of the system and to reduce vibration effects. During the measurement, the stage was allowed to come to a complete stop at each measurement point with a dwell time of 5 seconds. There were no visible effects of vibration influencing dial gauge readings as each measurement was recorded.

3.4 Verification of 3D measurement performance

In order to assess the 3D measurement performance of the 3D profilometer, it was necessary to utilise a 3D measurement artefact. However, the majority of commercially available 3D measurement standards that are calibrated accurate to the 1 micrometre range are specifically designed for either for Atomic Force Microscopes (AFM) or White Light Interferometers (WLI). The key issue around this lies in the fact that these standards are normally made from flat polished materials, such as silicon wafers [110]. While these extremely flat polished surfaces work well in the calibration of AFM and WLI systems, they are not ideally suited to optical microscopy, as imaging using this technique depends entirely on the ability to form a high-contrast image of an object. A surface with a minimum average roughness of 15 nm and a spatial period of 2 μm are required in order for the sample to be measurable using standard brightfield microscopy [80]. Little work has been performed in the area of the calibration of 3D profilometers utilising the depth-from-focus measurement technique that is in line with international ISO standards. Sun and Claverley utilised high grade tungsten carbide spheres in the range of 1.5mm to 3mm, with the aim of being able to acquire reliable calibration and verification measurement data within one field-of-view of the commercial measurement system [111]. This approach utilised the ISO 10360-8:2013 standard, which was specifically designed for the calibration of micro-co-ordinate measurement machines. The conclusion of the work was that different sampling patterns across the field-of-view resulted in different levels of measurement error, which measurement errors of up to 20 micrometres found when utilising a 50x microscope objective.

In order to test the step-height measurement performance of the 3D optical profilometer, a purpose machined measurement artefact was manufactured. This block was manufactured from brass material utilising a 0.75mm end mill tool as shown in Figure 23.

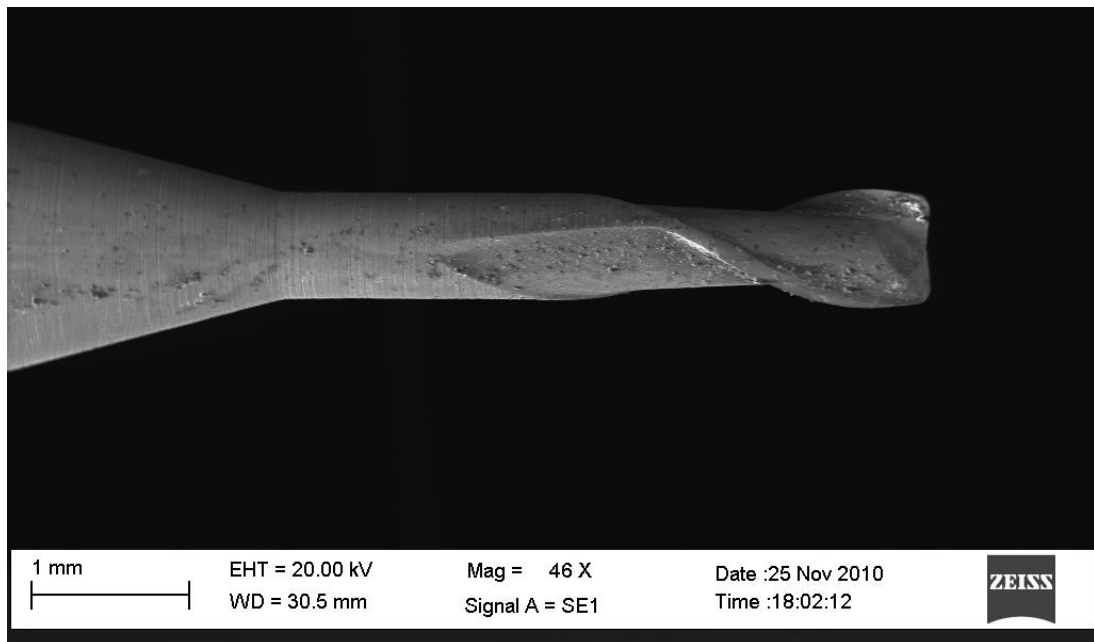


Figure 23: SEM image of a 0.75 mm milling tool utilised for manufacturing the measurement artefact.

The brass block was machined to leave long regular columns protruding at the top surface. Each column was 160 micrometres in width and 100 micrometres in step height, subject to general machining tolerances. An oblique image of the measurement artefact is presented in Figure 24.

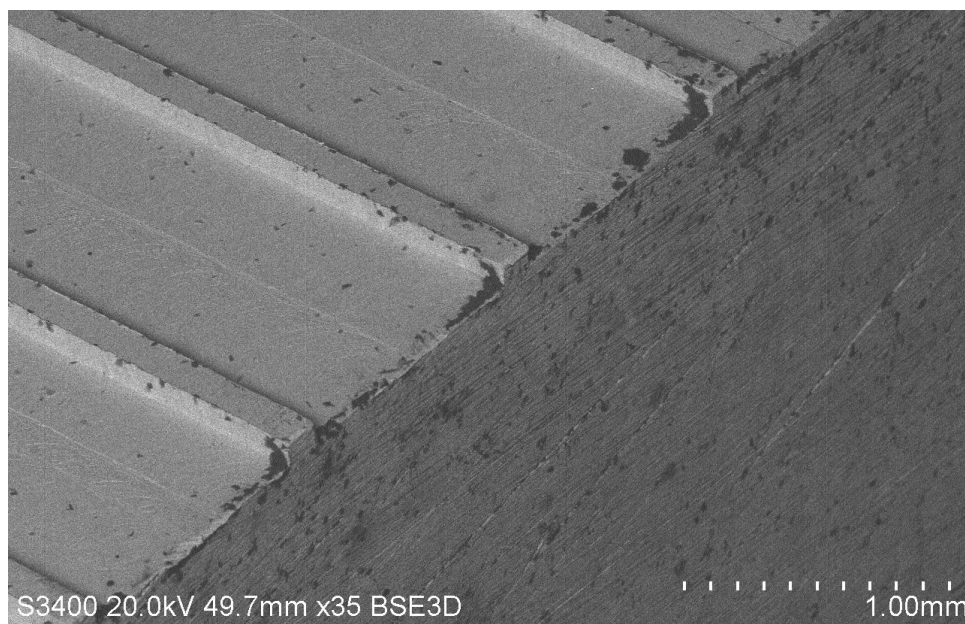


Figure 24 - Wide field Backscatter Electron SEM image of machined brass sample

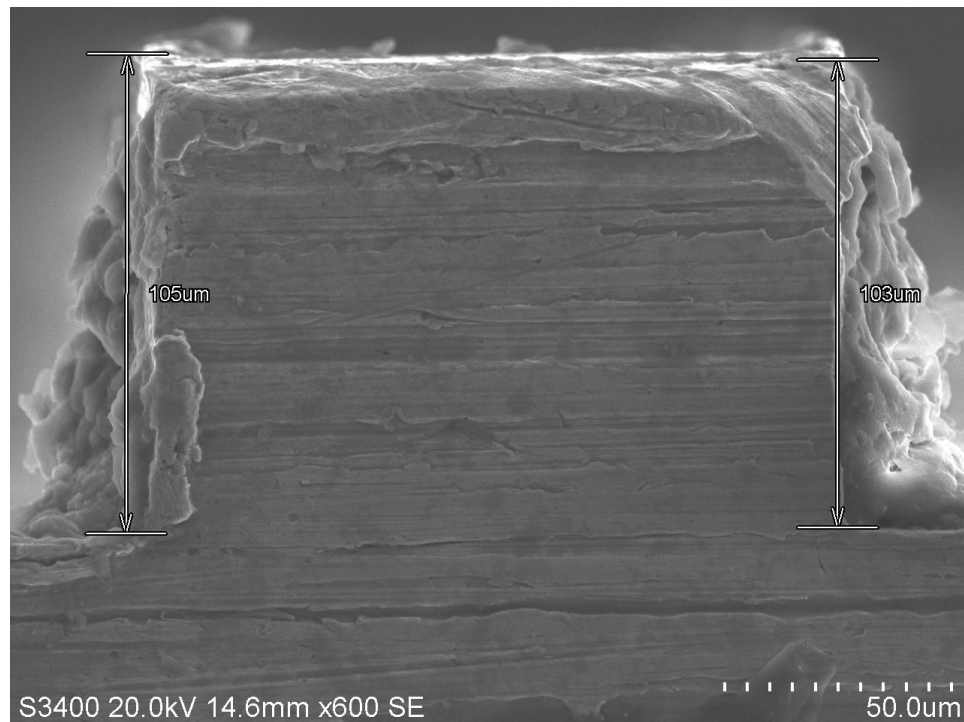


Figure 25 - Secondary Electron SEM image of end face of a pillar on the machined brass sample. Machining debris is visible at the end face of the measurement artefact.

In order to initially verify the dimensions of the columns, an SEM view of the end face of the measurement artefact was obtained, as shown in Figure 25. The step height of the sample was measured to be between 103 micrometres and 105 micrometres for all columns. While this measurement acts as a good verification check, it cannot be utilised for the purposes of measuring and calibrating the sample over an area. In order to validate the brass artefact, it was necessary to take measurements of the same sample utilising other measurement equipment that had been adjusted using other certified calibrated reference artefacts. It must be mentioned that to produce a certified calibrated artefact requires a significant amount of investment, and was outside the main scope of this work. The main aim of this work was to verify that the performance of the developed measurement system was in an expected range in order to show that the measurement technique could be used for micrometre scale measurement of optically rough transparent superstrates. For this level of verification, it was acceptable to utilise other available laboratory measurement systems in order to gain an initial understanding of the capabilities of the developed optical profilometry device,

however for the evaluation of the absolute measurement accuracy of the system significantly more investigation and statistical analysis of the artefact would be required. In this instance, the verification equipment consisted of a Bruker DEKTAK V200Si Stylus Profilometer, and a Veeco WYKO NT1100 White Light Interferometer, with both instruments are sensitive well into the sub-100nm measurement range. In an effort to maintain measurement consistency, all measurements taken in this analysis were taken at the same point on the measurement artefact, the location of which was marked on the sample. The measurement taken with these White Light Interferometer is shown in Figure 26 and Figure 27.

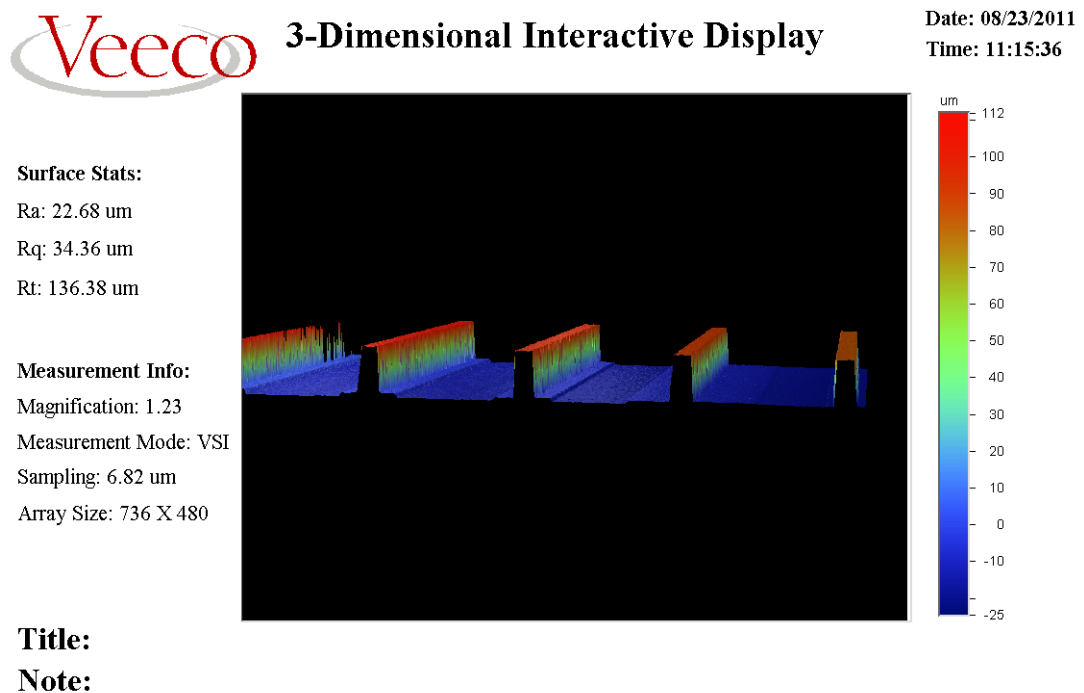
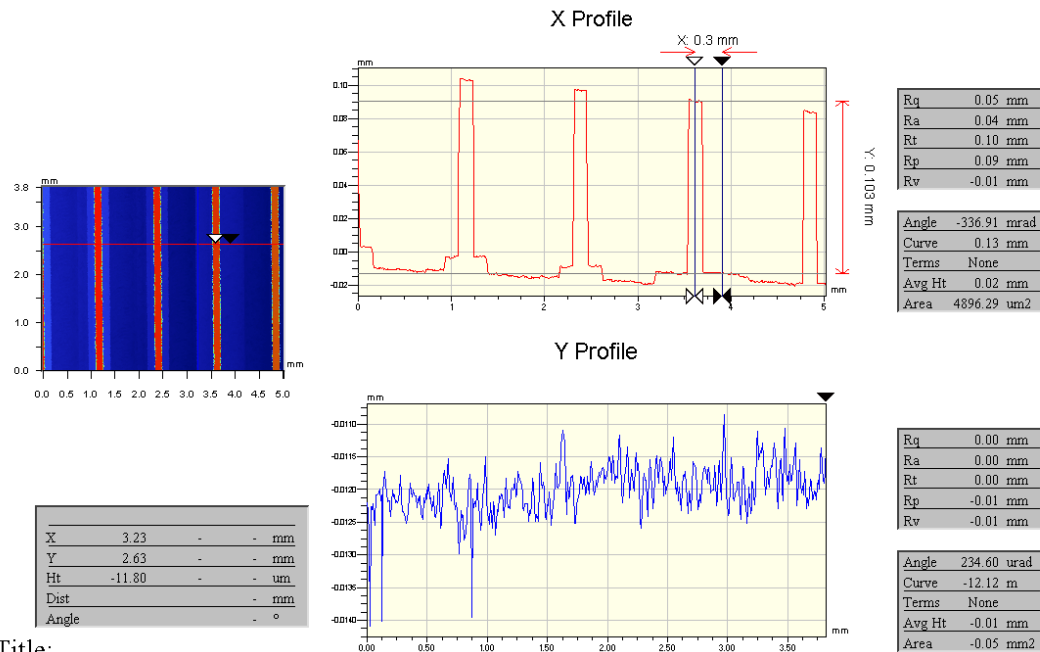


Figure 26 - 3D surface measurement of the machined brass sample using a Wyko NT1100 white light interferometer



Title:

Note:

Figure 27 - Cross sectional Wyko NT1100 measurement data of machined brass sample. Step height is measured as 103μm.

The measurement data shown in Figure 27 indicates the step height at the desired measurement location to be 103μm. The step height measurement taken at the desired measurement location using the stylus profilometer is shown in 3D in Figure 28 and a 2D cross-section is shown in Figure 29. It can clearly be seen in these Figures that the edge definition of the brass artefact column is lost when measuring with the stylus profilometer, as might be expected. Overall, there was a very close correlation between the results from the SEM, WLI, and stylus profilometer in measuring the step height of the brass artefact, especially considering the preliminary nature of this investigation. The results output from the measurement instruments are presented in Table 11.

Table 11: Measurement results of brass sample step height taken by the various instruments

Instrument	SEM	WLI	Stylus
Result in μm	104	103	102

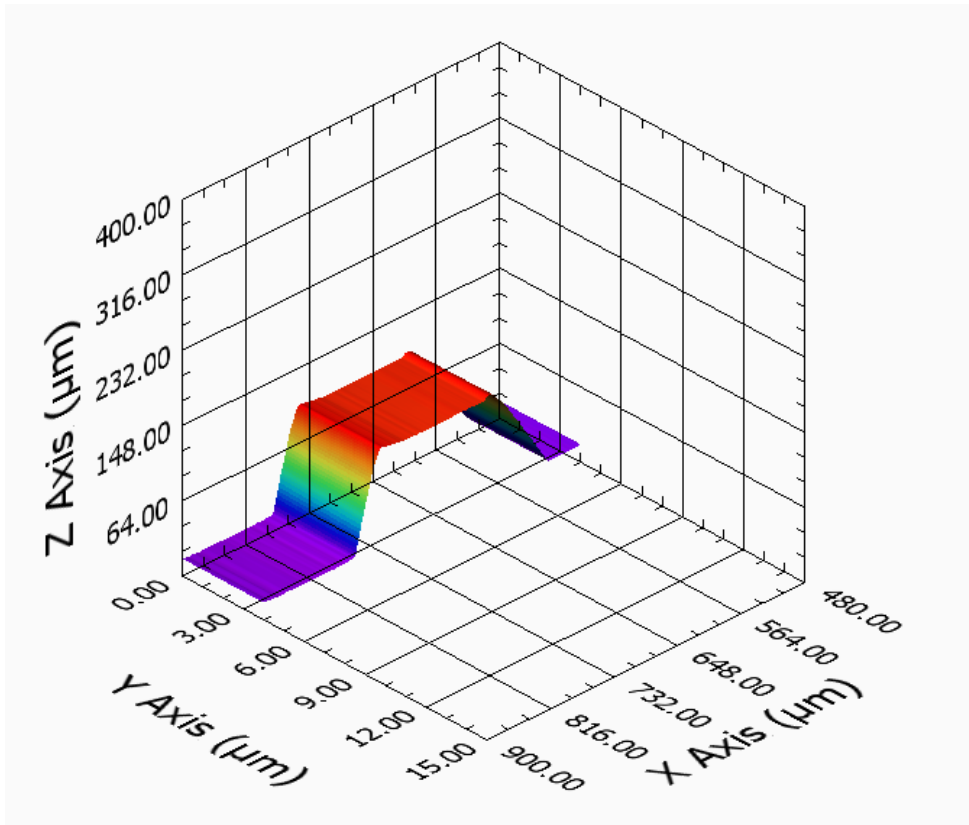


Figure 28 - 3D surface profile of the machined brass sample using a DEKTAK V200Si Stylus profilometer

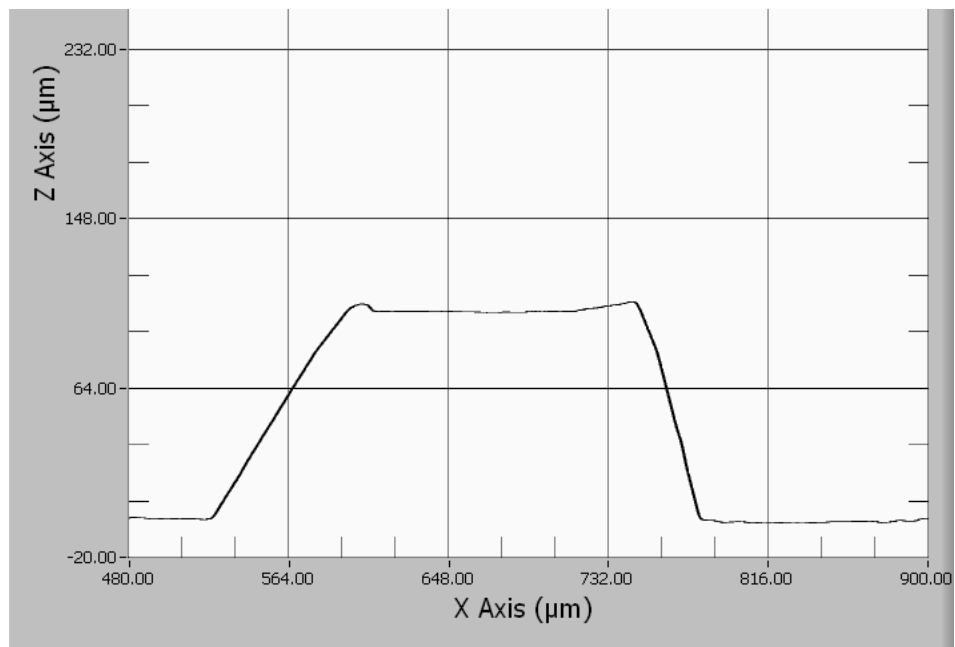


Figure 29 - Cross sectional profile of machined brass samples acquired using DEKTAK V200Si Stylus profilometer

3.4.1 Testing procedure of the 3D measurement performance of the Optical Profilometer

In order to evaluate the 3D measurement performance of the Optical Profilometer, a dual scale measurement approach was taken. A multifactorial Design of Experiments was utilised to evaluate the performance over measurement ranges of 103 μm and 512 μm respectively. For the 103 μm measurement, the purpose machined brass block described in section 3.4 was utilised. For the 512 μm measurement, a nominal 500 μm gauge block from a Mitutoyo Rectangular Gauge Block Set (as shown in Figure 30) was used. This gauge block was first verified by WLI, and the results of this are shown in Figure 31.

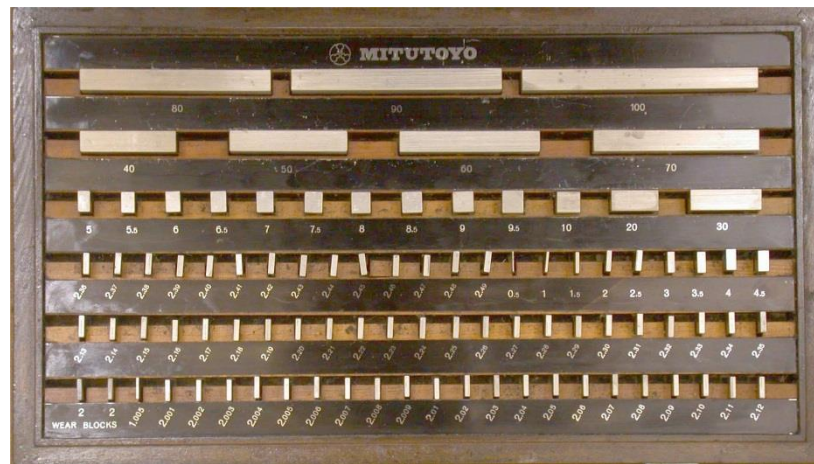
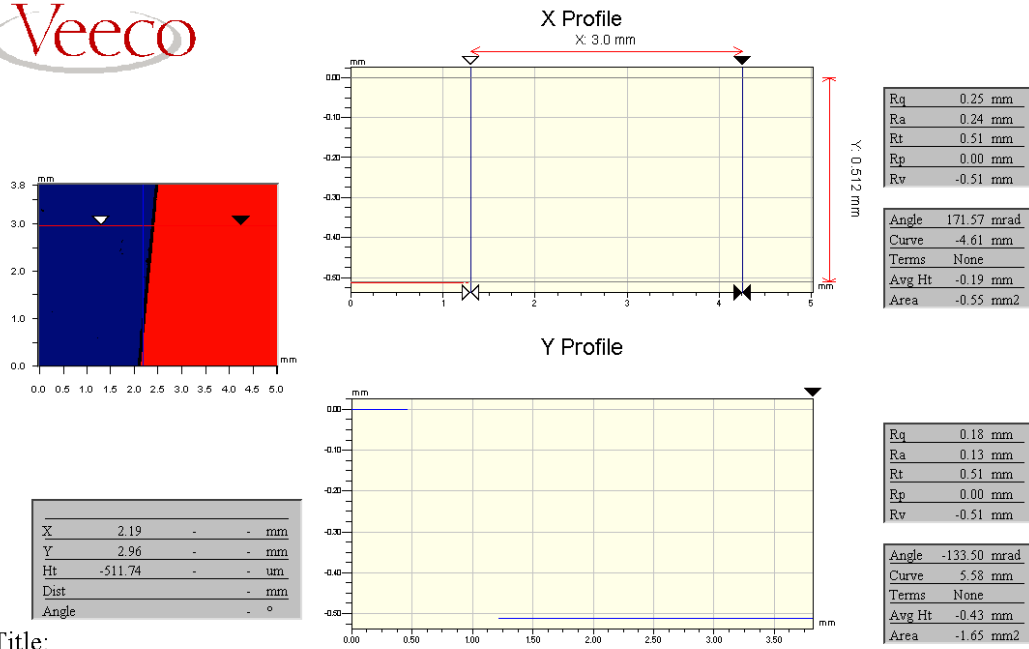


Figure 30: Mitutoyo Rectangular Gauge Block Set (Grade 1)



Title:

Note:

Figure 31: Step height of nominal 500µm Mitutoyo Rectangular Gauge Block. The WLI measurement verified the dimension of the block to be 512µm.

To evaluate the 3D measurement performance of the 3D Optical Profilometer, a testing procedure was designed in the absence of a formal ISO standard for the evaluation of this type of instrument. Accuracy and repeatability can be determined by direct comparison of measurement of a sample with a known dimension. However, as a certified calibrated artefact was not available, this became a challenging aspect. By utilising the purpose machined brass artefact and the Mitutoyo gauge block as the step-height references it is only possible to verify the estimated accuracy of the system as the absolute accuracy of the artefacts is not certified or traceable. The estimated accuracy is sufficient for an initial evaluation of the system, but for absolute accuracy verification further work would be required. The accuracy is evaluated by taking nominal step height to be the average of the three measurements, as detailed in Table 11. While this approach does not give absolute accuracy information, it is designed to give some credibility to the investigation in measuring at this scale. The repeatability of the measurements is an aspect that can be evaluated, as this doesn't depend on the absolute accuracy of the artefact. Having a repeatable measurement can be considered more important, as the accuracy of the system can easily be improved at a later date providing the system is repeatable.

To evaluate the 3D measurement performance of the system the following procedure was formulated. Firstly, the most important measurement parameters had to be calculated. In this instance, the most important controllable measurement parameter was sampling height on the Z-axis. As outlined in section 3.1.4, the profilometer system operates by recording a series of images along the optical axis of the instrument, which is parallel with the Z-axis. Hence, by controlling the physical distance between each image recorded in that sequence, it is possible to evaluate the 3D measurement accuracy as a function of sampling interval. This correlation is of interest from a practical point of view, as it is vital to know the limitations of such a measurement device. By having larger sampling intervals, it is equally possible to increase the speed of acquisition and measurement, as less images would need to be recorded over a given measurement height and less images would need to be post-processed to produce the results. The sampling intervals explored in this investigation are outlined in Table 12. Each measurement was taken at a similar location along the Z-axis in order to maintain consistency between the measurements. Also, all measurements were taken at the same locations on the sample. Five repetitions of measurements with the same sampling interval were also performed to assess the repeatability of the measurements. Each measurement in Table 12 was performed 6 times in a row, which also gives some data around the short-term repeatability of a measurement.

Table 12: Design of Experiments with specified sampling intervals

Run	Reference step height (μm)	Sampling Interval (μm)
1	512	0.6
2	512	1
3	103	0.6
4	103	0.6
5	103	0.6
6	103	0.2
7	103	1
8	512	0.2
9	103	0.6
10	103	0.6

In order to remove extraneous noise from the results, for example, due to areas with steep flanks, the resulting height maps were post processed to remove unwanted noise. An example of this is seen in Figure 32, which is a measurement of the brass measurement artefact recorded with the developed system. The areas shown as white in Figure 32 (d) are removed from the results, as the aim in this work is to evaluate the step-height via the upper and lower plane locations only. This is a similar approach to that used by Sun and Claverley, as 95% of measurement points are selected for evaluation with the removal of outliers [111]. The procedure for fitting planes to the data involved the selection of the upper and lower planes in the height map, calculating the average height of the plane, and then subtracting Lower Plane Height from the Upper Plane Height. The data for these calculations are available in Appendix G. The accuracy is then calculated based on how close the average step height measurement is to those of the estimated artefacts, while the standard deviation of the measurements provides data about the repeatability of the measurements.

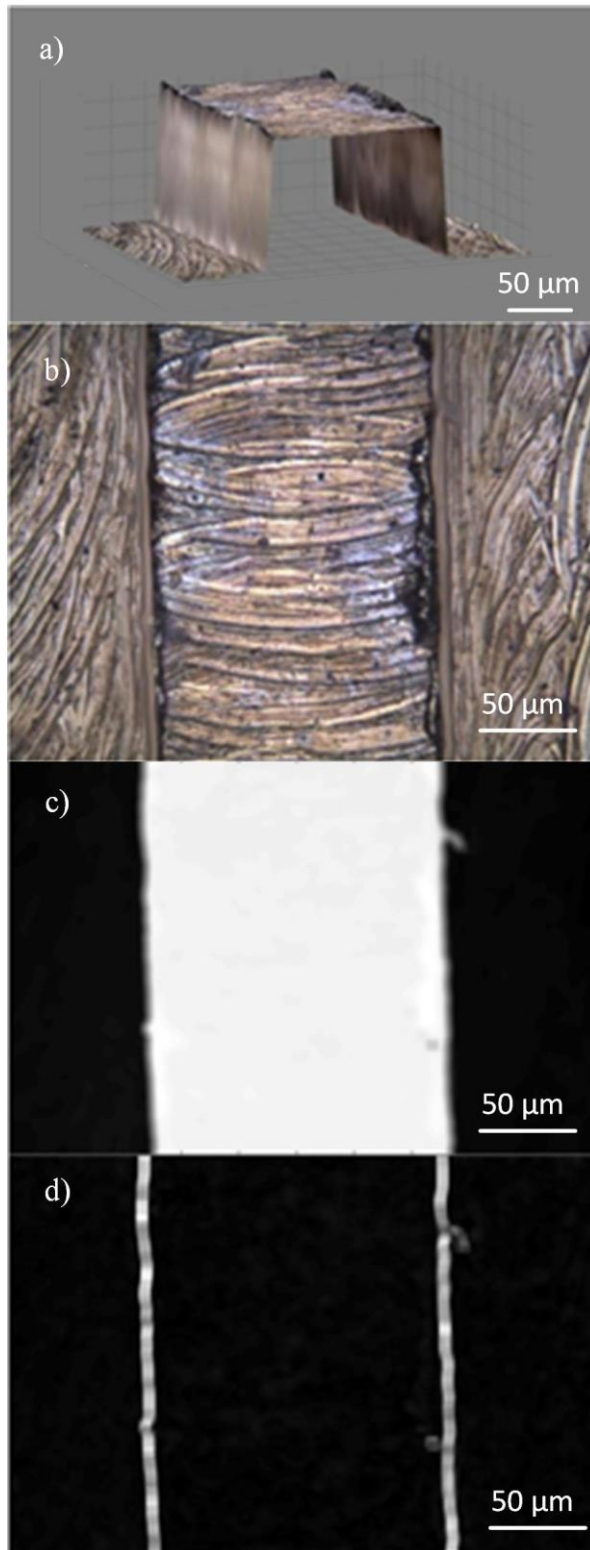


Figure 32: a) 3D view of measurement, b) Fully focused image from a step height measurement, c) the height map from this measurement, d) the areas of high un-repeatability and noise due to steep flanks.

3.4.2 Potential sources of measurement uncertainty in the 3D measurement

There are several potential sources of measurement uncertainty when considering the 3D measurement of surfaces. The following is not an exhaustive list of potential sources, but are considered to be the most significant in this investigation.

Z-axis accuracy

As the vertical position of any point on the surface to be measured is correlated to the on-axis position of the Z-axis, the accuracy of the Z-axis is critical to the overall accuracy of the measurement system. In this work the Z-axis accuracy is evaluated of small measurement distances to gain an understanding of the how the Z-axis influence the overall 3D measurement performance of the system.

Principal optical aberrations

There aberrations include spherical, comatic, chromatic, astigmatism, field curvature, and distortion. The influence of these aberrations on the measurement can be greatly reduced by using high-quality optics. The Nikon CFI60 LU Plan objective utilised in the developed system is well corrected for chromatic, spherical, and field curative aberrations. More details on these types of aberrations can be found in literature [80, 112].

Spatial resolution

The minimum resolvable distance between two point sources is known as the Rayleigh criterion [80]. In the developed profilometer, the optical resolution of the objective lens is the limiting factor for spatial resolution, which is 0.5 μm using the 50x Nikon objective with a numerical aperture of 0.55. The limiting of the spatial resolution determines the limit of the spatial roughness frequencies that can be resolved by such an optical system.

3.5 CO₂ Laser System hardware and specifications

The laser chosen for the texturisation of the glass surface was a Rofin DC-015 CO₂ laser operating at 10.6 μm wavelength. This laser was chosen as it operates in the infra-red (IR) spectrum, which is absorbed well by the fused quartz glass. As this wavelength is also well absorbed by carbon based materials these lasers are well suited to cutting polymers and other organic materials such as wood [39]. These lasers are also available with high continuous powers (up to several kW) making them ideal for the gas-assisted cutting of thick materials and metals. This particular model laser also offers operation in pulsed and continuous wave modes, allowing for fine process tuning and control. According to the supplier specifications, the laser power stability to $\pm 5\%$ over the operating range of the laser, which may be attributed to the fact the laser cavity and active medium is diffusion cooled through the use of water cooled electrodes, allowing for better output stabilities due to more consistent temperatures [113]. This laser was integrated onto a CNC motion control system built by Mectronic Systems Ltd. and is capable of machining 2D profiles from materials at velocities up to 1m/min.

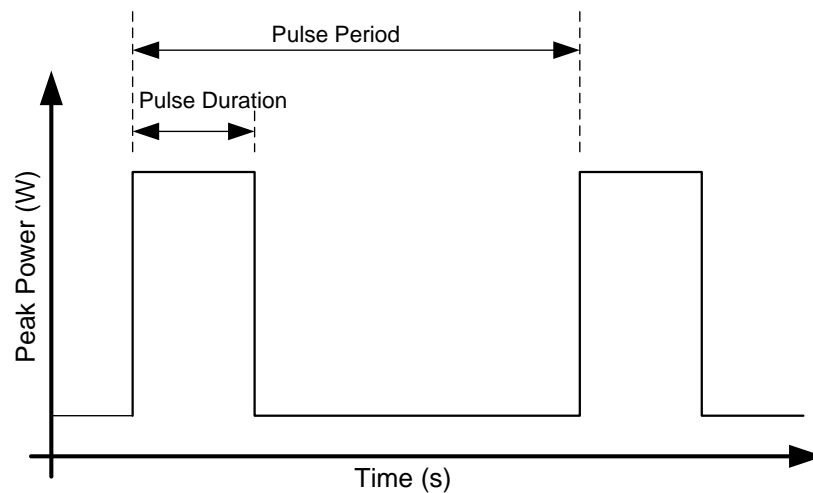


Figure 33. Graphic illustration of pulse period, duration and peak power within pulse width.

In order to control the output power of the laser, a modulation signal is fed from the CNC controller to the laser, the duty cycle of which is proportional to the instantaneous speed of the motion axes. This allows for greater control of the laser machining process during period where the motion axes undergo acceleration.

The percentage duty cycle was calculated as follows using (2).

$$Duty\ Cycle\ \% = \frac{Pulse\ Duration}{Pulse\ Period} \times 100 \quad (2)$$

Table 13. Laser parameters held constant during the experiments

Parameter	Value
Peak power	375 W
Assist gas and pressure	Argon at 1.5 bar
Nozzle standoff	5 mm
Focal position	On the top surface
Focal length of lens	127 mm
Beam diameter at focal point	Approx. 200 μm at $1/e^2$

3.6 Glass materials selection for solar cells superstrates

Following the consideration of the material characteristics required for this investigation, the decision was made to proceed with fused quartz material for the solar cell superstrates. This material provides favourable thermal shock characteristics and very good transmission properties across the UV-VIS-IR spectrum. The material was supplied by Multi-Lab Ltd. (Newcastle-upon-Tyne, UK), and was ordered in dimensions of 25 mm by 25 mm squares with thicknesses of 1 mm and 2 mm. The datasheet including properties and transmission spectrum for this material is available in Appendix E.

3.7 Design of Experiments

To carry out an analysis of the effects of laser processing parameters on the parasitic absorption of light (losses) in laser processed glass a Design of Experiments (DOE) was implemented. Through a process of parameter screening, it was observed that the

most influential process parameters were laser irradiance (W/mm^2), pulse repetition frequency (Hz), and traverse scanning speed (mm/s). A 3^3 central composite factorial design of experiments was then planned using levels determined during the screening process (Figure 34). The average power of the laser, and thus the irradiance of the beam, was altered by holding the peak power of the laser constant and adjusting the duty cycle of the pulses.

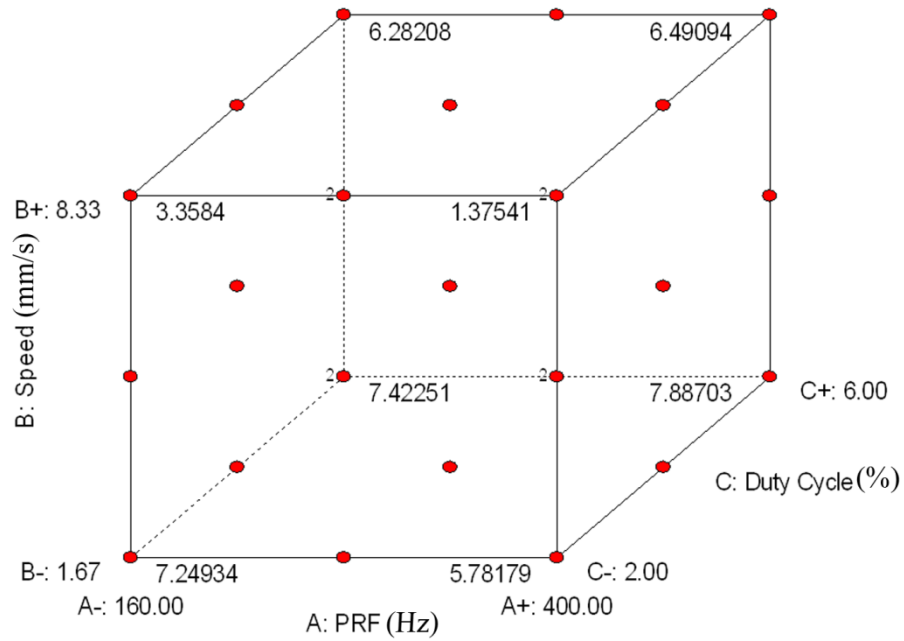


Figure 34. Central Composite Design of Experiments

Table 14. Laser process parameters used for DOE

	Duty Cycle (%)	PRF (Hz)	Speed (mm/s)
Level 1	2	160	1.67
Level 2	4	280	5.00
Level 3	6	400	8.33

The processes used for each sample in the DOE are presented in Table 15. These parameters represent the combination of all the parameters listed in Table 14 that were used on each particular sample with made of the 3³ multifactorial DOE. The column labelled Average Power (W) is a calculated parameter from the Duty Cycle % value listed and the Laser Peak Power setting defined in Table 13.

Table 15: Laser micromachining parameters for each sample produced in the DOE.

Channel #	Duty Cycle (%)	Average Power (W)	PRF (Hz)	Speed (mm/s)
1	2.00%	7.5	160	1.67
2	2.00%	7.5	276	1.67
3	2.00%	7.5	400	1.67
4	4.00%	15	160	1.67
5	4.00%	15	276	1.67
6	4.00%	15	400	1.67
7	6.00%	22.5	160	1.67
8	6.00%	22.5	276	1.67
9	6.00%	22.5	400	1.67
10	2.00%	7.5	160	5.00
11	2.00%	7.5	276	5.00
12	2.00%	7.5	400	5.00
13	4.00%	15	160	5.00
14	4.00%	15	276	5.00
15	4.00%	15	400	5.00
16	6.00%	22.5	160	5.00
17	6.00%	22.5	276	5.00
18	6.00%	22.5	400	5.00
19	2.00%	7.5	160	8.33
20	2.00%	7.5	276	8.33
21	2.00%	7.5	400	8.33
22	4.00%	15	160	8.33
23	4.00%	15	276	8.33
24	4.00%	15	400	8.33
25	6.00%	22.5	160	8.33
26	6.00%	22.5	276	8.33
27	6.00%	22.5	400	8.33

3.8 ANOVA Analysis

During the creation of the Response Surface Model (RSM) an Analysis of Variance (ANOVA) was also carried out to determine how well the model data fitted to the actual process values, and a description of the Response Surface Methodology can be found in Appendix B. This statistical analysis was performed using Design Expert V8.0. In order to evaluate the experimental data, a quadratic model was fitted to the data points in the design space shown in Figure 34. This allowed for the analysis of the linear interactions and quadratic effect of each of the parameters used in the Design of Experiments. The fitted quadratic model was represented by the following form as shown in (3).

$$\sqrt{\% \text{ Absorp.}} = b_0 + b_1x_1 + b_2x_2 + b_3x_3 + b_4x_1x_2 + b_5x_1x_3 + b_6x_2x_3 + b_7x_1^2 + b_8x_2^2 + b_9x_3^2 \quad (3)$$

where x_1 represents the Pulse Repetition Frequency (Hz), x_2 represents the Traverse Speed (mm/s), and x_3 represents the Duty Cycle (%).

3.9 Etching of processed glass with Hydrofluoric Acid (HF)

In order to further reduce the amount of parasitic light absorption in the laser textured glass, it was necessary to post-process the surface using a chemical etching technique. Hydrofluoric acid is widely used in electronics for the removal of SiO₂. In order to assess the effect of the chemical etching on the surface, 9 samples of the 27 (numbers 19-27) were immersed in HF (40%) for a period of 5 minutes. Following etching they were rinsed for 3 periods of 5 minutes in de-ionised water. The integrating sphere setup described in section 3.10 was then used to measure any change in the light absorption characteristics of the textured glass due to acid etching.

3.10 Integrating sphere setup for reflection / absorption / transmission measurements

In order to measure the effect of the laser processing on light absorption in the fused quartz glass, an integrating sphere with spectrometer setup was designed. Integrating spheres have the ability to collect diffuse and specular reflections and transmissions from samples when irradiated with light [114]. As these specialised spheres are coated with highly reflective diffuse coatings, it is possible to average any transmission or reflection over the whole sphere. This makes it possible to obtain an accurate average of any transmitted or reflected light, regardless of directionality of the light rays. The integrating sphere (Labsphere model 4P-GPS-040-SF) used in this setup was 100 mm in diameter with three 25.4 mm diameter ports at 0°, 90° and north pole locations, and a 38 mm port at 180°. A baffle was located between the 90° and 180° ports to reduce measurement error due to light falling directly on the detector from the sample. To further improve the accuracy of the measurement a cosine corrector was utilised, which aids the elimination of any directionality from the measurement. The spectrometer (Ocean Optics model USB650-VIS-NIR Red Tide) had a spectral resolution of 1nm and a spectral measurement range from 360 nm to 1000 nm, however, due to weak UV illumination provided by a broadband light source a significant amount of noise could occur until approximately 420 nm. Data below this wavelength are not utilised.

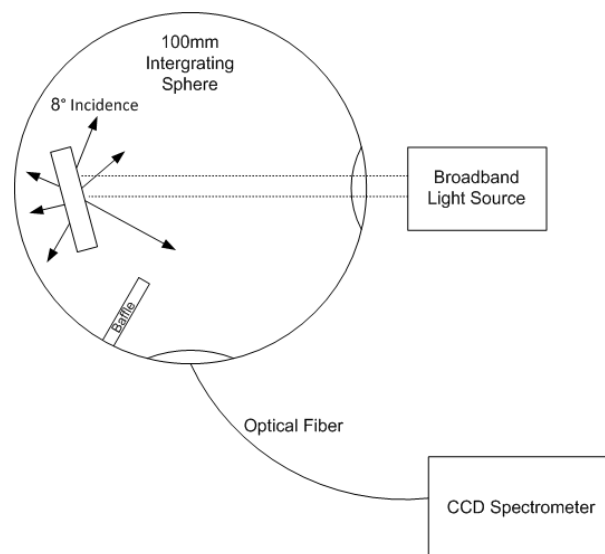


Figure 35. Integrating sphere setup for absorption measurements.

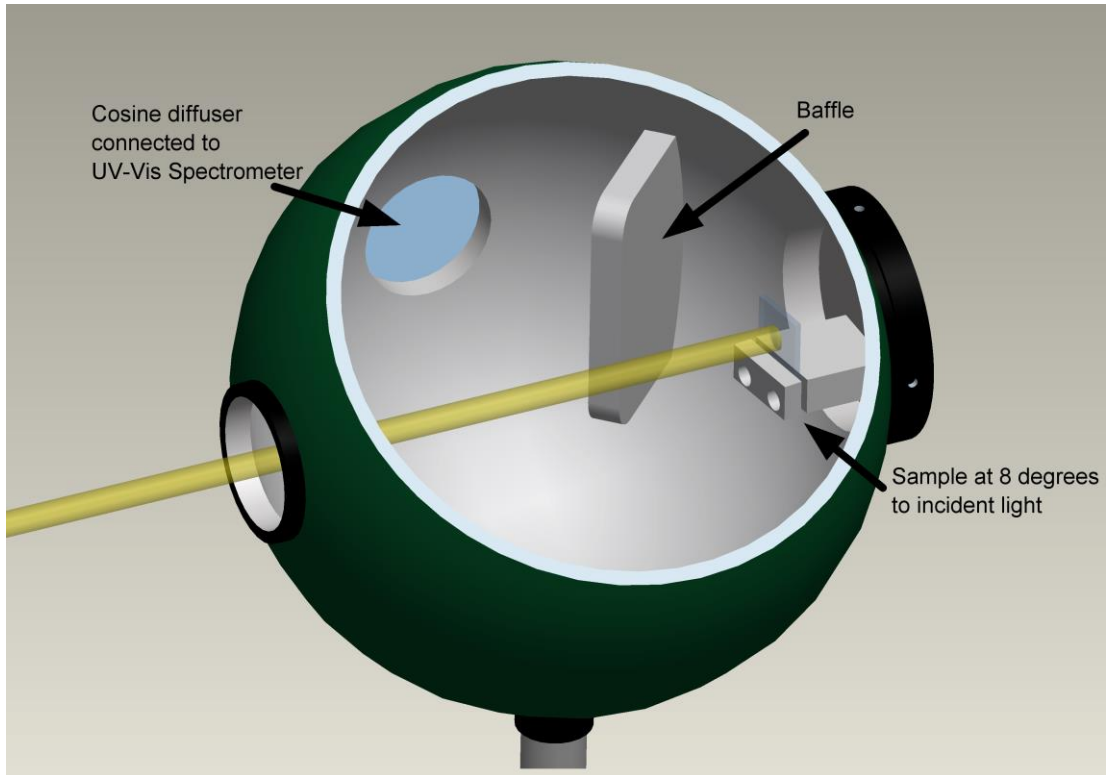


Figure 36. Cut-away view of the integrating sphere setup

To accurately measure the light absorption in the laser processed fused quartz, the samples were held inside the closed sphere with the illumination source incident at 8° . This allowed all the scattered light to be collected including transmitted and reflected, diffuse and specular. By measuring the amount of light collected in comparison to that of a reference measurement with clear unprocessed fused quartz, the absorption could be calculated using the following equation (4).

$$Absorption = 1 - (T + R) \quad (4)$$

where T is the transmitted light and R is the reflected light.

3.11 Correcting absorption data to AM1.5G solar irradiance spectrum

In order to evaluate the absorption in the glass for solar cell applications the measured absorption values were transposed with solar spectral energy distribution data. The measured data was corrected using spectral data from the AM1.5G standard using the following method.

1. The measured data had a spectral range from 420nm to 1000nm, however the irradiance data obtained spanned a larger spectrum from 280nm to 4000nm [14]. The data was presented as W/m²/nm and it was first necessary to convert the irradiance data to a percentage of the measurement spectrum using (5).

$$\% \text{ Spectral irradiance}_\lambda = \frac{I_\lambda}{I_T} \times 100 \quad (5)$$

where I_λ is the irradiance at a given wavelength, and I_T is the total solar irradiance between 420nm and 1000nm of the AM1.5G spectrum.

2. The data from the previous operation was then multiplied by the co-efficient of absorption found during the initial measurement, as shown in (6).

$$\% \text{ Absorption of AM1.5G spectrum} = \% \text{ Spectral irradiance}_\lambda \times \% \text{ Absorption}_\lambda \quad (6)$$

3.12 SEM and EDXS Analysis

A Zeiss EVO LS15 scanning electron microscope (SEM) was utilised to visualise the surface topographies of the laser processed samples. This device was also used to perform energy dispersive x-ray spectroscopy analyses on the processed surfaces using an INCA detection and analysis system supplied by Oxford Instruments. Ten random points were selected for compositional analysis of the sample surfaces. The EDXS parameters used to perform this analysis are shown in Table 16.

Table 16. EDXS compositional analysis parameters

Parameter	Value
Accelerating voltage	10kV
Probe Current	1nA
Working Distance	8.5mm
Magnification	x1000

3.13 Channel Dimensional Analysis

To assess the different dimensions of channels created by laser micromachining it was necessary view the cross section of the channels. This was achieved by laser cutting the material to reveal a cross-section of the channel, and then imaging of the cross-section by SEM as described in section 3.12. This approach proved effective in the analysis of the dimensions, as the cross-sections reveal that some of the machined channels have a large aspect ratio, making depth measurements difficult using other measurement methods. The cross-sections were performed in three random locations along the channel in order to achieve an average depth, taking into account variations that might occur in the depth due to the nature of the process.

Three measurement were recorded at each inspection locations, as shown in Figure 36 and Figure 38. The “Depth” was measured from the top surface of the material to the visible bottom of the channel cross-section. The “Width 50%” was recorded at 50% depth in the channel cross-section. In order to take repeatable measurements of the “Width Top” dimension, it was necessary to employ a procedure by which the location of the channel opening was placed. In this instance an imaginary reference line was drawn across the surface of the material, and the “Width Top” measurement locations were placed at the point where the channel opens up below the reference line, as is shown in Figure 38. All measurements were recorded to the nearest micrometre.

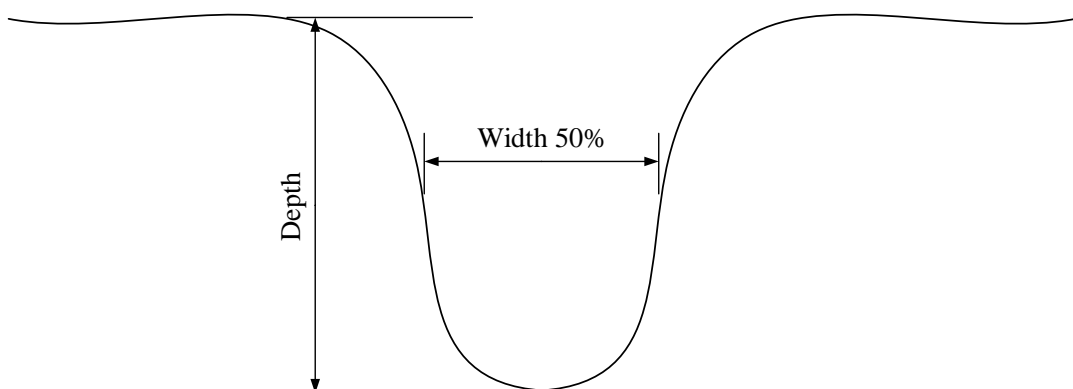


Figure 37: Diagram showing the SEM measurement locations on a cross sectional view of laser micro-machined channel.

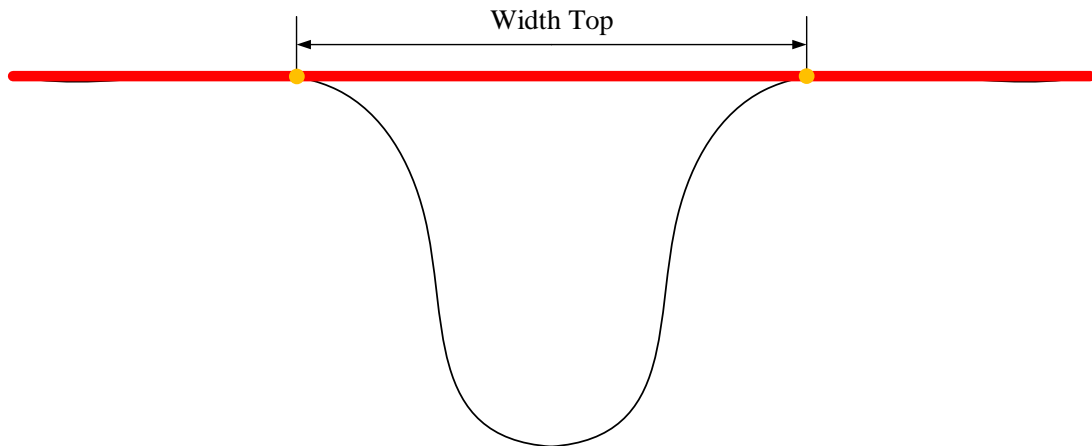


Figure 38: Diagram showing the SEM measurement locations for the measurement of the Width (top) parameter. Top surface is represented by red line, and measurement locations are shown in orange.

3.14 Solar cell selection and preparation

Commercially available solar cells (Evergreen Solar, String Ribbon™ wafers) were diced into eight by eight millimetre sections using a 355 nm nanosecond pulsed laser source (Blueacre Technology Ltd.). The front and rear contacts of the solar cells were soldered manually. To provide refractive index matching media in the void between the solar cell and the superstrate, the solar cells were encapsulated in an elastic transparent resin (ACC Silicones, QSil 215) and allowed to set at room temperature for 24 hours.

3.15 Measurements of I-V vs angle of incidence

The set-up for I-V curve measurement of the solar cell is shown in Figure 39 and Figure 40. This measurement was performed for samples 20, 21, and an untextured reference as superstrates at varying angles of incidence between a normal incidence angle (90°) and an incidence angle of 10° in increments of 10° . The textured glass superstrate and the encapsulated solar cell were held in contact using the device shown in Figure 40 whereby securing screws allowed for the application of sufficient pressure in order to eliminate air gaps at the glass/encapsulant interface. The photovoltaic measurements (I-V characteristic) of the solar cell in conjunction with different textured superstrates were carried out using a Newport Oriel solar simulator. The solar simulator was equipped with a 450W Xe lamp filtered to AM1.5G spectral conditions and an illumination area of 78 cm^2 . The light intensity was adjusted for using a NREL-

calibrated reference silicon cell. The data was recorded using an automated data acquisition system (Gamry PCL4 300 series) under $870\text{W}/\text{m}^2$ solar simulated irradiance and an externally applied bias potential. The backside of the cell was carefully shielded to avoid any influence of stray light.

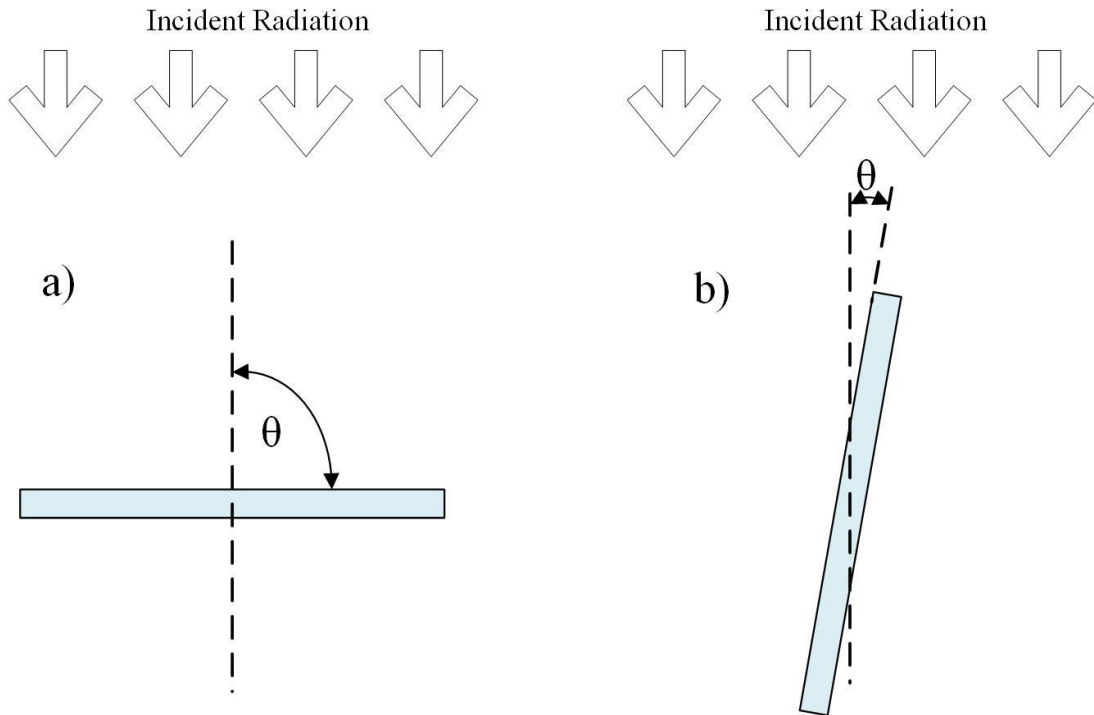


Figure 39. a) Angle of incidence of 90° , and b) angle of incidence of 10° .

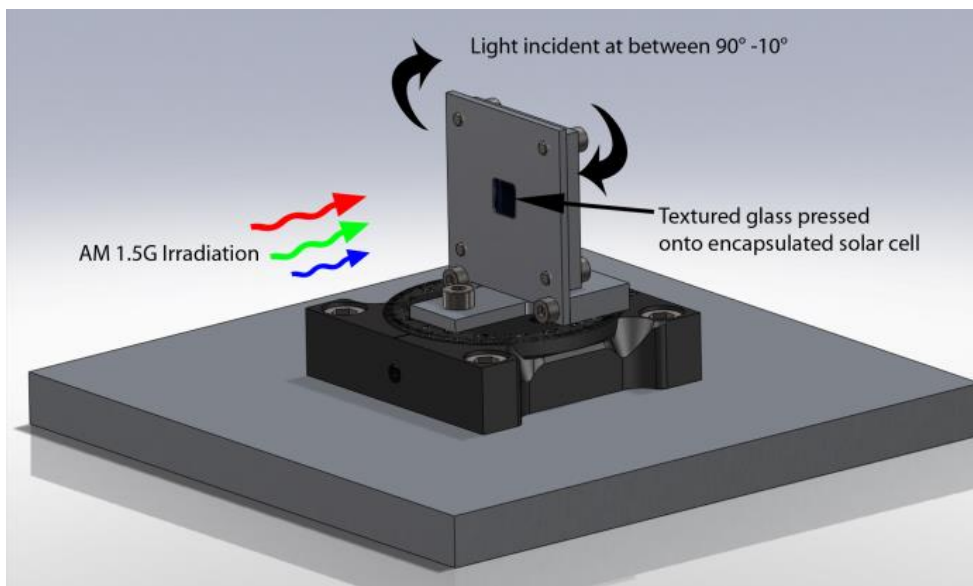


Figure 40. Mounting device constructed to hold textured superstrate and encapsulated solar cell in contact. The rotational stage allowed for measurements of varying angles of incidence to be performed.

3.16 Optical characterisation of alkyl-capped silicon quantum dots

The silicon quantum dots utilised in this work were produced by collaborators using a procedure already reported [59]. An outline of the procedure and parameters utilised in the preparations of this material is provided below [115].

3.16.1 Preparation

Luminescent silicon nanocrystals (quantum dots) were produced by electrochemical etching of silicon. Porous silicon (PS) with a nanoscale internal structure was produced by a standard etching procedure from silicon. The starting point was to remove the native oxide layer from a silicon chip by dipping it in HF for a short time, washing with de-ionized water and blowing with a stream of nitrogen. The chip was then clamped between two O-rings in a Teflon cell of diameter 6 or 10 mm, which contains a HF–ethanol (electrolyte) mixture in the ratio 1:1. Due to the hydrophobic character of the clean Si surface, absolute ethanol is usually added to the aqueous solution to increase the wettability of the silicon surface. In fact, ethanoic solutions infiltrate the pores, while purely aqueous HF solutions do not. This is very important for the lateral homogeneity and the uniformity of the porous silicon layer in depth. Another important reason for adding ethanol is that during the reaction hydrogen evolution occurs, bubbles are formed and stick on the Si surface in pure aqueous solutions, whereas they are promptly removed if ethanol is added. The electrical contact was obtained via thin copper wire in the base of the Teflon cell. A coiled tungsten wire (0.5 mm) was used as the counter electrode. Silicon nanoparticles were obtained after 15 min etching at current density of (380-400 mA /cm²). The electrolyte was removed from the cell while the nanocrystals remained on the chip. These particles were dried in a Schlenk flask under vacuum. The dried nanocrystals were introduced into a flask containing a mixture of the 2 ml of toluene or mesitylene and 0.1 ml of undecenol solution. The solution was refluxed for 2-6 hrs under nitrogen atmosphere. During this refluxing process, the whole internal structure of the nanocrystals is modified. This process is termed alkylation. During this reflux only the smallest silicon nanoparticles broke off the porous silicon matrices and dissolved in the solution. The particles have been called silicon nanocrystals due to their size (3-5 nm in diameter).

3.16.2 Silicon quantum dots size evaluations

In order to validate the size of the silicon quantum dots, our collaborators in this project performed some additional investigations. The material was cast onto a mica substrate and characterised by Atomic Force Microscopy (tapping mode), as shown in Figure 41 [115]. The results indicate that some individual quantum dots are on the order of 5 nm in diameter, there are also clusters of quantum dots which form after subsequent depositions on the substrate, with diameters of up to 30 nm to 40 nm found, which can be attributed to inhomogeneous evaporation of the solvent. A previous study by the same group on the surface topography by AFM on the similarly produced sample indicated a uniform nanocrystal size distribution of between 3-5 nm [116, 117]. STEM analysis on the same sample has also been previously performed to verify the dimensions of these silicon nanocrystals [117].

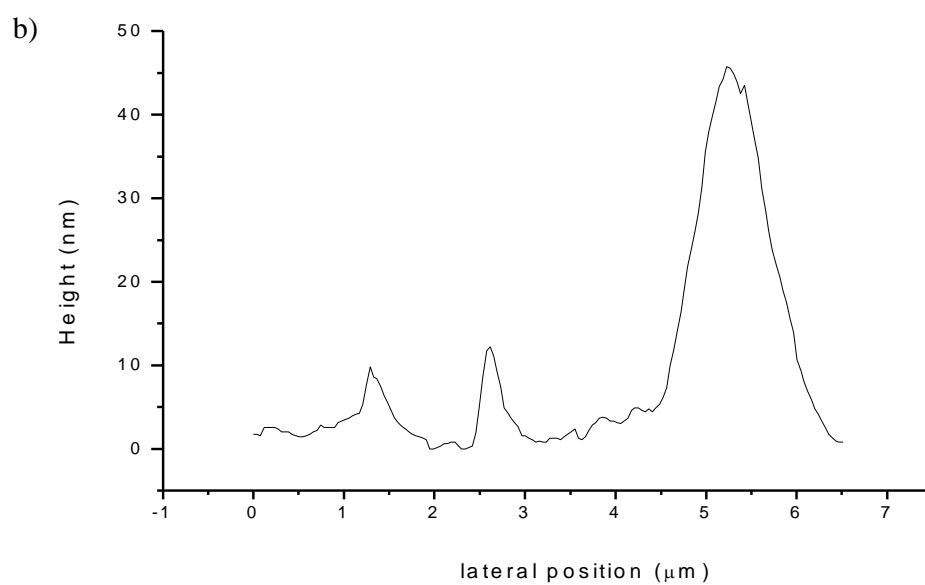
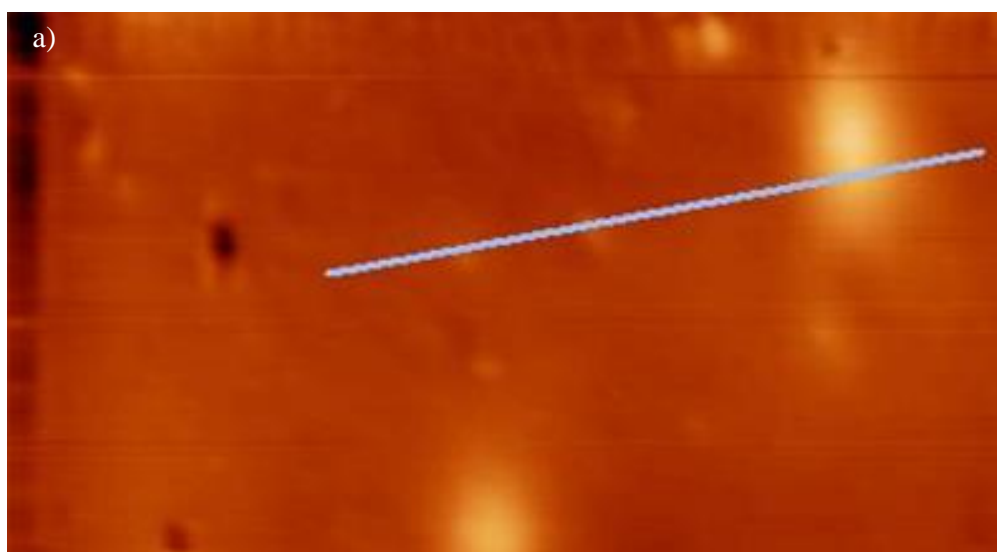


Figure 41: The AFM image was taken on the Si-QDs cast onto mica. From the profile along the line (a), one can find out the height of clusters was about 10 nm, which is equivalent to the height of two layers of Si-QDs, as shown in (b) [115].

3.16.3 Deposition of silicon quantum dots onto textured glass superstrates

For optical absorption characterisation fused quartz glass was used as a superstrate. This 1 mm thick glass was laser cut into 10 mm by 10 mm square sections and cleaned using Piranha solution (3:1 mixture, concentrated H₂SO₄, 30% H₂O₂) at 90°C for 25 minutes. The Si-QD was dispersed in dichloromethane [118] and then deposited using the drop deposition method. 4 ml of the solution was dropped per deposition, and the substrate allowed dry for 24 hours in a clean environment to allow for complete evaporation of the solvent.

To evaluate the initial absorption characteristics of the material, three depositions were performed in total for measurement made on untextured fused quartz superstrates.

To evaluate the increase in absorption in the Silicon quantum dots when used in conjunction with laser textured superstrates, five depositions were performed in total for measurement made on both untextured and textured fused quartz superstrates. The textured superstrates used in this investigation were subject to the same laser parameters and HF etching post treatment as outline in section 3.7 and section 3.9 respectively.

It is important to note that in this measurement the absorption results have not been weighted against the AM1.5G solar spectrum, as the aim of this study was purely to investigate the absorption characteristics of the Si quantum dots relative to air. This was to allow proper correlation of the absorption spectrum with the band-gap of the material, and also to facilitate comparison of the results with those reported in literature.

3.17 Focused Ion Beam Serial Sectioning

Silica monolithic rods (MonoTrap RCC18) used in this work were obtained from GL Sciences (Tokyo, Japan) and used as received. The carbon monoliths utilised in this work were produced by collaborators using a procedure already reported [119-122]. An outline of the procedure and parameters utilised in the preparations of this material is provided below.

3.17.1 Chemicals

1-Butanol and ferric chloride (99 %) were obtained from Riedel-De Haen (Seelze, Germany). Resorcinol (99 %), formaldehyde (37 wt % in water) and concentrated hydrofluoric acid (HF, 38-40 %) were obtained from Sigma-Aldrich (Gillingham, UK). Silica beads with a diameter of 5 μm (surface area, 94 $\text{m}^2 \text{g}^{-1}$; pore size, 15 nm) were used as templates for the preparation of the carbon monolithic rods. Deionised water (18.2 $\text{M}\Omega\cdot\text{cm}$) was obtained from a Millipore Direct-Q™ 5 water purification system (Millipore, Bedford, MA, USA).

3.17.2 Preparation of carbon monolith

The carbon monolith was prepared according to a procedure adapted from that reported by Eltmimi et al. [123]. A 1 g portion of 5 μm silica particles were dispersed in 1.5 g of 1-butanol under sonication for 1 h. This was followed by the addition of 0.18 g of ferric chloride and 0.367 g of resorcinol. A gentle shaking was applied to dissolve the resulting mixture and form the resorcinol/Fe complex. Then, 0.3 g of ice-cooled, 37% formaldehyde solution in water was added to the mixture and stirred for 1 h in an ice-water bath. The resultant mixture was polymerised in 6 mm ID glass tubes kept at 90°C for 16 h in a water bath (GFL, model 1013, Laborgerateborse GmbH, Burladingen, Germany). The resulting phenolic resin/silica rods were then removed from the glass tubes and aged for 72 h in a fume hood to slowly evaporate the majority of the residual solvent. Finally, the rods were dried under vacuum at 80°C overnight using an EHRET thermovacuum oven (Ehret Labor and Pharmatechnik GmbH, KG, Emmendingen, Germany), and further cured at 135°C for 4 h to ensure complete polymerisation.

A desktop alumina tube furnace (model GSL1300X, MTI, Richmond, VA, USA) purged with N_2 was then used to pyrolyse the rods. Initially, the temperature was ramped from room temperature to 800 °C at a rate of 2.5 °C min^{-1} , and held at this

temperature for 2 h. A second ramp was applied from 800 °C to 1250 °C at a rate of 10 °C min⁻¹, keeping this temperature for a further 1 h. Then, the furnace was allowed to cool down to room temperature. Next, the silica particles and the iron catalyst were removed from the rods by etching in 38% HF for 5 h and a subsequent wash with copious amounts of deionised water. Finally, the carbon monolithic rods were thoroughly dried under vacuum at 80 °C for 16 h.

3.17.3 Image acquisition

A small portion of the carbon and silica monolithic rods were subjected to FIB-SEM analysis with a FEI Quanta 3D FEG DualBeam instrument (FEI Ltd, Hillsboro, USA) integrating a Ga⁺ liquid metal ion source (spot size < 5 nm). Prior to the FIB-SEM analysis, the samples were fixed onto the stub using silver paste and subsequently coated with a thin layer of gold (thickness, ~ 7 nm) using a Emitech K575X Sputter Coating Unit (Quorum Technologies, UK). FIB sectioning was carried out at an acceleration voltage of 30 kV to etch a section of approximately 60 x 50 µm to a depth of 100 nm for the carbon monolith (current, 0.3 nA), and of 55 x 40 µm to a depth of 66.7 nm for the silica monolith (current, 0.5 nA). A 2D image of each section was automatically acquired by the SEM at a magnification of 2000x, an acceleration voltage of 5 kV, and a nominal current of 5.92 pA for the carbon monolith and of 1.5 pA for the silica monolith. This FIB-SEM sequence was automatically repeated 100 times for the carbon monolith and 150 times for the silica monolith in a set routine. A total of 100 images were thus collected for the carbon monolith, each one being 100 nm further into the structure compared to the preceding image. Likewise, a total of 150 images were collected for the silica monolith, each one being 66.7 nm further into the structure. The angle of image acquisition was 52° in relation to the direction of the FIB as shown in Figure 42. The volumes and dimensions of the acquisition are presented in Table 17 and Table 18.

Table 17: Acquisition details for carbon monolith

Original Volume	0.000045262 mm ³
Analysed Volume	0.000015119 mm ³
Slice thickness	100 nm
Pixel dimension	74 nm
Number of Slices	93
Dimensions of Analysed volume	58.24 μm x 26.49 μm x 9.30 μm

Table 18: Acquisition details for silica monolith

Original Volume	0.000049073 mm ³
Analysed Volume	0.000014732 mm ³
Slice thickness	66 nm
Pixel dimension	74 nm
Number of Slices	150
Dimensions of Analysed volume	44.69 μm x 33.74 μm x 9.90 μm

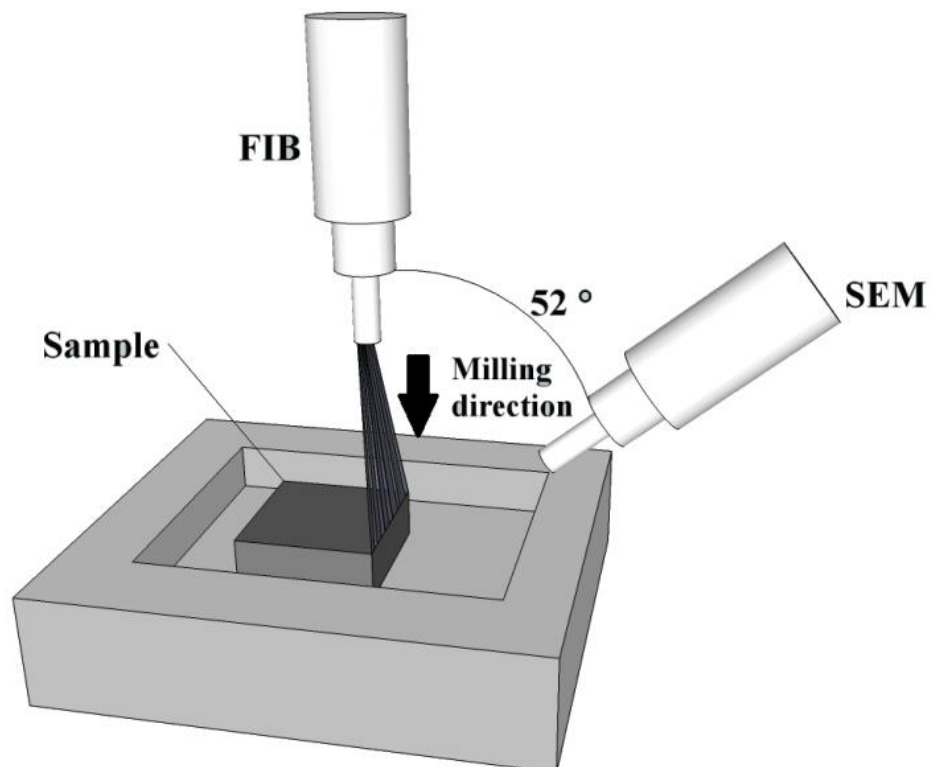


Figure 42: Sketch of the sample/FIB-SEM system set-up for serial sectioning and imaging.

3.17.4 Image processing

The SEM images resulting from the FIB serial sectioning procedure (Figure 43 and Figure 44) were processed via image analysis routines to extract the pore boundaries and reconstruct the 3D structure. First, the images were resized anisotropically to correct for the image acquisition angle of 52° , after which the images were subjected to an image registration processes where landmarks were identified in the sequence of images. These landmarks were then used to calculate the necessary translation required to minimise any image alignment error. This was achieved using the formula for a rigid body translation (7),

$$\mathbf{x} = \{(\cos \theta, -\sin \theta), (\sin \theta, \cos \theta)\} \cdot \mathbf{u} + \Delta \mathbf{u} \quad (7)$$

where \mathbf{u} and \mathbf{x} are the input and output vectors of the landmarks, respectively, $\Delta \mathbf{u}$ is a constant vector that gives the amount of translation, and θ is the angle of rotation in the image sequence.

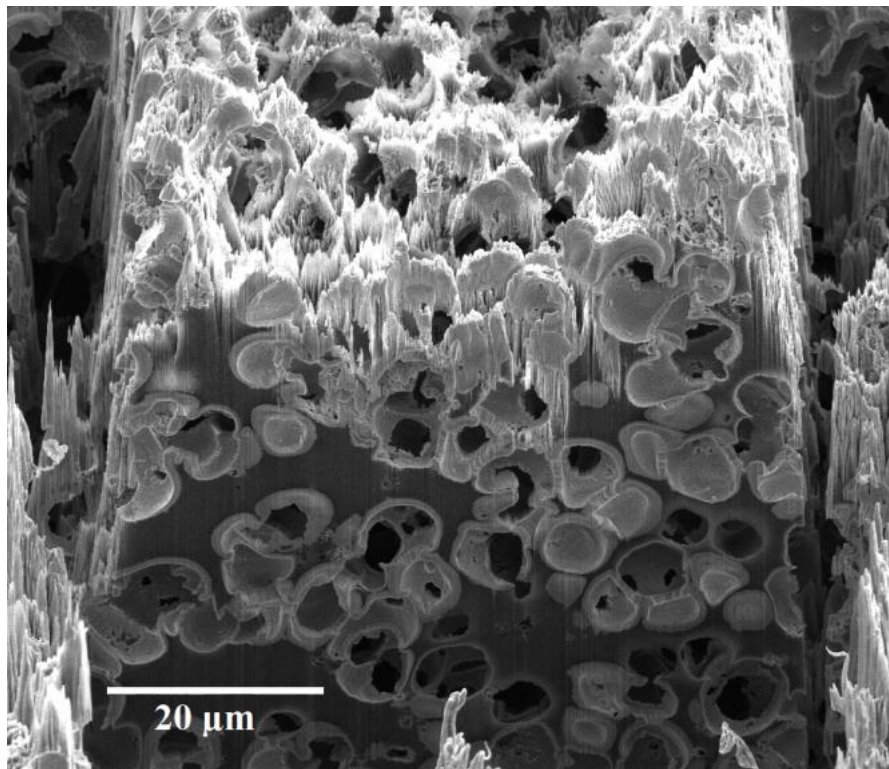


Figure 43 Image captured by SEM after FIB sectioning of the carbon monolith.

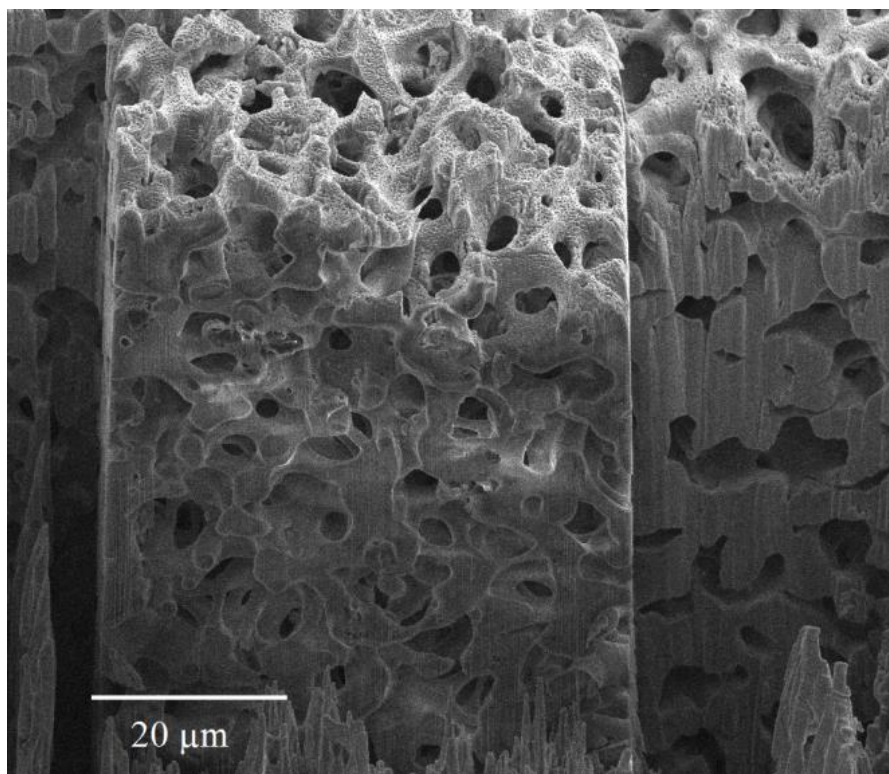


Figure 44 Image captured by SEM after FIB sectioning of the silica monolith.

The resulting images were then cropped to reduce the area of analysis to approximately $58.2\ \mu\text{m} \times 26.5\ \mu\text{m}$ (width x height) for the carbon monolith and $44.7\ \mu\text{m} \times 33.7\ \mu\text{m}$ for the silica monolith, with a resolution of $74\ \text{nm}/\text{pixel}$. From the images captured for the carbon monolith, only the first 93 were used for analysis. Thus, the depth of the final image stack was $9.3\ \mu\text{m}$, with a resolution of $100\ \text{nm}/\text{pixel}$ in the depth direction. The depth of the final image stack employed for the reconstruction of the silica monolith was $10\ \mu\text{m}$, with a resolution of $66.7\ \text{nm}/\text{pixel}$ in the depth direction.

No attempt was made to increase the resolution of the captured images by increasing the SEM magnification, thus decreasing the size of the detectable pores. The scope of this work was simply to demonstrate the suitability of FIB-SEM analysis for reconstruction of the bulk porous structure in conducting and non-conducting monolithic materials, as have applications in chemistry and in next generation solar cells. Therefore, a rather large reconstructed volume was considered to be more representative of the overall monolith morphology, as compared to a reconstructed volume just a few cubic micrometres in size that would have been needed for visualisation of the nanoporous structure.

Finally, the two image stacks were binarised after manual outlining and filling of the porous structures, as shown in Figure 45.

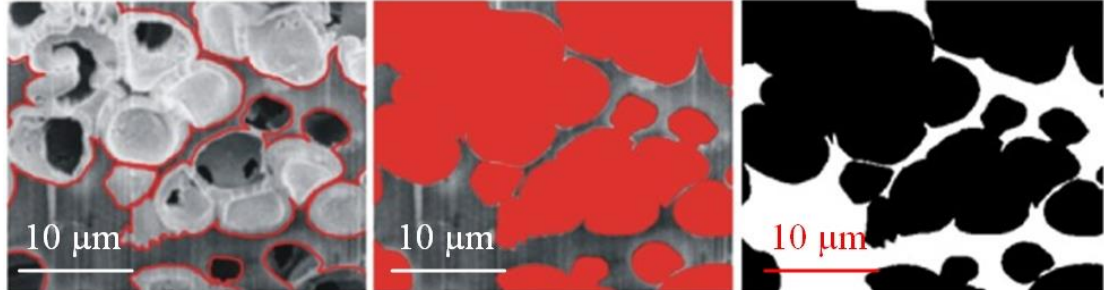


Figure 45 From L to R: Outline of the pores, filling of pores and binarisation applied to the image stack obtained for the carbon monolith.

3.17.5 3D reconstruction and morphological analysis

Following binarisation, a 3D histogram of each of the image stacks was produced, enabling the calculation of the total macroporosity of the volume under analysis by (8).

$$\% \text{ Porosity} = \frac{\text{Number of voxels representing pores}}{\text{Total number of voxels in volume}} \times 100 \quad (8)$$

To assess the accuracy of the resulting macroporosity values, Mercury Intrusion Porosimetry (MIP) measurements were also carried out with the carbon and silica monoliths by collaborators [122]. MIP is an established porosity measurement technique used in the characterisation of open pore materials with pore size ranges from 3.5 nm up to 500 μm [124]. The total porosity and pore size distribution were determined with an Autopore IV 9500 Series (Micromeritics Instrument Corporation). Dried samples with weights ranging from 36 mg to 47 mg were used for these measurements.

The 3D reconstruction of both monoliths from their respective image stacks was then performed using the volume rendering technique available within the Materialise Mimics 13.0 software (Materialise NV, Belgium). This allow for the 3D visualisation of the porous structure and allows for a much better understanding of the connectivity of the pores within the material.

Chapter 4

Verification of the 3D non-contact optical profilometer

4.1 Positional Analysis of the XYZ stage system

In order to assess the quality of the low-cost 3D imaging system it was necessary to measure the accuracy and repeatability of the motion systems used during data acquisition. The microscope had three automated axes: X and Y axes to position the sample in the optical plane, and the Z axis to position the sample along the optical axis to vary the focal position.

The X and Y axes by design were constructed in a manner to reduce the cost of the positioning system. The purpose of the X and Y axes were twofold; firstly, the axes would be used to position the sample accurately for data acquisition, and secondly the axes would be used for the automated acquisition of large area measurements through the use of area stitching. The theoretical positioning resolution was designed to be 5 μm through the use of a low-cost stepper motor / thread-bar leadscrew arrangement, which consisted of a 200 steps/revolution stepper motor combined with a 1mm pitch leadscrew. Theoretically this would mean that the XY stage could position the sample to the nearest 5 μm (16 pixels in the image), which from an area stitching perspective was sufficient as additional data processing for accurate area stitching would be to allow for accurate combination of acquired images. There is also the option of micro-stepping the stepper motors which can greatly increase positioning resolution, however for the purposes of this study full-step stepper motor drivers were utilised.

The Z axis forms a critical part of the accuracy of the 3D measurement capabilities of the system. The control software was developed such that images were recorded at varying user defined focal positions along the optical axis. However the exact values of those positions are constrained by the accuracy and repeatability of the Z axis. Hence it was necessary to assess the performance of this axis in order to evaluate the overall potential of the system as a low-cost 3D metrology solution. The axis utilised for the Z axis motion was selected on the basis of several important engineering

considerations, namely compact size, resolution, minimum incremental movement performance, and cost.

The following analyses utilises the ISO 230-2 standard to assess the motion performance of these axes. Two performance characterisation tests were completed; a large scale movement analysis test and a small scale movement analysis test. This dual scale approach was utilised in order to measure the performance of the low cost linear stages for 3D profilometry applications. The large scale analysis was performed with a Mahr MarCator 810SW dial gauge indicator with a measurement accuracy of $\pm 17 \mu\text{m}$ over the 10 mm range of travel. The small scale analysis was performed with a Mitutoyo 513-405E dial gauge with an accuracy of $\pm 3 \mu\text{m}$ over the 0.2 mm range of travel.

4.1.1 Large scale positional analysis

The target positions and stage movement results for the large scale analysis for the X, Y, and Z axes are presented in Figure 46, Figure 47, and Figure 48 respectively. The calculated repeatability and accuracy results for these stages are presented in Table 19, Table 20, and Table 21 respectively.

Further results involved in the calculation of the stage accuracy and repeatability from this investigation are presented in Appendix A.

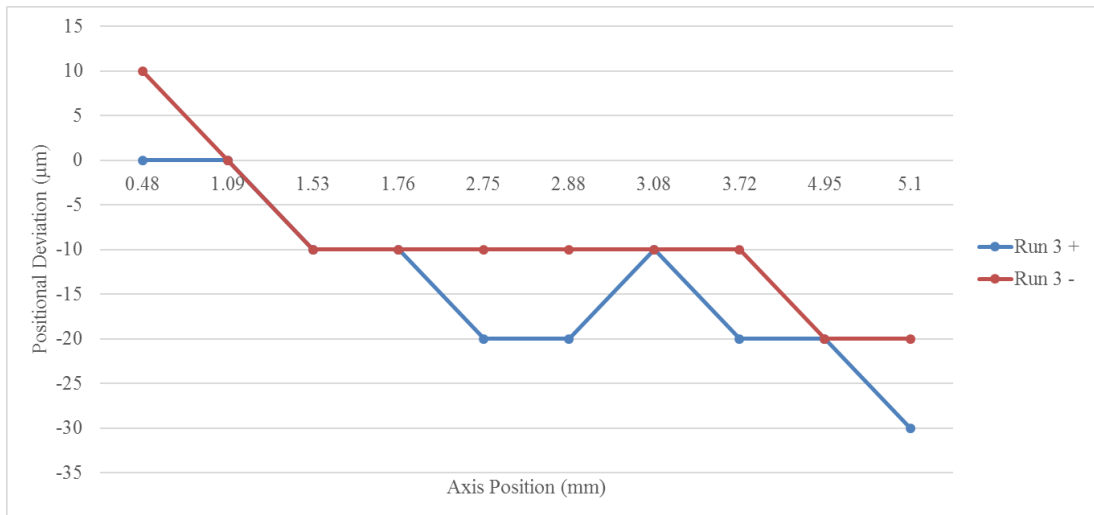
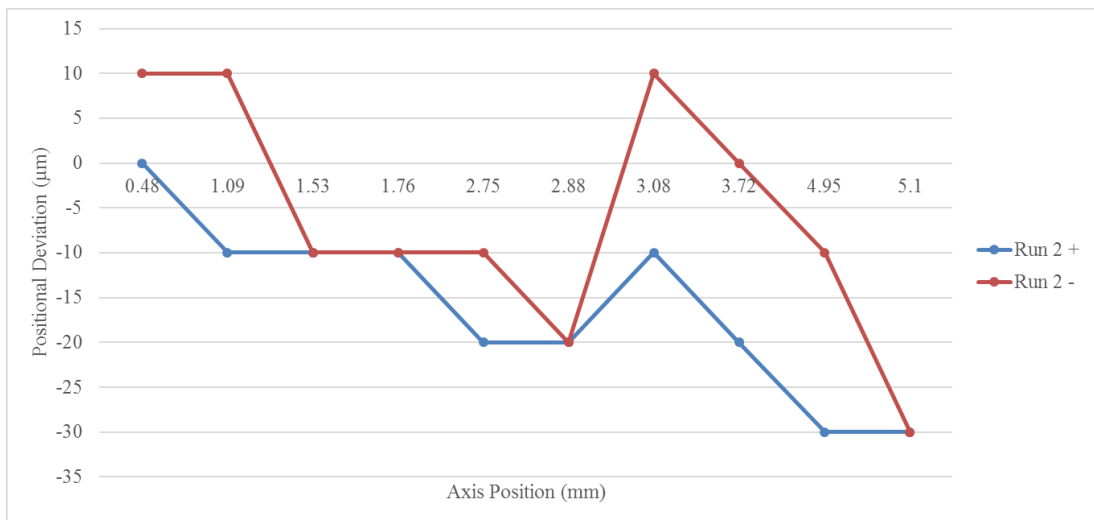
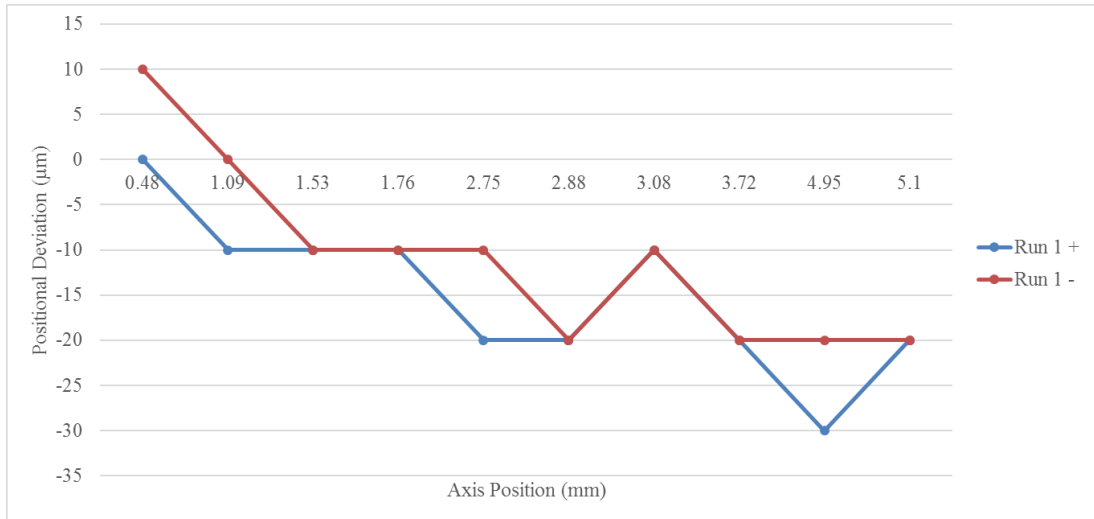


Figure 46: Large scale positional analysis along X axis.

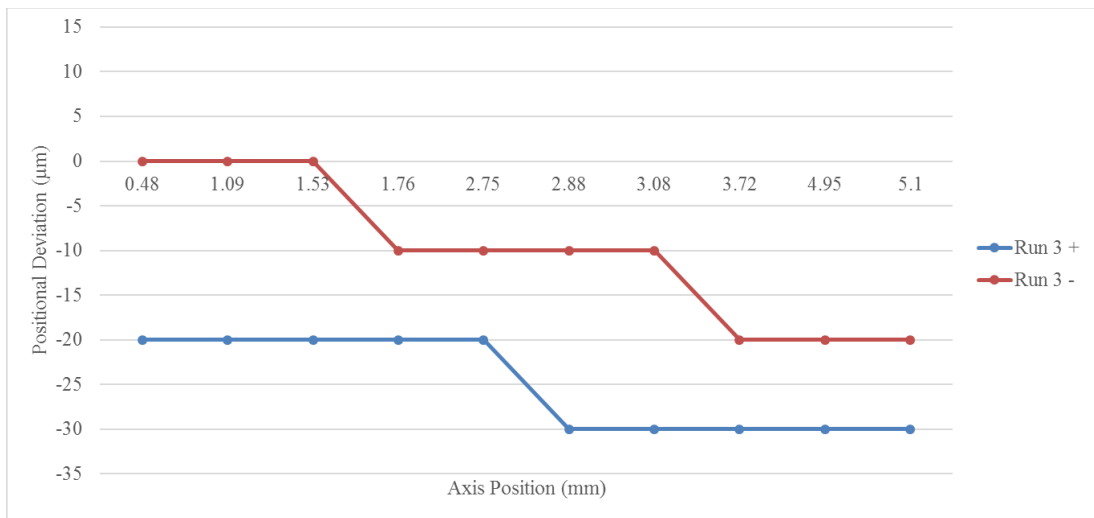
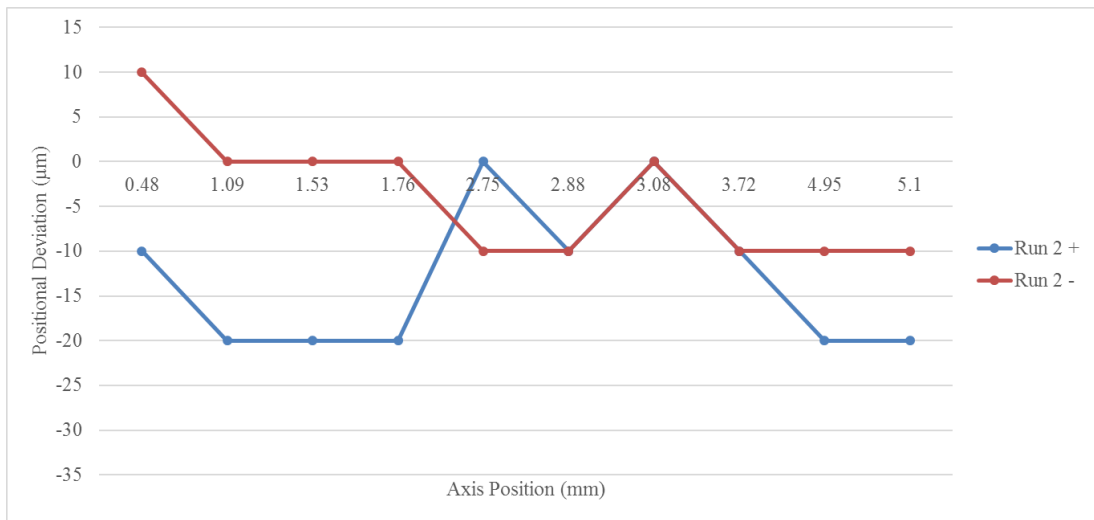
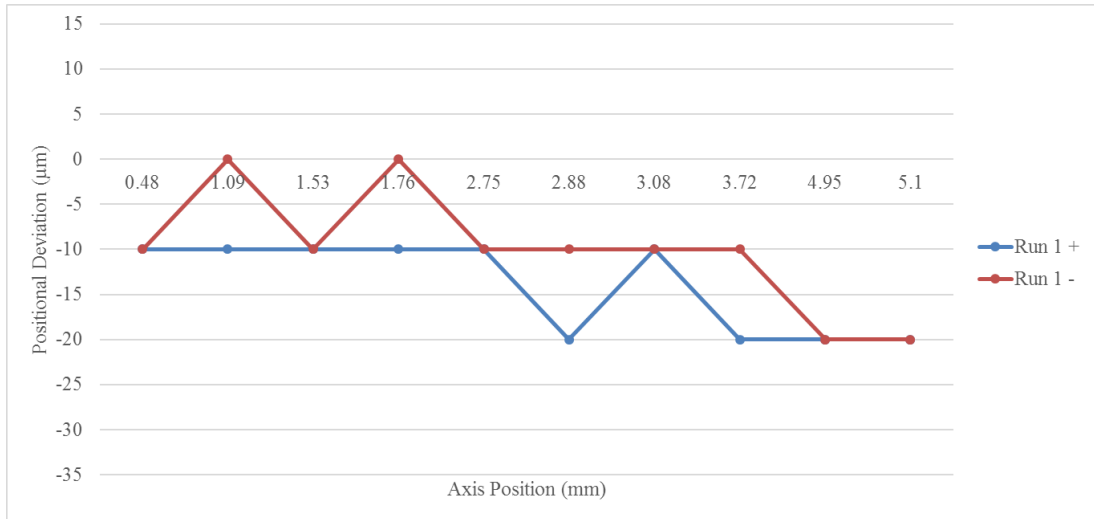


Figure 47: Large scale positional analysis along Y axis.

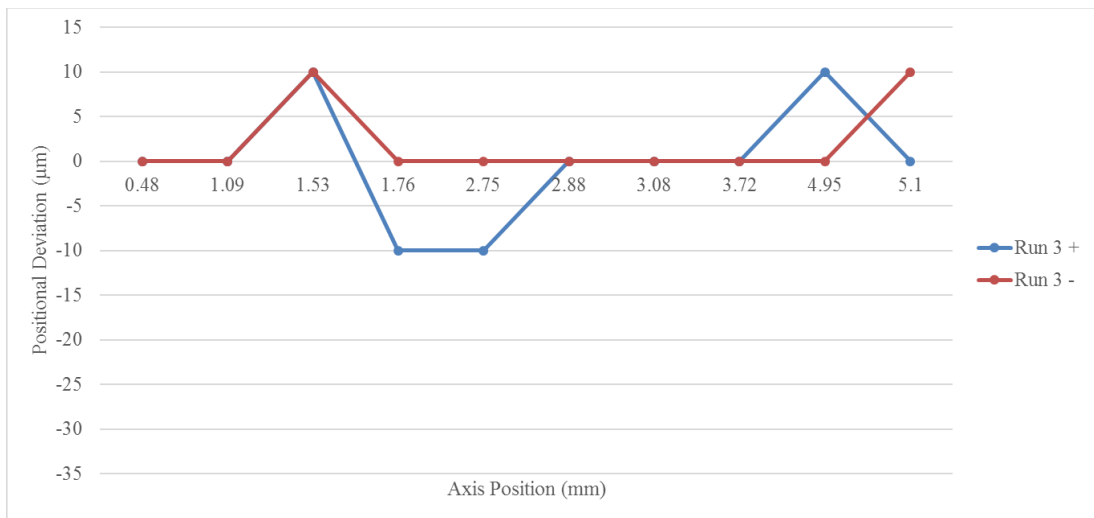
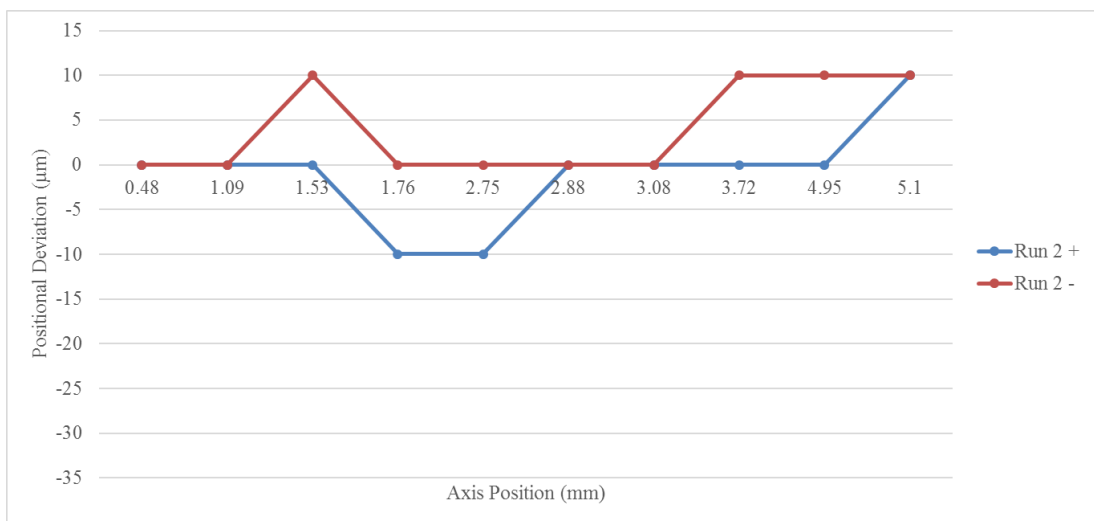
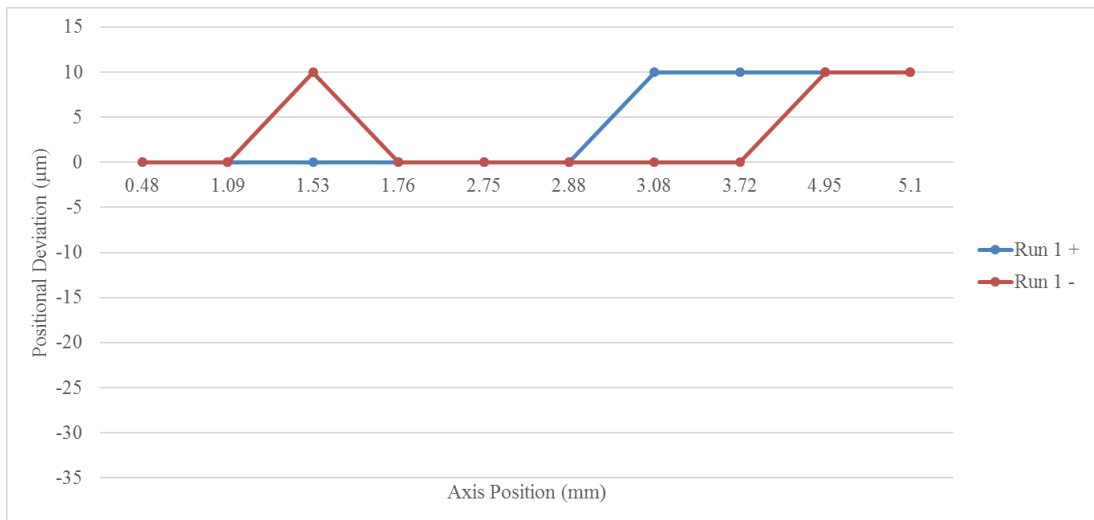


Figure 48: Large scale positional analysis along Z axis.

Table 19: Results from large scale positional analysis along X axis

Axis Deviation (all in μm)	Unidirectional +	Unidirectional -	Bidirectional
Reverse value B	NA	NA	10
Mean Reverse value \bar{B}	NA	NA	1
Range mean bidirectional positional deviation M	NA	NA	40
Systematic positional deviation E	30	30	40
Repeatability R	40	40	80
Accuracy A	60	60	60

Table 20: Results from large scale positional analysis along Y axis

Axis Deviation (all in μm)	Unidirectional +	Unidirectional -	Bidirectional
Reverse value B	NA	NA	20
Mean Reverse value \bar{B}	NA	NA	2
Range mean bidirectional positional deviation M	NA	NA	10
Systematic positional deviation E	10	20	20
Repeatability R	80	40	140
Accuracy A	80	60	80

Table 21: Results from large scale positional analysis along Z axis

Axis Deviation (all in μm)	Unidirectional +	Unidirectional -	Bidirectional
Reverse value B	NA	NA	10
Mean Reverse value \bar{B}	NA	NA	1
Range mean bidirectional positional deviation M	NA	NA	20
Systematic positional deviation E	20	10	20
Repeatability R	40	40	80
Accuracy A	60	50	60

The results from the large scale positional analysis indicate that, as expected, the highest bi-directional performance was achieved by the servo driven Z-axis, closely followed in terms of performance by the X-axis. According to this analysis the Z-axis operates with similar repeatability in both directions when moving uni-directionally. When the 3D non-contact optical profilometer is performing a measurement, the Z-axis only moves uni-directionally during the measurement. Hence it could be argued that the uni-directional is the most important performance factor for the Z-axis. While this axis provided the best performance of the three axes, it should be noted that the Z axis was tested over a smaller travel range than the X and Y axes, due to the limitation in travel displacement available from the Z-axis.

The X and Y axes are both identical in design, differing only in the mass loaded on the stages. The X axis supports the sample platform and the Z-axis actuator, while the Y axis supports the same load in addition to the mass of the X axis. From an operational perspective, the bi-directional performance of the X and Y axes are important, as if a large area 3D measurement is being performed then the positioning repeatability of the sample in the XY plane of the profilometer is of importance. The X and Y axes achieve almost identical performance when considering the results calculated from the *Unidirectional* – movements. In the *Unidirectional* + movements, the difference in the accuracies reported is within the limit of error of the Mahr MarCator 810SW dial gauge indicator. This indicates that the X and Y axes operate at similar performance levels over the nominal 5 mm range investigated. The most significant sources of positioning error for the X and Y axes can be attributed to manufacturing defects in the leadscrews, inaccuracy in the step positions of the stepper motors, and the accuracy limitations of the measurement device.

4.1.2 Small scale positional analysis

The target positions and stage movement results for the small scale analysis for the X, Y, and Z axes are presented in Figure 49, Figure 50, and Figure 51 respectively. The calculated repeatability and accuracy results for these stages are presented in Table 22, Table 23, and Table 24 respectively.

Further results involved in the calculation of the stage accuracy and repeatability from this investigation are presented in Appendix A.

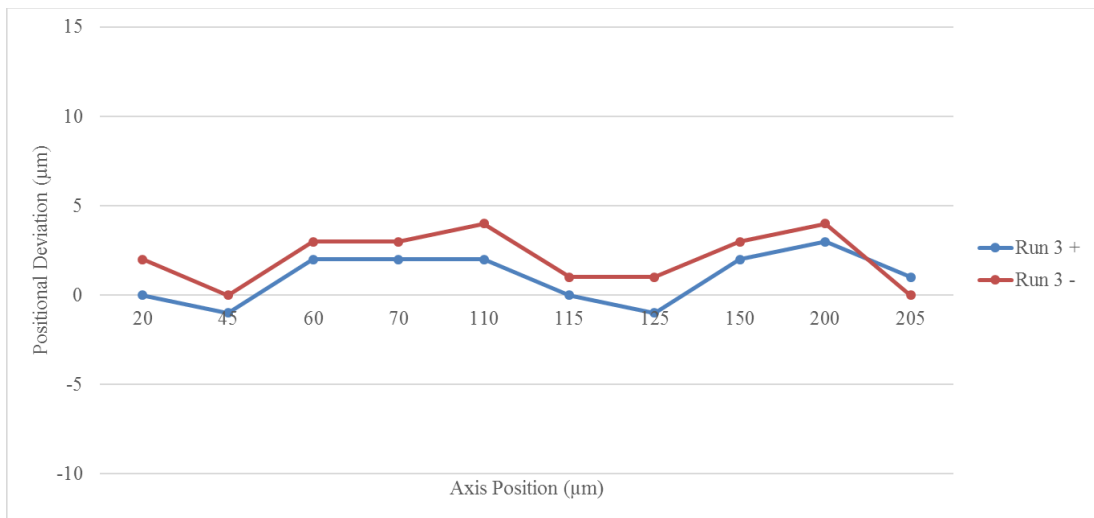
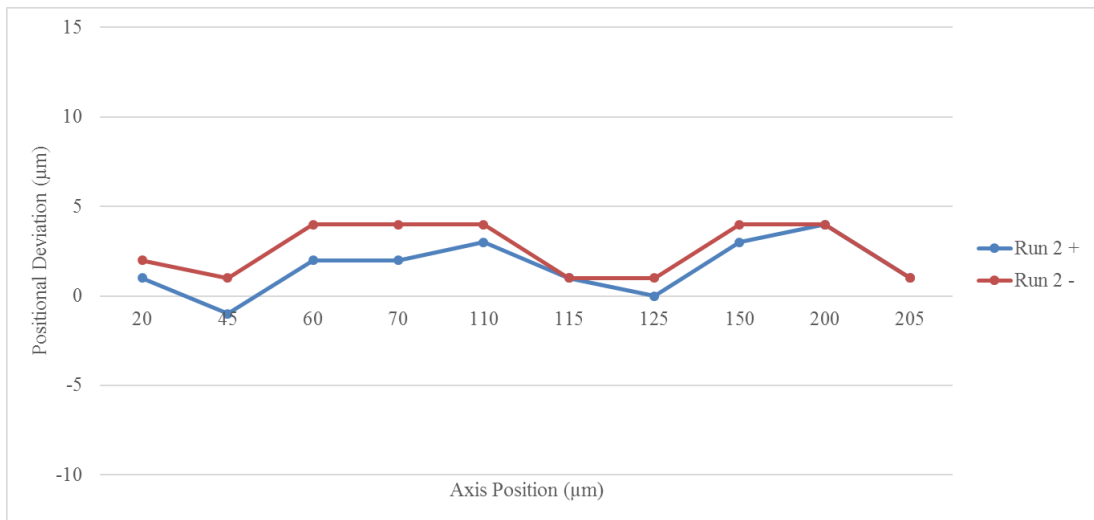
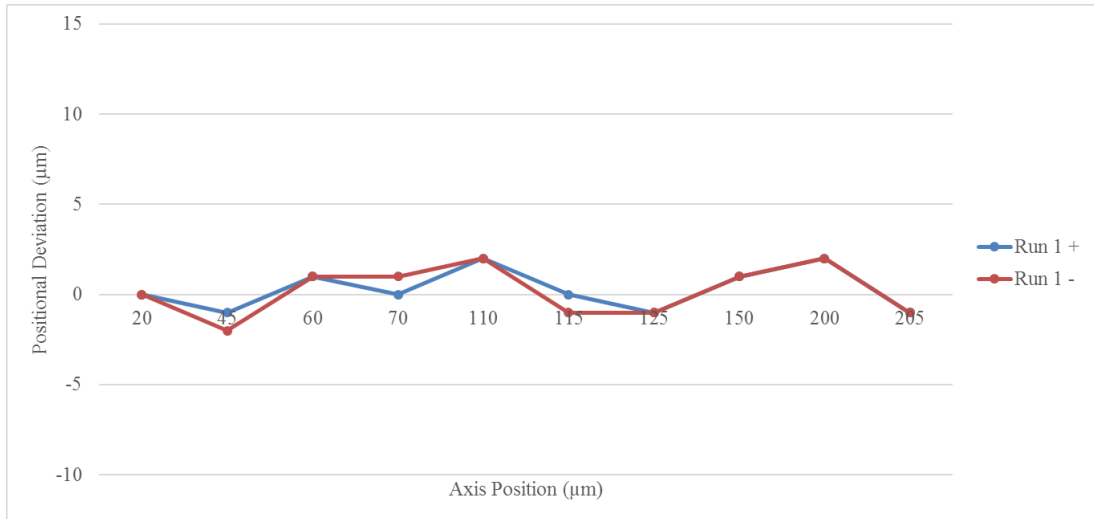


Figure 49: Small scale positional analysis along X axis.

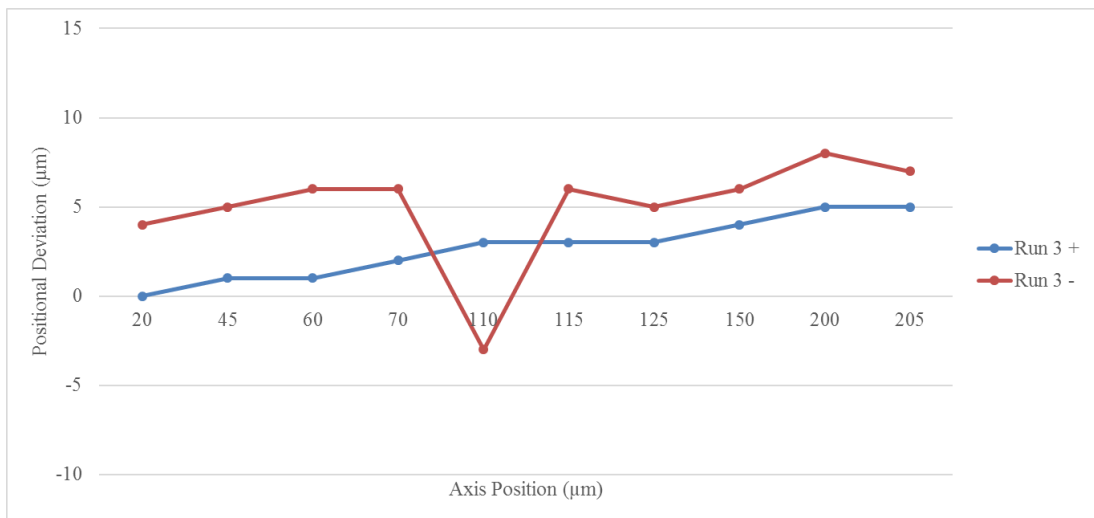
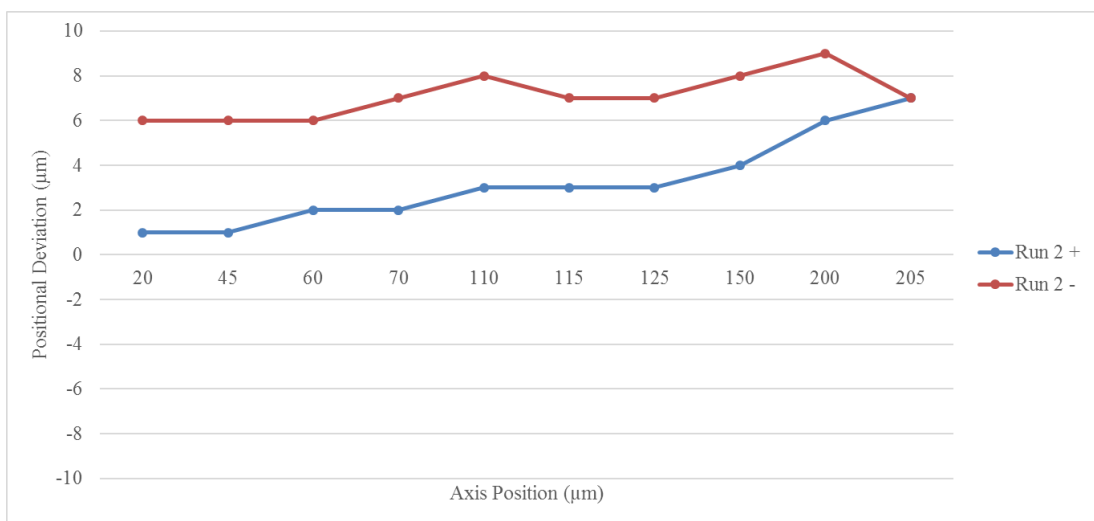
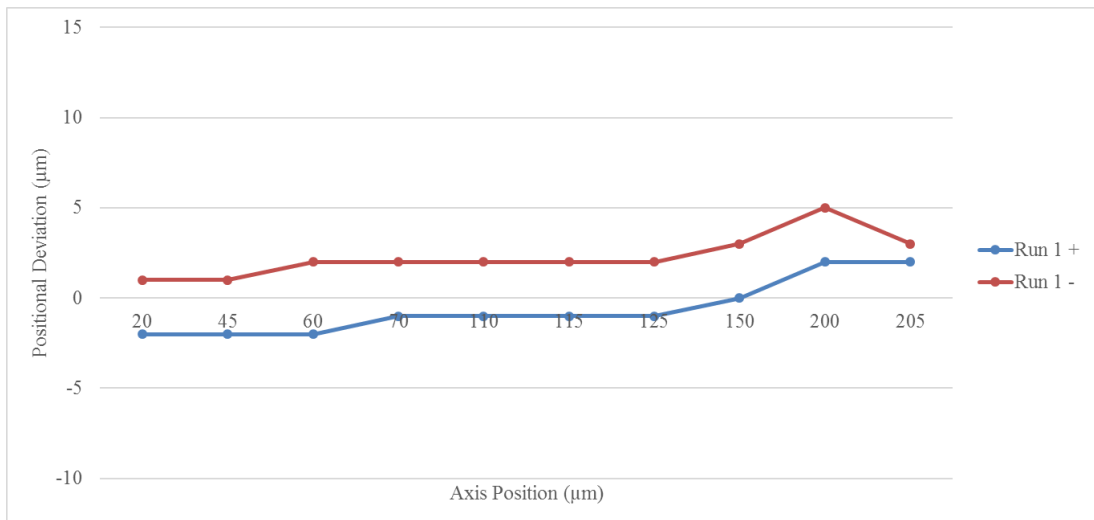


Figure 50: Small scale positional analysis along Y axis.

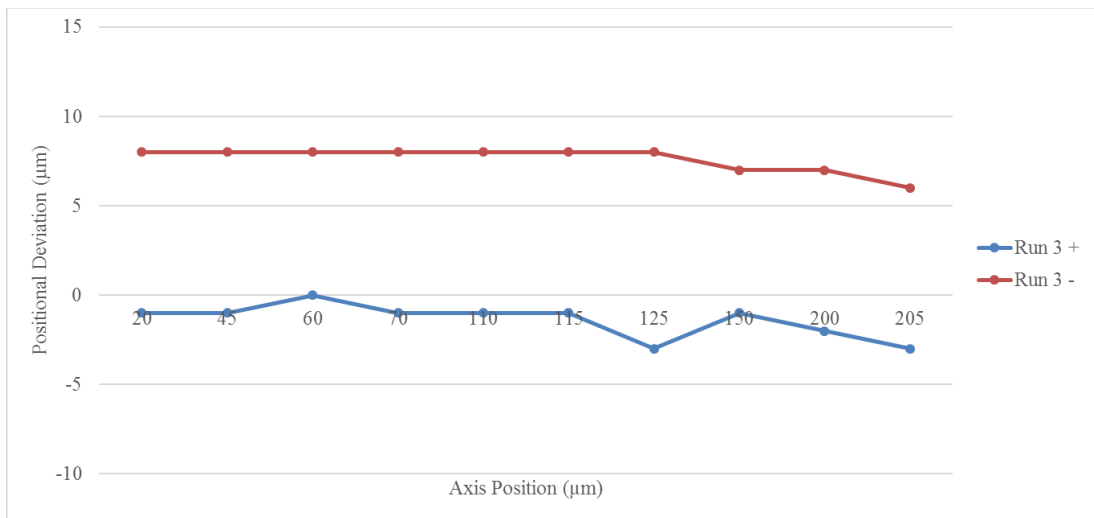
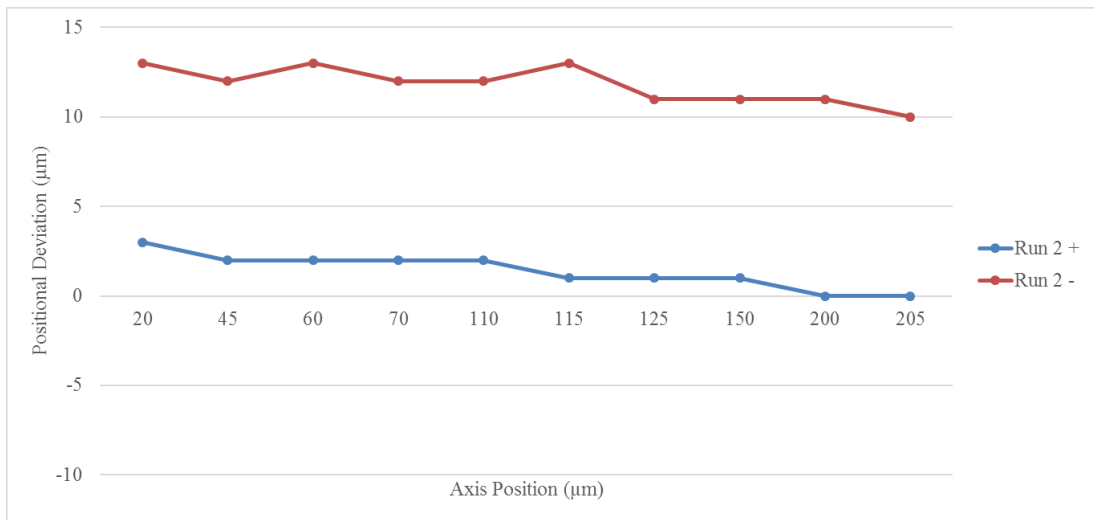
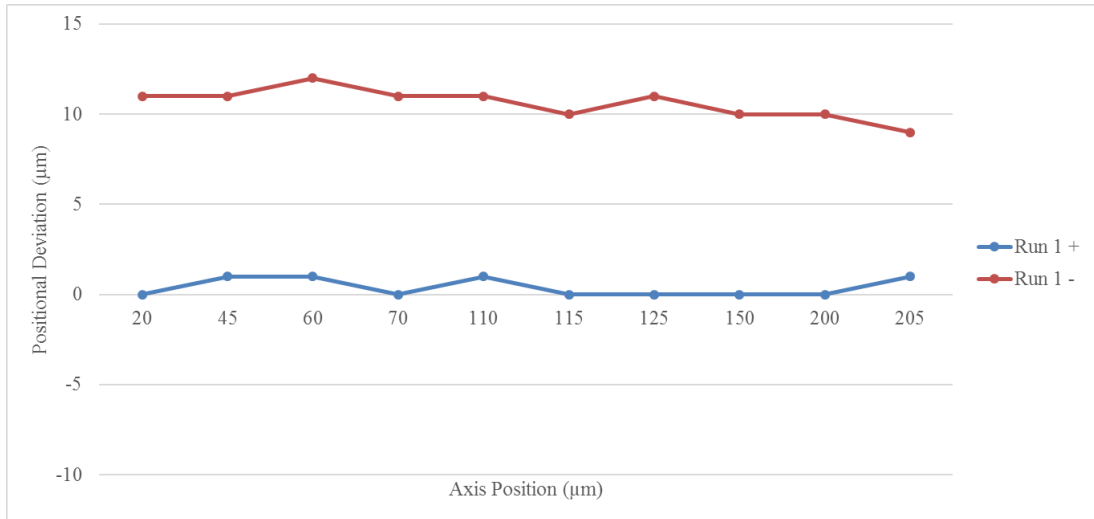


Figure 51: Small scale positional analysis along Z axis.

Table 22: Results from small scale positional analysis along X axis

Axis Deviation (all in μm)	Unidirectional +	Unidirectional -	Bidirectional
Reverse value B	NA	NA	2
Mean Reverse value \bar{B}	NA	NA	0
Range mean bidirectional positional deviation M	NA	NA	4
Systematic positional deviation E	4	3	4
Repeatability R	4	8	14
Accuracy A	8	11	8

Table 23: Results from small scale positional analysis along Y axis

Axis Deviation (all in μm)	Unidirectional +	Unidirectional -	Bidirectional
Reverse value B	NA	NA	5
Mean Reverse value \bar{B}	NA	NA	1
Range mean bidirectional positional deviation M	NA	NA	4
Systematic positional deviation E	5	5	7
Repeatability R	12	24	40
Accuracy A	15	24	15

Table 24: Results from small scale positional analysis along Z axis

Axis Deviation (all in μm)	Unidirectional +	Unidirectional -	Bidirectional
Reverse value B	NA	NA	11
Mean Reverse value \bar{B}	NA	NA	1
Range mean bidirectional positional deviation M	NA	NA	2
Systematic positional deviation E	2	3	12
Repeatability R	8	12	22
Accuracy A	10	13	11

The small scale positional analysis revealed some interesting results. Over these small scale movements, the stepper motor driven X-axis outperformed the servo motor driven Z-axis in terms of accuracy and repeatability, both uni-directionally and bi-directionally. The high performance of the X-axis bi-directionally can be ascribed to the fact the stage is directly driven by the motor, with minimised leadscrew backlash. However, the Z-axis operates with a small servo driven motor through a planetary gearbox. While gearboxes are an efficient means of transferring power, they can also introduce backlash into the motion system. Nevertheless, it is important to note that the X-axis set-up would not be a suitable replacement for the current Z-axis, as in order to record 3D measurements using a small depth with the depth-from-focus principle, the ability to move in repeatable small increments is required. In the current configuration the X-axis is limited to a positioning resolutions of 5 μm , which is too coarse a sampling interval for the measurement of micro-scale surface profiles.

The X-axis also outperformed the Y-axis in terms of accuracy and repeatability, which can be attributed to the fact that the Y-axis motor must drive a higher mass. The difference in performance between the two axes could potentially also be attributable to other factors, such as manufacturing variation between the respective leadscrews or motors.

The results from this investigation revealed that the stage performance in the small scale analysis is superior to the stage performance in the large scale analysis. For example, the X-axis bi-directional accuracy improves from 60 μm for the large scale displacement to only 8 μm for the small scale displacement, however one must also take into consideration that the former measurement is over a longer distance.

4.1.3 Verification of 3D measurement performance

For each verification experimental run listed in Table 25, the step height measurements were repeated six times. The complete list of displacement measurement results from these runs are presented in Appendix G.

Table 25: Accuracy results from the 6 sub-run measurements

Run	Reference step height (μm)	Sampling Interval (μm)	Avg. Height (μm)	Accuracy %	Std Dev (μm)
1	512	0.6	511.6	99.92	0.9
2	512	1	503.4	98.32	0.4
3	103	0.6	103.2	99.81	0.2
4	103	0.6	103.1	99.90	0.1
5	103	0.6	102.7	99.71	0.4
6	103	0.2	102.4	99.42	0.1
7	103	1	102.5	99.51	0.2
8	512	0.2	503.3	98.30	0.7
9	103	0.6	102.9	99.90	0.2
10	103	0.6	102.6	99.61	0.1

As can be seen from the results in Table 25, the accuracy for measurements taken with the two measurement artefacts was always in excess of 98%. While this is not confirmation of absolute accuracy, it does give some confidence that the system can measure effectively at the 100 μm step height and the 500 μm step height scales. The standard deviations across the run measurements are all below 1 μm , which offers a good reflection on the repeatability of the step height measurement process using the developed 3D non-contact optical profilometer. It can also be noted that the highest repeatability (lowest standard deviation) results were achieved when measuring over 103 μm , while the 512 μm measurement scale returned the lowest repeatability results. This contrasts well with the fact that the Z-axis manufacturer's specification indicates a minimum incremental movement of 0.2 μm . When sampling at 0.2 μm over the 103 μm step height, the results recorded a high degree of repeatability, however when the

same sampling interval is utilised over the 512 μm step height measurement, the repeatability is reduced. It could be argued that this small sampling interval is repeatable over distances of 100 μm , however due to manufacturing and operational variations in the Z-axis, that sampling interval is not as repeatable over a distance of 500 μm . It is also important to note that the Z axis verification measurements performed in section 4.1.2 are relative to an arbitrary zero point, and the repeatability of the stage is evaluated over several run with respect to that same fixed point in space. However, in the 3D measurement it is only the relative distance between the upper and lower plane positions that is evaluated for repeatability.

4.1.4 Comparison of measurement results with a commercially available system

In order to qualitatively evaluate the performance of the developed 3D non-contact optical profilometer in comparison with a commercially available system, a measurement of the machined brass sample was evaluated using a Keyence VHX-5000 series microscope. This system is based on a proprietary “depth-from-defocus” principle, and thus offers a good performance comparison with the system developed in this work. The measurement of the brass artefact by the Keyence VHX system is shown in Figure 52, and is a combination of two 1 mm x 1 mm measurements stitched together.

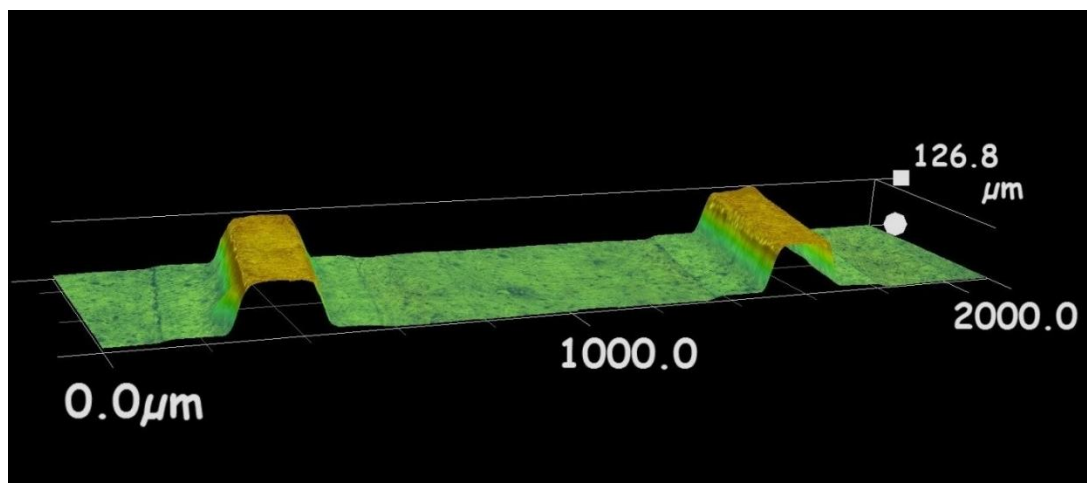


Figure 52: Measurement recorded using a Keyence VHX-5000 series 3D microscope.

The measurement taken with the 3D non-contact optical profilometer that was developed in this thesis is shown in Figure 53 and Figure 54, the first of which displays the fully focused full colour image output from the developed software, and the latter shows the 3D measured profile of the step-height. It can clearly be seen that the developed system preserves the edge sharpness of the machined brass step, as the steep flanks to the side of the column are more accurately represented in the measurement in Figure 54 compared with the measurement shown in Figure 52. The 3D profile shown in Figure 54 visually compares well with the cross sectional SEM image shown in Figure 25. While this is only a qualitative evaluation, it would be fair to say that the developed system performs at least comparatively with the commercially available Keyence system.



Figure 53: Fully focused true colour image of the machined brass sample

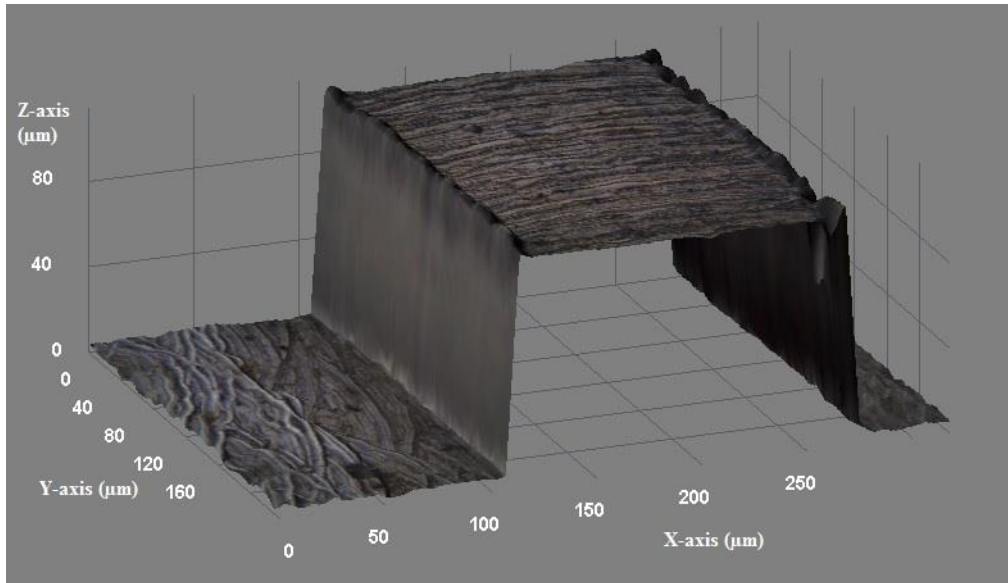


Figure 54: 3D representation of the surface profile of the machined brass sample.

4.1.5 Demonstration of capability in the measurement of translucent materials

The 3D profile shown in Figure 55 was recorded using the 3D non-contact optical profilometer developed in this thesis, and demonstrates the profilometer capabilities in measuring translucent laser micro-machined surfaces. The measurement area is approximately 1.2 mm by 0.9 mm, and is composed by the automatic stitching of 16 (four by four) 3D profile measurements.

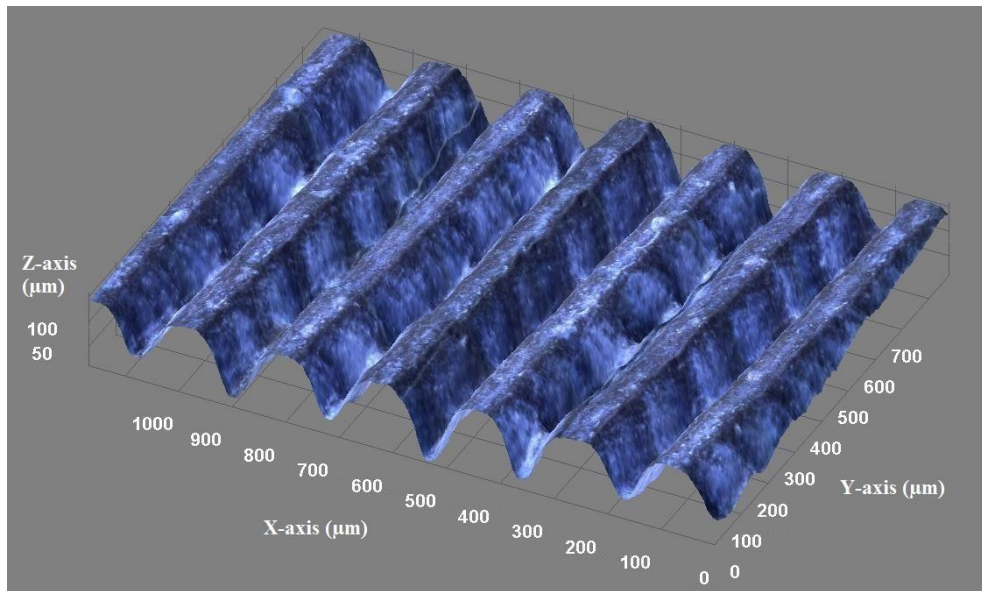
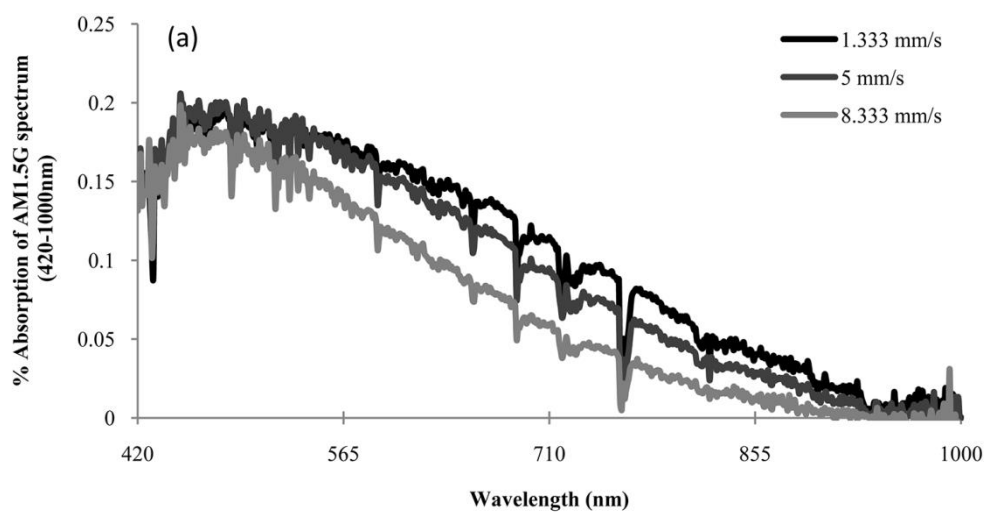


Figure 55: 3D measurement profile of laser micro-machined grooves in fused quartz glass. Axis values are in nm.

Chapter 5 Laser texturisation of glass superstrate for enhanced solar cell performance

5.1 Laser processing and parasitic light absorption losses

Significant alterations in the parasitic absorption loss characteristics of the glass due to different laser processing parameters were observed, as is shown in Figure 56(a) and Figure 56(b). Figure 56(a) shows the influence of traverse speed (mm/s) with the PRF and Duty Cycle fixed at levels of 400 Hz and 6% respectively. It can be seen that the light absorption is inversely related to the traverse speed. As the traverse speed increases the absorption of the processed surface decreases. Figure 56(b) displays the relationship between duty cycle (%), and thus average power (W), and the absorption properties of the surface. It can be observed that tuning the duty cycle of the pulse is critical, as with lower duty cycle it was feasible to achieve the desired low absorption characteristics. It is also clear from this figure that there is a proportional relationship between the laser duty cycle and the absorption. Longer duty cycles result in more energy used for the laser process, directly causing a more significant heat affected zone (HAZ). This more intensely modified surface directly contributes to the increased absorption of light which in turn would result in less light being available to the active solar cell medium for photocurrent generation.



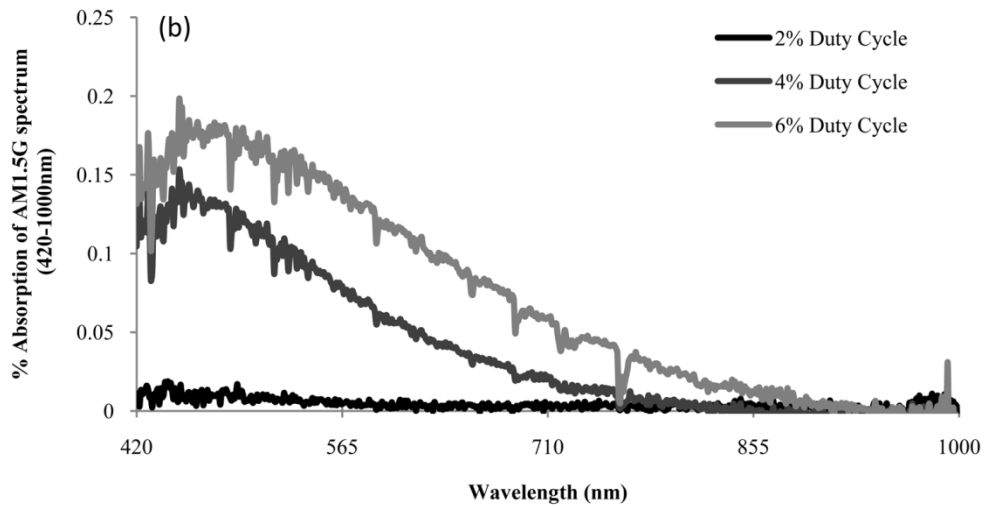


Figure 56. (a) Effect of Traverse Speed with PRF=400Hz and Duty Cycle=6%. (b) Effect of Duty Cycle with PRF=400Hz and Traverse Speed=8.333mm/s.

5.2 Design of Experiments and Response Surface Methodology (RSM)

The R-squared value obtained for this statistical analysis was 0.994 and the model F-value was 116.48, meaning that the model was significant and good correlations between process parameters and process outputs existed. Further information on the interpretation of these values is available in Appendix B. Figure 57 shows the predicted vs. actual values for the response surface model created using the experimental data. This graph shows that the generated model fit the experimental data very well. If the data points are located along the straight line, it is a sign that the predicted values are close to the actual experimental values.

Figure 58 displays the relationship between the two most influential factors in the laser process; traverse speed (mm/s) and duty cycle (%). It can clearly be observed that there is a non-linear relationship present over the investigated parameter range. The parameter interaction in this case has resulted in lowest absorption at high traverse speed and low duty cycle. The parasitic absorption loss under the AM1.5G spectrum was measured to be between 2.27% and 63.28%. This was largely attributed to the rough surface morphology remaining after laser processing.

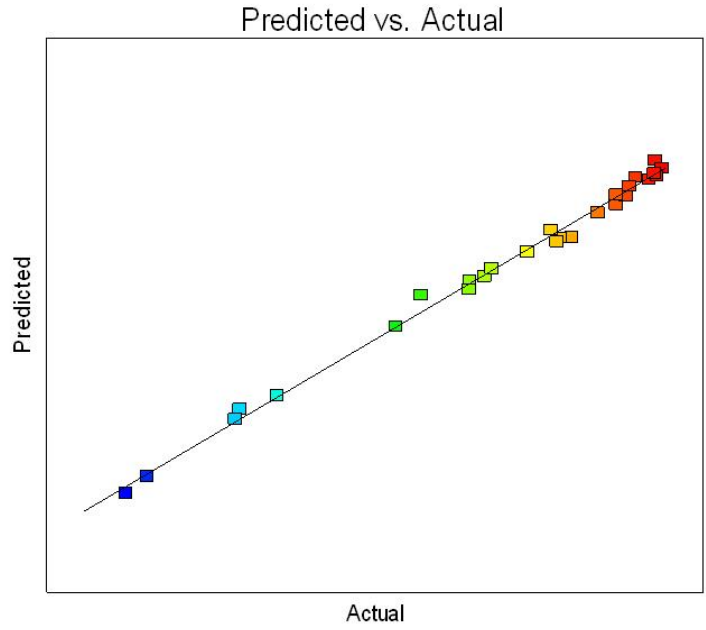


Figure 57. Values predicted by the model equation against the actual values. Points located along the line indicate the model provides an acceptable fit.

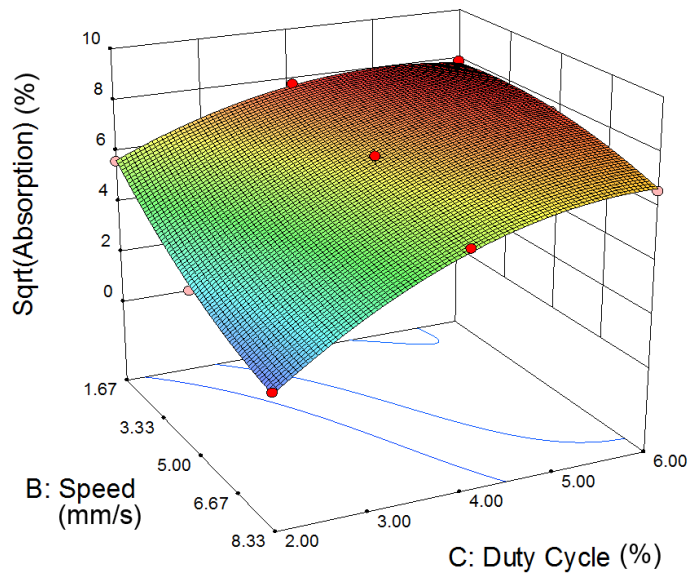


Figure 58. RSM surface plot showing the correlation between the significant input parameters and the resulting parasitic absorption in the processed material (PRF=280Hz).

5.3 ANOVA Analysis

Model equation

The regression co-efficients for the quadratic model fitted to the experimental data are presented in Table 26.

Table 26. The values of the Regression Co-Efficients for the quadratic response surface model shown in Figure 58.

Co-efficient	Value
b_0	15.73712
b_1	-0.06562
b_2	-1.87792
b_3	-0.88093
b_4	-5.4E-05
b_5	0.014494
b_6	0.44665
b_7	9.41E-05
b_8	0.090434
b_9	-0.12789

Table 27 presents the results of the Analysis of Variance and the calculation of the contributions of the most significant parameters to the overall model. It can be seen that x_3 (Duty cycle) provides the largest contribution to the model, while x_1 (PRF) provides the least contribution of the 3 main parameters.

Table 27. Contribution of the most significant factors to the quadratic response surface model.

Contribution of most significant factors:

Factor	x_1	x_2	x_3	$x_1 x_3$	$x_2 x_3$	$(x_3)^2$
% Contribution	0.5	9.8	43.91	7.0	13.6	17.2
p-Value	0.0631	<0.0001	<0.0001	<0.0001	<0.0001	<0.0001

The R-squared results for the model are presented in Table 28. The difference between the Adj R-Squared and the Pred R-Squared is less than 0.2, the model is considered to only have significant terms included. In this case the difference between the two values is 0.0381, which would indicate that all the terms of the quadratic model are significant.

Table 28: R-squared values for the RSM model

R-Squared	0.9692
Adj R-Squared	0.9528
Pred R-Squared	0.9147
Adeq Precision	27.719

5.4 SEM and EDXS Characterisation

The SEM images shown in Figure 59(a) and Figure 59(b) agree with the results presented in the model. A significant surface modification can be seen Figure 59(b), due to the low processing speed and high duty cycle. In contrast to this, the surface presented in Figure 59(a) is significantly smoother. The smoother surface can be attributed to the lower duty cycle and higher processing speed which reduced the overall laser energy absorbed by the surface as the beam traverses it. As less laser energy was absorbed, less surface material was ablated, which in turn results in less recast on the surface. Less ablation also resulted in a shallower channel in comparison to when a higher duty cycle was utilised.

Figure 60(a) and (b) show the cross-sections of the maximum and minimum texture depths achieved by laser processing. Some cracking due to thermal shock is visible at the bottom of the groove in Figure 60(a). The size of the textures varied from 72-974 μm in depth, and 146-213 μm in width at the widest point. Due to the ablation-vaporisation mechanism utilised in creating the micro-grooves, the surface roughness could be seen to increase with increasing laser power, as shown in Figure 59. This can be attributed to increased material removal rates and the re-solidification of material on the surface from cooling vapour.

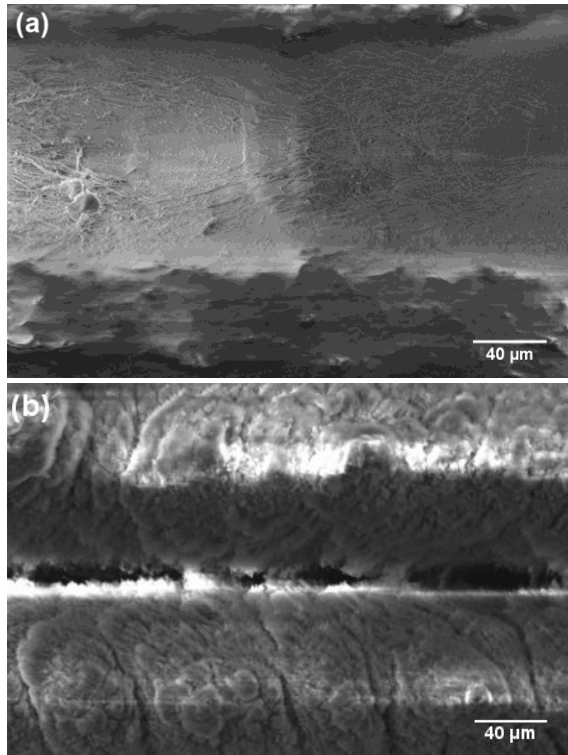


Figure 59. Top down view of laser micro-machined channels in Fused Quartz. (a) Sample 21 with low absorption properties (PRF=400 Hz, Speed=8.3 mm/s, Duty Cycle=2%). (b) Sample 9 with high absorption properties (PRF=400 Hz, Speed=1.7 mm/s, Duty Cycle = 6%).

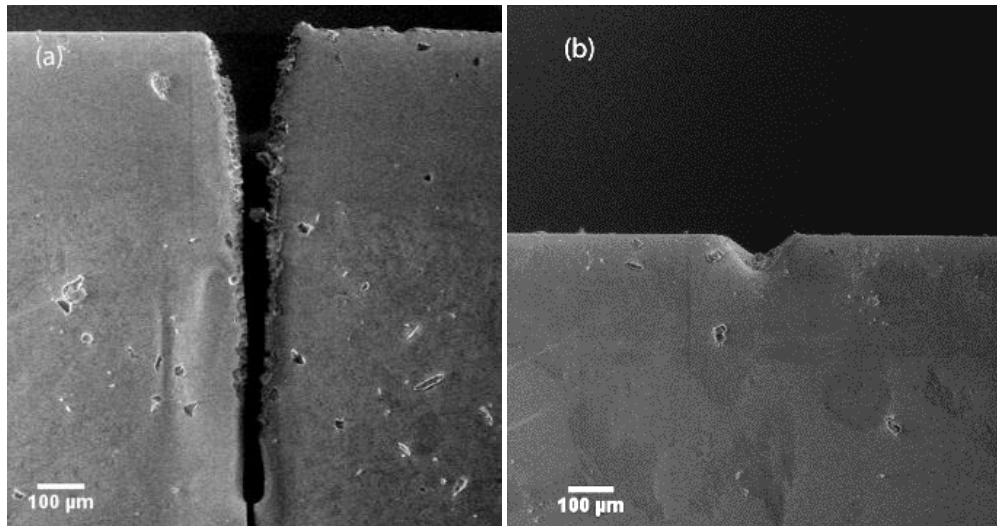


Figure 60. Cross sectional view of the groove texture.(a) Sample 16 with the maximum (duty cycle 6%, PRF 160 Hz, speed 5 mm/s) and (b) Sample 21 with the minimum texture depths achieved by laser ablation (duty cycle 2%, PRF 400 Hz, speed 8.33 mm/s).

A summary of the channel dimensions found in this study are available in Appendix F. The average channel depths, widths at top, and widths at 50% depth are presented in Figure 61, Figure 62, and Figure 63 respectively. The dimensions of laser micromachined channels in glass have been analysed extensively in other studies using ANOVA analyses [44, 81, 125]. This type of analysis has not been performed here as it is not a main objective of this work, however the results in this study correlate well with those reported in those studies.

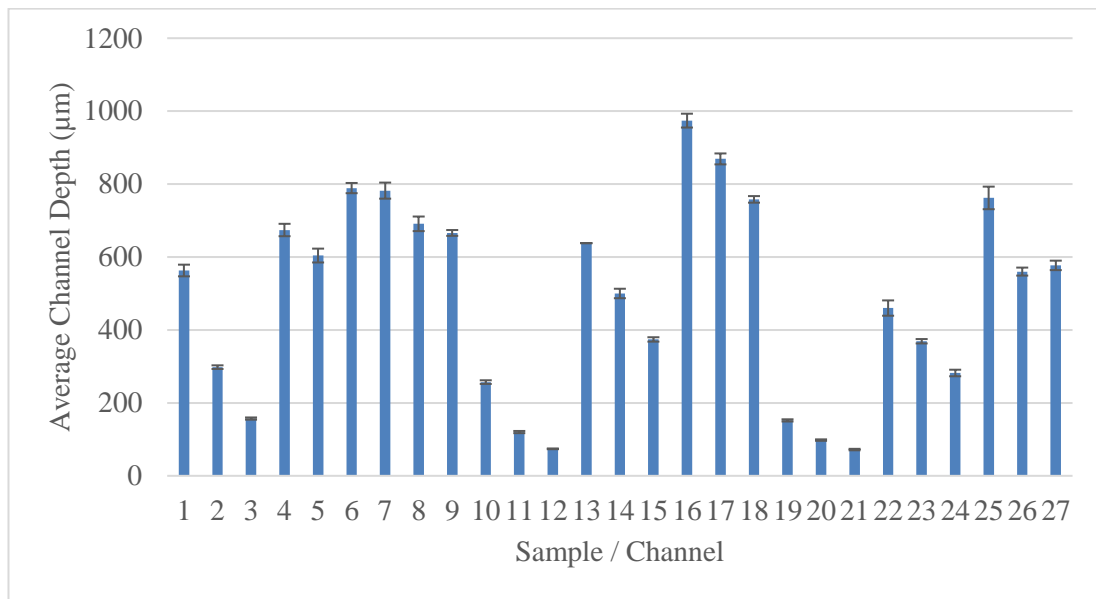


Figure 61: Average channel depths.

From the channel depth analysis it can be seen that the depth is quite repeatable at the measurement locations along the channels. The largest standard deviation reported across the three measurements is 31 µm, while the majority of the other standard deviations are below 20 µm. This level of repeatability is a good indication that the manufacturing process is repeatable and stable. The largest average channel depth measured was 974 µm, while the shallowest was just 72 µm.

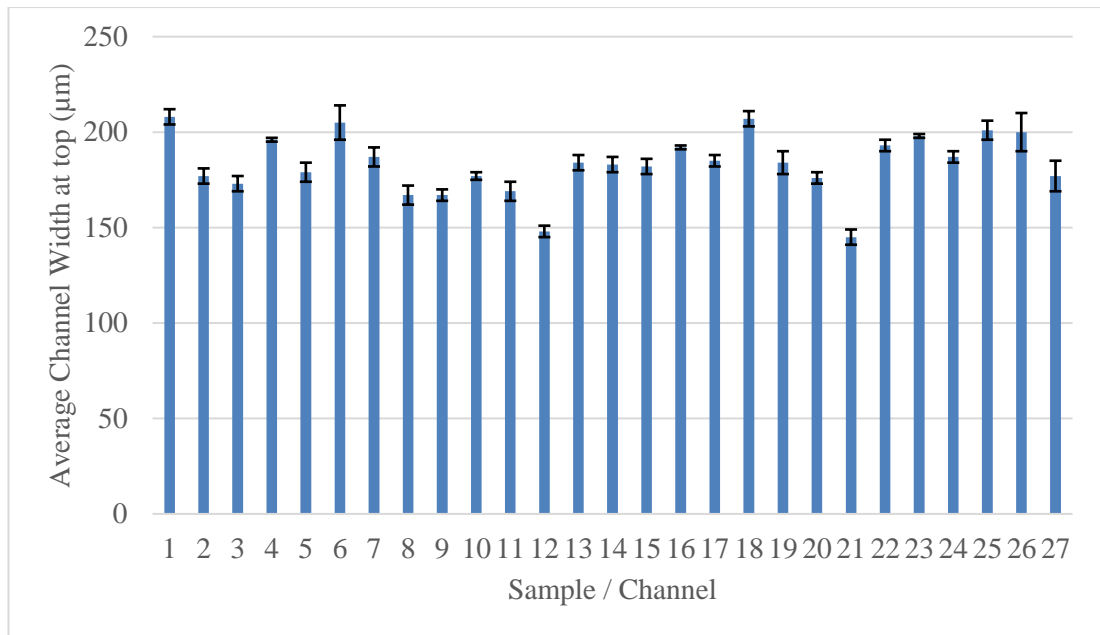


Figure 62: Average channel widths at the top surface.

From the channel width (top) analysis it can be seen that the width at the top of the channels only varies within a small range, from 169 μm to 208 μm. This can be attributed to the fact that the laser beam size at the focal spot is diffraction limited, and is not dependant on the laser parameters investigated in this work. A diffraction limited laser spot is the smallest size to which a laser beam can be focussed, where optical diffraction effects are the limiting factor as opposed to other optical aberrations. As the laser processing Average Power (W) is reduced (by reducing the Duty Cycle %), the amount of laser irradiance (W/m^2) delivered to the workpiece is also reduced. This causes a reduction in the width of the channel at the surface, as there is less thermal energy available to ablate the full width of the laser focal spot.

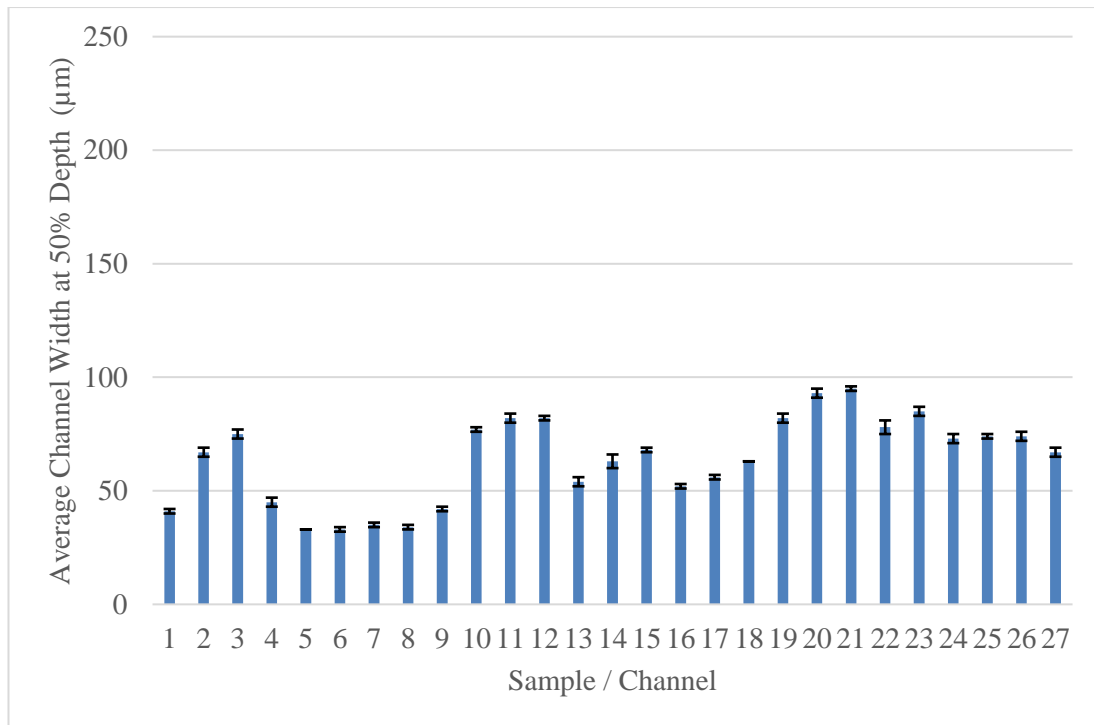


Figure 63: Average channel width at 50% depth.

From the channel width (50%) analysis it can be seen that the width at the 50% channel depth point is inversely proportional to the channel depth. This can be attributed to the fact that the deeper channels have quite steep sidewalls, as is shown in Figure 60(a). This channel profile can be attributed to a different thermal conduction mechanism deeper in the channel than is found on the surface [81]. There may also be an effect from the directionality of the laser assist gas flow, which causes the depth to be more directional at higher laser powers. Nevertheless, this measurement at 50% channel depth does give some insight into the overall aspect ratio of the channel.

Figure 64 presents a 3D display of channel geometry for sample 21 which was fabricated using the lowest duty cycle and highest traverse speed. The depth of the channel is 70-80 micrometres. In contrast, channels fabricated using the highest duty cycle had depths approaching approximately 1 millimetre. This 3D profile was recorded using the 3D non-contact optical profilometer developed during this work.

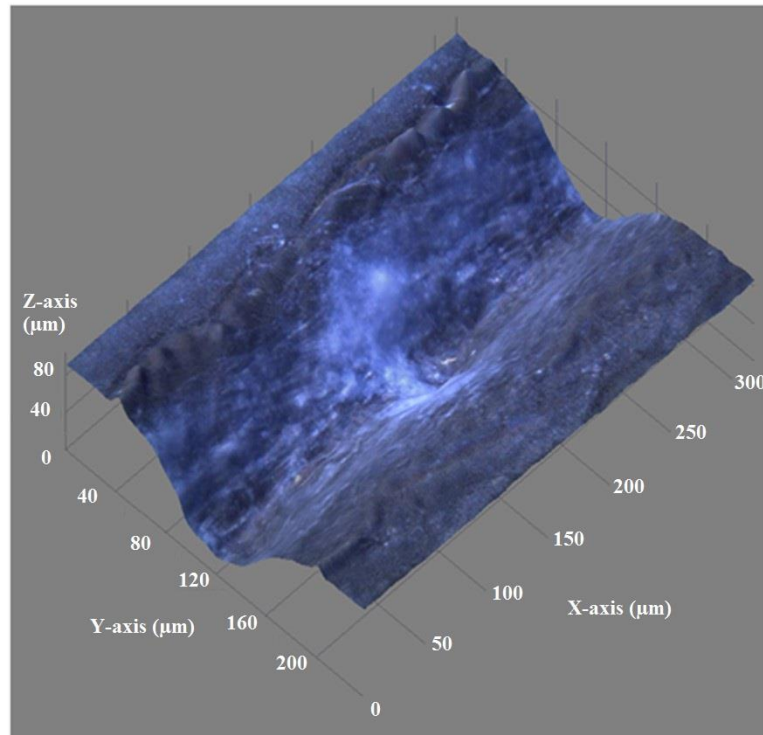


Figure 64: 3D surface profile of sample 21, 70-80 micrometres in depth, as captured by the 3D optical profilometer.

Figure 65 (a) and (b) are the corresponding EDXS spectra corresponding to the SEM images in Figure 59(a) and (b) respectively. Over the 10 randomly selected points for the EDXS analysis the average increase of silicon at the surface was 5% for Figure 59(a) over Figure 59(b). This change in composition could also be factor in the light absorption characteristics of samples processed with higher duty cycles. It can clearly be seen that the original untextured reference surface composition consisted of significant amount of oxides on the surface (Figure 65(c)). The results of the EDXS measurements are presented in Table 29.

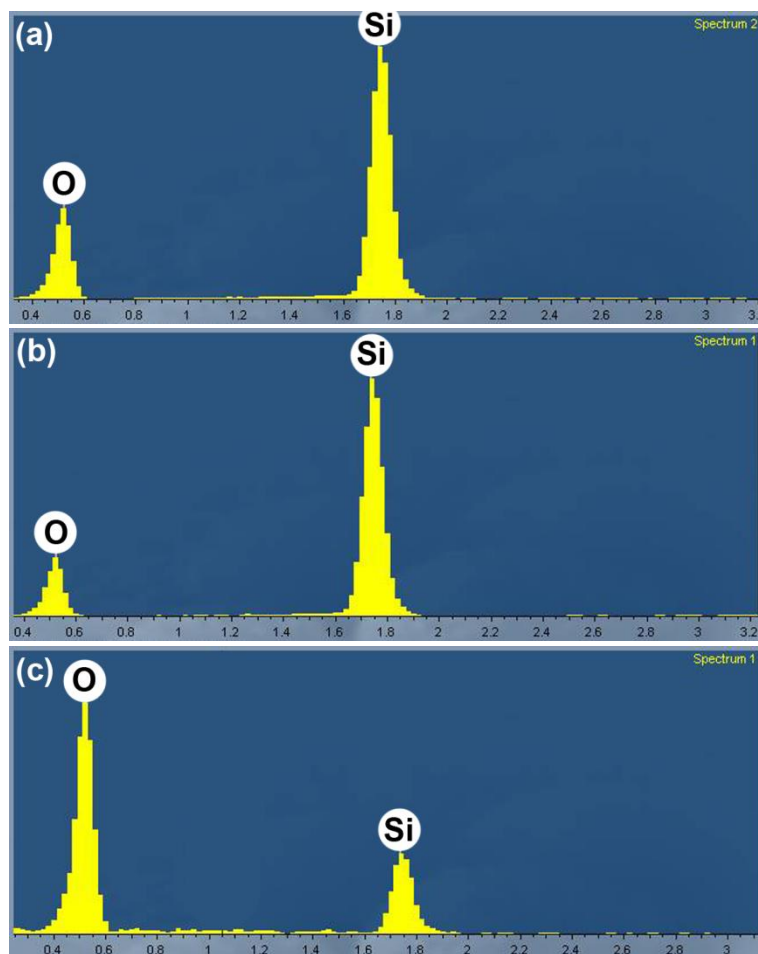


Figure 65. EDXS results for (a) Sample 21 with low absorption, (b) Sample 9 with high absorption, and (c) untextured Reference Sample

Table 29. Comparison of samples with highest and lowest light absorption properties.

Analysis	Sample 21	Sample 9	Reference
% Absorption	2.25%	61.82%	0%
Morphology	Smooth shallow channel with less recast	Rough dimpled surface structure	‘As received’ untextured Surface
EDXS (atomic %)	Si: 35.1%, O: 64.9%	Si: 40.5%, O: 59.5%	Si: 15.1% O: 84.9%

5.5 Effect of HF etching on absorption of light

As both the surface morphology and surface composition of the laser processed surface may influence the parasitic light absorption characteristics, an investigation into the effect of post-processing the textured surfaces using a hydrofluoric acid etch was completed. As presented in Figure 66, acid etching the laser treated samples greatly reduces the absorption of light at the surface. Figure 66 presents the average absorption of the light across the AM1.5G spectrum. All of the samples in this investigation, with the exception of sample 21, were found to absorb less light after 5 minutes of etching in HF.

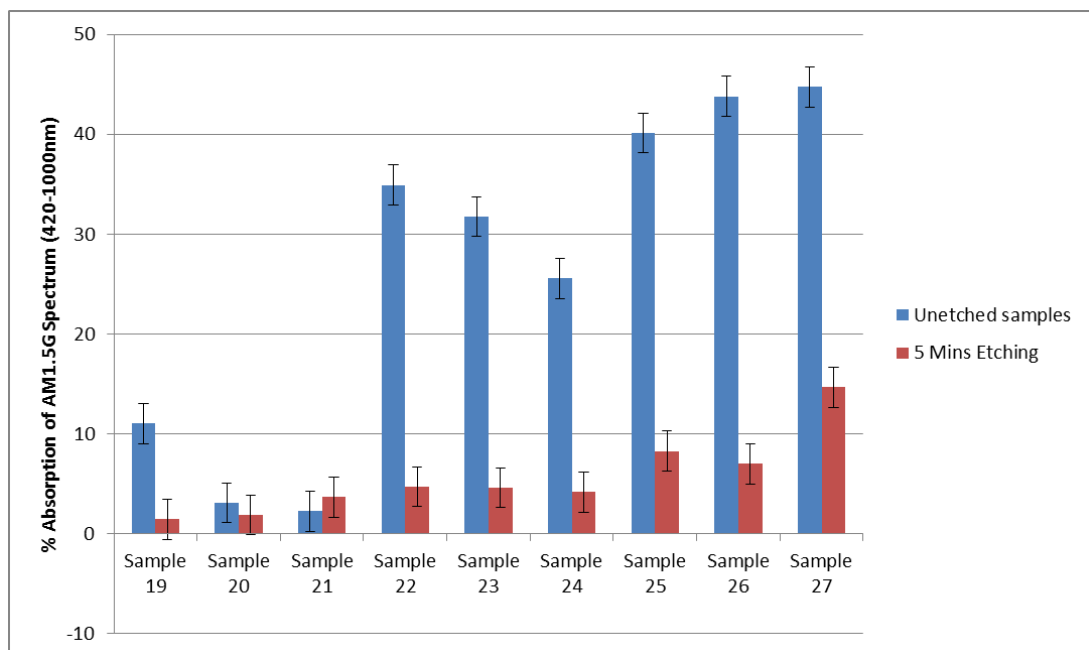


Figure 66. The effect of hydrofluoric acid (40%) etching on the absorption of light at the surface.

An investigation into the effect of HF etching on the surface morphology of the laser treated samples was also carried out. Electron microscopy and optical microscopy were utilised to analyse the sub-micrometre surface features and how their structures were altered with respect to the amount of time the acid etching was carried out. The unetched laser processed surface of sample 21 is presented in Figure 67. It can be observed that there are a range of surface features, which have been measured by SEM to range from about 400 nm to several microns in size. It is these structures that were

of interest as they are of the order of wavelength of visible light and can contribute to Mie Scattering within the superstrate [126]. The effect of HF etching on the surface morphology is visible in the images presented in Figure 68(a) and (b). It was observed that the acid etching dulls the appearance of these sub-micrometre structures, with the longer etching times causing the features to effectively elongate.

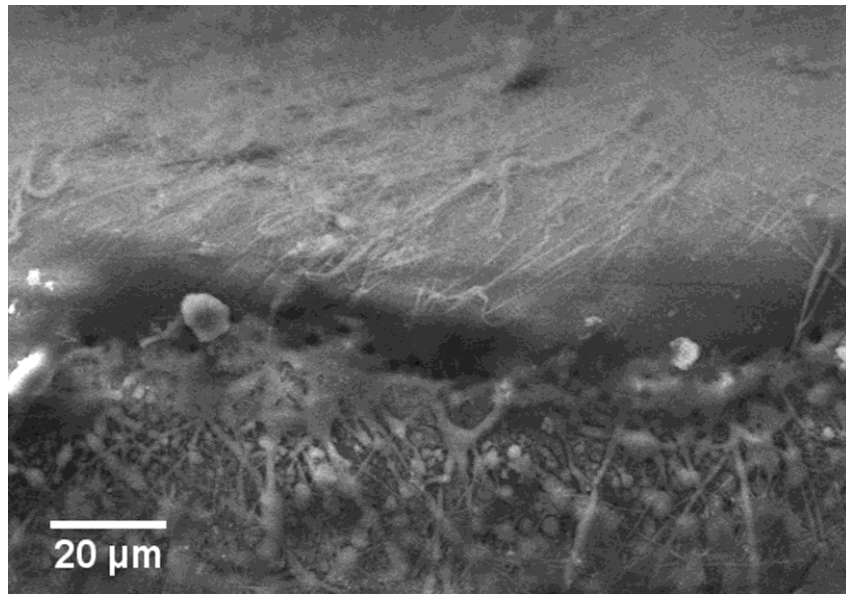


Figure 67. An electron microscope image of the surface of sample 21 before acid etching. It is possible to see a large amount of re-cast material. Visible feature sizes range from approximately 400 nm to several microns.

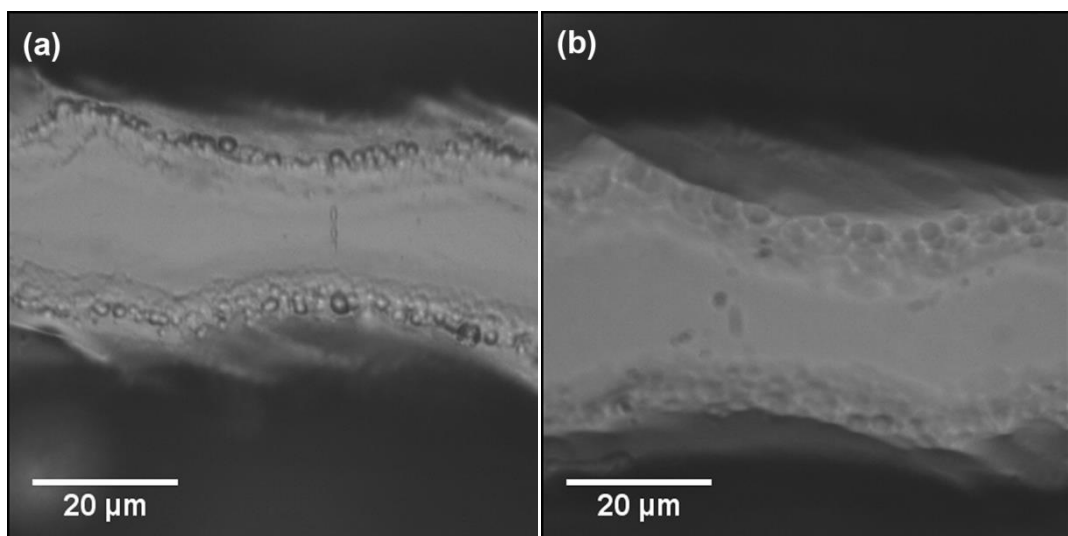


Figure 68. (a) Surface of sample 21 after 5 minutes HF etching, and (b) Surface of sample 21 after 10 minutes etching.

By acid etching with hydrofluoric (HF) acid for periods of 10 minutes it was possible to further observe the smoothing effect of the rough surface morphology as shown in Figure 69 [127, 128]. As the increase in parasitic absorption is attributed to increased laser power and vapour deposition during processing, surface material removal by HF treatment provided the highest benefits to the textures created using the higher powers. While most samples displayed improved transmission characteristics after etching, for the two samples (samples 20 and 21) with the lowest parasitic absorption losses, the effects of acid etching on transmission were negligible ($<1\%$) as shown in Figure 66.

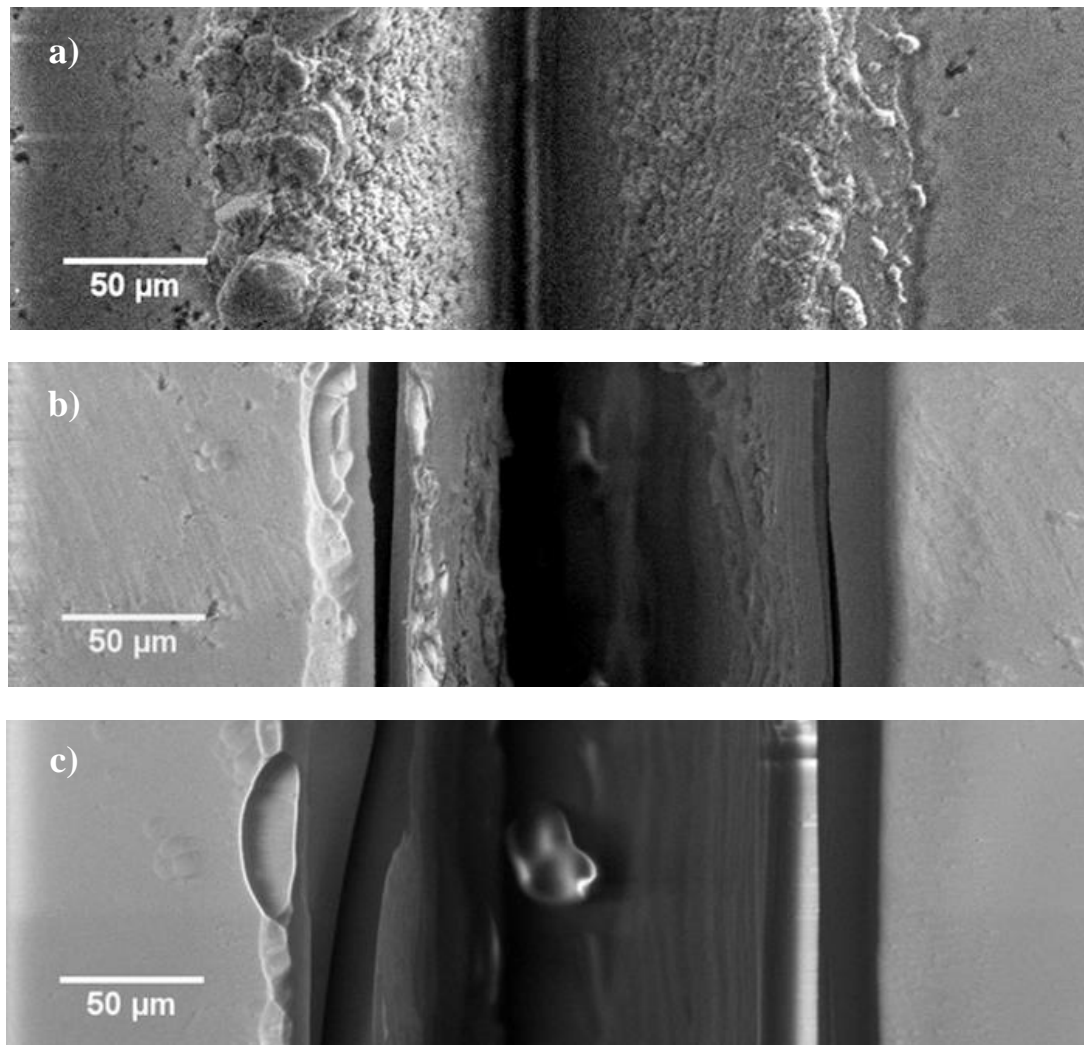


Figure 69. Top down view of the surface morphology of laser ablated channels (duty cycle 4%, PRF 400Hz, speed 1.67mm/s). unetched (a), after etching for 10 minutes (b) and after etching for 20 minutes (c).

Figure 70 illustrates the change in light absorption with respect to acid etching time. It can be observed from this data that there is a shift in the absorption peak towards the red end of the spectrum with increasing etching time. The EDXS results presented in Figure 71 and Table 30 indicate that there was little change in the surface chemistry of the laser textured glass after HF etching. This indicates that the increase in the absorption of light at the surface after laser processing may be attributed more significantly to the elongation of the acid etched features.

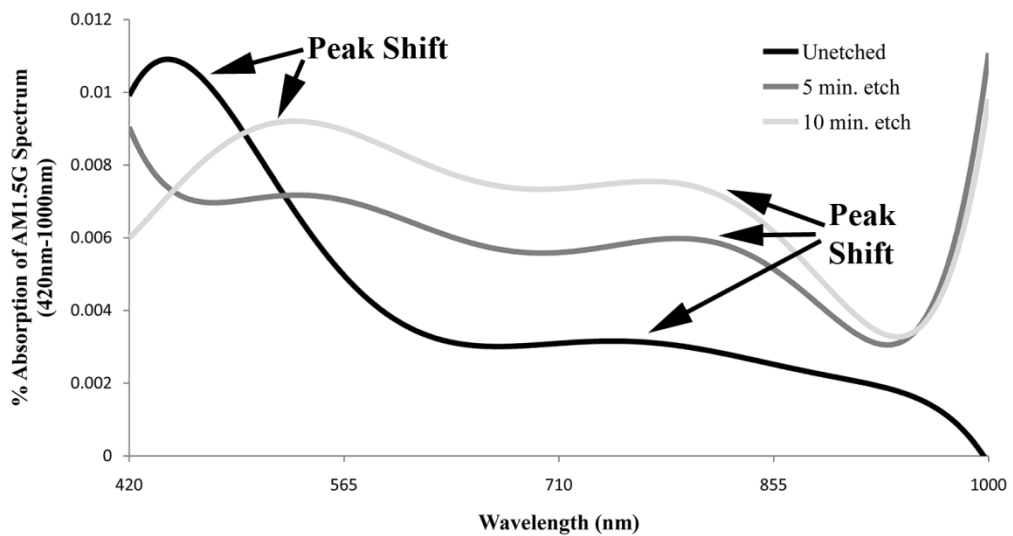


Figure 70. Absorption of AM1.5G spectrum by sample 21 with respect to etching time (data fitted with 6th order polynomial trend line for clarity). It can clearly be seen that etching causes a shift in absorption towards the red end of the spectrum. This can be directly correlated to the elongation of nanostructures on the surface due to acid etching.

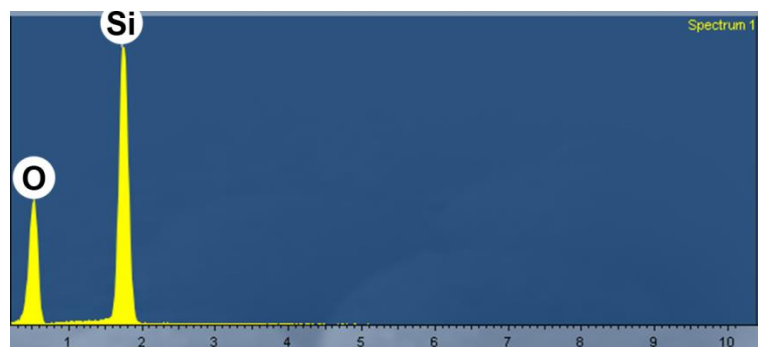


Figure 71. EDXS spectrum of sample 21 after etching with HF. Composition is close to that before HF etching (Figure 65(a))

Table 30 Comparison of surface composition before and after HF acid etching.

Analysis	Sample 21 before HF etching	Sample 21 after HF etching
% Absorption	2.25%	3.68%
Morphology	Smoother surface with elongated nanostructures	Smooth shallow channel with less recast
EDXS (atomic %)	Si: 33.2%, O: 66.8%	Si: 35.1%, O: 64.9%

5.6 Efficiency vs angle of incidence

In order to assess the possible gains of the textured superstrate it was necessary to test the efficiency of a solar cell used with the textured superstrate with varying angular incidence of light. Figure 72 displays the acquired I-V data for the same solar cell mounted under the three different superstrates; one untextured as a reference and the other two with the maximum transmission textures (samples 20 and 21). This data was acquired with the light incident at 10° to the surface. The texture characteristics and I-V data are presented in Table 31. The results indicate that at acute angles of incidence there is a significant improvement in the cell performance due to the enhanced light trapping effect caused by the textures on the superstrate. At 10° incidence to the surface plane a relative efficiency gain in the solar cell of 51% was found for sample 21 in comparison to the untextured reference. Voc, Isc, and fill factor were also improved relatively by 2.1%, 44.6%, and 2.7% respectively.

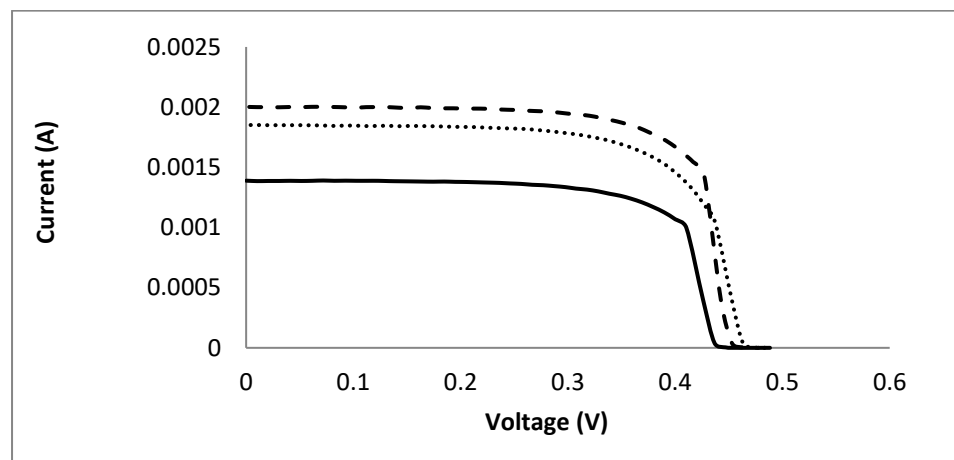


Figure 72. I-V curves for solar cell at the acute angle of 10° incidence. untextured reference (solid), sample 20 (dotted), and sample 21 (dashed).

Table 31. Parameters and results for I-V measurement with light incident at 10° to surface.

Sample	Untextured	Sample 20	Sample 21
Depth (μm)	-	95	72
Width (μm)	-	173	146
V _{oc} (V)	0.478	0.483	0.488
I _{sc} (A)	0.00139	0.00185	0.00201
Fill Factor (%)	67.20	67.15	69.01
Efficiency (%)	0.49	0.66	0.74

While there were significant efficiency gains at an angle of incidence of 10°, the solar cell efficiency was degraded relative to the untextured reference at higher angles of incidence. Figure 73 indicates that cell efficiency was only improved relative to the untextured reference for acute angles in the range of 20° to 10°. As shown in Figure 60(b) the surface of the samples tested have a somewhat sinusoidal shape. According to simulations performed by Sanches-Illescas et al. the highest benefit of the textured surface can be found at acute angles of incidence, which corresponds well with our findings [51]. The reduced performance at other angles could be attributed to the effect of laser processing on the surface quality itself, changes in surface composition, and also the increased path-lengths travelled by the light due to enhanced scattering, causing additional parasitic absorption losses in the superstrate.

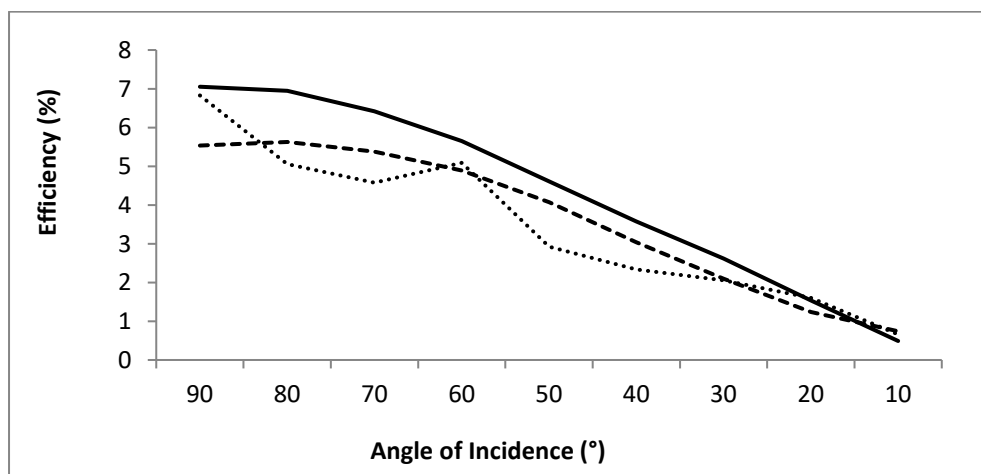


Figure 73. Solar cell efficiency with different angles of incidence for the untextured reference (solid), sample 20 (dotted), and sample 21 (dashed).

Chapter 6 Characterisation for Quantum Dot Solar Cells

Quantum dot based solar cells are an emerging field of research. Quantum dots offer great advantages in that they can be low-cost to produce, yet be tailored to optimise conversion efficiencies through size control. For the first part of the investigation of such a solar cell set-up, the optical absorption characteristics of alkyl-capped silicon quantum dots were investigated. It is envisaged that these quantum dots could be utilised in next generation solar cells. The second section of this investigation concentrates on the 3D characterisation of macroporous monolithic morphologies, which have wide applications in existing and next generation solar cell technologies. This is especially true for quantum dot based solar cells, where much work has concentrated around the use of porous semi-conductors on glass superstrates.

6.1 Absorption characteristics of alkyl-capped silicon quantum dots

Figure 74 shows the optical microscope image of the silicon nanocrystals taken immediately after a third repetition of the drop deposition technique. The silicon quantum dots appear to be about 1 μm in diameter, possibly due to diffraction broadening, significantly larger than shown by other topographical characterisation methods, such as AFM as shown in section 3.16.2. This could be attributed to the formation of clusters of nanocrystals on the surface of the substrate after subsequent depositions [117]. It is clearly visible from this image that the Si nanocrystals do not form a continuous layer on the substrate material. It can also be observed that there are varying degrees of surface coverage of the Si-QD with some areas more and some less sparsely populated. Surface coverage could likely be improved through optimisation of the Si-QD solution concentrations and the deposition method.

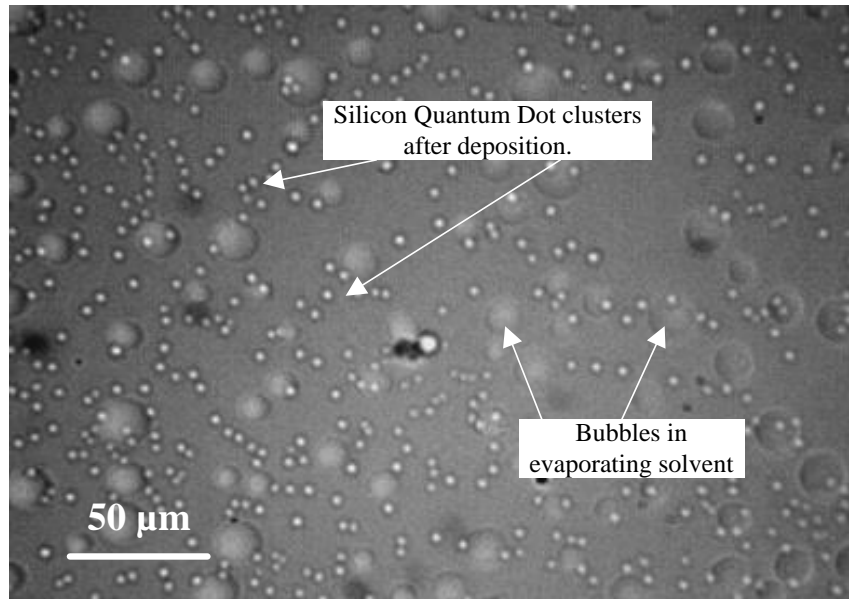


Figure 74: Optical microscope image of nanocrystalline silicon on substrate shortly after drop deposition. Bubbles indicate that the solvent is still present.

Figure 75 shows the absorption characteristics of the silicon quantum dots after they were bonded to the glass substrate. The absorption measurement was performed after each repetition of the drop deposition technique and subsequent drying time. It can clearly be seen that there is a small increase in absorption of the incident broadband light by the deposited nanocrystals between 420 nm and 520 nm. Increases in absorption in the same wavelength range have been found in studies where Si nanocrystals are embedded in a SiO₂ matrix [64, 65]. Other studies on alkyl-capped Si nanocrystals have found an increase in absorption only from approximately 325 nm and below [63, 129]. Vasiliev et al. simulated the effect of oxides on the optical absorption of Si nanocrystals using a confinement model revealing that for certain oxide configurations, the optical absorption gap was further lowered to 2.4 eV (520 nm), which correlates well with our results [130]. This indicated that it is the presence of oxides in our nanocrystals, as indicated by the XPS analysis performed by collaborators [115], was causing absorption at lower photon energies. However, it was not possible to achieve a uniform coverage of the substrate with the Si quantum dots, which may have led to further inconsistencies in the absorption measurement in this preliminary investigation. The source of this error is due to inhomogeneous distribution of the quantum dots, and is also due to the variation in the illumination

source intensity in the integrating sphere setup. The low population of silicon quantum dots on the substrate surface led to a lower signal to noise ratio during the measurements. By increasing the number of quantum dots on the substrate between each measurement an improved signal would be obtained. The variation in light source intensity could be corrected by creating several samples with different quantum dot populations and performing all of the absorption measurement in one session.

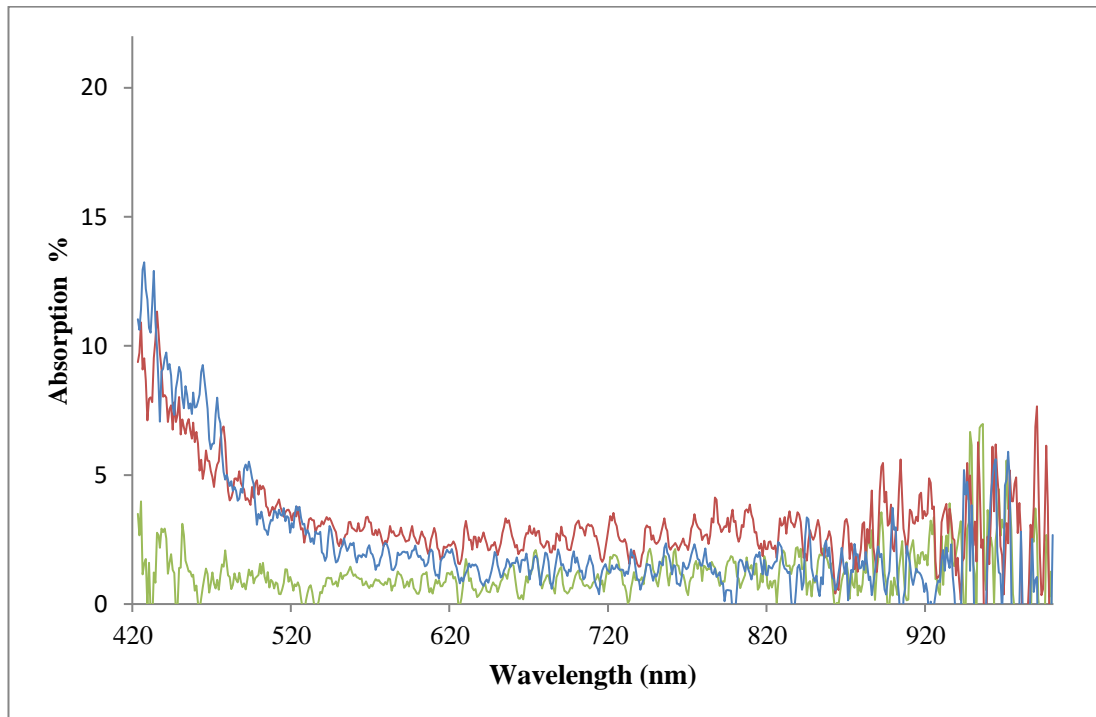


Figure 75: Light absorption characteristics of Si QDs after 1 deposition (green), 2 depositions (blue), 3 depositions (red). The absorption of the glass and the solvent have been subtracted from this data.

6.2 Absorption characteristics of alkyl-capped silicon quantum dots on laser textured superstrates

Taking the absorption results of the previous section, it was of interest to investigate the absorption characteristics of the silicon quantum dots when used in combination with laser textured superstrates, as investigated in Chapter 5. Three samples which exhibited low parasitic absorption losses after HF etching (Samples 19, 20, and 21) were chosen for this investigation. The absorption results for the three different textured superstrates are shown in Figure 76.

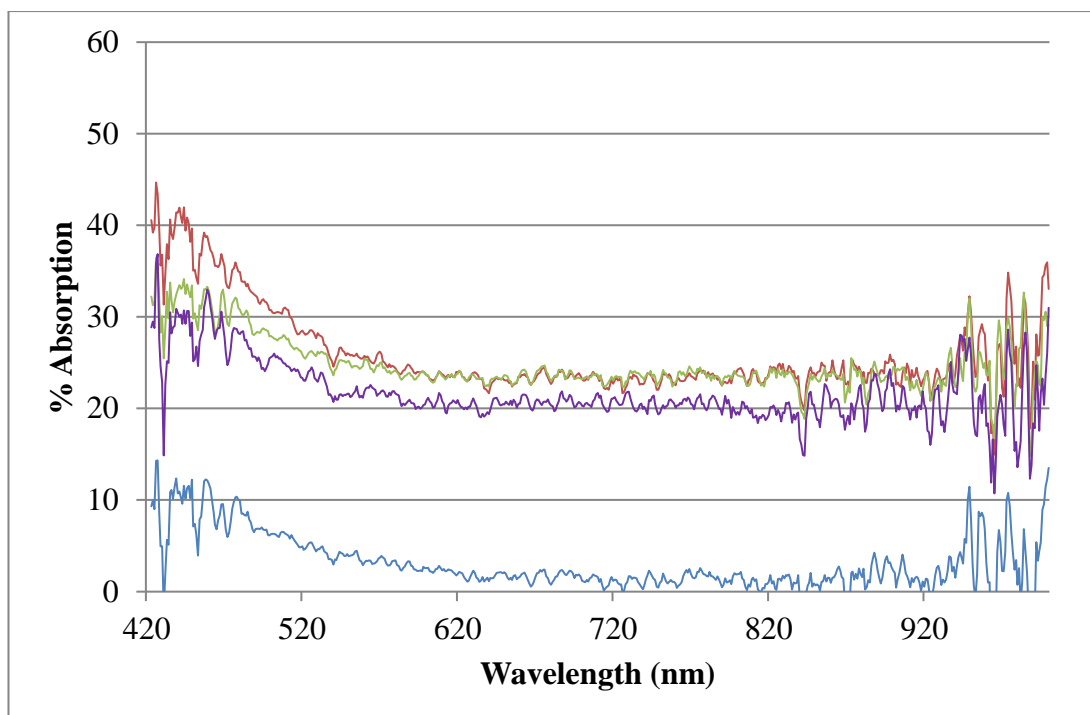


Figure 76: Light absorption characteristics of Si QDs on laser textured superstrates after drop casting. Untextured reference (blue), Sample 19 (red), Sample 20 (green), and Sample 21 (violet). The absorption of the glass and the solvent have been subtracted from this data.

The reference measurement itself indicated increased absorption between 420nm and 520nm when compared with the results from the initial absorption study, which can be attributed to the fact that five depositions of silicon quantum were performed for this measurement in an effort to increase the sensitivity and resolution of the results. Compared with the untextured reference superstrate, all three textured superstrates indicated increased absorption across the entire spectrum from 420nm to 1000nm. However, as was found in the initial absorption characterisation experiments, the silicon quantum dots used in this investigation absorb light mostly in the 420 nm to 520 nm range. The absorption across the remained of the spectrum from 520 nm to 1000 nm in this case could be attributed to several possible causes. Firstly, during deposition time was allowed for the solvent to evaporate. However, due to the increased amount of silicon quantum dots depositions (five depositions for this experiment), it is possible that, despite best efforts, some solvent remained on the superstrate at the time of measurement as there remained a ‘waxy’ residue on the surface. Secondly, the effect of light scattering caused by the laser textured superstrate

may have caused additional absorption in the remaining solvent. In order to specifically investigate the increase in absorption between 420 nm and 520 nm, the measurements were referenced relative to each other between 520 nm and 1000 nm, which contributed to the negation of the unaccounted effects of absorption in any unevaporated solvent. The highest increase in absorption over the 420 nm to 520 nm range was found for Sample 19, the spectrum of which is indicated in Figure 77. An approximate increase of 5% in absorption of across this wavelength region was found. While the gain is marginal, there is an indication that the laser textured glass does contribute to enhanced light absorption in the deposition silicon quantum dots. An increase in absorption in this wavelength region correlates well with the initial absorption spectra measured, and hence it could be deduced that the increase in absorption measured is due to increased absorption in the quantum dots and not just in any remaining solvent.

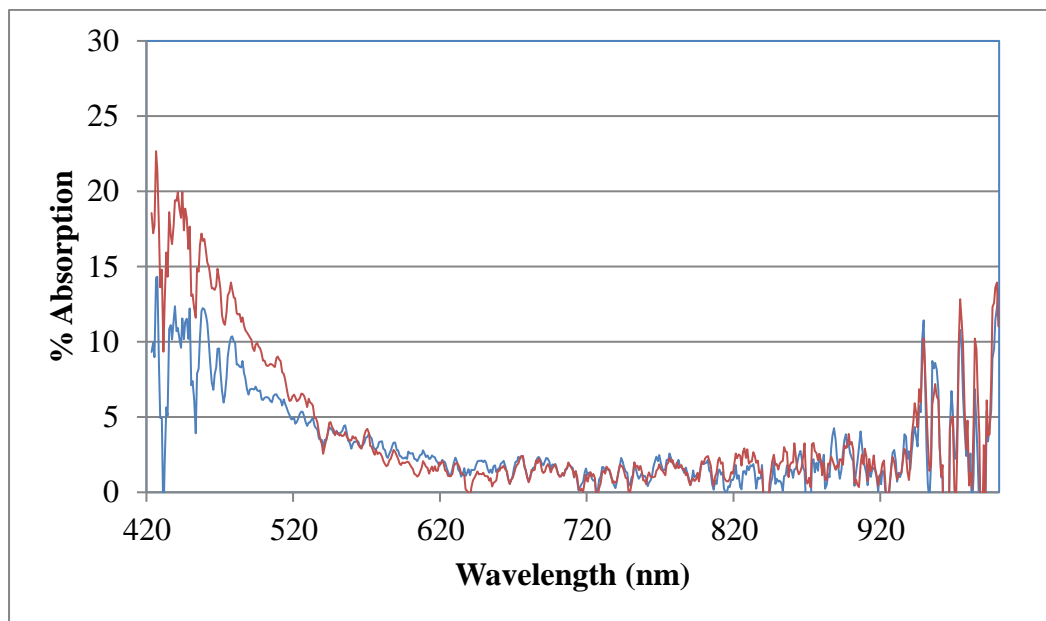


Figure 77: Spectra for untextured reference (blue) and Sample 19 (red).

The spectra have been reference matched from 520 nm to 1000 nm.

6.3 FIB serial sectioning for the 3D reconstruction of macroporous structures

Significant amounts of work have been done in the research of porous silicon for photovoltaic applications, as there are opportunities for enhanced light trapping performance when utilising the porous morphology architecture. Next generation solar cells, such as dye-sensitised solar cells and certain quantum dot solar cell architectures

also make use of macro- and nano-porous structures. These structures can play various roles depending on the exact cell type and design, however, one commonly cited effect of utilising such structures are the beneficial light trapping effects they provide. As part of this study, a method for characterising macro-scale porous structures in 3D was investigated utilising a focused-ion-beam (FIB) to serially section the sample, while simultaneously being able to image the sample cross section at high magnification using scanning electron microscopy (SEM). The materials investigated in this study were carbon and silica based monoliths. While these materials would potentially have some applications in solar cell architectures, the aim of work was to investigate the usefulness of the characterisation method for these structures, as opposed to specifically for these materials.

6.4 3D reconstruction and morphological analysis of the carbon monolith

The resulting 3D reconstruction of the porous carbon monolith from the 2D-image stack consisting of 93 images is shown in Figure 78. The volume reconstructed had a rectangular geometry with dimensions of $58.2\ \mu\text{m} \times 26.5\ \mu\text{m} \times 9.3\ \mu\text{m}$ in the X, Y and Z directions, respectively. As shown in Figure 78, the reconstructed carbon monolith exhibited an interconnected porous structure formed by quasi-spherical macropores with sizes mostly ranging from approximately $4\ \mu\text{m}$ to $7.5\ \mu\text{m}$. Moreover, the 3D reconstruction revealed a non-homogeneous spatial distribution of the inter-skeleton macropores within the volume analysed. The latter could be attributed to a non-uniform packing density of the silica particles within the phenolic resin used for preparation of the carbon monolith. Likewise, the relatively broad range of macropore sizes observed in the monolith reconstruction could be attributed to the use of silica particles with non-uniform sizes as templates, which could also largely affect the packing density of the silica particles in the silica/phenolic resin mixture.

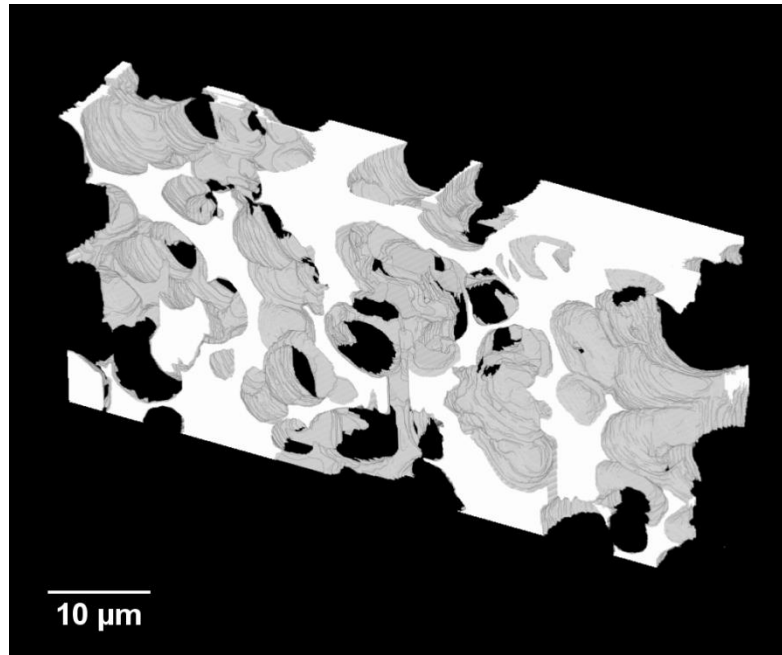


Figure 78: 3D reconstruction of the porous carbon monolith

Furthermore, the presence of pores with sizes between ca. 10 μm and 15 μm range is a clear indication of the formation of voids in the space between the silica particles during preparation of the monolith. This could be explained by the limited infiltration of the phenolic resin into the inter-particle space due to poor mixing of the silica particles with the phenolic resin and/or high viscosity of the phenolic resin during preparation. This non-homogeneous macro-pore morphology is consistent with previous results obtained by Eltmimi et al. in carbon monoliths prepared with 5 μm silica particles as templates, where the presence of inter-particle voids was already suspected based on experimental evidence [123].

Therefore, the direct confirmation of the real morphology of a monolith via reconstruction and visualisation of its porous structure (including voids) represents a clear advantage of this FIB-SEM methodology, which can significantly contribute to speeding up the optimisation of the porous structure morphology in view of improving its applications specific performance. The total macroporosity of the volume analysed following binarisation of the corresponding image stack was found to be 72.9%. This value agrees well with the results obtained on the same sample type by MIP, where the total porosity was found to be 76.8% and 80.2% for two consecutive analyses. MIP measurements also allowed determination of the pore size distribution, as shown in

Figure 79. A median pore diameter (in volume terms) of 2.6 μm and 2.9 μm was obtained for the two consecutive MIP analyses, respectively. This diameter range was well within the size range suitable for manual outlining when processing the images, which is why the porosity values correlate well.

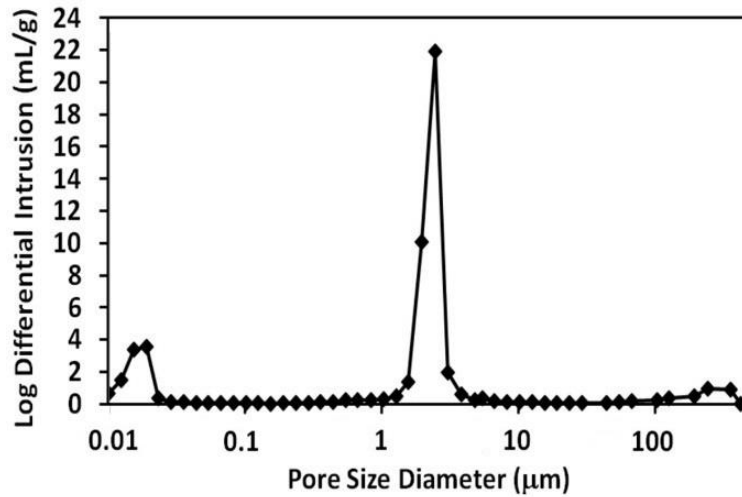


Figure 79: Mercury porosimetry results showing pore size distribution in the carbon monolith [122].

6.5 3D reconstruction and morphological analysis of the silica-based monolith

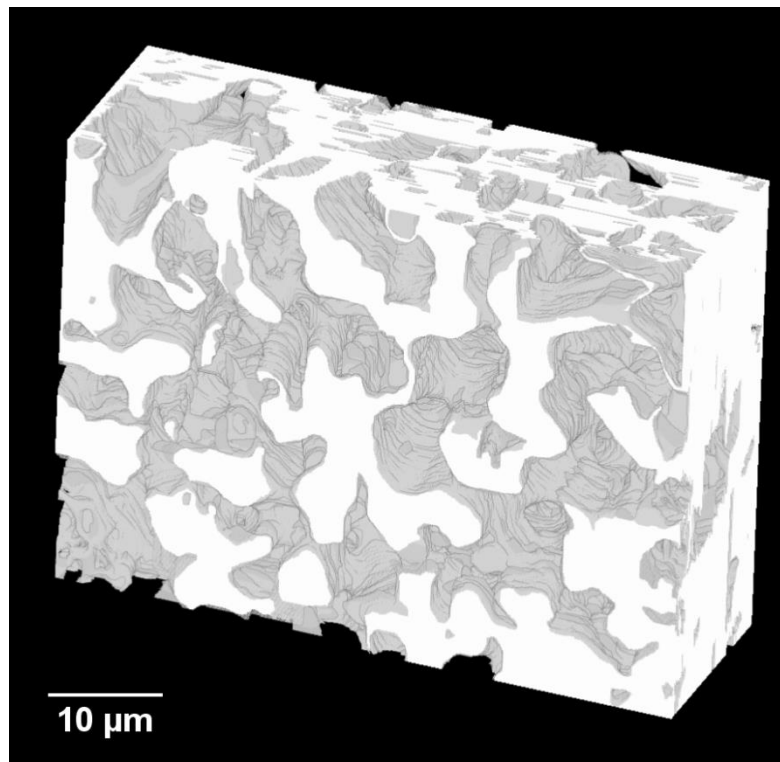


Figure 80: 3D reconstruction of the porous silica monolith (Monotrap).

The 3D reconstruction of a commercial porous silica-based monolith from the corresponding 150-image stack obtained by FIB-SEM analysis is shown in Figure 80. The reconstructed volume also had a rectangular geometry with dimensions of 44.7 μm x 33.7 μm x 10 μm in the X, Y and Z directions, respectively. As can be seen in Figure 80, the reconstructed volume exhibited a rather homogeneous spatial distribution of interconnected macropores with irregular shapes and variable sizes, which contrasts well with the mainly spherical shaped pores found during the analysis of the carbon monolith as shown in Figure 78. Therefore, the modification of the silica monolith skeleton with activated carbon proved to be highly effective for successful reconstruction and visualisation of the silica-based monolith macropore structure by FIB-SEM analysis. The electrical conductivity provided by the carbon assisted in the minimisation charge build-up during SEM analysis, typically arising in non-conducting materials such as silica, and successfully allowed FIB-SEM analysis. Although no specific information on how this commercial carbon-modified silica-based monolith was produced, protocols for the preparation of carbon-silica composites have been already described in previous works. The total macroporosity of the volume analysed for the carbon-modified silica-based monolith was found to be 52.9%, which agrees well with the 56.0% value for total porosity obtained by MIP. The pore size distribution of the silica-based monolith can be seen in Figure 81, with a median pore diameter (in volume terms) of 2.7 μm .

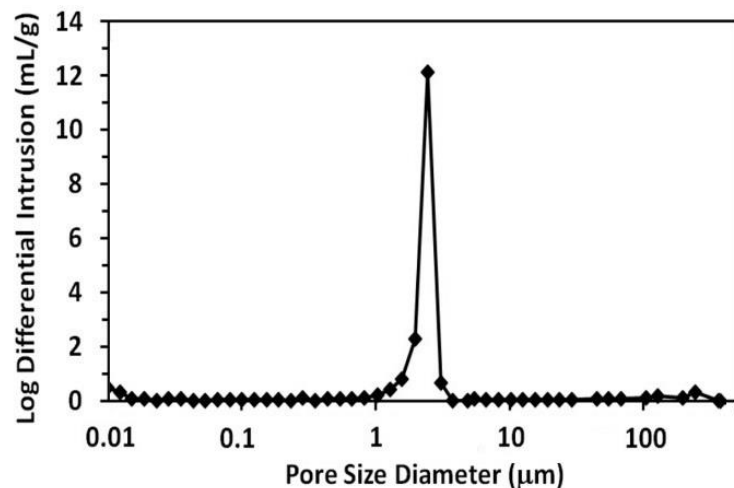


Figure 81: Mercury porosimetry results showing pore size distribution in the silica-based monolith [122].

Overall, the results of this investigation indicate that FIB-SEM serial sectioning is a useful method by which to evaluate the 3D morphology of porous materials. This study has found that the FIB-SEM method has comparable accuracy in terms of porosity evaluation of porous materials where the pore size distribution is above 1 μm diameter. One of the main advantages of this characterisation method is that it can evaluate the true porosity of a material, which includes both open and closed pores, whereas other characterisation methods such as MIP do not offer this functionality. This especially has application in the evaluation of porous materials in solar cells, as in the case with materials such as porous TiO_2 , closed pores may have a great effect on the light scattering and electron transport mechanisms within the solar cell.

While the FIB-SEM approach definitely has merit in the evaluation of the porous materials, there also remain some challenges with this method. Firstly, there is a high cost associated with the process as it involves high vacuum, and it is also time consuming. Secondly, there remains some research to be completed on the use of the FIB-SEM approach with higher SEM magnifications. This is especially true for non-conducting materials such as silica, where the sample can become charge saturated at high magnifications, which reduces SEM image quality considerably. Another challenge lies in the fact that at high magnification, the depth-of-field of the SEM is reduced which makes it even more time consuming.

Chapter 7 Conclusions

Verification of the 3D non-contact optical profilometer

Verification investigations performed on the developed 3D noncontact optical profilometer included measurement of the linear stage performance using a dual scale analysis, and the evaluation of the 3D measurement performance. The analysis of the linear stage performance was performed in line with ISO 230-2 standards for the calculation of stage accuracy and repeatability. The investigation confirmed the suitability of the design for 3D profilometry use. The performance of the stepper motor axes designed was considered to be acceptable considering the low-cost nature of the design. The stepper motor driven X and Y axes performed considerably better in the small scale analysis, with bi-directional accuracies of $\pm 8 \mu\text{m}$ and $\pm 15 \mu\text{m}$, which can be attributed to the shorter travel range of the investigation and also the superior accuracy of the dial gauge indicator utilised in the small scale measurement analysis. There XY positioning accuracies are acceptable over this measurement range for the purposes of image stitching if sufficient image overlap is allowed as to enable software to perform accurate alignment of the measurement data. The Z-axis performed with acceptable uni-directional accuracy of $10 \mu\text{m}$ over the $200 \mu\text{m}$ small scale analysis displacement. When considering the possible sources of measurement error in this exercise, it would be worthwhile suggesting that an alternative method of stage measurement, such as laser interferometry, be implemented to gain a better understanding of the various aspects of the linear stage performance. Laser interferometry would provide a method of measurement over the full travel range with nanometre level accuracy, data which can then be used to calibrate the system to a much higher level of accuracy.

To evaluate the 3D measurement performance of the system, a procedure was implemented to evaluate the performance over a dual scale analysis. As it was difficult to source a suitable traceable calibrated step height reference in this size range and with the appropriate surface characteristics for this type of optical instrument it was necessary to design and manufacture a purpose build step height artefact. This was achieved by milling a brass measurement artefact to the desired dimensions, with a

nominal 100 μm step height. This sample was subsequently measured by Scanning Electron Microscope (SEM), White Light Interferometry (WLI), and Stylus Profilometry (SP). These three measurement methods returned almost identical step-height measurement results of 103 μm . A nominal 500 μm thick metrology gauge block was utilised as the other sample in the dual scale analysis, and was also measured using WLI and SP, with the resulting step height of 512 μm . While these measurements are not traceable metrology standards for the evaluation of the absolute accuracy of the system, they were designed to give some initial indication of the estimated accuracy of the system. The investigation demonstrated the capability of the developed system to measure step heights in the range of 100 μm to 500 μm , however the evaluation of the absolute accuracy of the system would require significantly more work around the manufacture and statistical analysis of the measurement artefact. The accuracy evaluation of depth-from-focus based profiling instruments is on-going work within the field of metrology, where National Metrology Institutes have suggested that further investigation and standardisation is required [111]. These artefact measurement values were then used in the evaluation of the 3D measurement performance of the developed profilometer. Results were calculated from a Design of Experiments carried out using different Z-axis sampling intervals, with step height reported after data post-processing. Accuracies reported on the measurement of the 103 μm step-height were as good as 99.95%, which gives initial indication that the performance of the system is within an expected range. While acknowledging that this accuracy measurement is only indicative and not absolute, one can equate this performance to a measurement uncertainty of $\pm 4 \mu\text{m}$ over the 103 μm step height. This value correlates well with the with the 10 μm uni-directional accuracy performance of the the Z-axis in the initial linear axis performance investigation which was carried out over a 200 μm travel range. These performance characteristics compare well with those reported by Sun and Claverley who performed calibration analyses on a commercially available instrument with a similar principle of operations, whose measurement of spherical reference samples resulted in 3D measurement accuracies in a range between -7 μm and +19 μm [111]. The methods of step height evaluation reported in this work contribute to the analyses of depth-from-focus based measurement instrumentation and to the calibration and verification issues reported by Sun and Claverley.

Measurement repeatability was another output of this investigation. When the absolute accuracy of an artefact cannot be certified, the same artefact can be used to assess the repeatability of the measurement technique through the repetition of measurements. This investigation found the largest standard deviation of the mean plane heights across six measurement runs to be between 0.1 μm and 0.9 μm . This compares well with Sun and Claverley's investigation, which found the standard deviation of sphere size measurements to be in the sub-micrometre range [111]. It can be derived from these repeatability measurements that the developed device may be suitable for the evaluation of structures with height in the sub-10 μm range, however further investigation is required in order to verify this and to establish what measurement conditions are most favourable for this outcome.

It has been reported that 3D profilometry instruments based on the depth-from-focus principle have limitations in the measurement of surface topographies of translucent materials, particularly in the presence of micro-scale surface roughness [80]. However, in this work it has been clearly demonstrated that the 3D non-contact optical profilometer developed in this thesis offers capabilities in the measurement of laser micro-machined translucent materials in the presence of micro-scale surface roughness, which is a new result in this research field.

It is envisaged that this device can be utilised in gaining further understanding of surface micro-structures. The usefulness of this device includes the surface topography analysis of various micro-structures used in solar cell applications. Using the 3D non-contact optical profilometer to measure the surface topography of laser structured glass for example, would allow for real surface topologies, including roughness, to be characterised and used in simulations of the light trapping effect in solar cells. This approach should therefore provide a new level of highly accurate data and simulation realism to this research field.

Laser texturisation for enhanced light trapping performance

Laser textures were created on fused silica glass using a CO₂ laser operating in pulsed mode, for which the parameters were defined by Design of Experiments. The size of the textures varied from 72 μm to 974 μm in depth, and 146 μm to 213 μm in width. The parasitic absorption loss of light in the laser textured glass was measured using an integrating sphere and spectrometer setup, and losses ranged from 2.25% to 63.28%. The surface morphology was smoothed by HF etching for up to 20 minutes and resulted in improved transmission for most samples. The increase in transmission after acid etching of the two samples with the lowest parasitic absorption losses (samples 20 and 21) were negligible. The I-V data for the solar cell under different textures was assessed by encapsulating the solar cell in transparent resin and placing it in contact with the flat side of the laser textured front cover glass. This allowed the measurement of the characteristics of the solar cell under the textured superstrate by measuring the I-V data at varying angles of incidence. While increased performance was not found at all angles of incidence, for acute angles of incidence (10°) the relative efficiency increased by up to 51% with an increase in the V_{oc} of 2.1% and in the I_{sc} of 44.6%. An improvement in the fill factor of 2.7% was also observed.

While these results indicate that this particular laser processing approach is not favourable at all angles of incidence as experienced in an everyday practical situation, the evidence does point to the fact that there have been some improvements achieved with this process. It is postulated that by using different laser sources more suited to the fine ablation control required to further optimise this process, that much improved solar cell performances could be achieved. Indeed, when considering the results reported by Kang et al., it is certainly feasible with a different laser source, and with improved glass processing, that building integrated solar photovoltaics would benefit from micro-structured solar cell superstrates [38].

Characterisation for Quantum Dot Solar Cells

From the perspective of absorption in next generation solar cell materials, the absorption of light by alkyl-capped silicon quantum dots was investigated. The absorption of the alkyl-capped Si quantum dots drop deposited onto a 1 mm thick fused quartz substrate was measured using an integrating sphere and spectrometer setup. Subsequent depositions indicated that there is an increase in absorption of broadband light in the 420 nm to 520 nm range. However, the non-uniformity of the drop deposited layer may have led to inconsistencies in the absorption measurement. Much work needs to be done in order to control the layer by layer depositions and to understand the properties of this novel material. By using other deposition techniques, such as evaporation, it will be possible to control the thickness of silicon quantum on the surface of the substrate, which may improve the understanding of the material properties.

Subsequent investigations were completed to evaluate the effect of light trapping when the silicon quantum dots are deposited directly on a laser textured superstrate. Deposition cycles consisting 4 ml drops on to the target for five cycles were prepared and evaluated. Additional absorption across the spectrum from 420 nm to 1000nm was observed, however the increase in absorption from 520 nm to 1000 nm is thought to have originated from increase light trapping within solvent remaining on the superstrate. When the data was adjusted to allow for this effect, an increase in absorption of up to 5% in the 420 nm to 520 nm was observed. This can be attributed to additional light trapping effects in the silicon quantum dots and fused quartz superstrate. This increase correlated well with initial observations on the absorption characteristics of these silicon quantum dots, and represents novel results in the field.

As porous material morphologies are increasingly common in the design of next generations solar cells, an investigation into a 3D characterisation method which could be used to gain a better understanding of the pore connectivity and topology. To achieve this a Focused-Ion Beam (FIB) milling technique was utilised to provide serial sectioning capabilities within a Scanning Electron Microscope (SEM). Both conducting and non-conducting materials were investigated, in the forms of a carbon monolith and silica monolith respectively. The serial sectioned images were post-

processed utilising software developed to correct for dimensional anomalies due to the imaging angle of the SEM. After manual image segmentation and subsequent 3D reconstruction, the porosity of the materials was analysed, and the results compared directly with those of an established porosity measurement technique, Mercury Intrusion Porosimetry (MIP). Porosity results for the carbon monolith were found to be 72.9% and (averaged) 78.5% for the FIB-SEM analysis and MIP analysis respectively. For the silica based monolith, porosity results were found to be 52.9% and 56% for FIB-SEM and MIP analyses respectively. This indicates that the FIB-SEM technique is a suitable technique for the evaluation of macroporous materials. One main advantage of the FIB-SEM method is that it is possible to evaluate all of the pores in a macroporous material, whereas traditional measurement techniques such as MIP can only measure open and connected pore structures. In a comprehensive review by Cocco et al. on three-dimensional micro-structure imaging methods for energy materials, there was no report of the FIB-SEM characterisation method being utilised for the characterisation of photovoltaic materials [131]. It is envisaged that this characterisation method can be used to gain a better understanding of macroporous solar cell materials, and also can be used as a real 3D surface measurement instrument, data from which can be utilised in simulations of the interaction of solar cell materials with light and the light trapping effect created by such porosity.

7.1 Future Work

There are several possible end-uses for the technology developed in this research. While the main focus of this research lies in the improvement of light trapping for photovoltaic cells for solar energy harvesting, the technology may also be transferable to other fields. The geometrical light trapping effect is of great importance in thin-film and quantum dot based solar cells also, mainly due to the fact that there is less light absorbing material present. In order to preserve the potential efficiency of these types of solar cells, it is necessary to improve the chances of absorption. In thin-film solar cells, this takes place not only through the light trapping effect, but also through the longer path lengths the photons must take to traverse the cell. Simulations in the literature have shown that the light trapping effect can increase the effective thickness of thin-film solar cell materials by up to 40 times [8]. There are other possible uses in the field of optics, for example, improving the absorption efficiency across a wider

range of angles in optical detectors is also of interest. It is believed that by varying the texture it will be possible to control the sensitivity of the optical detectors at certain angles, which operate in a similar fashion to large scale photovoltaic devices.

The 3D non-contact optical profilometer developed in this work may be leveraged in several approaches. This tool can be used to evaluate the surface morphology of laser processed surfaces, to evaluate micro-sized features in 3D and to evaluate surface roughness. This surface data can also be exported for simulation purposes, which will allow for more realistic manufactured surfaces to be utilised in simulation investigations. This is of particular importance where this simulation involves interaction with light, as features and roughness on the microscale greatly influence the characteristics of the interactions of that material. However, there remains further work to improve the characterisation of the capabilities of the developed system, both in terms of accuracy of the motion axes and accuracy of the overall 3D measurement system. There are multiple possible sources of error which should be minimised, and a more accurate linear measurement technique such as laser interferometry should be utilised to improve the performance of the technique and to widen the understanding of the influence of various sources of inaccuracy on the overall 3D measurement performance of the system. The work in this thesis has provided initial results to verify the feasibility of the technique, however further work must be undertaken to validate the use of such an instrument and configuration as a metrology tool suitable for measurement at the micrometre scale.

The evaluation of silicon quantum dots has shown great promise in this work. The absorption spectra measured correlated well with the estimated material band-gap. While the results found were positive initial results, further work is needed on the deposition of the quantum dots on the superstrates, which will greatly improve the understanding of the interaction of this novel material with light. Further work could include the development of a quantum dot solar cell based on the alkyl-capped silicon quantum dots used in this work, however, much work needs to be done in designing and optimising a solar cell architecture.

In a similar way the method developed through the use of FIB-SEM serial sectioning can be utilised for the evaluation of porous macro-structures. While more work must be done on the development of this method to work with smaller pore diameters and with larger volumes, the indications from the results in this work are that this method is a suitable method for the evaluation of pores with diameters on the order of 1 μm equivalent diameter and greater, with accurate results available in the measurement of porosity. Therefore, it is suggested that future work leverage the developed FIB-SEM work to improve the simulation realism through the utilisation of improved surface models based on real morphological data.

References

- [1] A. Luque and S. Hegedus. *Handbook of Photovoltaic Science and Engineering, 2nd Ed* 2011 Available: <http://prism.talis.com/dcu/items/595709>.
- [2] Fraunhofer Institute for Solar Energy Systems ISE, "Photovoltaics report," Fraunhofer, Freiburg., Aug 2015. 2015.
- [3] S. J. C. Irvine. *Materials Challenges: Inorganic Photovoltaic Solar Energy* 2014. DOI: 10.1039/9781849733465.
- [4] Y. Hamakawa. *Thin-film solar cells: Next generation photovoltaics and its applications*. 2004.
- [5] A. J. McEvoy, L. Castaner and T. Markvart. *Solar Cells: Materials, Manufacture and Operation* (2nd ed. ed.) 2012.
- [6] K. A. Jackson. *Silicon Devices: Structures and Processing* 1998.
- [7] J. Wu and Z. M. Wang. *Quantum Dot Solar Cells* (1st ed.) 2013.
- [8] Jianhua Zhao, Aihua Wang, P. Campbell and M. A. Green. A 19.8% efficient honeycomb multicrystalline silicon solar cell with improved light trapping. *Electron Devices, IEEE Transactions On* 46(10), pp. 1978-1983. 1999.
- [9] C. S. Solanki. *Solar Photovoltaics: Fundamentals, Technologies and Applications* 2009 Available: <http://prism.talis.com/dcu/items/595702>.
- [10] A. Manickavasagan and H. Jayasuriya. *Imaging with Electromagnetic Spectrum: Applications in Food and Agriculture* 2014.
- [11] P. Würfel Dr. *Physics of Solar Cells: From Basic Principles to Advanced Concepts* (2nd updated and expanded ed. ed.) 2009.
- [12] American Society for Testing and Materials G173-03, "Standard Tables for Reference Solar Spectral Irradiances: Direct Normal and Hemispherical on 37° Tilted Surface." 2012.
- [13] International Standards Organisation ISO 9845-1, "Solar energy -- Reference solar spectral irradiance at the ground at different receiving conditions -- Part 1: Direct normal and hemispherical solar irradiance for air mass 1.5." 1992.
- [14] National Renewable Energy Laboratory. (). *Solar Spectral Irradiance: Air Mass 1.5*. Available: <http://rredc.nrel.gov/solar/spectra/am1.5/>.

- [15] G. Kumaravelu, M. M. Alkaisi, A. Bittar, D. Macdonald and J. Zhao. Damage studies in dry etched textured silicon surfaces. *Current Applied Physics* 4(2-4), pp. 108-110. 2004. . DOI: DOI: 10.1016/j.cap.2003.10.008.
- [16] L. A. Dobrzański, A. Drygała, K. Gołombek, P. Panek, E. Bielańska and P. Zięba. Laser surface treatment of multicrystalline silicon for enhancing optical properties. *Journal of Materials Processing Technology* 201(1-3), pp. 291-296. 2008. . DOI: DOI: 10.1016/j.jmatprotec.2007.11.278.
- [17] H. B. T. Li, R. H. Franken, J. K. Rath and R. E. I. Schropp. Structural defects caused by a rough substrate and their influence on the performance of hydrogenated nano-crystalline silicon n-i-p solar cells. *Solar Energy Materials and Solar Cells* 932008. . DOI: DOI: 10.1016/j.solmat.2008.11.013.
- [18] D. Iencinella, E. Centurioni, R. Rizzoli and F. Zignani. An optimized texturing process for silicon solar cell substrates using TMAH. *Solar Energy Materials and Solar Cells*, 87(1-4), pp. 725-732. 2005.
- [19] P. Papet, O. Nichiporuk, A. Kaminski, Y. Rozier, J. Kraiem, J. -. Lelievre, A. Chaumartin, A. Fave and M. Lemiti. Pyramidal texturing of silicon solar cell with TMAH chemical anisotropic etching. *Solar Energy Materials and Solar Cells*, 90(15), pp. 2319-2328. 2006.
- [20] E. Forniés, C. Zaldo and J. M. Albella. Control of random texture of monocrystalline silicon cells by angle-resolved optical reflectance. *Solar Energy Materials and Solar Cells* 87(1-4), pp. 583-593. 2005. . DOI: DOI: 10.1016/j.solmat.2004.07.040.
- [21] G. Kumaravelu, M. M. Alkaisi and A. Bittar. Surface texturing for silicon solar cells using reactive ion etching technique. *Photovoltaic Specialists Conference, 2002. Conference Record of the Twenty-Ninth IEEE* pp. 258-261. 2002.
- [22] T. Sakoda, K. Matsukuma, Y. Sung, K. Otsubo, M. Tahara and Y. Nakashima. Additional plasma surface texturing for single-crystalline silicon solar cells using dielectric barrier discharge. *Japanese Journal of Applied Physics, Part 1: Regular Papers and Short Notes and Review Papers* 44(4), pp. 1730-1731. 2005. Available: <http://dx.doi.org/10.1143/JJAP.44.1730>.
- [23] Z. Xu, Y. Yao, E. P. Brueckner, L. Li, J. Jiang, R. G. Nuzzo and G. Logan Liu. Black silicon solar thin-film microcells integrating top nanocone structures for broadband and omnidirectional light-trapping. *Nanotechnology* 25(30), pp. 305301. 2014. . DOI: 10.1088/0957-4484/25/30/305301.
- [24] H. L. Chen, K. T. Huang, C. H. Lin, W. Y. Wang and W. Fan. Fabrication of sub-wavelength antireflective structures in solar cells by utilizing modified illumination and defocus techniques in optical lithography. *Microelectronic Engineering* 84(5-8), pp. 750-754. 2007. . DOI: DOI: 10.1016/j.mee.2007.01.026.

- [25] Y. Ein-Eli, N. Gordon and D. Starosvetsky. Reduced light reflection of textured multicrystalline silicon via NPD for solar cells applications. *Solar Energy Mater. Solar Cells* 90(12), pp. 1764-1772. 2006. . DOI: DOI: 10.1016/j.solmat.2005.10.024.
- [26] Christian Schmiga, Jan Schmidt, Axel Metz, Arthur Endrös, Rudolf Hezel, "17.6% efficient tricrystalline silicon solar cells with spatially uniform texture," *Progress in Photovoltaics: Research and Applications*, vol. 11, pp. 33, 2003.
- [27] S. K. Srivastava, P. Singh, M. Yameen, P. Prathap, C. M. S. Rauthan, Vandana and P. K. Singh. Antireflective ultra-fast nanoscale texturing for efficient multi-crystalline silicon solar cells. *Solar Energy* 115pp. 656-666. 2015. . DOI: http://dx.doi.org.dcu.idm.oclc.org/10.1016/j.solener.2015.03.010.
- [28] B. Parida, J. Choi, S. Palei and K. Kim. Nanopyramid formation by ag metal-assisted chemical etching for nanotextured si solar cells. *Transactions on Electrical and Electronic Materials* [[Online]]. 16(4), pp. 206-211. 2015. . DOI: 10.4313/TEEM.2015.16.4.206.
- [29] E. Manea, E. Budianu, M. Purica, I. Cernica and F. Babarada. Technological process for a new silicon solar cell structure with honeycomb textured front surface. *Solar Energy Materials and Solar Cells* 90(15), pp. 2312-2318. 2006. . DOI: DOI: 10.1016/j.solmat.2006.03.036.
- [30] E. Manea, E. Budianu, M. Purica, D. Cristea, I. Cernica, R. Muller and V. Moagar Poladian. Optimization of front surface texturing processes for high-efficiency silicon solar cells. *Solar Energy Materials and Solar Cells* 87(1-4), pp. 423-431. 2005. . DOI: DOI: 10.1016/j.solmat.2004.06.013.
- [31] M. Abbott and J. Cotter. Optical and electrical properties of laser texturing for high-efficiency solar cells. *Progress in Photovoltaics: Research and Applications* 14pp. 225. 2006.
- [32] R. Hendel. Laser applications in solar cell manufacturing. *Laser Technik Journal* 5pp. 32. 2008.
- [33] H. J. Booth. Recent applications of pulsed lasers in advanced materials processing. *Thin Solid Films*, 453-454pp. 450-457. 2004.
- [34] W. T. Silfvast. *Laser Fundamentals* 2000.
- [35] J. Zhao, B. Huettner and A. Menschig. Microablation with ultrashort laser pulses. *Optics & Laser Technology* 33(7), pp. 487-491. 2001. . DOI: DOI: 10.1016/S0030-3992(01)00066-4.
- [36] C. Molpeceres, S. Lauzurica, J. J. García-Ballesteros, M. Morales, G. Guadaño, J. L. Ocaña, S. Fernández, J. J. Gandía, F. Villar, O. Nos and J. Bertomeu. Selective ablation of photovoltaic materials with UV laser sources for monolithic interconnection of devices based on a-si:H. *Materials Science and Engineering: B In Press, Corrected Proof*. DOI: DOI: 10.1016/j.mseb.2008.09.012.

- [37] S. Rim, S. Zhao, S. R. Scully, M. D. McGehee and P. Peumans. An effective light trapping configuration for thin-film solar cells. *Appl. Phys. Lett.* 91(24), pp. 243501. 2007. Available: <http://link.aip.org/link/?APL/91/243501/1>; 10.1063/1.2789677.
- [38] J. Kang, C. Cho and J. Lee. Design of asymmetrically textured structure for efficient light trapping in building-integrated photovoltaics. *Organic Electronics* 26pp. 61-65. 2015. . DOI: <http://dx.doi.org/10.1016/j.orgel.2015.07.021>.
- [39] W. M. Steen. *Laser Material Processing* 1991.
- [40] H. Klank, J. P. Kutter and O. Geschke. CO₂-laser micromachining and back-end processing for rapid production of PMMA-based microfluidic systems. *Lab on a Chip* 2(4), pp. 242-246. 2002.
- [41] D. Snakenborg, H. Klank and J. P. Kutter. Microstructure fabrication with a Co₂ laser system. *J Micromech Microengineering* 14(2), pp. 182-189. 2004. Available: <http://dx.doi.org/10.1088/0960-1317/14/2/003>.
- [42] S. J. Qin and W. J. Li. Process characterization of fabricating 3D micro channel systems by laser-micromachining. *Sensors and Actuators A: Physical* 97-98pp. 749-757. 2002. . DOI: DOI: 10.1016/S0924-4247(02)00016-X.
- [43] G. A. J. Markillie, H. J. Baker, F. J. Villarreal and D. R. Hall. Effect of vaporization and melt ejection on laser machining of silica glass micro-optical components. *Appl. Opt.* 41(27), pp. 5660-5667. 2002.
- [44] A. Issa, D. Brabazon and M. S. J. Hashmi. 3D transient thermal modelling of laser microchannel fabrication in lime-soda glass. *J. Mater. Process. Technol.* 207(1-3), pp. 307-314. 2008. . DOI: DOI: 10.1016/j.jmatprotec.2008.06.056.
- [45] S. Nikumb, Q. Chen, C. Li, H. Reshef, H. Y. Zheng, H. Qiu and D. Low. Precision glass machining, drilling and profile cutting by short pulse lasers. *Thin Solid Films*, 477(1-2), pp. 216-221. 2005.
- [46] P. Kazansky, Y. Shimotsuma, J. Qiu, E. Bricchi and K. Hirao. "Nanostructuring of transparent materials by light," in bragg gratings, photosensitivity, and poling in glass waveguides. *Technical Digest, Optical Society of America Paper WA52003*.
- [47] T. H. R. Crawford and H. K. Haugen. Sub-wavelength surface structures on silicon irradiated by femtosecond laser pulses at 1300 and 2100 nm wavelengths. *Appl. Surf. Sci.* 253(11), pp. 4970-4977. 2007. . DOI: DOI: 10.1016/j.apsusc.2006.11.004.
- [48] Hsiao-Yen Chung, Chiun-Hsun Chen, and Hsin-Sen Chu, "Analysis of Pyramidal Surface Texturization of Silicon Solar Cells by Molecular Dynamics Simulations," *International Journal of Photoenergy*, vol. vol. 2008, pp. 6 pages, 2008.

- [49] P. Campbell and M. A. Green, "Light trapping properties of pyramidally textured surfaces," *Journal of Applied Physics*, vol. 62, pp. 243-249, 1987.
- [50] P. Campbell and M. A. Green. High performance light trapping textures for monocrystalline silicon solar cells. *Solar Energy Materials and Solar Cells* 65(1-4), pp. 369-375. 2001. . DOI: DOI: 10.1016/S0927-0248(00)00115-X.
- [51] P. J. Sánchez-Illescas, P. Carpena, P. Bernaola-Galván, M. Sidrach-de-Cardona, A. V. Coronado and J. L. Álvarez. An analysis of geometrical shapes for PV module glass encapsulation. *Solar Energy Mater. Solar Cells* 92(3), pp. 323-331. 2008. . DOI: DOI: 10.1016/j.solmat.2007.09.008.
- [52] J. Deubener, G. Hensch, A. Moiseev and H. Bornhöft. Glasses for solar energy conversion systems. *Journal of the European Ceramic Society In Press, Corrected Proof*2008. . DOI: DOI: 10.1016/j.jeurceramsoc.2008.08.009.
- [53] M. Callies, Y. Chen, F. Marty, A. Pépin and D. Quéré. Microfabricated textured surfaces for super-hydrophobicity investigations. *Microelectronic Engineering* 78-79pp. 100-105. 2005. . DOI: DOI: 10.1016/j.mee.2004.12.093.
- [54] M. A. Green, P. A. Basore, N. Chang, D. Clugston, R. Egan, R. Evans, D. Hogg, S. Jarnason, M. Keevers, P. Lasswell, J. O'Sullivan, U. Schubert, A. Turner, S. R. Wenham and T. Young. Crystalline silicon on glass (CSG) thin-film solar cell modules. *Solar Energy* 77(6), pp. 857-863. 2004. . DOI: DOI: 10.1016/j.solener.2004.06.023.
- [55] J. Muller, G. Schope, B. Rech, H. Schade, P. Lechner, R. Geyer, H. Stiebig and W. Reetz. Role of the glass/TCO substrate in thin film silicon solar cells. *Photovoltaic Energy Conversion, 2003. Proceedings of 3rd World Conference On* 2pp. 1839-1842 Vol.2. 2003.
- [56] J. Müller, B. Rech, J. Springer and M. Vanecek. TCO and light trapping in silicon thin film solar cells. *Solar Energy* 77(6), pp. 917-930. 2004. . DOI: DOI: 10.1016/j.solener.2004.03.015.
- [57] A. J. Nozik. Quantum dot solar cells. *Physica E: Low-Dimensional Systems and Nanostructures* 14(1-2), pp. 115-120. 2002. . DOI: DOI: 10.1016/S1386-9477(02)00374-0.
- [58] M. Dasog, K. Bader and J. G. C. Veinot. Influence of halides on the optical properties of silicon quantum dots. *Chem. Mater.* 27(4), pp. 1153-1156. 2015. Available: <http://dx.doi.org/10.1021/acs.chemmater.5b00115>. DOI: 10.1021/acs.chemmater.5b00115.
- [59] L. H. Lie, M. Duerdin, E. M. Tuite, A. Houlton and B. R. Horrocks. Preparation and characterisation of luminescent alkylated-silicon quantum dots. *J Electroanal Chem* 538–539pp. 183-190. 2002. . DOI: [http://dx.doi.org.dcu.idm.oclc.org/10.1016/S0022-0728\(02\)00994-4](http://dx.doi.org.dcu.idm.oclc.org/10.1016/S0022-0728(02)00994-4).

- [60] H. F. Wilson, L. McKenzie-Sell and A. S. Barnard. Shape dependence of the band gaps in luminescent silicon quantum dots. *J. Mater. Chem. C* 2(44), pp. 9451-9456. 2014. Available: <http://dx.doi.org/10.1039/C4TC01312C>. DOI: 10.1039/C4TC01312C.
- [61] D. Kovalev, H. Heckler, G. Polisski, J. Diener and F. Koch. Optical properties of silicon nanocrystals. *Optical Materials* 17(1-2), pp. 35-40. 2001. . DOI: DOI: 10.1016/S0925-3467(01)00017-9.
- [62] P. M. Fauchet. Light emission from si quantum dots. *Materials Today* 8(1), pp. 26-33. 2005. . DOI: DOI: 10.1016/S1369-7021(04)00676-5.
- [63] M. Rosso-Vasic, E. Spruijt, B. v. Lagen, L. D. Cola and H. Zuilhof. Alkyl-functionalized oxide-free silicon nanoparticles: Synthesis and optical properties. *Small* 4(10), pp. 1835-1841. 2008. Available: <http://dx.doi.org/10.1002/sml.200800066>.
- [64] P. Mishra and K. P. Jain. Raman, photoluminescence and optical absorption studies on nanocrystalline silicon. *Materials Science and Engineering B* 95(3), pp. 202-213. 2002. . DOI: DOI: 10.1016/S0921-5107(02)00234-9.
- [65] X. J. Hao, E. -. Cho, G. Scardera, E. Bellet-Amalric, D. Bellet, Y. S. Shen, S. Huang, Y. D. Huang, G. Conibeer and M. A. Green. Effects of phosphorus doping on structural and optical properties of silicon nanocrystals in a SiO₂ matrix. *Thin Solid Films* 517(19), pp. 5646-5652. 2009. . DOI: DOI: 10.1016/j.tsf.2009.02.076.
- [66] S. Giménez, I. Mora-Seró, L. Macor, N. Guijarro, T. Lana-Villarreal, R. Gómez, L. J. Diguna, Q. Shen, T. Toyoda and J. Bisquert. Improving the performance of colloidal quantum-dot-sensitized solar cells. *Nanotechnology* 20(29), pp. 295204. 2009. Available: <http://stacks.iop.org/0957-4484/20/i=29/a=295204>.
- [67] M. Samadpour, Z. Ghane, N. Ghazyani, F. Tajabadi and N. Taghavinia. Monolithic quantum dot sensitized solar cells. *J. Phys. D* 46(48), pp. 485101. 2013. Available: <http://stacks.iop.org/0022-3727/46/i=48/a=485101>.
- [68] K. Kalyanasundaram. *Dye-Sensitized Solar Cells* 2010 Available: <https://books.google.ie/books?id=1n1QC2snf-AC>.
- [69] T. Soga. *Nanostructured Materials for Solar Energy Conversion, 1st Ed* 2006 Available: <http://prism.talis.com/dcu/items/595708>; <http://www.loc.gov/catdir/enhancements/fy0665/2006050753-d.html>.
- [70] A. Pattantyus-Abraham, I. J. Kramer, A. R. Barkhouse, X. Wang, G. Konstantatos, R. Debnath, L. Levina, I. Raabe, M. K. Nazeeruddin, M. Grätzel and E. H. Sargent. Depleted-heterojunction colloidal quantum dot solar cells. *ACS Nano* 4(6), pp. 3374-3380. 2010. Available: <http://dx.doi.org/10.1021/nn100335g>. DOI: 10.1021/nn100335g.

- [71] R. A. Synowicki, B. D. Johs and A. C. Martin. Optical properties of soda-lime float glass from spectroscopic ellipsometry. *Thin Solid Films* 519(9), pp. 2907-2913. 2011. . DOI: 10.1016/j.tsf.2010.12.110.
- [72] H. Y. Zheng, W. Zhou, H. X. Qian, T. T. Tan and G. C. Lim. Polarisation-independence of femtosecond laser machining of fused silica. *Appl. Surf. Sci.* 236(1-4), pp. 114-119. 2004. . DOI: DOI: 10.1016/j.apsusc.2004.04.034.
- [73] L. Gallais, P. Cormont and J. Rullier. Investigation of stress induced by CO₂ laserprocessing of fused silica optics for laser damagegrowth mitigation. *Opt.Express* 17(26), pp. 23488-23501. 2009. Available: <http://www.opticsexpress.org/abstract.cfm?URI=oe-17-26-23488>.
- [74] T. L. H Y Zheng and. Studies of CO₂ laser peeling of glass substrates. *J Micromech Microengineering* 15(11), pp. 2093. 2005. Available: <http://stacks.iop.org/0960-1317/15/i=11/a=014>.
- [75] C. Iliescu, B. Chen and J. Miao. On the wet etching of pyrex glass. *Sensors and Actuators A: Physical* 143(1), pp. 154-161. 2008. . DOI: DOI: 10.1016/j.sna.2007.11.022.
- [76] J. Wong, J. L. Ferriera, E. F. Lindsey, D. L. Haupt, I. D. Hutcheon and J. H. Kinney. Morphology and microstructure in fused silica induced by high fluence ultraviolet 3 ω (355 nm) laser pulses. *Journal of Non-Crystalline Solids* 352(3), pp. 255-272. 2006. . DOI: DOI: 10.1016/j.jnoncrysol.2005.11.036.
- [77] K. L. Chopra and S. R. Das. *Thin Film Solar Cells* 1983.
- [78] D. Mukherjee and S. Chakrabarti. *Fundamentals of Renewable Energy Systems* 2004.
- [79] J. Petzing, J. Coupland and R. Leach. Good practice guide no. 116 - the measurement of rough surface topography using coherence scanning interferometry. *Npl* (116), 2010.
- [80] R. K. Leach. *Optical Measurement of Surface Topography* 2011.
- [81] A. Issa, "Computational Control of Laser Systems for micro-machining," vol. 1, 2007.
- [82] S. K. Nayar. Shape from focus. Robotics Institute. Pittsburgh, PA,. 1989.
- [83] e. a. F Marinello. Development and analysis of a software tool for stitching three-dimensional surface topography data sets. *Measurement Science and Technology* 18(5), pp. 1404. 2007. Available: <http://stacks.iop.org/0957-0233/18/i=5/a=028>.
- [84] e. a. F Marinello. Increase of maximum detectable slope with optical profilers, through controlled tilting and image processing. *Measurement Science and*

Technology 18(2), pp. 384. 2007. Available: <http://stacks.iop.org/0957-0233/18/i=2/a=S09>.

[85] L. Fan, F. Song and S. Jutamulia. Edge detection with large depth of focus using differential Haar–Gaussian wavelet transform. *Opt. Commun.* 270(2), pp. 169-175. 2007. . DOI: DOI: 10.1016/j.optcom.2006.09.015.

[86] P. Grossmann. Depth from focus. *Pattern Recog. Lett.* 5(1), pp. 63-69. 1987. . DOI: DOI: 10.1016/0167-8655(87)90026-2.

[87] M. F. Hansen, G. A. Atkinson, L. N. Smith and M. L. Smith. 3D face reconstructions from photometric stereo using near infrared and visible light. *Comput. Vision Image Understanding* 114(8), pp. 942-951. 2010. . DOI: DOI: 10.1016/j.cviu.2010.03.001.

[88] F. S. Helmlı and S. Scherer. Adaptive shape from focus with an error estimation in light microscopy. Presented at Image and Signal Processing and Analysis, 2001. ISPA 2001. Proceedings of the 2nd International Symposium On. 2001, .

[89] M. Hocaoglu and M. Unel. HK segmentation of 3D micro-structures reconstructed from focus. 5226pp. 1173-1180. 2008. . DOI: 10.1007/978-3-540-87442-3_145.

[90] W. Huang and Z. Jing. Evaluation of focus measures in multi-focus image fusion. *Pattern Recog. Lett.* 28(4), pp. 493-500. 2007. . DOI: DOI: 10.1016/j.patrec.2006.09.005.

[91] A. S. Malik, Seong-O Shim and Tae-Sun Choi. Depth map estimation using a robust focus measure. Presented at Image Processing, 2007. ICIP 2007. IEEE International Conference On. 2007, .

[92] A. S. Malik and Tae-Sun Choi. Analysis of effects of texture reflectance and source illumination on focus measures for microscopic images. Presented at Computer and Electrical Engineering, 2009. ICCEE '09. Second International Conference On. 2009, .

[93] A. S. Malik and T. Choi. Consideration of illumination effects and optimization of window size for accurate calculation of depth map for 3D shape recovery. *Pattern Recognit* 40(1), pp. 154-170. 2007. . DOI: DOI: 10.1016/j.patcog.2006.05.032.

[94] A. S. Malik and T. Choi. A novel algorithm for estimation of depth map using image focus for 3D shape recovery in the presence of noise. *Pattern Recognit* 41(7), pp. 2200-2225. 2008. . DOI: DOI: 10.1016/j.patcog.2007.12.014.

[95] M. Niederöst, J. Niederöst and J. Skucka. Shape from focus fully automated 3D reconstruction and visualization of microscopic objects.

- [96] M. Noguchi and S. K. Nayar. Microscopic shape from focus using a projected illumination pattern, *Math. Comput. Model.* 24(5-6), pp. 31-48. 1996. . DOI: DOI: 10.1016/0895-7177(96)00114-8.
- [97] S. Shim and T. Choi. Depth from focus based on combinatorial optimization. *Opt. Lett.* 35(12), pp. 1956-1958. 2010. Available: <http://ol.osa.org/abstract.cfm?URI=ol-35-12-1956>.
- [98] A. G. Valdecasas, D. Marshall, J. M. Becerra and J. J. Terrero. On the extended depth of focus algorithms for bright field microscopy. *Micron* 32(6), pp. 559-569. 2001. . DOI: DOI: 10.1016/S0968-4328(00)00061-5.
- [99] J. Vitrià and J. Llacer. Reconstructing 3D light microscopic images using the EM algorithm. *Pattern Recog. Lett.* 17(14), pp. 1491-1498. 1996. . DOI: DOI: 10.1016/S0167-8655(96)00104-3.
- [100] T. V. Vorburger and E. C. Teague. Optical techniques for on-line measurement of surface topography. *Precis Eng* 3(2), pp. 61-83. 1981. . DOI: DOI: 10.1016/0141-6359(81)90038-6.
- [101] Y. Wu and C. Wang. Extended depth of focus image for phytolith analysis. *Journal of Archaeological Science* 36(10), pp. 2253-2257. 2009. . DOI: DOI: 10.1016/j.jas.2009.06.010.
- [102] Yu Song, Mantian Li and Lining Sun. A new auto-focusing algorithm for optical microscope based automated system. Presented at Control, Automation, Robotics and Vision, 2006. ICARCV '06. 9th International Conference On. 2006, .
- [103] Yu Sun, S. Duthaler and B. J. Nelson. Autofocusing algorithm selection in computer microscopy. Presented at Intelligent Robots and Systems, 2005. (IROS 2005). 2005 IEEE/RSJ International Conference On. 2005, .
- [104] J. C. Russ. *The Image Processing Handbook* (6th ed. ed.) 2011.
- [105] V. K. Narasimhan and C. Yi. Nanostructures for photon management in solar cells. *Nanophotonics* 2pp. 187. 2013. . DOI: 10.1515/nanoph-2013-0001.
- [106] International Standards Organisation 4287, "Geometrical Product Specifications (GPS) -- Surface texture: Profile method -- Terms, definitions and surface texture parameters," 1997.
- [107] International Standards Organisation 4288, "Geometrical Product Specifications (GPS) -- Surface texture: Profile method -- Rules and procedures for the assessment of surface texture," 1996.
- [108] International Standards Organisation 230-2, "Test code for machine tools- Part 2: Determination of accuracy and repeatability of positioning numerically controlled axes." 2006.

- [109] D. J. Whitehouse. *Surfaces and their Measurement* 2002.
- [110] D. G. Chetwynd, J. A. Greenwood and E. Mainsah. *Metrology and Properties of Engineering Surfaces* 2001.
- [111] W. Sun and J. D. Claverley. Verification of an optical micro-CMM using the focus variation technique: Aspects of probing errors. *CIRP Ann. Manuf. Technol.* 64(1), pp. 511-514. 2015. . DOI: <http://dx.doi.org/10.1016/j.cirp.2015.04.089>.
- [112] K. J. Gåsvik. *Optical Metrology* (3rd ed. ed.) 2002.
- [113] Rofin-Baasel Ltd, "Rofin DC-015 CO2 laser operation manuals," 2004.
- [114] S. L. Storm and A. Springsteen, "Choosing the Right Sphere Size for Your Application," .
- [115] D. Moore, S. Krishnamurthy, Y. Chao, Q. Wang, D. Brabazon and P. J. McNally. Characteristics of silicon nanocrystals for photovoltaic applications. *Physica Status Solidi (a)* 208(3), pp. 604-607. 2011. Available: <http://dx.doi.org/10.1002/pssa.201000381>. DOI: 10.1002/pssa.201000381.
- [116] Y. Chao, S. Krishnamurthy, M. Montalti, L. H. Lie, A. Houlton, B. R. Horrocks, L. Kjeldgaard, V. R. Dhanak, M. R. C. Hunt and L. Šiller. Reactions and luminescence in passivated si nanocrystallites induced by vacuum ultraviolet and soft-x-ray photons. *J. Appl. Phys.* 98(4), pp. 044316. 2005. . DOI: <http://dx.doi.org/10.1063/1.2012511>.
- [117] Y. Chao, L. Šiller, S. Krishnamurthy, P. R. Coxon, U. Bangert, M. Gass, L. Kjeldgaard, S. N. Patole, L. H. Lie, N. O'Farrell, T. A. Alsop, A. Houlton and B. R. Horrocks. Evaporation and deposition of alkyl-capped silicon nanocrystals in ultrahigh vacuum. *Nature Nanotechnology* (8), pp. 486-489. 2007. . DOI: 10.1038/nano.2007.224.
- [118] Y. Chao, A. Houlton, B. R. Horrocks, M. R. C. Hunt, N. R. J. Poolton, J. Yang and L. Siller. Optical luminescence from alkyl-passivated si nanocrystals under vacuum ultraviolet excitation: Origin and temperature dependence of the blue and orange emissions. *Appl. Phys. Lett.* 88(26), pp. 263119. 2006. Available: <http://link.aip.org/link/?APL/88/263119/1>. DOI: 10.1063/1.2216911.
- [119] E. Duffy, X. He, E. P. Nesterenko, D. Brabazon, A. Dey, S. Krishnamurthy, P. N. Nesterenko and B. Paull. Thermally controlled growth of carbon onions within porous graphitic carbon-detonation nanodiamond monolithic composites. *RSC Adv.* (29), pp. 22906. 2015. . DOI: 10.1039/C5RA00258C.
- [120] X. He, K. B. Male, P. N. Nesterenko, D. Brabazon, B. Paull and J. H. T. Luong. Adsorption and desorption of methylene blue on porous carbon monoliths and nanocrystalline cellulose. *ACS Appl. Mater. Interfaces* (17), pp. 8796. 2013. . DOI: 10.1021/am403222u.

- [121] X. He, E. P. Nesterenko, P. N. Nesterenko, D. Brabazon, L. Zhou, J. D. Glennon, J. H. T. Luong and B. Paull. Fabrication and characterization of nanotemplated carbon monolithic material. *ACS Appl. Mater. Interfaces* (17), pp. 8572. 2013. . DOI: 10.1021/am402030m.
- [122] M. Vazquez, D. Moore, X. He, A. Ben Azouz, E. Nesterenko, P. Nesterenko, B. Paull and D. Brabazon. Focussed ion beam serial sectioning and imaging of monolithic materials for 3D reconstruction and morphological parameter evaluation. *Analyst* (1), pp. 99. 2013. . DOI: 10.1039/C3AN01827J.
- [123] A. H. Eltmimi, L. Barron, A. Rafferty, J. P. Hanrahan, O. Fedyanina, E. Nesterenko, P. N. Nesterenko and B. Paull. Preparation, characterisation and modification of carbon-based monolithic rods for chromatographic applications. *Journal of Separation Science* 33(9), pp. 1231-1243. 2010. . DOI: 10.1002/jssc.200900845.
- [124] H. Giesche. Mercury porosimetry: A general (practical) overview. *Particle & Particle Systems Characterization* 23(1), pp. 9-19. 2006. . DOI: 10.1002/ppsc.200601009.
- [125] S. M. Karazi, A. Issa and D. Brabazon. Comparison of ANN and DoE for the prediction of laser-machined micro-channel dimensions. *Optics and Lasers in Engineering* 47(9), pp. 956-964. 2009. Available: <http://www.sciencedirect.com/science/article/pii/S0143816609000943>.
- [126] K. Jäger, O. Isabella, L. Zhao and M. Zeman. Light scattering properties of surface-textured substrates. *Physica Status Solidi (C)* 7(3-4), pp. 945-948. 2010. Available: <http://dx.doi.org/10.1002/pssc.200982695>.
- [127] M. Kolli, M. Hamidouche, N. Bouaouadja and G. Fantozzi. HF etching effect on sandblasted soda-lime glass properties. *Journal of the European Ceramic Society* 29(13), pp. 2697-2704. 2009. . DOI: DOI: 10.1016/j.jeurceramsoc.2009.03.020.
- [128] J. Zhao, J. Sullivan and T. D. Bennett. Wet etching study of silica glass after CW CO₂ laser treatment. *Applied Surface Science* 225(1-4), pp. 250-255. 2004. . DOI: DOI: 10.1016/j.apsusc.2003.10.012.
- [129] C. Yang, R. A. Bley, S. M. Kauzlarich, H. W. H. Lee and G. R. Delgado. Synthesis of alkyl-terminated silicon nanoclusters by a solution route. *J. Am. Chem. Soc.* 121(22), pp. 5191-5195. 1999. Available: <http://dx.doi.org/10.1021/ja9828509>. DOI: 10.1021/ja9828509.
- [130] I. Vasiliev, J. R. Chelikowsky and R. M. Martin. Surface oxidation effects on the optical properties of silicon nanocrystals. *Phys.Rev.B* 65(12), pp. 121302. 2002. . DOI: 10.1103/PhysRevB.65.121302.
- [131] A. P. Cocco, G. J. H. Nelson W.M., A. Nakajo, T. D. Myles, A. M. Kiss, J. J. Lombardo and W. K. S. Chiu. Three-dimensional microstructural imaging methods

for energy materials. *Phys. Chem. Chem. Phys.* (39), pp. 16377. 2013. . DOI: 10.1039/C3CP52356J.

[132] Design-Expert software, "v9, user's guide, Technical manual", Stat-Ease Inc., , " *Stat-Ease Inc.*, 2015.

Appendix A : Positional Analysis

The following tables contain the results and calculations performed in analysing the performance characteristics of the stage of the microscope.

Table 32: Large scale positional analysis of X axis using Mahr 810SW dial gauge indicator (1-5)

Position Number i		1		2		3		4		5	
Approach Direction		+	-	+	-	+	-	+	-	+	-
Target Position (mm)		0.48		1.09		1.53		1.76		2.75	
Positional Deviations (μm)	1	0	10	-10	0	-10	-10	-10	-10	-20	-10
	2	0	10	-10	10	-10	-10	-10	-10	-20	-10
	3	0	10	0	0	-10	-10	-10	-10	-20	-10
Mean unidirectional positional deviation \bar{x}_i (μm)		0	10	-10	0	-10	-10	-10	-10	-20	-10
Estimator of standard uncertainty s_i (μm)		0	0	10	10	0	0	0	0	0	0
$2s_i$		0	0	20	20	0	0	0	0	0	0
$\bar{x}_i - 2s_i$		0	10	-30	-20	-10	-10	-10	-10	-20	-10
$\bar{x}_i + 2s_i$		0	10	10	20	-10	-10	-10	-10	-20	-10
Unidirectional Repeatability $R_i = 4s_i$ (μm)		0	0	40	40	0	0	0	0	0	0
Reverse value B_i (μm)		-10		-10		0		0		-10	
Bidirectional repeatability R_i (μm)		10		80		0		0		10	
Mean bidirectional positional deviation \bar{x}_i (μm)		10		-10		-10		-10		-20	

Table 33: Large scale positional analysis of X axis using Mahr 810SW dial gauge indicator (6-10)

Position Number i		6		7		8		9		10	
Approach Direction		+	-	+	-	+	-	+	-	+	-
Target Position (mm)		2.88		3.08		3.72		4.95		5.1	
Positional Deviations (μm)	1	-20	-20	-10	-10	-20	-20	-30	-20	-20	-20
	2	-20	-20	-10	10	-20	0	-30	-10	-30	-30
	3	-20	-10	-10	-10	-20	-10	-20	-20	-30	-20
Mean unidirectional positional deviation \bar{x}_i (μm)		-20	-20	-10	0	-20	-10	-30	-20	-30	-20
Estimator of standard uncertainty s_i (μm)		0	10	0	10	0	10	10	10	10	10
$2s_i$		0	20	0	20	0	20	20	20	20	20
$\bar{x}_i - 2s_i$		-20	-40	-10	-20	-20	-30	-50	-40	-50	-40
$\bar{x}_i + 2s_i$		-20	0	-10	20	-20	10	-10	0	-10	0
Unidirectional Repeatability $R_i = 4s_i$ (μm)		0	40	0	40	0	40	40	40	40	40
Reverse value B_i (μm)		0		-10		-10		-10		-10	
Bidirectional repeatability R_i (μm)		60		60		60		80		80	
Mean bidirectional positional deviation \bar{x}_i (μm)		-20		-10		-20		-30		-30	

Table 34: Large scale positional analysis of Y axis using Mahr 810SW dial gauge indicator (1-5)

Position Number i		1		2		3		4		5	
Approach Direction		+	-	+	-	+	-	+	-	+	-
Target Position (mm)		0.48		1.09		1.53		1.76		2.75	
Positional Deviations (μm)	1	-10	-10	-10	0	-10	-10	-10	0	-10	-10
	2	-10	10	-20	0	-20	0	-20	0	0	-10
	3	-20	0	-20	0	-20	0	-20	-10	-20	-10
Mean unidirectional positional deviation \bar{x}_i (μm)		-10	0	-20	0	-20	0	-20	0	-10	-10
Estimator of standard uncertainty s_i (μm)		10	10	10	0	10	10	10	10	10	0
$2s_i$		20	20	20	0	20	20	20	20	20	0
$\bar{x}_i - 2s_i$		-30	-20	-40	0	-40	-20	-40	-20	-30	-10
$\bar{x}_i + 2s_i$		10	20	0	0	0	20	0	20	10	-10
Unidirectional Repeatability $R_i = 4s_i$ (μm)		40	40	40	0	40	40	40	40	40	0
Reverse value B_i (μm)		-10		-20		-20		-20		0	
Bidirectional repeatability R_i (μm)		80		60		80		80		60	
Mean bidirectional positional deviation \bar{x}_i (μm)		-10		-10		-10		-10		-10	

Table 35: Large scale positional analysis of Y axis using Mahr 810SW dial gauge indicator (6-10)

Position Number i		6		7		8		9		10	
Approach Direction		+	-	+	-	+	-	+	-	+	-
Target Position (mm)		2.88		3.08		3.72		4.95		5.1	
Positional Deviations (μm)	1	-20	-10	-10	-10	-20	-10	-20	-20	-20	-20
	2	-10	-10	0	0	-10	-10	-20	-10	-20	-10
	3	-30	-10	-30	-10	-30	-20	-30	-20	-30	-20
Mean unidirectional positional deviation \bar{x}_i (μm)		-20	-10	-10	-10	-20	-10	-20	-20	-20	-20
Estimator of standard uncertainty s_i (μm)		10	0	20	10	10	10	10	10	10	10
$2s_i$		20	0	40	20	20	20	20	20	20	20
$\bar{x}_i - 2s_i$		-40	-10	-50	-30	-40	-30	-40	-40	-40	-40
$\bar{x}_i + 2s_i$		0	-10	30	10	0	10	0	0	0	0
Unidirectional Repeatability $R_i = 4s_i$ (μm)		40	0	80	40	40	40	40	40	40	40
Reverse value B_i (μm)		-10		0		-10		0		0	
Bidirectional repeatability R_i (μm)		60		140		80		80		80	
Mean bidirectional positional deviation \bar{x}_i (μm)		-20		-10		-20		-20		-20	

Table 36: Large scale positional analysis of Z axis using Mahr 810SW dial gauge indicator (1-5)

Position Number i		1		2		3		4		5	
Approach Direction		+	-	+	-	+	-	+	-	+	-
Target Position (mm)		0.05		0.11		0.15		0.18		0.28	
Positional Deviations (μm)	1	0	0	0	0	0	10	0	0	0	0
	2	0	0	0	0	0	10	-10	0	-10	0
	3	0	0	0	0	10	10	-10	0	-10	0
Mean unidirectional positional deviation \bar{x}_i (μm)		0	0	0	0	0	10	-10	0	-10	0
Estimator of standard uncertainty s_i (μm)		0	0	0	0	10	0	10	0	10	0
$2s_i$		0	0	0	0	20	0	20	0	20	0
$\bar{x}_i - 2s_i$		0	0	0	0	-20	10	-30	0	-30	0
$\bar{x}_i + 2s_i$		0	0	0	0	20	10	10	0	10	0
Unidirectional Repeatability $R_i = 4s_i$ (μm)		0	0	0	0	40	0	40	0	40	0
Reverse value B_i (μm)		0		0		-10		-10		-10	
Bidirectional repeatability R_i (μm)		0		0		60		60		60	
Mean bidirectional positional deviation \bar{x}_i (μm)		0		0		10		-10		-10	

Table 37: Large scale positional analysis of Z axis using Mahr 810SW dial gauge indicator (6-10)

Position Number i		6		7		8		9		10	
Approach Direction		+	-	+	-	+	-	+	-	+	-
Target Position (mm)		0.29		0.31		0.38		0.50		0.51	
Positional Deviations (μm)	1	0	0	10	0	10	0	10	10	10	10
	2	0	0	0	0	0	10	0	10	10	10
	3	0	0	0	0	0	0	10	0	0	10
Mean unidirectional positional deviation \bar{x}_i (μm)		0	0	0	0	0	0	10	10	10	10
Estimator of standard uncertainty s_i (μm)		0	0	10	0	10	10	10	10	10	0
$2s_i$		0	0	20	0	20	20	20	20	20	0
$\bar{x}_i - 2s_i$		0	0	-20	0	-20	-20	-10	-10	-10	10
$\bar{x}_i + 2s_i$		0	0	20	0	20	20	30	30	30	10
Unidirectional Repeatability $R_i = 4s_i$ (μm)		0	0	40	0	40	40	40	40	40	0
Reverse value B_i (μm)		0		0		0		0		0	
Bidirectional repeatability R_i (μm)		0		60		80		80		60	
Mean bidirectional positional deviation \bar{x}_i (μm)		0		0		0		10		10	

Table 38: Small scale positional analysis of X axis using Mitutoyo MT513-405E dial gauge indicator (1-5)

Position Number i	1		2		3		4		5		
Approach Direction	↑	↓	↑	↓	↑	↓	↑	↓	↑	↓	
Target Position (mm)	0.020		0.045		0.060		0.070		0.110		
Positional Deviations (μm)	1	0	0	-1	-2	1	1	0	1	2	2
	2	1	2	-1	1	2	4	2	4	3	4
	3	0	2	-1	0	2	3	2	3	2	4
Mean unidirectional positional deviation \bar{x}_i (μm)	0	1	-1	0	2	3	1	3	2	3	
Estimator of standard uncertainty s_i (μm)	1	1	0	2	1	2	1	2	1	1	
$2s_i$	2	2	0	4	2	4	2	4	2	2	
$\bar{x}_i - 2s_i$	-2	-1	-1	-4	0	-1	-1	-1	0	1	
$\bar{x}_i + 2s_i$	2	3	-1	4	4	7	3	7	4	5	
Unidirectional Repeatability $R_i = 4s_i$ (μm)	4	4	0	8	4	8	4	8	4	4	
Reverse value B_i (μm)	-1		-1		-1		-2		-1		
Bidirectional repeatability R_i (μm)	8		12		14		14		8		
Mean bidirectional positional deviation \bar{x}_i (μm)	1		-1		3		2		3		

Table 39: Small scale positional analysis of X axis using Mitutoyo MT513-405E dial gauge indicator (6-10)

Position Number i		6		7		8		9		10	
Approach Direction		↑	↓	↑	↓	↑	↓	↑	↓	↑	↓
Target Position (mm)		0.115		0.125		0.150		0.200		0.205	
Positional Deviations (μm)	1	0	-1	-1	-1	1	1	2	2	-1	-1
	2	1	1	0	1	3	4	4	4	1	1
	3	0	1	-1	1	2	3	3	4	1	0
Mean unidirectional positional deviation \bar{x}_i (μm)		0	0	-1	0	2	3	3	3	0	0
Estimator of standard uncertainty s_i (μm)		1	1	1	1	1	2	1	1	1	1
$2s_i$		2	2	2	2	2	4	2	2	2	2
$\bar{x}_i - 2s_i$		-2	-2	-3	-2	0	-1	1	1	-2	-2
$\bar{x}_i + 2s_i$		2	2	1	2	4	7	5	5	2	2
Unidirectional Repeatability $R_i = 4s_i$ (μm)		4	4	4	4	4	8	4	4	4	4
Reverse value B_i (μm)		0		-1		-1		0		0	
Bidirectional repeatability R_i (μm)		8		8		14		8		8	
Mean bidirectional positional deviation \bar{x}_i (μm)		0		-1		3		3		0	

Table 40: Small scale positional analysis of Y axis using Mitutoyo MT513-405E dial gauge indicator (1-5)

Position Number i		1		2		3		4		5	
Approach Direction		+	-	+	-	+	-	+	-	+	-
Target Position (mm)		0.020		0.045		0.060		0.070		0.110	
Positional Deviations (μm)	1	-2	1	-2	1	-2	2	-1	2	-1	2
	2	1	6	1	6	2	6	2	7	3	8
	3	0	4	1	5	1	6	2	6	3	-3
Mean unidirectional positional deviation \bar{x}_i (μm)		0	4	0	4	0	5	1	5	2	2
Estimator of standard uncertainty s_i (μm)		2	3	2	3	2	2	2	3	2	6
$2s_i$		4	6	4	6	4	4	4	6	4	12
$\bar{x}_i - 2s_i$		-4	-2	-4	-2	-4	1	-3	-1	-2	-10
$\bar{x}_i + 2s_i$		4	10	4	10	4	9	5	11	6	14
Unidirectional Repeatability $R_i = 4s_i$ (μm)		8	12	8	12	8	8	8	12	8	24
Reverse value B_i (μm)		-4		-4		-5		-4		0	
Bidirectional repeatability R_i (μm)		22		22		16		22		40	
Mean bidirectional positional deviation \bar{x}_i (μm)		2		2		3		3		2	

Table 41: Small scale positional analysis of Y axis using Mitutoyo MT513-405E dial gauge indicator (6-10)

Position Number i		6		7		8		9		10	
Approach Direction		+	-	+	-	+	-	+	-	+	-
Target Position (mm)		0.115		0.125		0.150		0.200		0.205	
Positional Deviations (μm)	1	-1	2	-1	2	0	3	2	5	2	3
	2	3	7	3	7	4	8	6	9	7	7
	3	3	6	3	5	4	6	5	8	5	7
Mean unidirectional positional deviation \bar{x}_i (μm)		2	5	2	5	3	6	4	7	5	6
Estimator of standard uncertainty s_i (μm)		2	3	2	3	2	3	2	2	3	2
$2s_i$		4	6	4	6	4	6	4	4	6	4
$\bar{x}_i - 2s_i$		-2	-1	-2	-1	-1	0	0	3	-1	2
$\bar{x}_i + 2s_i$		6	11	6	11	7	12	8	11	11	10
Unidirectional Repeatability $R_i = 4s_i$ (μm)		8	12	8	12	8	12	8	8	12	8
Reverse value B_i (μm)		-3		-3		-3		-3		-1	
Bidirectional repeatability R_i (μm)		22		22		22		16		22	
Mean bidirectional positional deviation $\bar{\bar{x}}_i$ (μm)		4		4		5		6		6	

Table 42: Small scale positional analysis of Z axis using Mitutoyo MT513-405E dial gauge indicator (1-5)

Position Number i		1		2		3		4		5	
Approach Direction		+	-	+	-	+	-	+	-	+	-
Target Position (mm)		0.019		0.044		0.061		0.070		0.110	
Positional Deviations (μm)	1	0	11	1	11	1	12	0	11	1	11
	2	3	13	2	12	2	13	2	12	2	12
	3	-1	8	-1	8	0	8	-1	8	-1	8
Mean unidirectional positional deviation \bar{x}_i (μm)		1	11	1	10	1	11	0	10	1	10
Estimator of standard uncertainty s_i (μm)		2	3	2	2	1	3	2	2	2	2
$2s_i$		4	6	4	4	2	6	4	4	4	4
$\bar{x}_i - 2s_i$		-3	5	-3	6	-1	5	-4	6	-3	6
$\bar{x}_i + 2s_i$		5	17	5	14	3	17	4	14	5	14
Unidirectional Repeatability $R_i = 4s_i$ (μm)		8	12	8	8	4	12	8	8	8	8
Reverse value B_i (μm)		-10		-9		-10		-10		-9	
Bidirectional repeatability R_i (μm)		22		17		20		18		17	
Mean bidirectional positional deviation \bar{x}_i (μm)		6		6		6		5		6	

Table 43: Small scale positional analysis of Z axis using Mitutoyo MT513-405E dial gauge indicator (6-10)

Position Number i		6		7		8		9		10	
Approach Direction		+	-	+	-	+	-	+	-	+	-
Target Position (mm)		0.115		0.123		0.149		0.198		0.204	
Positional Deviations (μm)	1	0	10	0	11	0	10	0	10	1	9
	2	1	13	1	11	1	11	0	11	0	10
	3	-1	8	-3	8	-1	7	-2	7	-3	6
Mean unidirectional positional deviation \bar{x}_i (μm)		0	10	-1	10	0	9	-1	9	-1	8
Estimator of standard uncertainty s_i (μm)		1	3	2	2	1	2	1	2	2	2
$2s_i$		2	6	4	4	2	4	2	4	4	4
$\bar{x}_i - 2s_i$		-2	4	-5	6	-2	5	-3	5	-5	4
$\bar{x}_i + 2s_i$		2	16	3	14	2	13	1	13	3	12
Unidirectional Repeatability $R_i = 4s_i$ (μm)		4	12	8	8	4	8	4	8	8	8
Reverse value B_i (μm)		-10		-11		-9		-10		-9	
Bidirectional repeatability R_i (μm)		20		19		15		16		17	
Mean bidirectional positional deviation \bar{x}_i (μm)		5		5		5		4		4	

Appendix B : RSM Procedure

To produce and evaluate a RSM to model on the effect of laser micromachining parameters on the parasitic absorption loss in the textured superstrates, the following steps need to be performed:

The identification of the key process input variables.

The key factors can be defined from the previous literature or by conducting a screening study. In the case of the work completed in this thesis, a combination of both was completed. A previous study had worked using the same laser micromachining system for the micro-ablation of channels in a different glass material [81]. Using this information as a starting point, the process variables were further investigated through a screening study to ensure compatibility with the materials used in this study. The process input factors were laser power (Duty Cycle), pulse repetition frequency (PRF), and translation speed (U).

The determination of each input ranges.

The screening study also helped finding the ranges of each factor. The criterion of selecting the working ranges was getting a smooth, uniform, and continuous micro-channel.

Testing the significance of the model terms

In order to ensure that the model terms are significant, an analysis of the following terms was completed [132].

The F value is calculated by term mean square divided by residual mean square.

The p-value shows whether the model/term is significant or not. The p-value is the probability of getting an F Value of this size if the model/term did not have an effect on the response. In general, a term that has a probability value less than 0.05, which is the significance threshold that sets the risk level in significance/non-significance detection, would be considered a significant effect.

The R-Squared is a measure of the amount of variation around the mean explained by the model. A low R-Squared value indicates variation around the average predictions of the model.

The Adj R-Squared is a measure of the amount of variation around the mean explained by the model, adjusted for the number of terms in the model. The adjusted R-Squared plateaus as the number of terms in the model increases if those additional terms do not add value to the model.

The Pred R-Squared is a measure of the amount of variation in new data explained by the model. This value decreases when too many insignificant terms are added to the model.

The Adequate Precision is a signal to noise ratio. It compares the range of the predicted values at the design points to the average prediction error. This value should be larger than 4 to indicate that the model signal is strong.

The automatic Stepwise regression method was utilised in the Design Expert software to eliminate insignificant terms in this work.

Appendix C : Dial Gauge Technical Specifications

Mahr MarCator 810W / SW Dial Gauge Specifications

Mahr

Dial Indicators

Dial Indicators shockproof version according to DIN 878



803



803 W



810/810 L



810 W

Features

Small Dial Indicator 803 where available space is limited

- Shockproof via sleeve which floats over the spindle
- Constant measuring force
- Protective housing (back wall integrated in housing)
- Raising of measuring spindle via lifting cap
- Adjustable tolerance markers
- Delivered in plastic case

Small Dial Indicator 803 W waterproof and oilproof

- Design features identical to 803, but
- Upper protective cap on measuring spindle as well as bezel and transparent dial cover with O-rings hermetically sealed
- Measuring spindle sealed by means of rubber sleeve, thus preventing contamination by liquids and impurities
- Delivered in plastic case

Dial Indicator 810 standard version

- Shockproof via sleeve which floats over the spindle
- Constant measuring force
- Protective housing (back wall integrated in housing)
- Raising of measuring spindle via lifting cap or cable release 951 (accessory)
- Adjustable tolerance markers
- Delivered in plastic case

Dial Indicator 810 L

- Design features identical to 810, but with tapped holes for mounting lugs 961 and 962 (accessories)
- Delivered in plastic case

Dial Indicator 810 W waterproof and oilproof

- Design features identical to 810, but upper protective cap on measuring spindle as well as bezel and transparent dial cover with O-rings hermetically sealed
- Measuring spindle sealed by means of rubber sleeve, thus preventing contamination by liquids and impurities
- Delivered in plastic case

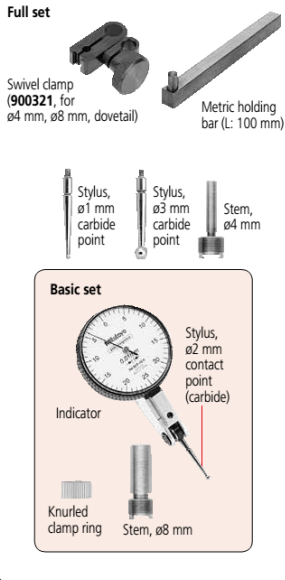
Technical Data

	Range	Readings	Dial dia.	Overtravel	Measuring force	Accuracy (DIN 878)		f_u	Order no.
	mm	mm	mm	mm	N	f_e μm	f_{ges} μm	μm	
803	3	0,01	35	0,2	1,1 N	10	12	3	4324110
803 W	3	0,01	35	0,2	1,1 N	10	12	3	4326100
810	10	0,01	50	1,1	1,0 N	15	17	3	4311110
810 L	10	0,01	50	1,1	1,0 N	15	17	3	4327110
810 W	10	0,01	50	1,1	1,0 N	15	17	3	4315100
810 B	0,8(±0,4)	0,01	50	0,05	1,0 N	7	9	3	4317110

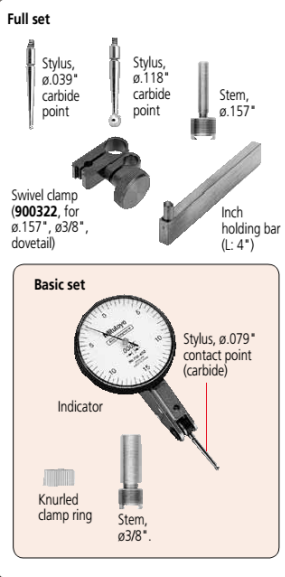
	Range	Readings	Dial dia.	Overtravel	Measuring force	Accuracy (DIN 878)		f_u	Order no.
	inch	inch	inch	inch	N	f_e inch	f_{ges} inch	inch	
803 Z	.120"	.0005"	1.4"	.008"	1,1 N	.0004"	.0005"	.00012"	4324911
810 Z	.400"	.0005"	2.0"	.040"	1,0 N	.0006"	.0007"	.00012"	4311911

Mitutoyo 513-405E Dial Gauge Specifications

Set Configuration: Metric and Metric/Inch



Set Configuration: Inch and Inch/Metric



SPECIFICATIONS

Metric						
Code No.	Graduation	Range	Accuracy	Scale	Measuring force	Price
Basic Set						
513-424E	0.01 mm	0.5 mm	5 µm	0-25-0	0.3 N or less	£80.90
513-414E	0.01 mm	0.5 mm	10 µm	0-25-0	0.2 N or less	£82.10
513-404E	0.01 mm	0.8 mm	8 µm	0-40-0	0.3 N or less	£72.30
513-474E*	0.01 mm	0.8 mm	8 µm	0-40-0	0.3 N or less	£83.80
513-415E	0.01 mm	1 mm	10 µm	0-50-0	0.2 N or less	£89.20
513-426E	0.01 mm	1.5 mm	8 µm	0-25-0	0.4 N or less	£83.30
513-405E	0.002 mm	0.2 mm	3 µm	0-100-0	0.3 N or less	£87.80
513-425E	0.002 mm	0.6 mm	6 µm	0-100-0	0.4 N or less	£102.00
513-401E	0.001 mm	0.14 mm	3 µm	0-70-0	0.3 N or less	£87.80

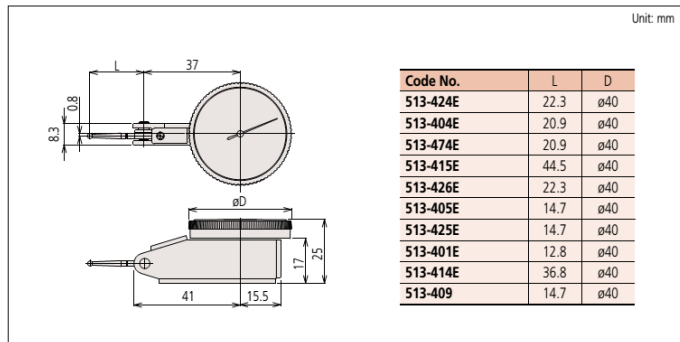
Full Set						
513-424T	0.01 mm	0.5 mm	5 µm	0-25-0	0.3 N or less	£99.70
513-414T	0.01 mm	0.5 mm	10 µm	0-25-0	0.2 N or less	£116.00
513-404T	0.01 mm	0.8 mm	8 µm	0-40-0	0.3 N or less	£87.50
513-415T	0.01 mm	1 mm	10 µm	0-50-0	0.2 N or less	£108.00
513-405T	0.002 mm	0.2 mm	3 µm	0-100-0	0.3 N or less	£106.00

Inch						
Code No.	Graduation	Range	Accuracy	Scale	Measuring force	Price
Basic Set						
513-402	.0005"	.03"	±.0005"	0-15-0	0.3 N or less	£72.00
513-412	.0005"	.03"	±.0005"	0-15-0	0.2 N or less	£104.00
513-403	.0001"	.008"	±.0001"	0-4-0	0.3 N or less	£94.00
Full Set						
513-402T	.0005"	.03"	±.0005"	0-15-0	0.3 N or less	£102.00
513-412T	.0005"	.03"	±.0005"	0-15-0	0.2 N or less	£125.00
513-403T	.0001"	.008"	±.0001"	0-4-0	0.3 N or less	£125.00

Metric/inch						
Code No.	Graduation	Range	Accuracy	Scale	Measuring force	Price
Full Set						
513-409T	0.002 mm / .0001"	0.2 mm / .0075"	3 µm	0-10-0 / 0-3.8-0	0.3 N or less	£115.00
Inch/metric						
Full Set						
513-406T	.0005" / 0.01 mm	.03" / 0.7 mm	±.0005"	0-15-0 / 0-35-0	0.3 N or less	£108.00

* Provided with a ø2 mm ruby contact point as a substitute for ø2 mm carbide contact point.

DIMENSIONS



Appendix D : ISO 230-2

Definitions

Target position - P_i ($i = 1$ to m): The position to which the moving part is commanded to move. i identifies the particular position among other selected target positions along the axis.

Actual position - P_{ij} ($i = 1$ to m ; $j = 1$ to n): The measured position reached by the moving part on the j^{th} approach to the i^{th} target position.

Positional deviation - x_{ij} : Actual position reached by the moving part minus the target position. It can be calculated according to (9).

$$x_{ij} = P_{ij} - P_i \quad (9)$$

Unidirectional: The approach to a target position is always made in the same direction. The symbol \uparrow signifies an approach in the positive direction and \downarrow signifies an approach in the negative direction e.g. $x_{ij} \uparrow$ or $x_{ij} \downarrow$.

Bi-directional: the approach to the target position is made in either direction.

Expanded uncertainty: the result of a measurement that is likely to encompass a large portion of the distribution of values.

Coverage factor: This is a multiplier of the combined standard uncertainty in order to obtain an expanded uncertainty.

Temperature: All measurements were carried out at room temperature 20° C. If this was not the case, certain expansion coefficients may change. This could alter the effectiveness of the results attained.

Formulae

Mean unidirectional positional deviation at a position ($\bar{x}_i \uparrow$ or $\bar{x}_i \downarrow$): Arithmetic mean of the positional deviations obtained by a series of n unidirectional approaches to a position P_i . They can be calculated according to (10) and (11).

$$\bar{x}_i \uparrow = \frac{1}{n} \sum_{j=1}^n x_{ij} \uparrow \quad (10)$$

$$\bar{x}_i \downarrow = \frac{1}{n} \sum_{j=1}^n x_{ij} \downarrow \quad (11)$$

Mean bi-directional positional deviation at a position (\bar{x}_i): Arithmetic mean of the mean unidirectional positional deviations, $\bar{x}_i \uparrow$ and $\bar{x}_i \downarrow$ obtained from the two directions of approach at a position P_i . It can be calculated according to (12).

$$\bar{x}_i = \frac{\bar{x}_i \uparrow + \bar{x}_i \downarrow}{2} \quad (12)$$

Reversal value at a position (B_i): Value of the difference between the mean unidirectional positional deviations obtained from the two directions of approach at a position P_i . It can be calculated according to (13).

$$B_i = \bar{x}_i \uparrow - \bar{x}_i \downarrow \quad (13)$$

Reversal value of an axis (B): Maximum of the absolute reversal values $|B_i|$ at all target positions along or around the axis. It can be calculated according to (14).

$$B = \max. [|B_i|] \quad (14)$$

Mean reversal value of an axis (\overline{B}): Arithmetic mean of the reversal values B_i at all target positions along or around the axis. It can be calculated according to (15).

$$\overline{B} = \frac{1}{m} \sum_{i=1}^m B_i \quad (15)$$

Estimator of the unidirectional axis repeatability of positioning at a position ($S_i \uparrow$ or $S_i \downarrow$): Estimator of the standard uncertainty of the positional deviations obtained by a series of n unidirectional approaches at a position P_i . They can be calculated according to (16) and (17).

$$s_i \uparrow = \sqrt{\frac{1}{n-1} \sum_{j=1}^n (x_{ij} \uparrow - \bar{x}_i \uparrow)^2} \quad (16)$$

$$s_i \downarrow = \sqrt{\frac{1}{n-1} \sum_{j=1}^n (x_{ij} \downarrow - \bar{x}_i \downarrow)^2} \quad (17)$$

Unidirectional repeatability of positioning at a position ($R_i \uparrow$ or $R_i \downarrow$): Range derived from the expanded uncertainty of unidirectional positional deviations at a position P_i using a coverage factor of 2. They can be calculated according to (18) and (19).

$$R_i \uparrow = 4s_i \uparrow \quad (18)$$

$$R_i \downarrow = 4s_i \downarrow \quad (19)$$

Bi-directional repeatability of positioning at a position (R_i): It can be calculated according to (20).

$$R_i = \max. [2s_i \uparrow + 2s_i \downarrow + |B_i|; R_i \uparrow; R_i \downarrow] \quad (20)$$

Unidirectional repeatability of positioning (R): Maximum value of the repeatability of positioning at any position P_i along or around the axis. It can be calculated according to (21) and (22).

$$R \uparrow = \max. [R_i \uparrow] \quad (21)$$

$$R \downarrow = \max. [R_i \downarrow] \quad (22)$$

Bi-directional repeatability of positioning of an axis R : Maximum value of the repeatability of positioning at any position P_i along or around the axis. It can be calculated according to (23).

$$R = \max. [R_i] \quad (23)$$

Unidirectional systematic positional deviation of an axis ($E \uparrow$ or $E \downarrow$): The difference between the algebraic maximum and minimum of the mean unidirectional positional deviations for one approach direction $\bar{x}_i \uparrow$ or $\bar{x}_i \downarrow$ at any position P_i along or around the axis. They can be calculated according to (24) and (25).

$$E \uparrow = \max. [\bar{x}_i \uparrow] - \min. [\bar{x}_i \uparrow] \quad (24)$$

$$E \downarrow = \max. [\bar{x}_i \downarrow] - \min. [\bar{x}_i \downarrow] \quad (25)$$

Bi-directional systematic positional deviation of an axis (E): The difference between the algebraic maximum and minimum of the mean unidirectional positional deviations for both approach direction $\bar{x}_i \uparrow$ or $\bar{x}_i \downarrow$ at any position P_i along or around the axis. It can be calculated according to (26).

$$E = \max. [\bar{x}_i \uparrow; \bar{x}_i \downarrow] - \min. [\bar{x}_i \uparrow; \bar{x}_i \downarrow] \quad (26)$$

Range mean bi-directional positional deviation of an axis (M): The difference between the algebraic maximum and minimum of the mean bi-directional positional deviations x_i at any position P_i along or around the axis. It can be calculated according to (27).

$$M = \max. [\bar{x}_i] - \min. [\bar{x}_i] \quad (27)$$

Unidirectional accuracy of positioning of an axis ($A \uparrow$ or $A \downarrow$): Range derived from the combination of the unidirectional systematic deviations and the estimator of the standard uncertainty of unidirectional positioning using a coverage factor of 2. They can be calculated according to (28) and (29).

$$A \uparrow = \max. [\bar{x}_i \uparrow + 2s_i \uparrow] - \min. [\bar{x}_i \uparrow - 2s_i \uparrow] \quad (28)$$

$$A \downarrow = \max. [\bar{x}_i \downarrow + 2s_i \downarrow] - \min. [\bar{x}_i \downarrow - 2s_i \downarrow] \quad (29)$$

Bi-directional accuracy of positioning of an axis (A): Range derived from the combination of the bidirectional systematic deviations and the estimator of the standard uncertainty of bi-directional positioning using a coverage factor of 2. It can be calculated according to (30).

$$A = \max. [\bar{x}_i \uparrow + 2s_i \uparrow; \bar{x}_i \downarrow - 2s_i \downarrow] - \min. [\bar{x}_i \uparrow - 2s_i \uparrow; \bar{x}_i \downarrow + 2s_i \downarrow] \quad (30)$$

Appendix E : Fused Quartz Datasheet



Tynevale Works, Newburn, Newcastle upon Tyne, NE15 8LN, England
 Tel: (00 44) 191 264 6801 • Fax: (00 44) 191 229 0028
 e-mail: sales@multi-lab.co.uk • www.multi-lab.co.uk

Purity

Element	Trace Elements in ppm (typical)	
	TSC-3	
Al	1.5	
Ca	0.5	
Cr	< 0.01	
Cu	< 0.01	
Fe	0.1	
K	0.2	
Li	0.2	
Mn	0.01	
Na	0.1	
Nd	0.01	
Ti	1.3	
Y	< 0.1	
Zr	1.3	
OH	170	

Thermal Properties

Thermal coefficient of expansion	0.54×10^{-6}	K^{-1}
Specific heat at 20°C	7.5×10^2	$J.kg^{-1}.K^{-1}$
Heat conductivity at 20°C	1.38	$W.m^{-1}.K^{-1}$
Strain point	1080	°C
Annealing Point	1200	°C
Softening Point	1730	°C

Mechanical Properties

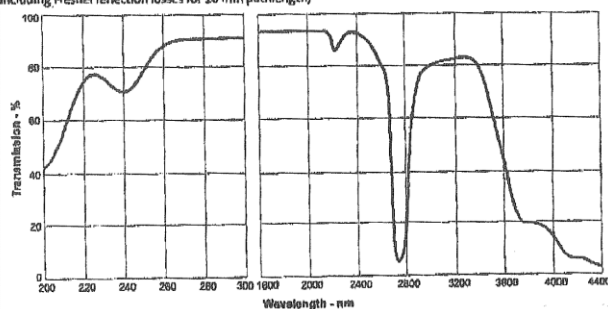
Density	2.2	g/cm^3
Hardness	7	Mohs scale
Tensile strength	50	MPa
Compressive strength	1100	MPa
Bending strength	65	MPa
Torsion strength	90	MPa
Young's modulus	72	GPa
Poisson's coefficient	0.16	-

Electrical Properties

Dielectric constant	3.78	-
Loss factor at 1 MHz	1×10^{-4}	-
Dielectric rigidity	3.7×10^7	$V.m^{-1}$
Resistivity at 20°C	1×10^{20}	$\Omega.m$
Resistivity at 800°C	5×10^4	$\Omega.m$
Resistivity at 1000°C	1×10^6	$\Omega.m$

Optical Properties

Typical External Transmission
 (including Fresnel reflection losses for 10 mm pathlength)



Refractive index at 587.56 nm 1.4585

Multi-lab Limited

High Temperature / Industrial Ceramics
 Transparent, Satin & Opaque Quartz

Multi-sil Slip Cast Quartz Products. Glassblowing, Fabrication, Grinding & Polishing



Certificate No: 952586

Appendix F

Channel Dimension Analysis

Table 44: Results from channel depth analysis

Sample / Channel	Depth 1 (µm)	Depth 2 (µm)	Depth 3 (µm)	Depth Average (µm)	Depth Std. Dev. (µm)
1	545	572	572	563	16
2	297	294	303	298	5
3	157	160	154	157	3
4	661	668	694	674	17
5	608	584	620	604	19
6	781	804	781	789	14
7	769	769	807	782	22
8	703	668	703	691	20
9	670	657	670	666	8
10	262	257	252	257	5
11	122	121	117	120	3
12	74	73	75	74	1
13	638	638	638	638	0
14	498	488	513	500	13
15	375	379	368	374	6
16	974	993	955	974	19
17	852	878	878	869	15
18	748	763	763	758	9
19	155	152	149	152	3
20	95	100	98	98	2
21	72	75	71	72	2
22	462	439	480	460	21
23	364	368	375	369	6
24	286	289	272	282	9
25	757	734	795	762	31
26	551	557	573	560	11
27	569	569	592	577	13

Table 45: Results from channel width (top) analysis

Sample / Channel	Width 1 (µm)	Width 2 (µm)	Width 3 (µm)	Width Average (µm)	Width Std. Dev. (µm)
1	213	207	204	208	4
2	176	181	174	177	4
3	172	177	170	173	4
4	197	195	197	196	1
5	182	173	182	179	5
6	206	214	196	205	9
7	193	183	185	187	5
8	170	162	170	167	5
9	170	167	165	167	3
10	179	175	175	177	2
11	167	175	165	169	5
12	149	145	149	148	3
13	185	187	179	184	4
14	179	186	184	183	4
15	185	178	183	182	4
16	191	193	191	192	1
17	188	182	186	185	3
18	209	209	203	207	4
19	185	189	178	184	6
20	173	180	176	176	3
21	146	147	140	145	4
22	191	197	191	193	3
23	197	199	197	198	1
24	185	191	185	187	3
25	206	200	196	201	5
26	200	210	190	200	10
27	178	185	169	177	8

Table 46: Results from channel width (50%) analysis

Sample / Channel	Width 50% 1 (µm)	Width 50% 2 (µm)	Width 50% 3 (µm)	Width 50% Average (µm)	Width 50% Std. Dev. (µm)
1	41	40	42	41	1
2	65	68	68	67	2
3	77	75	73	75	2
4	45	43	46	45	2
5	33	34	34	33	0
6	33	35	32	33	1
7	34	35	36	35	1
8	35	34	34	34	1
9	42	43	42	42	1
10	77	76	78	77	1
11	83	79	83	82	2
12	83	82	81	82	1
13	54	53	56	54	2
14	63	60	66	63	3
15	66	68	69	68	1
16	51	51	53	52	1
17	54	57	56	56	1
18	63	64	64	63	0
19	84	82	81	82	2
20	91	95	94	93	2
21	95	97	94	95	1
22	77	81	75	78	3
23	83	87	85	85	2
24	74	71	75	73	2
25	72	74	75	74	1
26	74	75	71	74	2
27	66	69	67	67	2

Appendix G : 3D Analysis

Measurement results from the evaluation of the 3D measurement performance.

Run 1

	Lower Plane Height (μm)	Upper Plane Height (μm)	Measured Height (μm)
Sub-run 1	5.4	516.2	510.8
Sub-run 2	6.5	516.9	510.4
Sub-run 3	5.1	517.2	512.1
Sub-run 4	4.7	516.9	512.2
Sub-run 5	4.3	517.2	512.9
Sub-run 6	3.9	515.2	511.3

Average Measured Height (μm)	511.6
Step Height (μm)	512

Accuracy (%)	99.92
Standard Deviation (μm)	0.9

Run 2

	Lower Plane Height (μm)	Upper Plane Height (μm)	Measured Height (μm)
Sub-run 1	3.0	506.8	503.8
Sub-run 2	2.9	506.3	503.4
Sub-run 3	2.3	506.2	503.8
Sub-run 4	2.5	505.4	502.9
Sub-run 5	2.3	505.1	502.8
Sub-run 6	2.2	505.6	503.4

Average Measured Height (μm)	503.4
Step Height (μm)	512

Accuracy (%)	98.32
Standard Deviation (μm)	0.4

Run 3

	Lower Plane Height (μm)	Upper Plane Height (μm)	Measured Height (μm)
Sub-run 1	3.6	106.7	103.1
Sub-run 2	3.6	106.7	103.1
Sub-run 3	3.6	106.8	103.1
Sub-run 4	3.1	106.5	103.4
Sub-run 5	3.6	107.1	103.5
Sub-run 6	3.6	106.7	103.1

Average Measured Height (μm)	103.2
Step Height (μm)	103

Accuracy (%)	99.81
Standard Deviation (μm)	0.2

Run 4

	Lower Plane Height (μm)	Upper Plane Height (μm)	Measured Height (μm)
Sub-run 1	3.1	106.2	103.1
Sub-run 2	3.4	106.5	103.1
Sub-run 3	3	106.3	103.2
Sub-run 4	3	106.2	103.2
Sub-run 5	3.3	106.2	102.9
Sub-run 6	3.5	106.6	103.1

Average Measured Height (μm)	103.1
Step Height (μm)	103

Accuracy (%)	99.90
Standard Deviation (μm)	0.1

Run 5

	Lower Plane Height (μm)	Upper Plane Height (μm)	Measured Height (μm)
Sub-run 1	4.4	107	102.6
Sub-run 2	4.4	107.1	102.7
Sub-run 3	4.5	107.8	103.3
Sub-run 4	4.1	106.9	102.8
Sub-run 5	4.7	107.4	102.7
Sub-run 6	4.7	106.8	102.1

Average Measured Height (μm)	102.7
Step Height (μm)	103

Accuracy (%)	99.71
Standard Deviation (μm)	0.4

Run 6

	Lower Plane Height (μm)	Upper Plane Height (μm)	Measured Height (μm)
Sub-run 1	3.4	105.8	102.4
Sub-run 2	3.5	106	102.5
Sub-run 3	3.6	106.1	102.5
Sub-run 4	3.5	106	102.4
Sub-run 5	3.6	106	102.4
Sub-run 6	3.5	105.9	102.4

Average Measured Height (μm)	102.4
Step Height (μm)	103

Accuracy (%)	99.42
Standard Deviation (μm)	0.1

Run 7

	Lower Plane Height (μm)	Upper Plane Height (μm)	Measured Height (μm)
Sub-run 1	4.1	106.5	102.4
Sub-run 2	3.9	106.4	102.6
Sub-run 3	4.1	106.9	102.7
Sub-run 4	3.8	106.1	102.3
Sub-run 5	3.8	105.9	102.1
Sub-run 6	3.5	106.1	102.6

Average Measured Height (μm)	102.5
Step Height (μm)	103

Accuracy (%)	99.51
Standard Deviation (μm)	0.2

Run 8

	Lower Plane Height (μm)	Upper Plane Height (μm)	Measured Height (μm)
Sub-run 1	2.5	506.7	504.2
Sub-run 2	2.8	506.4	503.6
Sub-run 3	2.9	506.6	503.7
Sub-run 4	2.8	505.8	503
Sub-run 5	3.3	505.9	502.7
Sub-run 6	2.8	505.3	502.5

Average Measured Height (μm)	503.3
Step Height (μm)	512

Accuracy (%)	98.30
Standard Deviation (μm)	0.7

Run 9

	Lower Plane Height (μm)	Upper Plane Height (μm)	Measured Height (μm)
Sub-run 1	15.6	118.7	103.1
Sub-run 2	15.7	118.7	103
Sub-run 3	15.5	118.3	102.8
Sub-run 4	15.6	118.7	103.1
Sub-run 5	15.7	118.5	102.7
Sub-run 6	15.8	118.7	102.9

Average Measured Height (μm)	102.9
Step Height (μm)	103

Accuracy (%)	99.90
Standard Deviation (μm)	0.1

Run 10

	Lower Plane Height (μm)	Upper Plane Height (μm)	Measured Height (μm)
Sub-run 1	2.1	104.8	102.7
Sub-run 2	2.4	104.9	102.6
Sub-run 3	2.5	105.1	102.5
Sub-run 4	2.3	105	102.7
Sub-run 5	2.5	105	102.5
Sub-run 6	2.2	104.9	102.7

Average Measured Height (μm)	102.6
Step Height (μm)	103

Accuracy (%)	99.61
Standard Deviation (μm)	0.1